Thermal shrinkage cracking in steel fibre reinforced underwater concrete floors

A probabilistic finite element approach

D.A.H. Slockers

TU Delft

abt

Thermal shrinkage cracking in steel fibre reinforced underwater concrete floors

A probabilistic finite element approach

Master's Thesis, by

D.A.H. Slockers

to obtain the degree of Master of Science in Civil Engineering
at the Delft University of Technology,

to be defended publicly on Wednesday 15:00, 21 June 2023.

Student number:	4382579	
Date:	16 June 2023	
Thesis committee:	Prof. dr. ir. M.A.N Hendriks	TU Delft
	Dr. ir. L.J. van der Meer	ABT
	Dr. ir. A. de Boer	Ane de Boer Advies
	Dr. ir. S.C. Barbosa Nunes	TU Delft
	Dr. ir. O. Morales Napoles	TU Delft

TU Delft

abt

Preface

This thesis is the final chapter of the master Structural Engineering at the faculty of Civil Engineering and Geosciences at the Delft University of Technology. The research was performed under the supervision of my graduation committee and it was made possible by the engineering and consultancy firm ABT. A CROW committee is currently creating a recommendation on permanent steel fibre reinforced underwater concrete floors, from which the topic of this thesis was derived.

I want to thank all of my supervisors for their support, feedback and guiding me through the process of doing research and writing a thesis. First of all, I want to express my gratitude towards ABT for giving me the opportunity and tools to complete this thesis. Lex van der Meer, thank you for your advice and encouragement and for taking the time to help me with complex topics and DIANA. Especially at the beginning, there was quite a steep learning curve. I appreciate that you were always available for a usually longer than planned meeting because there was so much to discuss. I enjoyed your enthusiasm about the topic, which is perfectly illustrated by a quote from you during a meeting this last week: ”I don’t think we are going to find the answer to this problem in this last week, but I am truly fascinated by this”. Ane de Boer, thank you for sharing all your expertise and providing me with critical notes on my work. I really appreciate the experience that you shared about finite element modelling. I think it is very valuable to hear your stories on how this technology used to be and how it has advanced over time. I enjoyed it when you asked for my models after presenting them and then getting an e-mail the day after with your own results, asking to compare them to mine. This shows how involved Lex and Ane were with the topic, which was a great motivator during my thesis. I learned a lot about finite element analysis from both, and their enthusiasm greatly deepened my interest in this field. I want to thank Max Hendriks, the chair of my graduation committee, for guiding the process towards a good end, overseeing the scientific relevance of this project and his advice on how to properly and clearly convey the message of this thesis. Sandra Barbosa Nunes, thank you for sharing your expertise about FRC, giving your opinion about specific concrete topics and providing me with extensive feedback and helpful additional articles. Oswaldo Morales Napoles, thank you for your time discussing the probabilistic part of this thesis, connecting me to people with similar topics who could share their experience and for your supportive words. Finally, I want to thank all the colleagues from ABT, who took the time, to talk about the topic and provide me with information and to Panagiotis Evangeliou and Angelo Garofano from DIANA FEA for their support with PROBAB during the first half of my thesis.

This thesis also marks the end of my time as a student in Delft, and I would like to thank all of my friends for the wonderful time we spent together and all the fun activities we did and are still doing. Besides that, I want to express my appreciation to Wouter and Wim for the excellent company and (extended) coffee breaks in the library, especially during my thesis. A special mention goes to Bojan, with whom I spend a lot of fun times during my Master, but also on a serious note during my thesis. Thank you for our valuable discussions and insights about my results, and your help and advice with coding.

Finally, I want to thank my family for their support during my entire studies. Thanks to my sister Lindsay for keeping me sane and for the parties we went to. Thank you, Berber for always encouraging and being there for me, especially during this last year. I haven not always been easy, but thanks for sticking around with me, and I am looking very much forward to what lies ahead. Last but not least, to my parents, I want to express my everlasting gratitude for always being there for me and for their unconditional support during my entire study. I could not have done it without you.

D.A.H. Slockers
Delft, 15 June 2023

Summary

This thesis explores a suitable method and appropriate input to determine the failure probability of thermal shrinkage cracking in a steel fibre-reinforced underwater concrete floor by examining the factors that influence this failure probability.

An underwater concrete (UWC) floor is a common construction type in the Netherlands that is often applied to create building pits under the groundwater table. Usually, these (generally unreinforced) UWC floors only function as a watertight bottom layer of the building pit with only a temporary sealing function. Water tightness and crack prevention are very important aspects of this type of construction. A permanent reinforced structural top floor is frequently used on top of the temporary UWC floor to make a completely watertight construction, which is not the most sustainable and cost-efficient solution. Advances in concrete technology such as fibre-reinforced concrete have made it possible to integrate both the UWC and structural top floor or even use the UWC floor as the permanent structural floor. In these cases, the UWC floor should already function as a watertight barrier and controlling leakage by limiting the crack width becomes even more important. The addition of fibres to concrete may prevent through crack formation in the UWC slab and the possible consequent leakage. An important cause of cracking in UWC floors is thermal shrinkage during the cooling phase of the hardening reaction shortly after casting the UWC floor.

Currently, there are no guidelines for the construction of fibre-reinforced concrete (FRC) floors and the prevention or limitation of thermal shrinkage cracking. A CROW-committee ”Steel fibre reinforced underwater concrete (SFRUWC) floor as permanent structural floor” has been formed. This committee aims to set up a design recommendation and part of that is addressing the thermal shrinkage cracking problem. There is a lot of uncertainty in geometry, material properties and boundary conditions associated with SFRUWC floor design and construction. Because of this, there is a need for a probabilistic approach to investigate the influence of these uncertainties and tolerances on crack formation in SFRUWC floors during the hardening phase. This research aims to determine a suitable probabilistic method to investigate the failure probability of SFRUWC floors and the parameters that influence this.

In order to achieve this, a finite element model was developed that determines the shrinkage cracking behaviour in a part of a UWC floor in a building pit. Before this model could be developed, all the necessary input parameters and design equations were collected from literature and existing guidelines. To set up a model, first the behaviour of UWC floors was studied, followed by the development of a finite element model that includes the hardening behaviour and strength development of young concrete. An important aspect of this finite element model is the use of random fields to introduce spatial variation in the strength properties of the SFRUWC floor, which is a first step to include stochastic variation in the model for the probabilistic analysis. A probabilistic sensitivity study was performed with the finite element model by calculating multiple samples for each set of input parameters. Separate input parameters were varied and the influence on the results was investigated. The parameters that were considered, include the random field properties, material properties and thermal properties. Finally, a full Monte Carlo analysis was performed to give a proof of concept on how to calculate the failure probability regarding thermal shrinkage cracking in SFRUWC floors.

In order to prevent leaking cracks and satisfy the crack width criterion, the tension-hardening behaviour of FRC has to be utilised. Tension hardening behaviour will lead to a distributed cracking pattern, consisting of multiple small cracks which can satisfy the crack width criterion as opposed to a single large separation crack which does not satisfy the maximum allowable crack width criterion. It was found

that the tensile behaviour of FRC and the use of random fields to model this tensile behaviour were major parameters that influenced the crack width and the occurrence of a distributed crack pattern. An important parameter is the standard deviation of the random field, which influences the difference between the maximum and minimum tensile strength in different locations in the slab. Looking at material behaviour, the main conclusion was that the introduction of a small hardening branch in the tensile material model was the governing influence factor. Both the standard deviation of the random field and the introduction of a hardening branch in the tensile behaviour affect the ratio between the tensile strength of the ordinary concrete and the residual tensile strength of the fibre-reinforced concrete. These two factors in combination with the model that was used, turned out to be dominating the results in such a way that the other input parameters only had a relatively small influence on the crack widths.

To determine maximum crack widths in SFRUWC floor it is essential to consider multiple samples with different random fields to find out if only a distributed crack pattern is possible or whether also single localised cracks can occur. The possibility of both these results being able to occur, leads to a large possible error in the maximum crack width. The results of this thesis have shown that the random field parameters remain uncertain and experimental research is needed to determine these correctly. Until then, it is important to investigate how significantly these parameters influence the results. It is recommended to extend this research by improving the model by making it more realistic and finding out if these two factors are still the dominating input parameters.

Samenvatting

Deze scriptie onderzoekt een geschikte methode en de bijbehorende invoerparameters om de faalkans van thermische krimpscheuren in staalvezelversterkte onderwaterbetonvloeren te bepalen door de factoren die deze faalkans beïnvloeden te onderzoeken.

Een onderwaterbeton (OWB) vloer is een veelvoorkomende constructie, die in Nederland vaak wordt toegepast om bouwputten onder het grondwaterniveau te creëren. Gewoonlijk functioneren deze (meestal ongewapende) OWB-vloeren alleen als een water afdichtende onderlaag van een bouwput, waarbij die slechts een tijdelijke functie vervuld. De waterdichtheid en de beperking van scheurvorming is hier dus een belangrijk aspect. Momenteel wordt er meestal een constructieve vloer boven op de tijdelijke OWB-vloer gestort, om zo een waterdichte constructie te creëren, maar dit is niet de goedkoopste en meest duurzame oplossing. De ontwikkeling van staalvezelversterkt beton maakt het mogelijk om de onderwaterbetonvloer en de constructieve vloer te integreren of om zelfs alleen een OWB-vloer te gebruiken, die dan functioneert als de definitieve constructieve vloer. In deze ontwerpen moet de OWB-vloer al goed presteren als waterdichte barrière, en het beheersen van lekkage door de scheurwijdte te beperken is in deze ontwerpen nog belangrijker. Het toevoegen van staalvezels aan beton kan het ontstaan van gelokaliseerde doorgaande scheuren in de OWB-plaat voorkomen en daarmee mogelijke lekkage voorkomen. Een belangrijke oorzaak van scheuren in OWB-vloeren is thermische krimp tijdens de afkoelfase van de hydratatiereactie kort na het storten van de OWB-vloer.

Op dit moment zijn er nog geen richtlijnen voor het ontwerpen van vezel versterkte betonnen vloeren en de preventie of beperking van thermische krimpscheuren. Er is een CROW-commissie ”Staalvezelversterkte onderwaterbeton (SVVOWB) vloer als definitieve constructievloer” opgericht met het doel om richtlijnen op te stellen, waarbij ook het probleem van thermische krimpscheuren wordt meegenomen. Er is veel onzekerheid over de uitvoeringstoleranties, materiaaleigenschappen en randvoorwaarden die gepaard gaan met het ontwerpen en realiseren van SVVOWB-vloeren. Hierdoor is er een noodzaak aan een probabilistische benadering om de invloed van deze onzekerheden en toleranties op scheurvorming in SVVOWB-vloeren tijdens de uithardingsfase te onderzoeken. Deze scriptie heeft als doel om een geschikte probabilistische methode te bepalen om de faalkans van thermische krimpscheuren in OWB-vloeren, en de parameters die hier invloed op hebben te onderzoeken.

Om dit te bereiken is er een eindig elementen model (EEM) ontwikkeld dat het scheurgedrag ten gevolge van uithardingskrimp bepaalt in een deel van een OWB-vloer in een bouwkuip. Voordat dit model kon worden ontwikkeld, zijn alle benodigde invoerparameters verzameld uit de literatuur en bestaande richtlijnen. Eerst is het constructieve gedrag van OWB-vloeren bestudeerd. Vervolgens is het verhardingsgedrag en de sterkteontwikkeling van beton gemodelleerd in een eindig elementen model. Een belangrijk aspect van dit eindige elementenmodel is het gebruik van zogenaamde “random fields” om ruimtelijke variatie in de sterkte eigenschappen van een SVVOWB-vloer te introduceren. Dit is de eerste stap om stochastische variatie in het model voor de probabilistische analyse mee te nemen. Met behulp van het eindige elementenmodel, werd er een probabilistische gevoeligheidsanalyse uitgevoerd door meerdere realisaties te berekenen voor verschillende combinaties van invoerparameters. De invloed op de resultaten is onderzocht door afzonderlijke invoerparameters te variëren. De belangrijkste parameters waren de random field, materiaal- en thermische eigenschappen. Ten slotte is er een volledige Monte Carlo-analyse uitgevoerd om te laten zien hoe de faalkans met betrekking tot thermische krimpscheuren in SVVOWB-vloeren kan worden berekend.

Het tension-hardening gedrag wat SVV beton kan vertonen is een belangrijk aspect wat moet worden gebruikt om gelokaliseerde watervoerende scheuren te voorkomen. Tension-hardening gedrag leidt tot een verdeeld scheuren patroon, wat bestaat uit meerdere kleine scheuren die allemaal kleiner zijn dat de maximaal toelaatbare scheurwijdte. Hiertegenover staat het ontstaan van een grote doorgaande scheur, die niet voldoet aan het scheurwijdte criterium. Er is vastgesteld dat het trekgedrag van vezelversterkt beton en het gebruik van random fields om dit gedrag te modelleren, belangrijke aspecten zijn die invloed hebben op het ontstaan van een verdeeld scheuren patroon en de bijbehorende maximale scheurwijdte. Een belangrijke parameter is hier de standaardafwijking van het random field, wat invloed heeft op de verhouding tussen de maximale en minimale treksterkte op verschillende locaties in de vloer. Wat het materiaalgedrag betreft, is de belangrijkste conclusie dat de introductie van een klein “hardeningstakje” in het trekgedrag de meest belangrijke invloedsfactor is. Zowel de standaardafwijking van het random field en de introductie van een tension-hardenings takje in het trekgedrag, beïnvloeden de verhouding tussen de treksterkte van het gewone beton en de resttreksterkte van het vezelversterkte beton. Het bleek dat in dit eindige elementen model, deze twee factoren de resultaten dusdanig beïnvloeden dat de andere invoerparameters slechts een relatief verwaarloosbare invloed hadden op de scheurwijdtes.

Om de maximale scheurwijdte in SVVOWB-vloeren te bepalen, is het essentieel om meerdere realisaties met verschillende random fields door te rekenen, om zo te achterhalen of er alleen een verdeeld scheurpatroon mogelijk is of dat ook enkele gelokaliseerde scheuren kunnen voorkomen. De mogelijkheid dat beide types kunnen optreden, leidt tot een grote potentiële fout in de bepaling van de maximale scheurwijdte. De resultaten van deze scriptie hebben aangetoond dat de keuze voor de parameters van het random field niet helemaal goed te beargumenteren is en dat hiervoor extra experimenteel onderzoek nodig is. Tot die tijd is het belangrijk om te onderzoeken hoe de aannames van deze parameters de resultaten beïnvloeden. Het wordt aanbevolen om dit onderzoek uit te breiden door het EEM te verbeteren met realistischere randvoorwaarden en te onderzoeken of deze twee factoren in dat geval nog steeds de overheersende invoerparameters zijn.

Contents

List of Figures

List of Tables

Symbols

Uppercase

Sign	Description	Unit
C_{av}	Average heat capacity of concrete during hydration	J / K
E_a	activation energy	J / mol
E_{c}	Young's modulus of concrete	MPa
E_{cm}	Mean Young's modulus of concrete	MPa
F_j	Load corresponding to point CMOD_j	N
FRCFAC	Stress scaling factor of the FRC stress-CMOD tensile behaviour graph	-
L	Length of the slab	m
L_c	Correlation length	m
M	Maturity of concrete	°C s
N	Total number of samples	-
N	Number of failing samples	-
N_x	Number of points in random field mesh in x-direction	-
N_y	Number of points in random field mesh in y-direction	-
N_z	Number of points in random field mesh in z-direction	-
P_f	Failure probability	-
Q_t	Heat that is exchanged with the surroundings	J
Q_{pot}	Maximum potential heat produced by the reaction	J
Q_t	Total heat that is produced up to a certain time	J
R	Universal gas constant, 8.314 J / (mol · °C)	J / (mol · °C)
T	Temperature	°C
T_0	Casting temperature	°C
T_{average}	Average component of the temperature distribution	°C
T_{Eigen}	Eigen component of the temperature distribution	°C
T_{ext}	External temperature / Temperature of environment	°C
T_{linear}	Linear component of the temperature distribution	°C
T_{ref}	Reference temperature, 20°C	°C
V_{P_f}	Coeficient of variation of the failure probability	-

Lowercase

Sign	Description	Unit
b	Width of specimen	m
c	Amount of cement	kg
c_c	Specific heat capacity of concrete	J / (kg · K)
c_h	Amount of hydrated cement	kg
$f_{\text{B/C/D/E/Q}}$	Residual tensile strength at point B, C, D, E or Q	MPa
f_{c}	Compressive strength of concrete	MPa
f_{cm}	Mean compressive strength of concrete	MPa

f_{ctm}	Mean tensile strength of concrete	MPa
f_{ctk}	Characteristic tensile strength of concrete	MPa
$f_{c\infty}$	Maximum compressive strength of concrete at $t = \infty$	MPa
f_{Fts}	Residual tensile strength at SLS	MPa
f_{Ftu}	Residual tensile strength at ULS	MPa
f_{Rj}	Mean residual flexural strength of point j for FRC	MPa
f_{Rjk}	Characteristic residual flexural strength of point j for FRC	MPa
h	Height of the slab	m
$h_{c,top}$	Heat transfer coefficient at the top edge	$W\,m^{-2}K^{-1}$
$h_{c,bottom}$	Heat transfer coefficient at the bottom edge	$W\,m^{-2}K^{-1}$
h_{sp}	Height of beam minus the notch height	m
l	Length of specimen	m
l_c	Correlation length	m
l_{el}	Element width	mm
q_c	Heat of hydration of cement	J / kg
q_i	Heat of hydration for each hydration phase i	J / kg
r	Degree of restraint	-
s	Coefficient, depending on the type of cement	-
t	Time	s
t_0	Starting time of hydration reaction.	s
t_{eq}	Equivalent age	s
$t_{T=T_{external}}$	Time where the reaction reaches the environmental temperature	s
$t_{T=T_{max}}$	Time where the reaction reaches the maximum temperature	s
w_{cr}	Crack width	mm
$w_{cr,lim}$	Maximum allowable crack width criterion	mm
$w_{cr,max}$	Maximum occurring crack width	mm
w_{ul}	Ultimate crack width in tensile strength diagram	mm

Greek

Sign	Description	Unit
α	Degree of reaction	-
α_c	Thermal expansion coefficient of concrete	$°C^{-1}$
β_{cc}	Age coefficient for concrete	-
ΔL	Elongation of the slab	m
ΔT	Temperature difference	°C
ε_T	Thermal strain [-]	
λ_c	Conductivity coefficient of concrete	W / (m °C)
μ	Mean / Poisson coefficient	- / -
$\xi(t)$	degree of hydration	-
$\xi(\infty)$	Maximum final degree of hydration	-
ρ	Specific mass / Density	$kg\,m^{-3}$
σ	Standard deviation / Stress	- / MPa
τ	Characteristic time constant, 28 days	s
φ_i	Weight ratio of constituent i	-
ψ	Relaxation factor	-

Abbreviations

B.C.	Boundary Condition
CMOD	Crack Mouth Opening Displacement
COV	Coefficient Of Variation
DARS	Directional Adaptive Response surface Sampling
DOR	Degree Of Reaction
DCP	Distributed Crack Pattern
DS	Directional Sampling
EC2	Eurocode 2 (1992-1-1)
FE	Finite Element
FEA	Finite Element Analysis
FORM-ARS	First Order Reliability Method on Adaptive Response Surface
FRC	Fibre Reinforce Concrete
FRCFAC	FRC-factor (see Definitions)
MC	Monte Carlo analysis
MC 2010	Model Code 2010
PFEA	Probabilistic Finite Element Analysis
PTK	Probabilistic Toolkit
RC	Reinforced Concrete
RF	Random field
SFRUWC	Steel Fibre Reinforced Under Water Concrete
SFRC	Steel Fibre Reinforced Concrete
SFEA	Stochastic Finite Element Analysis
SLC	Single Localised Crack
UWC	Under Water Concrete

Definitions

Boundary zones	The top and bottom zones of the UWC floor, including the top and bottom boundaries/edges.
Coefficient of variation	The coefficient of variation is a measure for the standard deviation and it is defined as a fraction of the mean. Standard deviation = COV · mean.
Correlation length	Measure of correlation (or covariance) within one random field.
Dip	The drop in strength after reaching the tensile strength of concrete, whereafter the strength increases again
FRC-factor / FRCFAC	Stress scaling factor of the FRC stress-CMOD tensile behaviour input graph.
Leaking crack	Crack that has a certain width through which flow of water is possible, causing leakage.
Integrated UWC floor	The UWC floor does not only have a temporary function but also contributes to the load-carrying capacity in the final phase. This is achieved by making the UWC floor and top floor work together by means of dowels (often fibres are added to the UWC mixture).
Middle zone	The centre of the UWC floor in the y-direction (over the height).
Ordinary / plain concrete	Concrete without the addition of steel fibres
Permanent SFRUWC floor	When the UWC floor (without conventional reinforcing bars) functions as the permanent structural floor. In most cases, this can only be achieved by adding fibers to the concrete mixture.
Phase A	Phase during the hardening process during which no external loads are present (before draining the building pit)
Phase B	Phase after the point that external loads are introduced to the UWC floor by draining the building pit
Random field	A function that introduces a spatially stochastic character to a material property.
Separation crack	See ”Through crack”
Structural top floor	The reinforced concrete floor that is placed on top of the temporary UWC floor in a dry environment. This floor is of a higher quality than the temporary UWC floor, and is easier to reinforce, since this can be executed in a dry environment.
Temporary UWC floor	An under water concrete floor that fulfils a temporary function, mainly as water sealing. Here temporary does not mean that the floor will be removed later.
Through crack	Crack over the entire thickness of a concrete slab. If the crack width is large enough water transport through the crack is possible (see ”Leaking crack”).

1 Introduction

1.1. Motivation for this Research

Underwater concrete floors

Underwater concrete (UWC) floors are concrete slabs that are cast underwater. Currently, they are primarily used to make a temporary watertight seal for building pits below the groundwater level. Some typical projects where these floors are applied include tunnels, parking garages and lowered highways. These building pits will be excavated underwater, whereafter a watertight floor will also be cast underwater. The primary function of these UWC floors is to seal the building pit to prevent water from entering through the bottom. Another function is to provide ballast and resistance to prevent the upburst of the underlying soil layers due to upwards water pressure. Due to construction uncertainties and quality requirements, underwater concrete floors are often of insufficient quality to be used as structural floors. Another reason is that UWC floors are usually not reinforced due to the difficulties and additional costs that come with underwater construction. UWC floors are also called temporary underwater concrete floors. Not because the floor is removed after construction, but because it has a temporary function. After construction, the UWC floor remains in the ground but the permanent structural top floor takes over the function of keeping the water out. This structural top floor can then be constructed in a dry environment and cast directly on top of the underwater concrete floor or with an intermediate sand layer in between.

These different UWC floor design types are shown in Figure 1.1. For the first type (left panel Figure 1.1), the UWC floor is considered a temporary construction and is used in combination with a permanent structural top floor. This type is considered to be the traditional construction method. This method is accompanied by additional costs: the building pit has to be excavated deeper, more concrete is used and it takes additional labour (ABT, 2018).

An integrated design is also possible, where a structural floor is cast upon an existing UWC floor (middle panel figure 1.1). The combined structural capacity is then used in the design (van Tilburg et al., 2021), and the structural top floor can be thinner than in the traditional design. In the integrated design, the excavation level does not have to be as deep as the traditional design but also causes additional structural challenges. When a structural floor is cast directly upon UWC concrete, thermal shrinkage in the hardening top floor can be restrained by the existing hardened UWC floor. Therefore crack formation in the structural slab is not uncommon in this design (W. van der Woerdt and Bouwmeester - van den Bos, 2011 and CUR Rapport 2007-3, 2007), which is elaborated further in section 3. When cracks occur in the structural slab, the structural integrity and water tightness of the whole construction may be at risk.

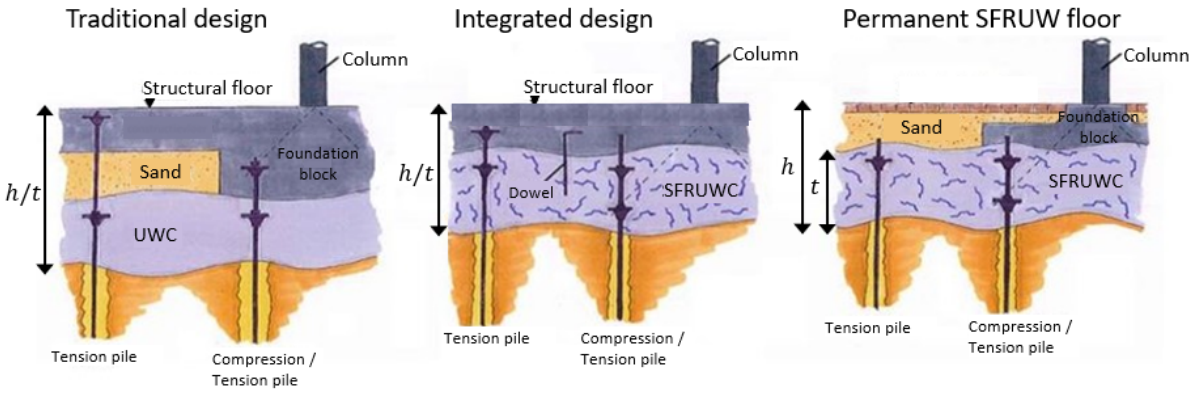

Figure 1.1: Design types of UWC floor construction. h indicates the excavation depth and t indicates the construction thickness. Modified from ABT (2016)

A more sustainable and structurally safe option would be when the UWC floor, besides the temporary water sealing function, can also function as the permanent structural floor (right panel in figure 1.1). In this design, no additional structural top floor is necessary. However, crack width control and leakage prevention are even more important than for the other designs. The main cause of crack formation is the restrained shrinkage deformation (den Boef, 1996). Especially the thermal shrinkage during the hardening phase is an issue. Surface cracks might grow into full separation cracks that are subjected to leakage. There have been quite some examples where separation cracks developed in underwater concrete (W. H. van der Woerdt, 2010). Steel fibre reinforced underwater concrete (SFRUWC) has proven to be a significant improvement in reducing the crack formation and therefore reducing the probability of leakage (Arkesteijn and Menting, 2013 and Meijdam et al., 2017). Also, since it is challenging and expensive to place reinforcement underwater in the traditional design, steel fibre-reinforced underwater concrete (SFRUWC) is a good solution to the problem (ABT, 2016). However, adequate guidelines and calculation methods have not yet been developed. There is a widespread need for the development of guidelines, especially about the control of thermal shrinkage cracking, even for regular UWC without fibres.

Reference Projects

Projects where the conventional construction method of creating a temporary SFRUWC floor with a structural top floor are for example the Mauritshuis in the Hague and the Groninger Forum. Projects with an integrated design are the Albert Cuyp parking garage and the dry dock Royal van Lent in Amsterdam. Permanent SFRUWC designs where the SFRUWC floor is directly used as the structural floor have not yet been realised.

1.2. Problem Statement

Currently, there are no guidelines for permanent structural SFRUWC floors. The guidelines that exist for regular UWC floors mostly discuss structural resistance but do not cover leakage, while this is an important design criterion for UWC floors. Another big challenge in designing these constructions is the uncertainty associated with placing concrete underwater. There is a lot of uncertainty about the geometry, material properties and spatial variability, but also how to model the boundary conditions and the degree of restraint of the slab. A deterministic finite element model (FEM) that predicts the formation of cracks, is under development. During the development of this model, questions arose about how to take the uncertainties into account. In order to take uncertainty into account in the design, a probabilistic approach is needed, where input parameters may be modelled with a stochastic character.

1.3. Objective

Goal

A CROW committee ”Steel fibre reinforced underwater concrete floor as permanent structural floor” is developing a CUR-CROW recommendation for permanent SFRUWC floors. Previously this same institution developed the guidelines for regular UWC floors (CUR-Recommendation 77, 2014). The committee consists of several subcommittees, one of which focuses on the problem of shrinkage cracking in SFRUWC floors. The main tasks of this subcommittee are to develop a finite element model to gain insight into the behaviour, to conduct a sensitivity analysis and to validate the model by theory and experiments. During the development of this model, it became clear that the input parameters can heavily influence the results. Besides that, there is a lot of variation in the input parameters, and the construction method also adds to the uncertainty. From these observations, it became clear that a probabilistic approach is needed to model the uncertainties that come with UWC floor construction. The aim of this graduation project is to look at the feasibility of a probabilistic finite element analysis (PFEA) regarding the prediction of thermal shrinkage cracking and to develop this method.

The overall objective of this thesis is to find a suitable method to determine the failure probability of a permanent SFRUWC floor. The focus will be on the probability of the formation of separation cracks caused by thermal shrinkage in the floor. This probability depends on the design choices, which are the input parameters for the model. Therefore it will also be necessary to investigate the influence these input parameters have on the (probabilistic) results in the form of a sensitivity analysis. Consequently, it is also important to evaluate if and how the results of this thesis can be used in the development of these new guidelines for permanent SFRUWC floors.

To sum up, the objectives of this thesis are:

- To develop a probabilistic approach that can be combined with a finite element model of a permanent SFRUWC floor;
- To determine how the failure probability of a SFRUWC floor regarding separation cracks caused by thermal shrinkage can be calculated and what is required for this;
- To investigate the influence of the input parameters with a sensitivity analysis;
- To make recommendations on how to incorporate the results of this thesis in the development of the new guidelines.

Research Questions

When taking the objectives into consideration, and in order to better define the scope of the thesis, research questions are formulated.

The main research question of this thesis is defined as:

- How can the failure probability of a SFRUWC floor subjected to thermal shrinkage cracking be determined, and which factors influence this failure probability?

Sub questions

In order to find an answer to the research question, several sub-questions were identified. The main research question can be addressed by answering these sub-questions.

- What does the structural behaviour of a young hardening UWC floor look like, and how can this be modelled?
- How is the failure of the SFRUWC floor defined when looking at thermal shrinkage cracking?

- What is a suitable probabilistic method that takes the uncertainties of SFRUWC floor construction into account and is compatible with FEA?
- What are appropriate stochastic definitions for the input parameters, and which of these parameters influence the results the most?
- How can the failure probability of a particular design be determined?

Follow-up questions

After the main research question and the sub-questions are answered, some follow-up questions can be investigated.

- How can shrinkage cracks be limited or mitigated, and what are the most important input parameters for mitigation?
- How can the results from the probabilistic approach contribute to the development of guidelines regarding permanent SFRUWC structural floors?

1.4. Methodology

This section follows the sub-questions from the previous section. For each sub-question, the methodology is presented. The numbers in brackets [...] correspond to the chapter in which the information is presented.

What does the structural behaviour of a young hardening UWC floor look like, and how can this be modelled?

The basis for modelling the structural behaviour of a young hardening SFRUWC floor was the development of a finite element model. The finite element analysis (FEA) was performed in the software DIANA FEA, which is a versatile finite element package. DIANA is capable of modelling the heat-flow and development in fresh concrete structures and performing a structural nonlinear analysis to determine thermal shrinkage cracking. The input parameters needed for this FE model were acquired from the literature and standards. Besides the FE-model, information was gathered from the literature. The literature research was split up into the three components of a young hardening SFRUWC floor (Young hardening concrete, FRC and UWC floors) and these are discussed in Chapter 2. After this, they are merged in Chapter 3 to investigate the combined structural behaviour of a SFRUWC floor.

- *Young hardening concrete*
  A literature study was done to investigate the process of the hardening of concrete and how this can be calculated. Equations and corresponding parameters were set up to calculate the maturity of the concrete. After that, it was evaluated how this corresponds with the development of the material properties [2]. These relations were then included in a finite element model, and the results and effects of the input parameters were discussed [4]. Finally, a sensitivity study was done to investigate the effects of varying the most important input parameters, such as material properties and the thermal boundary conditions [5].
- *Fibre reinforced concrete*
  A literature study was done to explore the behaviour of FRC and how this changes for different mix compositions. The differences with regular concrete and how the standards model the tensile behaviour of FRC were investigated. Literature and building codes were also consulted to estimate the standard deviation of the tensile strength of FRC [2]. The tensile strength models were adopted in the FE model of the floor [4], and the influence of varying parameters was investigated through a sensitivity analysis in chapter [5].
- *Underwater concrete floors*
  First, a literature study was performed to determine the construction method, structural system

and how the surrounding soil influences the boundary conditions of a UWC floor. The theory of shrinkage cracking due to restrained deformations and the parameters in which uncertainty is expected were reported [3]. The structural behaviour found in the literature was compared to the results of the FE model [4].

How is the failure of the SFRUWC floor defined when looking at thermal shrinkage cracking?
A failure criterion was defined as a function of leakage, which can be transformed into a function of the crack width. A literature review was done to study the formation of separation cracks and corresponding fluid transport mechanisms. Tightness criteria were obtained from theoretical literature and standards [2]. These criteria were used in a limit state for the probabilistic analysis in chapters 5.

What is a suitable probabilistic method that takes the uncertainties of SFRUWC floor construction into account?
In the first half of this thesis, the focus was mainly directed at discovering the built-in probabilistic module of the FE package DIANA and how this module could be combined with the UWC floor model. Because this module was built into the FE software, the advantage of this module was the shorter computation time to reach a certain probabilistic result. After a while, we concluded that there were too many issues to make this combination between the built-in module and our own model work as we envisioned. The findings and documented issues regarding the PROBAB module are reported in Appendix F. After this, it was decided to continue the thesis with our own probabilistic Python implementation. Code was written to automatically conduct multiple samples (FE analyses) of the same model with a different random field each time.

A part of the probabilistic approach was the implementation of random fields. The use of random fields turned out to be trivial in the FE model. An algorithm to generate random fields was programmed in Python, which was necessary to investigate the influence of the input parameters of the random fields. The random fields generated by the code were compared and verified with those generated by the built-in random field module from DIANA [Appendix D]. After this, a Monte Carlo analysis was combined with the finite element model, which calculates multiple samples with stochastic variation in the input. A sensitivity study was conducted to investigate the influence of these different input parameters, and the findings were reported in Chapter 5.

What are appropriate stochastic definitions for the input parameters and which parameters influence the results the most
The averages and standard deviations of the input parameters were obtained from literature or deduced from codes [2]. The influence of these assumptions was investigated and discussed in Chapter 5.

How can the failure probability of a particular design be determined?
A probabilistic method [5] was combined with the finite element model [4]. In this approach, multiple variables are made stochastic simultaneously. The findings are reported in Section 5.6.

1.5. Scope

Design process

In practice, the design process is divided into three general design phases. A linear static analysis is usually the starting point, sometimes followed by a nonlinear analysis. If even more accurate results are required, or uncertainty needs to be taken into account, a probabilistic analysis can be added, which is the third phase. Since the main focus of this thesis is the probability of failure due to crack formation, the linear elastic step is skipped and the focus will be on a probabilistic analysis in combination with a nonlinear structural model. The current guidelines describe a linear elastic calculation procedure to design UWC floors. This calculation procedure will be analysed in Section 3.7.

Time period
Crack width mitigation is an aspect that must be addressed during the entire service life of a UWC floor. However, this thesis focuses explicitly on crack formation during the hardening process caused by thermal shrinkage. Therefore only the first two weeks after casting are considered. For UWC floors, this hardening period corresponds to the period in which typically no external loads on the floor are present. Hence, the floor gets sufficient time to develop enough strength. After the hardening period, external loads, mainly due to upward water pressure and superstructure, are introduced to the floor, and existing cracks either increase or decrease. This effect during the period when external loads are present is left out of scope for this thesis.

External influences
The boundary conditions of a UWC floor are heavily influenced by external factors, such as soil conditions and the groundwater level. To correctly model the structural response of the floor, the soil around it and the adjacent sheet piles also have to be modelled. In this thesis, this aspect is simplified and boundary conditions are assumed that lead to an extreme crack width result. Only the floor is modelled, and the influence parameters are investigated when the boundary conditions are kept constant. This work purely focuses on how to model the thermal shrinkage cracking in SFRUWC floors and drying and autogenous shrinkage are excluded from this work.

1.6. Outline

Introduction and background information
In the current chapter, motivation is given for conducting the research in this thesis and what problems are to be adressed. This is followed by defining the scope and methodology.

The literature review (Chapter 2) explores the fundamental components that are needed in this thesis. This chapter includes background information on methods and input parameters that were required to construct the finite element model and define the probabilistic analysis in the later chapters. With these fundamental components, the full structural behaviour of UWC floors is described in Chapter 3. In this chapter, the construction method is also presented, together with the problems and uncertainties that come with UWC floor construction. Finally, the current existing guidelines for UWC floors without fibres are discussed.

Modelling
The FE model that determines thermal shrinkage cracking in a UWC floor is described in Chapter 4. In this chapter, the assumptions and concessions that were made and what effect these have on the results are discussed. It also includes results that are compared to expectations that are found in Chapter 2. A key part of the finite element model is the use of random fields. All relevant background information regarding Random fields is presented in Appendix D. All the parameters and settings of the finite element model, which are discussed in Chapter 4 are summarised in Appendix C. Finally, the results of the FE-model are discussed.

Probabilistic analysis
The probabilistic analysis is described in Chapter 5. This chapter starts with the assumed stochastic distributions of the input parameters. Together with the failure definition (limit state) and method, the results are obtained. For each category of parameters, the results of varying separate parameters is discussed. Finally, the findings and shortcomings are described in the conclusion and discussion.

Conclusion and recommendation
Finally, the research questions are answered in the conclusion (Chapter 6) and recommendations are given in Chapter 7.

2

Literature review

2.1. Young hardening concrete

2.1.1. Cement hydration reaction

The hardening process of concrete is the result of a chemical-physical reaction (van Breugel et al., 2016) which is also called the hydration reaction. This reaction is an exothermic process, meaning that heat is produced during this process. The total heat that is produced at any given time is a measure of the progression of the reaction, which is called the degree of reaction (DOR). The DOR can be determined by:

$$\alpha(t) = \frac{Q_t}{Q_{\text{pot}}} \tag{2.1}$$

Where:

- $\alpha(t)$ is the degree of reaction [-]
- $Q_t(t)$ is the total heat that is produced by the reaction up to a certain time [J]
- Q_{pot} is the maximum amount of heat that can be produced during the reaction [J]

The degree of reaction can also be determined by other concepts such as measuring the chemical shrinkage, the non-evaporable water content, the compressive strength of mortar cubes or doing a microscopic image analysis of the hydrated microstructures. The degree of reaction and heat production are important indicators for two reasons. Firstly, it corresponds with the development of the strength properties of concrete, which is important to know for taking shrinkage cracking in the early phase into account. Secondly, heat will cause the concrete to expand, and subsequently, it will cool down and shrink again. During this shrinking, cracks may develop in the concrete if free deformations are restrained..

2.1.2. Heat production and degree of reaction

Adiabatic temperature rise[1]

The maximum heat that is reached in a concrete specimen during hydration is dependent on how much heat is produced and how much heat, and especially how quickly heat can be dissipated. This process

[1] The information and equations from this section are gathered from multiple sources, including Torrenti et al. (2013), Ye (2020) and ASTM - C1074 (2004).

is captured in the following equation:

$$\Delta T(t) = \frac{Q_t(t) + Q_0(t)}{C_{\text{av}}} \tag{2.2}$$

Where:

- $\Delta T(t)$ is the temperature rise of the concrete at time t [K]
- $Q_t(t)$ is the heat that is produced at a certain time [J]
- $Q_0(t)$ is the amount of heat exchanged with the surroundings between mixing and time t [J]
- C_{av} is the average heat capacity of the concrete during the hydration reaction in [J/K]

The temperature rise is important to know in order to determine the maximum temperature a concrete specimen can reach which determines the potential shrinkage and possibility of cracking. The heat capacity of concrete can be determined as a summation of the heat capacity of the different constituents of cement, scaled by their respective weight ratios. $Q(t)$ can be determined with the following equation:

$$Q(t) = \xi(t) \cdot c \cdot q_c = c_h(t) \cdot q_c \tag{2.3}$$

Where:

- $Q_t(t)$ is the amount of heat produced by the hydration reaction within the concrete between mixing and time t [J]
- $\xi(t)$ is the degree of hydration at time t, defined by $\xi(t) = \alpha(t) \cdot \xi(\infty)$ [-]
- $\alpha(t)$ is the degree of reaction at time t where $\alpha(0) = 0$ and $\alpha(\infty) = 1$ [-]
- $\xi(\infty)$ is the final degree of hydration of the cement (the degree of hydration is not necessarily 100% at the end of the reaction, but may be lower, depending on the water to cement ratio) [-]
- c is the amount of cement [kg].
- $c_h(t)$ is the amount of hydrated cement at time t [kg]
- q_c is the cement's heat of hydration [J/kg]

The last parameter can be calculated with:

$$q_c = \sum (\varphi_i \, q_i) \tag{2.4}$$

Where:

- q_c is the cement's heat of hydration [J/kg]
- q_i is the phase's heat of hydration [J/kg]. See Table 2.1.
- φ_i is the weight ratio of constituent i [-]

Table 2.1: Heat of hydration for constituents of cement (Torrenti et al., 2013)

Constituent of cement	Heat of hydration q_i [J/kg]
C_3S	510
C_2S	260
C_3A	1100
C_4AF	410

The total heat production that is calculated in equation 2.3, is schematically presented in Figure 2.2, and this is defined as the integral of the heat rate graph from Figure 2.1. This graph (2.2 left) is also called the adiabatic curve of concrete, a material property needed for calculations with young hardening concrete.

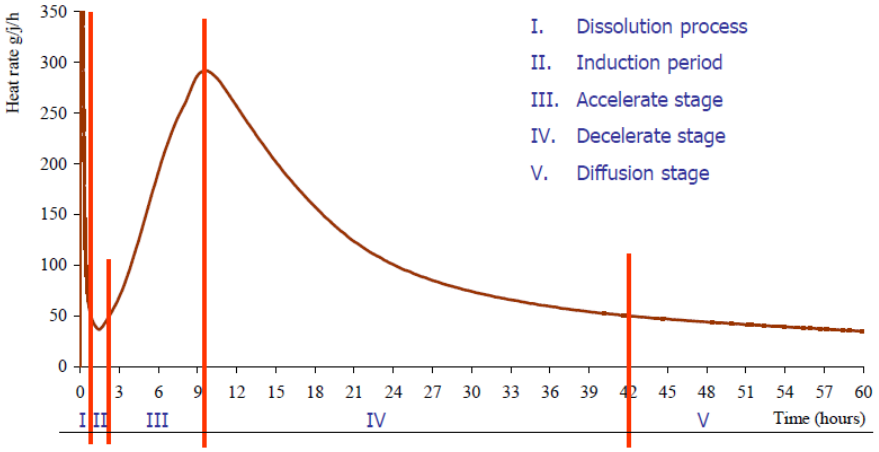

Figure 2.1: Heat production during the hydration reaction and it's different stages. Adapted from (Ye, 2020)

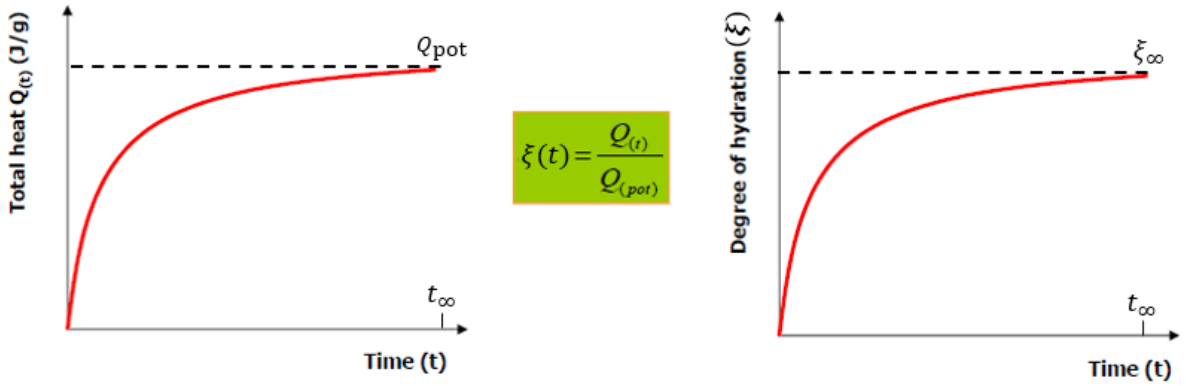

Figure 2.2: Left: total heat production under adiabatic conditions resulting from the heat production from Figure 2.1. Right: Corresponding degree of hydration. Modified from (Ye, 2020)

In Figure 2.2, it can be seen that the degree of hydration corresponds to the total heat production. It is important to know the degree of hydration because this is the main factor behind the development of the strength properties of young concrete.

Adiabatic curve

Adiabatic means that no heat is lost to the environment. So, the adiabatic hydration curve of a concrete mixture indicates the heat produced by the concrete without taking heat dissipation into account. This process is explained in the previous section. The adiabatic curve is an important input parameter for numerical tools to determine the temperature development in hardening concrete and an example can be seen in Figure 4.4. The shape of the adiabatic curve of a concrete mixture depends on the:

- Chemical composition of the cement
- Fineness of the cement
- Water to cement ratio
- Cement content
- Initial casting temperature
- Presence of additives or admixtures

Outside of lab experiments, in practice the hydration of concrete is never fully adiabatic, because heat will be dissipated to the surroundings. The temperature that will develop is lower than the potential

temperature that can develop under full adiabatic conditions. This means that the hydration process slows down, and therefore the strength properties will develop slower. This semi-adiabatic process is governed by the temperature, which then depends on the heat produced per unit of time. This interaction between the temperature and rate of hydration shows that a numerical, step-wise calculation procedure is needed to determine the entire hardening process. This thesis will use a non-linear finite element analysis with time steps to determine the actual temperature distribution and the reaction rate. This is called a transient heat analysis.

2.1.3. Thermal properties of hardening concrete

As mentioned before, the heat source in a hardening concrete specimen is the hydration reaction. When one looks at a concrete floor, the heat can be dissipated at the upper and lower edges to the surroundings. This will lead to a temperature distribution over the height of the slab, where the middle is hotter than the edges. For the calculation of this temperature distribution, the Fourier differential equation can be used (van Breugel et al., 2016). This differential equation can be solved by numerical methods like the finite difference method or the finite element method.

The temperature field is determined by the thermal properties of concrete and the thermal boundary conditions. The important thermal properties in concrete are the conduction coefficient λ_c and the specific heat capacity c_c, which depend on the concrete's mix composition. Values found in the literature were reported in appendix E. According to van Breugel et al. (2016), the conductivity coefficient ranges between 2 and 3 W/(m·K). It is predominantly influenced by the role of the aggregates in the concrete and therefore, strongly depends on the mix composition. The influence of temperature on the conductivity coefficient is minimal, but moisture in the concrete does have a significant influence (van Breugel et al., 2016). The specific heat capacity is a material property that relates to the heat capacity C from equation 2.2 according to:

$$C_{av} = \rho \cdot c_c \tag{2.5}$$

Where:

- ρ is the specific mass [$kg \cdot m^{-3}$]
- c_c is the specific heat [$J/(kg \cdot K)$]

"The specific heat of young hardening concrete varies between 1.0 and 1.15 $J/(kg \cdot K)$ and between 0.9 and 1.15 $J/(kg \cdot K)$ for hardened concrete. The c_c-value increases with increasing water content and slightly decreases with increasing degree of hydration" (van Breugel et al., 2016).

Another important aspect is the thermal boundary conditions. These determine how quickly heat can be dissipated. The boundary conditions are characterised by the heat-transfer coefficients and have the unit $W/(m^2K)$. The coefficients depend on the material that borders the concrete (sand, water or steel) and environmental conditions like the wind speed or water flow rate. The effect of the heat transfer coefficients is illustrated in figure 2.3. This figure displays a concrete plate of one meter thick on soil, where the topside is exposed to air with varying wind speeds. The different heat transfer coefficients in this figure: 5, 15 and 25 correspond with wind speeds of 0, 2 and 5 m/s. The heat transfer coefficient of the bottom is fixed to one value. Values used in other research are reported in appendix E.

Finally, the thermal expansion coefficient α_c determines how much the material expands during heating. The coefficient is different for the components of concrete (limestone, granite, sandstone, quartzite) but generally, one value for concrete can be used that is dependent on these four. Values from literature range between 5 and $15 \cdot 10^{-6}$ K^{-1}. Within the normal temperature range from 0 to 50 °C, the thermal expansion coefficient can be considered constant during the whole hydration process (Torrenti et al., 2013 and van Breugel et al., 2016).

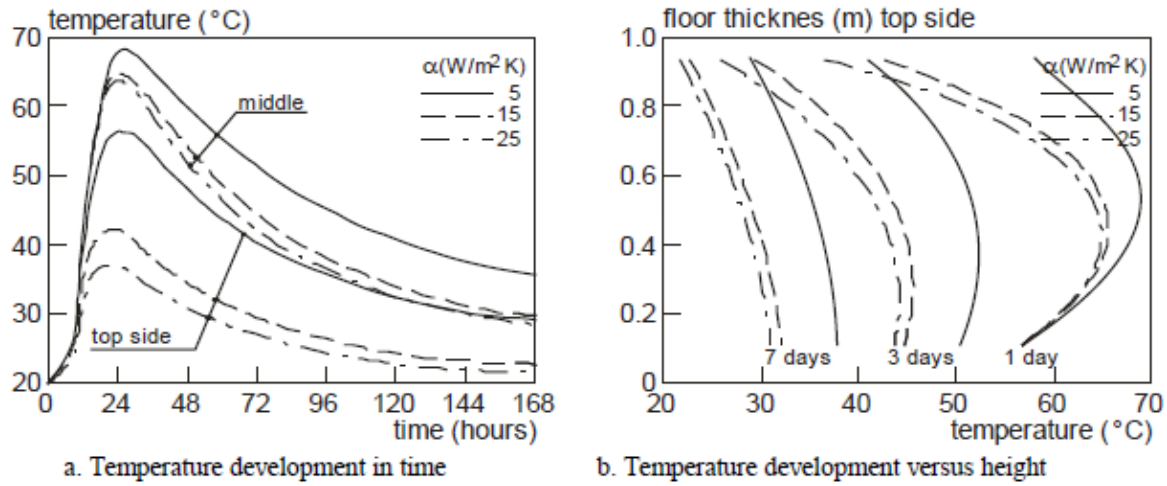

Figure 2.3: Influence of the heat transfer coefficient on the temperature development in a one meter thick concrete plate that is exposed to air on the topside. Adapted from van Breugel et al. (2016).

2.1.4. Development of the material properties

As discussed in section 2.1.2, the evolution of the degree of hydration is the main parameter that is needed to model the development of strength in young concrete. Since the tensile strength is proportional to the compressive strength, this chapter will use the general term strength. The development of strength for young concrete can be determined in three different ways:

1. The maturity concept
2. Degree of hydration
3. Equations provided by codes and standards

The degree of hydration concept was already explained in section 2.1.2. This section will explain the maturity concept and the link to the equations provided by codes.

Maturity concept

The maturity of concrete can be expressed in a temperature-time factor or as an ”equivalent age” and is (like the degree of hydration) a measure of the progression of the hardening process. The temperature-time factor is defined as

$$M(t) = \int_0^t T(t)\,dt \tag{2.6}$$

Where:

- $M(t)$ is the temperature-time factor (maturity) in [°Cs]
- t is the age of concrete [s]
- $T(t)$ is the temperature in the concrete at a specific time t [°C]

In Figure 2.4 (right), it can be seen that the development of strength is a function of the maturity in the form of a temperature-time factor. Another way to denote the maturity of concrete is with an ”equivalent or temperature-adjusted age” (Figure 2.4, left). The formula for the equivalent age is constructed by using the formula of Arrhenius in the following way:

$$t_{\text{eq}} = \int_0^t \exp\left(\frac{E_a}{R}\left(\frac{1}{(273 + T_{\text{ref}})} - \frac{1}{273 + (T(t))}\right)\right) dt \tag{2.7}$$

Where:

- t_{eq} is the equivalent age [s]
- E_a is the activation energy [J/mol]
- R is the universal gas constant, 8.314 J/(mol · °C)
- T_{ref} is the reference temperature, usually 20 °C
- $T(t)$ is the temperature in the concrete at a specific time t [°C]
- t is the time at which the equivalent age is evaluated [s]

Activation energy

This formula has the activation energy of concrete E_a as a variable. The activation energy depends on the composition of the cement. The numerical FE software DIANA uses a standard value of 50 kJ/mol, while values from literature (Kada-Benameur et al., 2000, D'aloia and Chanvillard, 2002 and Poole et al., 2007) tend to be lower in the range between 35 and 45 kJ/mol. Besides that, D'aloia and Chanvillard (2002) indicate that the activation energy is dependent on the degree of hydration, and therefore the time. Kada-Benameur et al. (2000) indicate that the activation energy is also temperature dependent. This is supported by Nielsen and Kaasgaard (2020) and van Breugel et al. (2016), who state that especially below the 20 °C, the activation energy is dependent on the temperature. All of this means that the value of the activation energy is different for each concrete mixture and the value has to be determined experimentally. An example of a method to determine the activation energy is described in the paper of Poole et al. (2007). Values of the activation energy for practical use are given by van Breugel et al. (2016) as:

- $E_a = 33.5$ kJ/mol for $T > 20$°C
- $E_a = 33.5 + 1.47 \cdot (20 - T)$ kJ/mol for $T < 20$°C

Both the Eurocode (2011) and MC 2010 (2010), define one fixed value for the activation energy of approximately $E_a = 33.3$ kJ/mol. Nielsen and Kaasgaard (2020) argue that the activation energy is also temperature dependent above 20 °C.

The graphs in Figure 2.4, can be described by an exponential function in the following shape:

$$f_c(M) = f_{c\infty} \cdot \exp\left\{-\left(\frac{\tau}{t_e q}\right)^{\alpha}\right\} \tag{2.8}$$

In which:

- $f_c(M)$ is the compressive strength at maturity M [MPa]
- $f_{c\infty}$ is the asymptotic value of the compressive strength at $t = \infty$ [MPa]
- τ is a characteristic time constant [days], usually taken as 28 days
- $t_e q$ is the maturity index (equivalent age) [days]

Equations provided by codes and standards

Eurocode 2 (2011) and fib Model Code 2010 (2010) apply a simpler model:

$$f_{\text{cm}}(t) = \beta_{\text{cc}}(t)\, f_{\text{cm}} \tag{2.9}$$

$$\beta_{\text{cc}}(t) = \exp\left\{s\left[1 - \left(\frac{28}{t}\right)^{1/2}\right]\right\} \tag{2.10}$$

In which:

- $f_{\text{cm}}(t)$ is the compressive strength at a certain age t [MPa]
- f_{cm} is the average compressive strength at $t = 28$ days [MPa]
- $\beta_{\text{cc}}(t)$ is coefficient that is dependent on the age t of concrete [-]

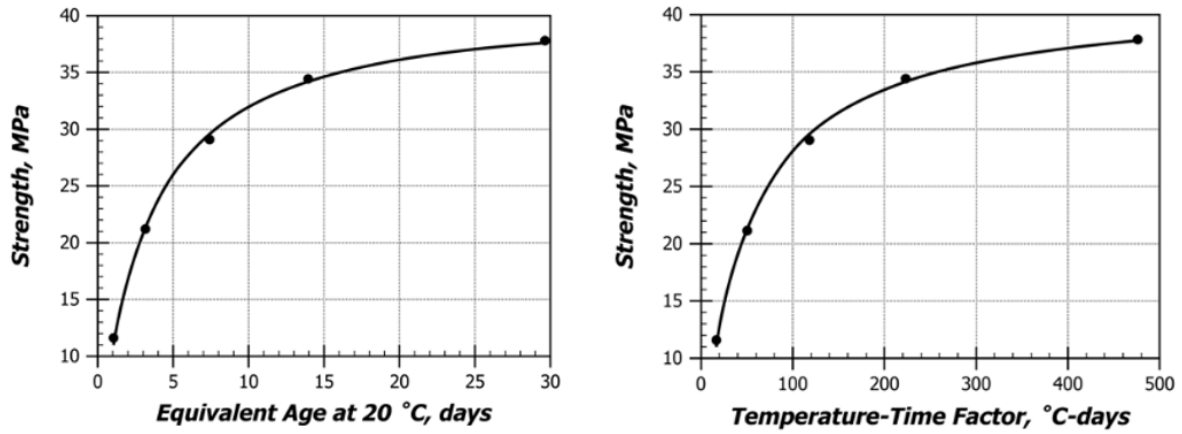

Figure 2.4: Left: Equivalent age vs. compressive strength of concrete. Right: Temperature-time factor vs. compressive strength of concrete. Adapted from ASTM - C1074 (2004).

- t is the age of concrete [days]
- s is a coefficient, depending on the type of cement [-]

The coefficient s is defined by the Eurocode as:

- Slow rate cements: s = 0.38 (CEM 32.5 N)
- Normal rate cements s = 0.25 (CEM 32.5 R and 42.5 N)
- Rapid rate cements s = 0.20 (CEM 42.5 R, 52.5 N and 52.5 R)

Nielsen and Kaasgaard (2020) compared the maturity method against the Eurocode method from equations 2.8 and 2.9, which is displayed in Figure 2.5.

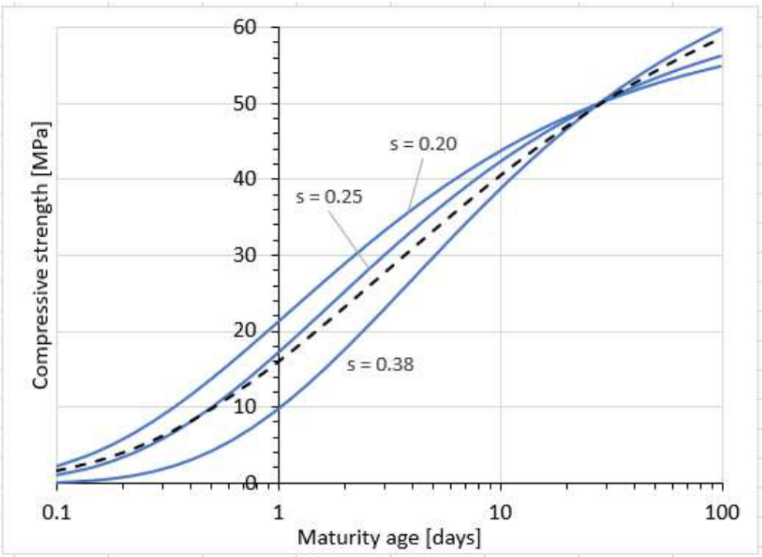

Figure 2.5: Comparison between the compressive strength development, determined by the maturity method (dotted line) and the Eurocode 2 method (blue lines) for a concrete with a value of $f_{cm} = 50$ MPa. Adapted from Nielsen and Kaasgaard (2020). This figure is only for illustrative purposes, UWC usually has a lower compressive strength

2.1.5. Thermal shrinkage and restrained deformation

In concrete, temperature variations result in thermal deformations. If these deformations are restrained, thermal stresses can develop. A source of temperature change during the hardening process comes from the heat from the exothermic hydration reaction (2.1.2). The thermal strain is given by:

$$\varepsilon_T(t) = \alpha_c \cdot \Delta T(t) \tag{2.11}$$

In which:

- α_c is the coefficient of thermal expansion of concrete $\left[°C^{-1}\right]$
- $\Delta T(t)$ is the temperature variation [°C]

There is a probability of cracking when the tensile stress becomes larger than the tensile strength as is displayed in Figure 2.6. This thesis focuses mainly on thermal shrinkage, but besides temperature variations, other possible causes of deformations are:

- Swelling
- Plastic shrinkage
- Chemical shrinkage
- Autogenous shrinkage

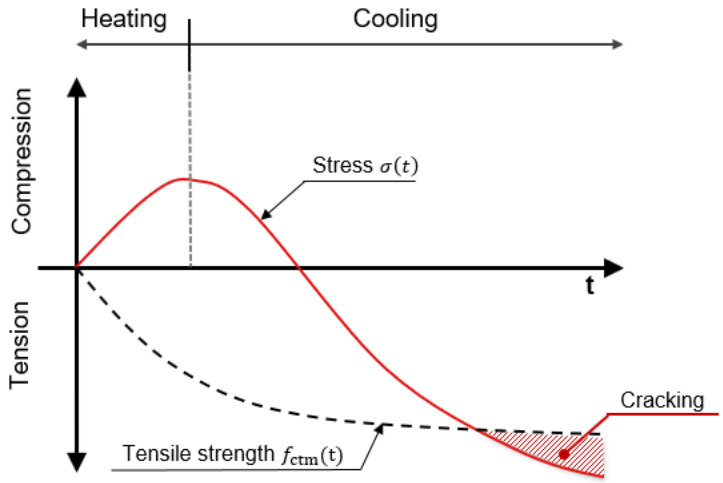

Figure 2.6: Probability of cracking illustrated: the tensile stress vs. the tensile strength. Cracking occurs when the tensile stress is larger than the tensile strength (in absolute sense). Modified from van Breugel et al. (2016)

Relaxation

The stress in concrete subjected to a constant force decreases due to relaxation. Stress reduction due to relaxation is an important issue in hardening concrete and it can play an important role in the stresses that may develop due to restrained deformation. Relaxation factors that are traditionally applied for hardened concrete are not applicable for hardening concrete. There is a large knowledge gap regarding relaxation in hardening concrete. The concept of relaxation is illustrated in Figure 2.7.

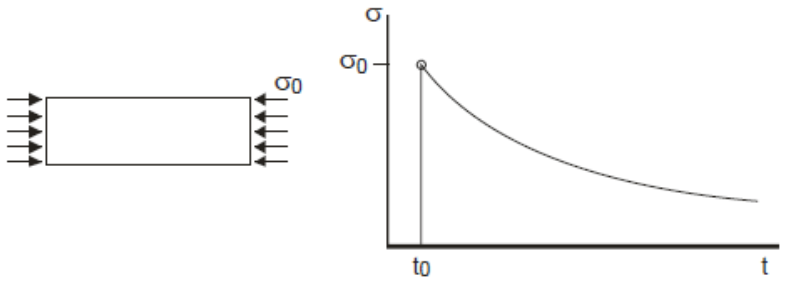

Figure 2.7: Relaxation in concrete under compression. Adapted from van Breugel et al. (2016)

Degree of restraint

The previous part states that stresses may develop when strains are restrained. The development of stresses due to restrained thermal shrinkage can be described by the following formula:

$$\sigma(t) = r \cdot \psi(t) \cdot \varepsilon_{\mathrm{T}}(t) \cdot E_{\mathrm{c}}(t) \tag{2.12}$$

Where:

- r is the degree of restraint: $r = 0…1$
- $\psi(t)$ is a relaxation factor
- $\varepsilon_{\mathrm{T}}(t)$ is the thermal strain as defined by Equation 2.11
- $E_{\mathrm{c}}(t)$ is the Young's modulus at time t

In this equation, it can be seen that the stresses are reduced by two reduction factors: the relaxation factor and the degree of restraint (DOR). When temperature-induced deformation is restrained this will cause thermal stresses. The DOR is a factor that denotes how much the deformations are restrained. At full restraint, when the degree of restraint $r = 1$, all resulting thermal strain develops into stress. An example of this is a beam that is fully clamped at two edges subjected to an increased temperature. Compare this to a similar structure supported by a roller on one side which means that the structure is free to extend. This indicates that the degree of restraint will be $r = 0$, which implies that no stresses will occur because there is no restrained deformation. Figure 2.8, shows this differencea UWC floor. This figure shows the stress development due to a temperature increase caused by cement hydration. The figure shows that stresses for a roller support (free-fixed boundary condition, $r = 0$) are smaller than those for the clamped situation (fixed-fixed boundary condition $r = 1$). In the case of $r = 1$, much higher stresses develop in the slab. This shows the influence of the degree of restraint. The stress for the case $r = 0$ is not 0 as explained before in this section, because there is internal restraint caused by a non-uniform temperature distribution over the height of the slab. Due to heat produced due to hydration, the centre of the beam will warm up more than the top and bottom. One can imagine a strip in the (hotter) centre of the beam, which is restrained by the cooler outer strips that expand less than the middle. This effect will be elaborated in Chapter 4. This shows that a structure can have multiple degrees of restraint for different degrees of freedom. In this example ther is a DOR for extension and an internal DOR. A construction that includes bending, might also have a DOR for rotation.

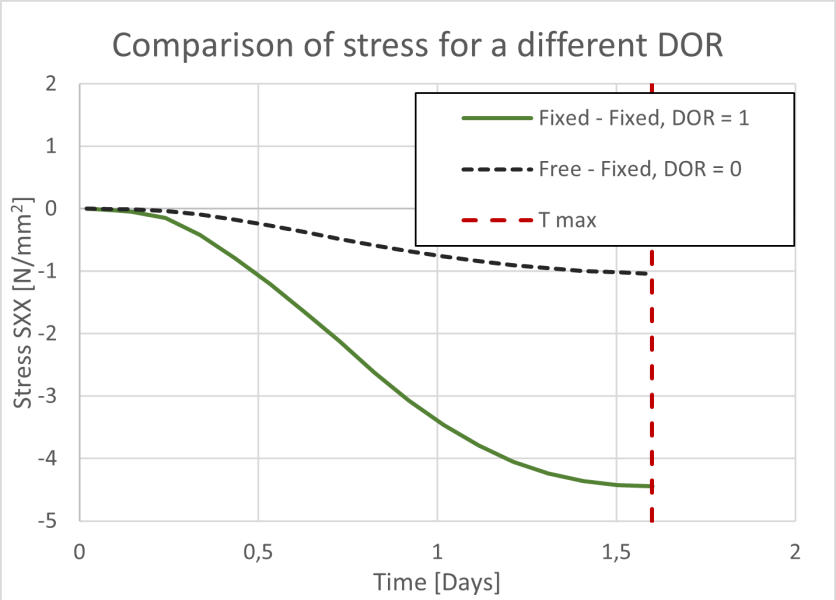

Figure 2.8: Comparison of developed thermal stresses due to thermal expansion with a degree of restraint of 0 and 1

2.2. Fibre reinforced concrete

2.2.1. General

The use of fibres to improve the physical properties of a material is an age old concept. For example, fibres made of straw or horsehair have been used to improve the properties of bricks for thousands of years. Nowadays, fibres are used in a large array of materials and applications such as clay bricks with natural fibres or high-strength fibre-reinforced polymers, used in the space industry (Balaguru & Shah, 1992). The material that the fibres are added to is called the matrix and this thesis is about cement-based matrices: fibre-reinforced cementitious composites, or more specifically fibre-reinforced concrete. Fibres can be broadly classified as metallic, polymeric, mineral, or naturally occurring fibres. This thesis focuses on metallic fibres that are made of steel.

The interaction between the fibre and the matrix affects the performance of a cement-based fibre composite material. A variety of factors that influence this interaction are (Balaguru & Shah, 1992):

- Condition of the matrix: uncracked or cracked
- Matrix composition
- Geometry of the fibre
- Material that the fibre is made of
- Surface characteristics of the fibre
- The ratio of the stiffness of the fibre and the matrix
- Orientation of the fibres: aligned or random distribution
- Volume fraction of fibres
- Rate of loading
- Durability of the fibre in the composite and the long-term effects

2.2.2. Stress-strain behaviour

The stress strain behaviour that FRC might show is dependant on the fibre volume that is present in the concrete mix. The different types of behaviour that might occur are illustrated in Figure 2.9. The stress-strain behaviour for high volume fractions can be divided into three regions which are identified as the initial elastic range, an inelastic range where cracking occurs, and a post-peak range, which is illustrated in Figure 2.10 (Balaguru & Shah, 1992, p. 41). The linear phase is always present, but the latter two may not be present, depending on the properties of the fibre-matrix system. The linear segment that represents the material before cracks occur, can be defined by the modulus of elasticity of the matrix. The second segment can be seen as a zone of nonlinear deformation between the first cracking of the matrix and the ultimate tensile strength of the matrix. The third segment of the curve representing the post-peak (residual) strength can be attributed to the fibre pull-out resistance and the tensile strength of the fibres. Depending on the fibre volume fraction, composition and geometry, this residual strength can vary from negligible to 140% of the peak strength (Balaguru & Shah, 1992, p. 44).

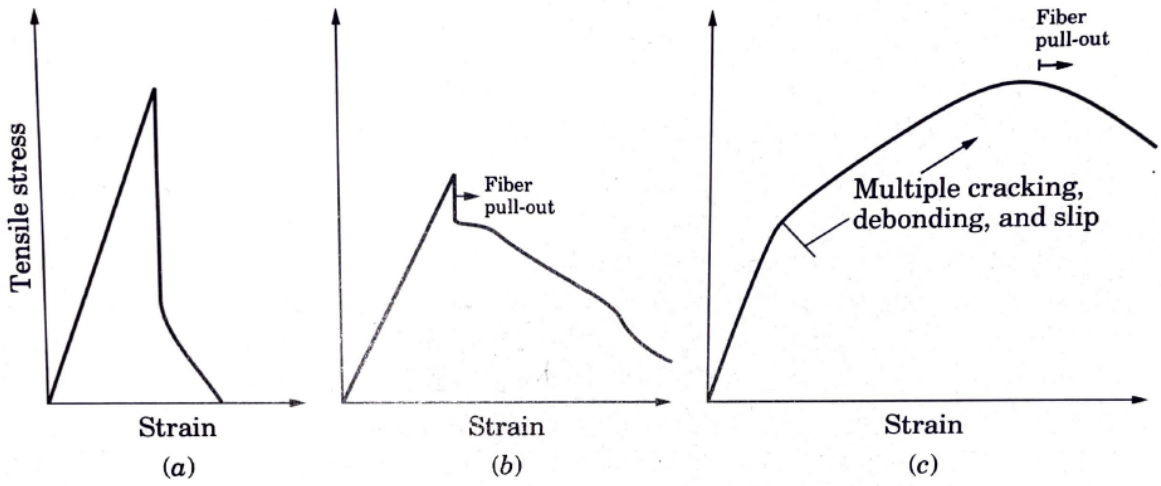

Figure 2.9: General FRC stress-strain curves for different fibre volumes fractions. (a) Low fibre volume fractions; (b) Intermediate fibre volume fractions; (c) High fibre volume fractions. From Balaguru and Shah (1992)

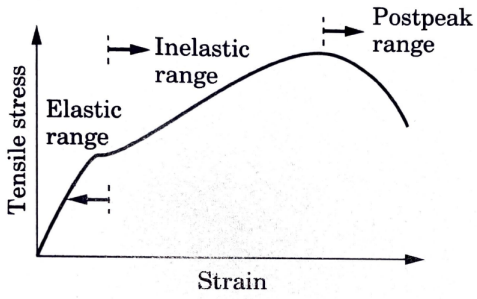

Figure 2.10: Three ranges of tensile stress-strain behaviour for high fibre volume composites. From Balaguru and Shah (1992)

Plain concrete specimens exhibit linear elastic behaviour up to about 50% of their tensile strength. The onset of inelastic behaviour before the peak load suggests the initiation of dispersed micro-cracking. After reaching the peak load, the deformations immediately become localised and cause the widening of a single crack. For SFRC, this behaviour is linearly elastic up to about 80% of the matrix tensile strength (Balaguru & Shah, 1992). The composite peak stress and corresponding displacements or

strains are larger than the corresponding values for the unreinforced matrix. After reaching the peak strength, the strength drops abruptly to the post-cracking strength. With a further increase in strain, the load-carrying capacity gradually drops linearly, which is attributed to the bond-slip relation of the pull-out resistance of the fibres (Balaguru & Shah, 1992).

The main advantage of adding steel fibres to concrete is the effect on the force distribution. After the appearance of the first micro-cracks, the fibres will be activated and lead to a certain residual tensile strength after cracking. This effect is illustrated in Figure 2.11. Here different stress-strain graphs are given for a tensile bar with different fibre volume fractions compared to plain concrete. Also, FRC shows a more ductile behaviour for compressive loading, meaning it can reach a larger failure strain, as shown in figure 2.12.

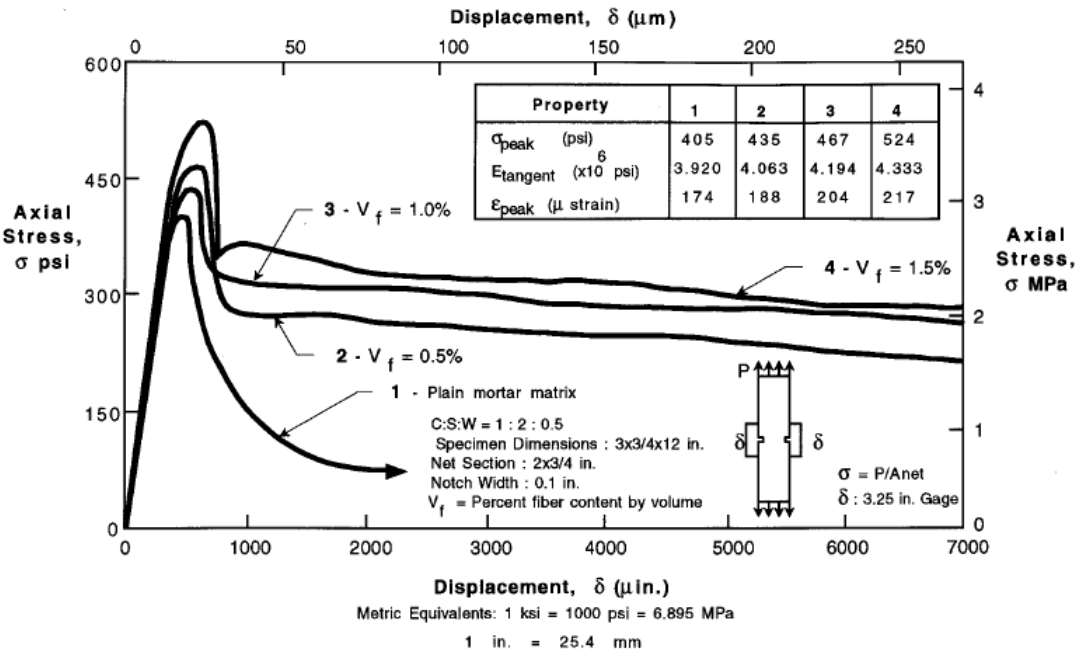

Figure 2.11: Pure tensile stress-strain response. Comparison of plain concrete and FRC. From ACI 544.1R-96 (2001)

There are different models to describe the stress-strain behaviour of FRC. One example is the the fib Model Code 2010 (MC 2010, 2010). According to the MC 2010, FRC is classified based on its post-cracking strength, called the residual strength. This post-cracking tensile behaviour continues until the steel fibres break or slip out of the cement matrix. The Model Code is discussed in the next section.

2.2.3. Model Code 2010

The Eurocode (NEN-EN 1992-1-1 2011) does not include a section about FRC. The following (Dutch) recommendations about FRC exist:

- CUR Report 245 Steel fibre reinforced concrete - state of the art (CUR rapport 245, 2012)
- CUR Report 246 Collection of current guidelines about steel fibre reinforced concrete (CUR rapport 246, 2012)
- Cur Recommendation 111 - SFRC industrial floors with pile foundations (CROW-CUR Aanbeveling 111:2018, 2011)

Besides these recommendations, there is the ACI ”Guide to Design with Fiber-Reinforced Concrete” (ACI 544.1R-96, 2001). However, this thesis primarily focuses on the fib Model Code 2010. It should

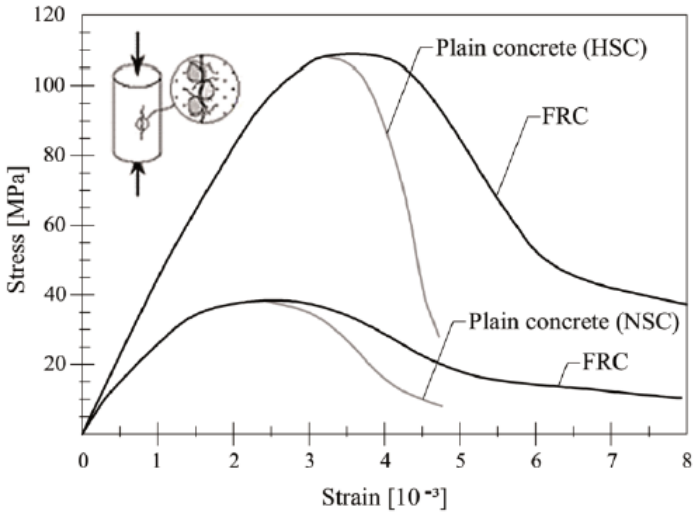

Figure 2.12: Main difference between ordinary concrete and FRC for normal strength concrete and high strength concrete under uniaxial compression. From MC 2010, 2010

be noted that the previous version of the model code, MC 1990 (1990) did not contain a section about FRC. This signifies that FRC is a relatively new material that is not yet applied on a large scale. In anticipation of the next edition of the Model Code, fib bulletin 105 (fib Bulletin 105, 2022) has been published recently. This is a current state-of-the-art report regarding FRC.

The tensile behaviour of FRC is the most important aspect of FRC. Since uniaxial tensile tests are difficult to perform, the tensile stress-strain behaviour is derived from the results from a 3-point bending proof of a notched FRC beam. A standardised test is used for this, which is described in NEN-EN 14651 (2007). The results are presented in a force-CMOD diagram. CMOD stands for crack mouth opening displacement, which is the increase in the distance at the bottom of the artificial notch of the FRC beam. A typical load-CMOD curve is illustrated in Figure 2.13. In this figure, four fixed CMOD values are defined, each corresponding to a certain load. From this data, the residual flexural tensile strength can be defined as:

$$f_{\mathrm{Rj}} = \frac{3\,F_{\mathrm{j}}\,l}{2\,b\,h_{\mathrm{sp}}^2} \tag{2.13}$$

Where:

- f_{Rj} is the residual flexural tensile strength corresponding to point CMOD_j [MPa]
- F_{j} The load corresponding to point CMOD_j [N]
- l is the length of between the supports [mm]
- b is the width of the beam [mm]
- h_{sp} is the height of the beam minus the height of the notch [mm] (standardised test: 125 mm)

The post-cracking strength of FRC is defined by the characteristic flexural residual strength f_{R1k} (SLS) and f_{R3k} (ULS) corresponding to CMOD_1 and CMOD_3 in Figure 2.13. Fib classifies FRC according to a number-letter combination (eg. 4c), where the number represents the lower bound of the strength interval into which f_{R1k} falls. The letter represents the ratio $f_{\mathrm{R3k}}/f_{\mathrm{R1k}}$. The exact strength intervals and ratios are defined in section 5.6.3 in the MC 2010.

The uniaxial tension behaviour can be deduced from the residual flexural tensile strength by applying a simplified linear post-cracking constitutive law (5.6.4 MC2010). The SLS residual strength f_{Fts} is defined as the post-cracking strength for serviceability crack openings, and f_{Ftu} represents the ultimate

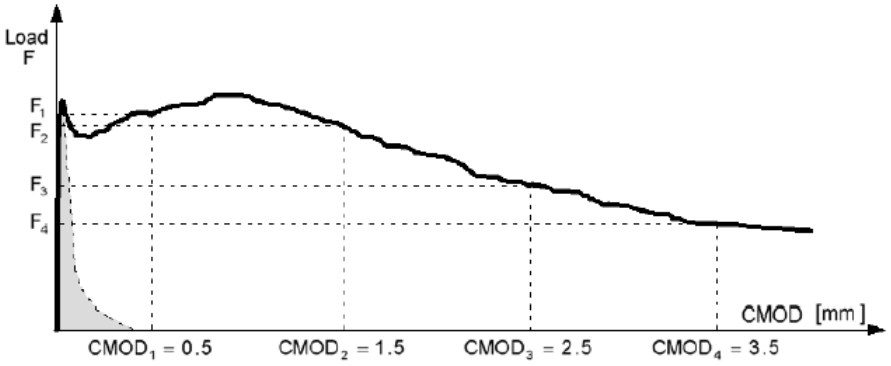

Figure 2.13: Typical load-CMOD curve for FRC and plain concrete.
The plain concrete behaviour is indicated by the shaded area.

residual strength (MC 2010). These values can be determined by:

$$f_{\text{Fts}} = 0.45\, f_{\text{R1}} \tag{2.14}$$

$$f_{\text{Ftu}} = 0.5\, f_{\text{R3}} - 0.2\, f_{\text{R1}} \tag{2.15}$$

With these values, a model of the post-cracking behaviour can be set up, which is displayed in Figure 2.14. In UWC floors, FRC is generally used that is characterised by tension-softening behaviour, which is modelled like CASE (I) in Figure 2.14a. This model adapts the regular concrete tensile behaviour until the peak tensile strength f_{ct}. In the post-cracking stage, a bilinear graph intersects the plain concrete graph at point C. The whole diagram can be constructed with the values f_{Fts} and f_{Ftu}. Cases 2 and 3 represent tension-hardening behaviour.

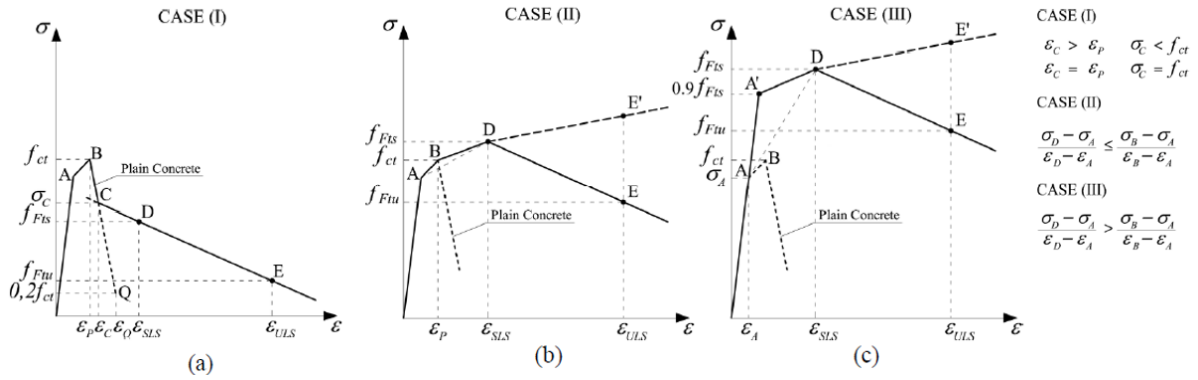

Figure 2.14: Stress-strain relations for the tensile behaviour of FRC for softening behaviour (a) hardening behaviour (b, c). From MC 2010, 2010

As shown in Figure 2.9, FRC can have either tension softening or tension-hardening behaviour, depending on the fibre dosage and concrete quality. The crack pattern is influenced by whether FRC exhibits softening or hardening behaviour. In Figure 2.15, it can be seen that deformations tend to localise in one single crack when FRC shows softening behaviour, but these deformations are spread across multiple cracks for hardening behaviour (MC 2010). As shown in figure A.5, tension softening behaviour might lead to either softening or hardening behaviour in bending. Whilst tension hardening behaviour will always lead to hardening behaviour in bending.

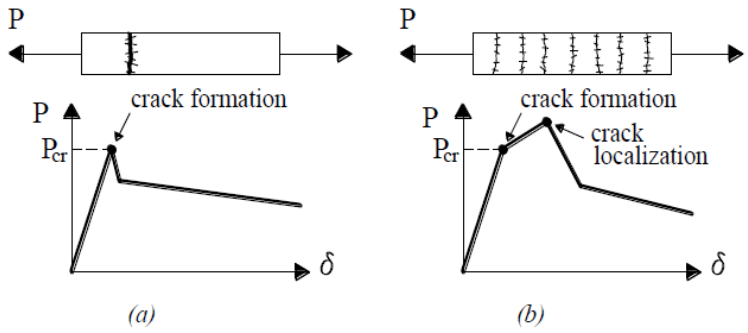

Figure 2.15: Tension softening (a) and hardening (b) behaviour in FRC subjected to axial tension. From MC 2010, 2010

2.2.4. Dip

Looking at Figure 2.13, a drop in force can be observed after the graph has reached the (flexural) tensile strength, after which the force increases again. This "dip" is a typically observed behaviour in tension-softening FRC, which is also reported in FIB 105 (2022). This behaviour can be explained by superimposing the individual tensile behaviour of plain concrete and steel fibres as displayed in Figure 2.16 Multiple experimental research studies have also shown this behaviour, for example: Beghini et al. (2007) and Soetens and Matthys (2014). The latter found the material model displayed in Figure 2.17, which clearly shows this dip.

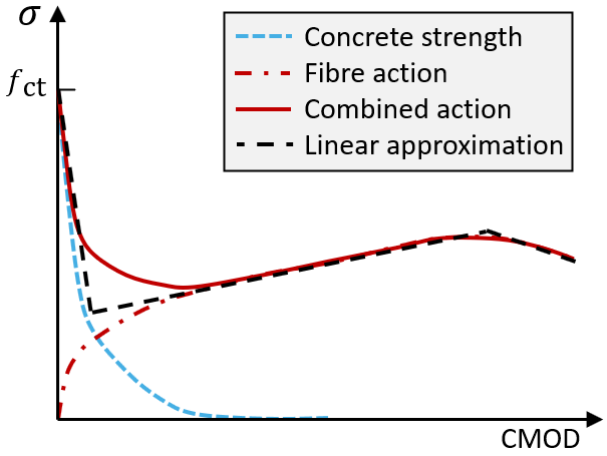

Figure 2.16: Fibre-concrete interaction: post-peak tensile behaviour. The FRC tensile behaviour is a superposition of the tensile strength of regular concrete and steel fibres. Modified from FIB bulletin 105 (2022)

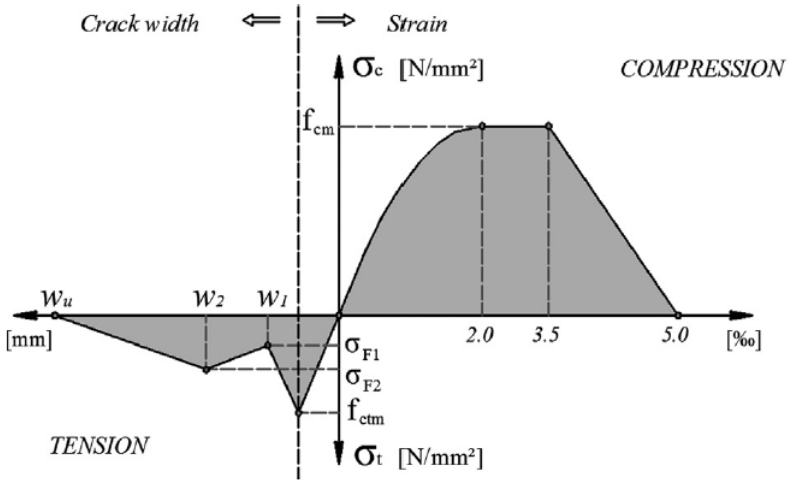

Figure 2.17: Schematic representation of the compressive and tensile behaviour of FRC. Source: Soetens and Matthys (2014)

2.3. Fluid tightness

2.3.1. Fluid transport through concrete

Concrete is a permeable material, which can never be 100% watertight. Although, without cracks present, the amount of water that permeates through uncracked material is so small that the structure can be considered watertight in normal applications. The aim for underwater concrete floors is to have a high degree of water tightness so the leakage remains below a certain critical level. Water transport through concrete can be divided into two components: transport through uncracked concrete and transport through cracked concrete. The flow rate of water through uncracked concrete is in the order of $10^{-3} - 10^{-2}$ l/day, while compared to cracked concrete it can be from 100 to even more than 1000 l/day, depending on the crack width and dimensions. The latter case is based on a cracked concrete floor of 1 meter thick, with a water head of 5 meters and a crack width of 0.1 to 0.2 mm (van Breugel, 2020). This shows that the flow rate through separation cracks can easily exceed the flow rate through uncracked concrete by a factor from $10^4 - 10^6$. Therefore, it can be concluded that transport through uncracked concrete can be neglected for the application of underwater concrete with the possibility of cracking.

Moreover in practice, it has occurred that leakage through non functioning joints can exceed leakage separation cracks by a factor 10^6 (Bomhard, 1992). So it is important to mention that proper joints are even more important than limiting crack width in UWC floors, but this is out of scope for this thesis.

2.3.2. Transport of fluids through cracked concrete

Factors determining the flow rate through cracked concrete can be distinguished in influences on a structural level and influences related to the crack characteristics. These include:

- Water pressure
- Length of the crack (equal to thickness of the floor in case of separation cracks)
- Crack width
- Number of cracks
- Type of cracks (separation cracks or flexural cracks)

- Roughness of the crack face and type of aggregate in the concrete
- Type of fluid (viscosity)
- Autogenous healing capacity

An important distinction has to be made between flexural cracks and separation cracks. Where separation cracks are continuous cracks over the entire thickness of the floor, flexural cracks only penetrate the floor until a concrete compression zone is reached. This is illustrated in Figure 2.18. This can occur when certain eccentricities occur in the UWC floor due to water pressure, anchors and the connection to the sheet piles. In the case of flexural cracks, a flow of water can occur through a certain part of the floor, which is then restricted by the compression zone. For the compression zone, the formulas for flow rate through uncracked concrete are applicable. In this case, the compression zone can be considered watertight, compared to separation cracks, as is explained in the previous paragraph. In this case, the fluid-tightness criterion can be formulated as a certain minimum height of the compression zone. For separation cracks, the criterion is formulated as a maximum allowable crack width. It can also occur that separation cracks are closed again due to the introduction of eccentric loading or loading perpendicular to the floor. For example due to the draining of the building pit.

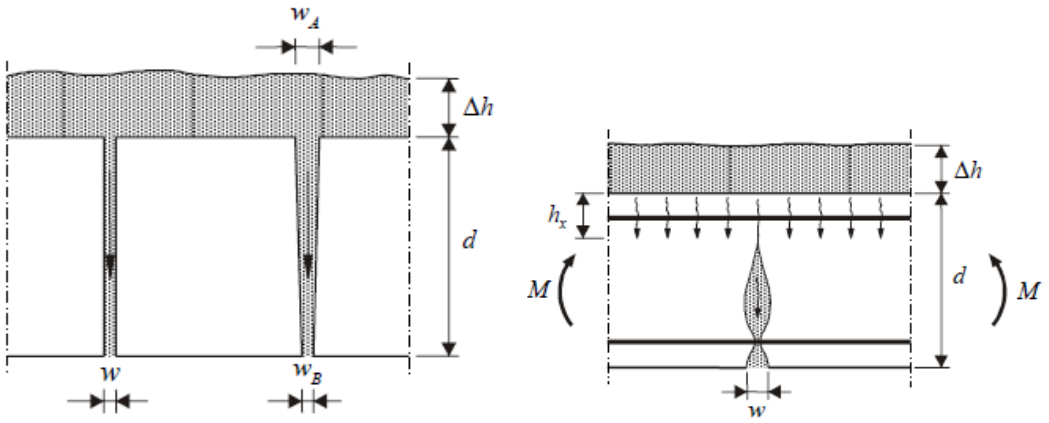

(a) Separation cracks (b) Flexural cracks

Figure 2.18: Fluid transport through different crack types. From van Breugel (2020).

To calculate the fluid transport through separation cracks, the Poiseuille formula can be used:

$$Q = \alpha \frac{w^3 \Delta p}{\mu d} l \tag{2.16}$$

Where:

- Q is the flow rate through a crack [m^3/s]
- α is an empirical factor depending on the roughness of the crack face [-]
- w is the crack width [m]
- Δp is the pressure difference [Pa]
- μ is the dynamic viscosity [Pa·s]
- d is the thickness of the concrete [m]
- l is the crack length [m]

It is difficult to say what the value of α should be, and this factor should be determined by experiments. However, van Breugel (2020) states that a value of $\alpha = 0.01$ can be used for many practical applications. It has to be noted that the formula of Poiseuille only holds for laminar flow, meaning that for very small crack widths ($w < 0.1$mm), the reliability is limited. Nevertheless equation 2.16 illustrates what

parameters are important to determine the flow rate, and therefore the possible leakage in a building pit. It has to be noted that the crack width is present in the formula as a factor to the third power, which shows that this is the most important factor in limiting leakage in UWC floors.

2.3.3. Tightness criteria

Requirements

Since there will always be cracks in a concrete construction, it is important to determine a maximum allowable crack width, in which case the amount of leakage is under a certain limit. A distinction can be made between local and global tightness. Local tightness is defined as follows: water evaporates faster than it can permeate through the concrete and it therefore remains dry. As mentioned before, this thesis focuses on separation cracks, and therefore global tightness criteria will be discussed. Global tightness criteria are usually formulated in an amount of leakage per day for the whole building pit. The goal of the SFRUWC floor is to function as the permanent floor in the whole construction, in which case no leakage or a very small amount is permitted. In this case, no cracks would be allowed in the UWC floor, which is practically impossible. Therefore, a tightness criterion can be transformed into a criterion for a maximum allowable crack width based on the ability of small cracks to be closed by self-healing.

Autogenous healing

Liquid tightness may be achieved even when separation cracks may occur due to the phenomenon of autogenous healing or self healing. This is the possibility of the cracks being filled up and therefore closed off due to:

- Continuous hydration
- Blockage of solid particles that are present in the passing fluid
- Closure of the crack by cement particles from the crack face
- Swelling of the cement paste

As presented by van Breugel (2020), experiments have been performed in which cracks with a width from 0.08 to 0.3 mm showed a drastic decrease of flow rate after the initial leakage in the first 24 hours of the experiment. In the same experiment, the reported crack width of 0.06 mm performed as a watertight structure after 24 hours of initial permeation.

According to Bomhard (1992), two important criteria for autogenous healing are that the crack width is limited to 0.2 mm and the flow rate through the crack is not too high. This is illustrated in Figure 2.19. Here it is also shown that for a higher hydraulic gradient, which is defined as the hydraulic head divided by the thickness of the concrete element, the maximum allowable crack width for self-healing is lower. The most conservative experiments were from Lohmeyer, which were based on practical observations. Meischner states that self-healing is possible in a larger range of conditions. However, these conclusions were based on laboratory experiments, in which conditions might not be comparable to practice. Later research from Schiessl was even more optimistic. However, the most conservative values that Lohemeyer found, based on practical observations, still have a preference nowadays[2] (van Breugel, 2020). For this thesis, the Lohmeyer graph illustrates that the maximum allowable crack width value should be between 0.05 and 0.2 mm.

[2]The original research on which the graph in this paragraph is based was not available. The lecture notes by (van Breugel, 2020), provide a small explanation behind these experiments on which the text in this paragraph is based.

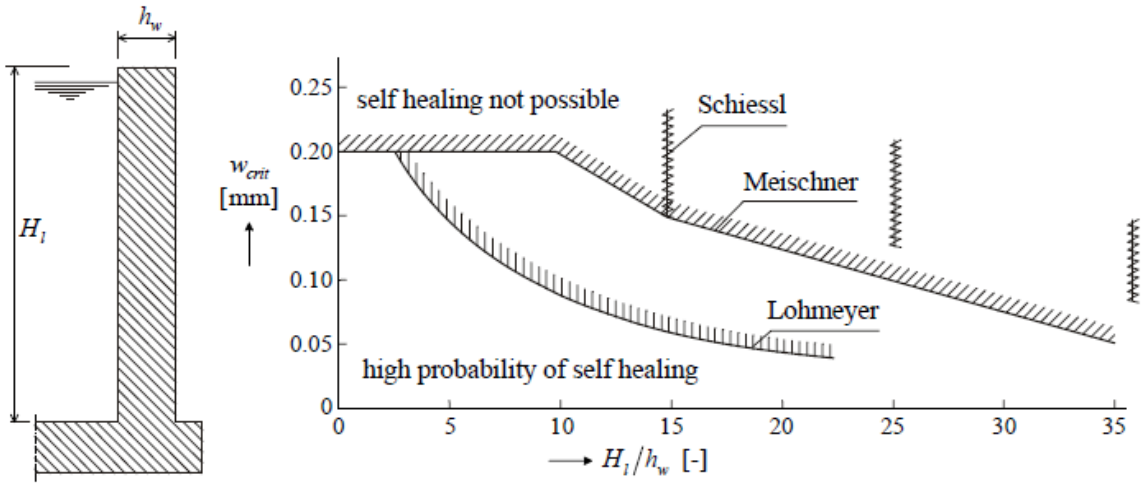

Figure 2.19: Critical crack width as a function of hydraulic gradient (hydraulic head / thickness of element) according to experiments by Lohmeyer, Meischner and Schiessl. From van Breugel (2020)

2.4. Probabilistic design

The uncertainty in the boundary conditions, material properties and tolerances that come with UWC floor construction are indicators that a probabilistic approach might be necessary to gain insight into the failure probability and the parameters that influence the failure probability the most. In this chapter, the basics of the probabilistic design methodology are summarised and it is explained which methods can be combined with FEA.

2.4.1. Probabilistic FEA

The finite element method gives good results for a set of input variables while it ignores the uncertainty corresponding with those variables. On the other hand, reliability methods take uncertainties into account but are only time-effective if an analytical description of the limit state function exists. To describe the behaviour of a structure as realistically as possible, FE models which do not have an explicit analytical limit state function are often used. The desirable features of both approaches need to be combined in a so-called stochastic finite element method (Haldar & Mahadevan, 2000).

Stochastic or probabilistic finite element methods (SFEM / PFEM) aim to combine finite element analysis with a probabilistic analysis. FEA is a commonly used effective tool to tackle a wide variety of engineering problems. Probabilistic analysis as the most general concept, refers to the handling of any uncertainty in any quantity that is used for aforementioned engineering problems. A common practice in engineering is to analyse structural systems by assuming that system parameters are exactly determined as one fixed value, but these situations are rarely encountered in reality. SFEM can roughly be divided into two categories. The first one is where the uncertainty will propagate through the FE algorithm. An example of this approach is described by Girolami et al. (2021). Existing methods in this category include the perturbation method and the spectral stochastic FE method (Arregui-Mena et al., 2016). This category aims to reduce calculation time with respect to the second category. The second category consists of Monte Carlo-based approaches, in which multiple samples (FE simulations) are carried out. This also illustrates why this is generally the slower approach, as opposed to category 1. Large or complex (nonlinear) FE models have considerable calculation times. A good overview of the available methods is presented in the papers by Arregui-Mena et al. (2016) and Stefanou (2009).

The Monte Carlo-based approach generates multiple instances of the same FE model, each with slightly

different input parameters. The input of these parameters will be a probabilistic distribution with a mean and standard deviation. There is also an option to use random fields for the spatial stochastic properties (section D). For each of the instances, the solution will be calculated with the regular deterministic nonlinear FEM. With all these samples, the failure probability can be determined, which is based on a certain limit state. All sorts of variations on the regular Monte Carlo approach have been invented to speed up the calculation process. Examples of these include importance sampling, subset simulation and directional sampling. Waarts (2000) investigated the efficiency and accuracy of these methods in his thesis. It turns out that using more efficient algorithms can save a lot of computation time. It was found that by using directional Monte Carlo simulation techniques, much fewer samples are needed compared to regular Monte Carlo simulation. Based on the results, Waarts advises three methods to use in combination with FEA. These are: directional sampling (DS), directional sampling with an adaptive response surface (DARS) and the first-order reliability method combined with an adaptive response surface (FORM-ARS). These methods will be elaborated in Section 2.4.4.

2.4.2. Probabilistic design methodology

Structural reliability is the probability that a certain system (in this case a design) does not fail in a given reference period. The failure probability, where a system does fail, can be calculated by analysing the reliability of the system.

$$Z = R - S \tag{2.17}$$

Where Z is the limit state, R stands for the resistance and S indicates the load. It is clear from this equation that when the load becomes larger than the resistance, Z will become negative, which indicates failure. The failure probability can be expressed as:

$$P_f = P\left(Z \leq 0\right) \tag{2.18}$$

All the variables that make up R and S are part of one structural model which is defined as a function:

$$g\left(\boldsymbol{X}\right) = Z \tag{2.19}$$

Where $g(\boldsymbol{X})$ is a function that represents the outcome of the model which is dependent on all the random input parameters $\boldsymbol{X}$. The failure probability then becomes:

$$P_f = P\left(Z \leq 0\right) = \left(g\left(\boldsymbol{X}\right) \leq 0\right) = \int_{g(\boldsymbol{X})<0} f_{\boldsymbol{X}(\boldsymbol{x})}\, d\boldsymbol{x} \tag{2.20}$$

Where $f_{\boldsymbol{X}(\boldsymbol{x})}$ is the n-dimensional probability density function of n random input variables. The evaluation of this integral can be done analytically for simple limit states, but for extensive engineering problems, this integral is usually determined in a numerical way (section 2.4.3).

Generally, there are 5 different ways to handle the uncertainty of a structure (Jonkman et al., 2017):

- **Level IV methods (risk-based):** In these type of methods not only the failure probability is taken into account, but also the consequences. Risk is defined as the consequence multiplied by the probability of failure, which is used as a measure of the reliability. In this way, designs can be compared based on uncertainty, costs and also benefits.
- **Level III methods (Joint distribution functions):** The uncertainties in a model are described with stochastic distributions. These methods are based on limit states, from which a joint distribution can be constructed. In level III methods, the failure probability is numerically or analytically calculated from these joint distributions. Analytical calculations are only possible with very simple cases and numerical integration is only practical when the number of variables is small. The more robust method for larger more complex models, is the Monte Carlo simulation and all it's subsidiaries such as importance sampling and directional sampling or a combination of these two.

- **Level II methods (approximation):** The uncertain variables are modelled by the mean values, standard deviations and the correlation coefficients. These methods are based on a simplification of the limit state and are approximated in the so called design point. This is the point with the highest failure probability. A linear approximation of the limit state is used in the first order reliability method (FORM) and a quadratic approximation function in the second order reliability method (SORM).
- **Level I methods (semi-probabilistic):** The uncertain variables are modeled by a characteristic value for the load and for the resistance. In the codes, safety coefficients are given, which increase the load and decrease the resistance, in such a way that they comply with the safety and reliability regulations.
- **Level 0 methods (non-probabilistic):** These are deterministic calculations. Level I calculations without the safety factors.

The reliability methods can be calibrated with a method of a higher order. For instance, the safety factors that are used in level I methods, can be determined from analyses with level II or level III methods.

The objective is to investigate the failure probability of SFRUWC floors regarding shrinkage cracking. Level 0 and 1 methods are not suitable for this. The level 4 methods are out of scope, hence Level 2 and 3 methods remain. By definition, Level 2 methods are performed on component level or on single failure modes, while structural reliability analysis covers the complete failure domain (Waarts, 2000). The difficulty is to identify all failure modes, which requires engineering judgement. In this case, level 2 methods such as FORM should be combined with a full system analysis. Therefore, the level III methods seem to be the most suitable when looking at the design of UWC floors.

2.4.3. Monte Carlo simulations and level III methods

As mentioned in the preceding chapter, level III methods evaluate the integral from Equation 2.20. This can be done analytically for easy problems, by (numerical) integration or by Monte Carlo simulations. With Monte Carlo methods, the failure probability is determined by the portion of failing model outcomes compared to the total number of model outcomes. The model outcome is given in the shape of a limit state (2.17) and can be the result of FE simulation or a hand calculation. Each model outcome is also called a sample. Every sample will give a different outcome because the input parameters of the model are drawn from a stochastic distribution. The failure probability can then be determined as:

$$P_f = \frac{N_f}{N} \tag{2.21}$$

Where:

- N is the total number of samples
- N_f is the number of failing samples

Enough samples have to be generated in order to reach a certain precision and certainty of the result. This precision is defined as a target coefficient of variation (relative error) can be determined by calculating the coefficient of variation V_{P_f} of the sample results. This can be approximated by (Jonkman et al., 2017, p. 123):

$$V_{P_f} = \frac{\sigma_{P_f}}{P_f} \cong \frac{1}{\sqrt{N \cdot P_f}} \tag{2.22}$$

It can be observed that this is dependent on the total number of samples and the calculated failure probability. A target coefficient of variation (V_{P_f}) can be defined which is used as a criterion when the results are of a certain precision and the analysis is done. Additionally, an estimate for the number of necessary samples can be calculated when the target V_{P_f} and estimated failure probability are known. As was explained in section 2.4.1, a number of variations on the MC algorithm were invented in order

to speed up the algorithm. Not all of these methods will be described, but since directional sampling is incorporated in the FE software that was used, it will be elaborated on in the next section.

2.4.4. Directional sampling

In the search for faster Monte Carlo algorithms, Deák (1980) suggested to transform the standard normal variables and its corresponding normal coordinates into polar coordinates $(\lambda, \underline{\theta})$. Where $\underline{\theta}$ is a unit direction vector and λ is a scalar which defines the length of the vector in standard normal space (U-space). Equation 2.20 will then turn into: [3]

$$P_f = \int_{g(\boldsymbol{X})<0} f_{\boldsymbol{X}(\boldsymbol{x})}\, d\boldsymbol{x} = \int P\left(g\left(\lambda\underline{\theta}\right) \leq 0\right) f\left(\underline{\theta}\right) d\underline{\theta} \tag{2.23}$$

Where $f\left(\underline{\theta}\right)$ is the density on the unit sphere. For each direction θ_i, the value of λ_i is determined in such a manner that the limit state function equals 0:

$$g_i = g(\lambda_i, \theta_i) = 0 \tag{2.24}$$

The value of λ_i indicates the distance to the limit state in the direction defined by vector $\underline{\theta}$ and it can be found through an iterative procedure. This is illustrated in figure 2.20.

Let us take an example of a limit state with two random variables (u_1 and u_2) as is illustrated in Figure 2.20. The limit state here can be defined as $g_i = -u_1^2 - u_2^2 + \lambda_i^2$, where $\lambda_i = R$, since it intersects the hypersphere. It can be observed that the limit state consists out of a sum of the squares of two independent standard Normal variables, which can be represented by the χ^2 distribution (Benjamin & Cornell, 2014). In general the sum of n independent normal variables can be represented by the χ_n^2 distribution, with n degrees of freedom, which corresponds to the number of variables. Under this assumption, Katsuki and Frangopol (1994) described in their paper that equation 2.23 can be transformed into:

$$P_f = \int \left(1 - \chi_n^2(\lambda^2(\underline{\theta})\right) d\underline{\theta} \tag{2.25}$$

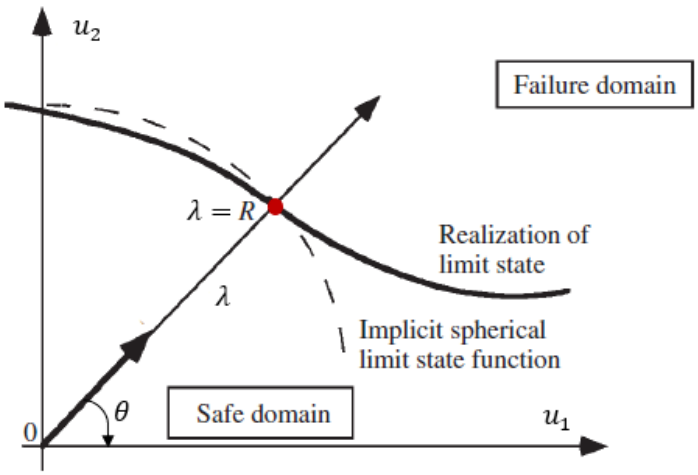

Figure 2.20: A directional sample in direction θ with length $\lambda = R$ at the intersection between the limit state and the approximated hyper sphere with radius R. Adapted from Melchers and Beck (2018, p.83)

Equation 2.25 still consists of an integral and can be solved with integration, which is called directional integration in this case, which is similar to the numerical integration in section 2.4.3. Instead of evaluating this integral, an estimate of the failure probability can be obtained by performing MC simulations

[3] Throughout this section, the explanation from the thesis by Waarts (2000) is adapted

of the $\underline{\theta}$-vector. In this case we are talking about directional MC simulations, or directional simulation shortly (Ditlevsen et al., 1988). The difference between these two methods is illustrated in Figure 2.21. The sample failure probability is than given by:

$$P_i = P\left(g\left(\lambda_i, \theta_i\right) < 0\right\} = 1 - \chi_n^2\left(\lambda_i^2(\theta)\right) \tag{2.26}$$

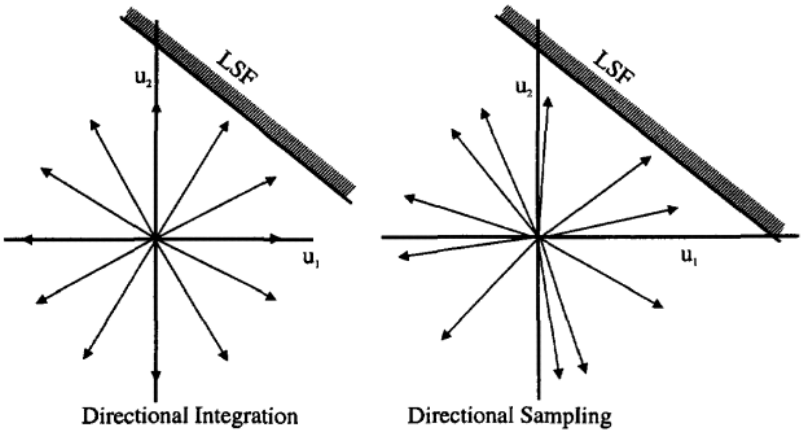

Figure 2.21: Directional integration and Directional sampling. From Waarts (2000)

The advantage of directional simulation, is that equation 2.26 can be evaluated analytically, which reduces the order of integration by one dimension (Melchers & Beck, 2018). Consequently, the failure probability can be calculated in a similar way as in section 2.4.3:

$$P_f = \frac{1}{n}\sum_{i=1}^{n} P_i \tag{2.27}$$

An estimate for the standard deviation is given by Ditlevsen et al. (1988):

$$\sigma^2(P_f) = \frac{1}{n(n-1)}\sum_{i=1}^{n}\left(P_i - P_f\right)^2 \tag{2.28}$$

This is needed to determine the coefficient of variation in order to determine the accuracy (and stop criterium) of the result. This can be done with:

$$V_{P_f} = \frac{\sigma_{P_f}}{P_f} \tag{2.29}$$

2.4.5. Directional sampling with an adaptive response surface

Directional sampling with an adaptive response surface (DARS) is the combination of regular DS and the response surface method. The standard response surface method is a method to substitute an analytical limit state function instead of the real response function. In fact the model result $g\left(\boldsymbol{X}\right)$ from equation 2.20, would be replaced by an analytical expression. The idea is that with a couple of FE simulations, a response surface can be determined. For the next samples, the result of the model function $g\left(\boldsymbol{X}\right)$ could be determined by the analytical response function instead of the FE simulation, which saves computational time. In fact, fewer limit state function evaluations (LSFE) using NLFEA are necessary. An important aspect of this method is to evaluate the accuracy of the response surface method, compared to the real response (Waarts, 2000).

A quadratic response surface can be fitted to the results in the shape of (Roy, 2019):

$$\hat{G}(\mathbf{u}) = a_0 + \sum_{i=1}^{n} a_i u_i + \sum_{i=1}^{n}\sum_{j=1}^{n} a_{ij} u_i u_j \tag{2.30}$$

Where the response surface is a function of the random variable from the u-space $u_{i/j}$ and the fitting parameters $a_{i/j}$. The DARS algorithm in DIANA is built up of three stages (Evangeliou, 2016). First, in level 1, the value of each random variable is varied individually until the limit state is reached. This gives an estimate of the failure probability. In the second stage, axis directional integration (ADI) is used to determine the zero point of the limit state function in the U-space and to estimate the response surface. In the final stage, random samples (directions) are chosen. The algorithm will use the response surface to determine the distance to the limit state λ_i (equation 2.26) instead of a finite element LSFE. "If this length is critical, meaning that the length along the direction is less than the minimum length found so far for other samples, a FEA will be performed to determine the LSFE. The result will be that a part of the samples will not need a FEA, meaning that the calculation will cost less time than regular DS (Evangeliou, 2016). Exact flow charts with all the steps of these algorithms (in DIANA) are presented in appendix K of the thesis of Evangeliou (2016), which is freely available online (see reference list).

2.5. Stochastic material properties

As explained in Section 2.4, the input for a probabilistic finite element analysis is a set of stochastic variables. Some properties will have to be assumed, but other properties can be obtained from literature or building codes. This section focuses on the latter. Some codes prescribe what the assumed standard deviation of certain material properties of concrete should be. When looking at cracking, the tensile strength of concrete is the most relevant property, the focus of this paragraph will be on this property.

2.5.1. Standard deviation of tensile strength

Eurocode 2

The Eurocode (2011) gives values for the 95% and 5% characteristic value of the tensile strength of concrete. These values correspond in the standard normal distribution to 1.64 times the standard deviation σ. This leads to a coefficient of variation of:

$$\text{COV} = \frac{\sigma}{\mu} = \frac{\left(f_{\text{ctm}} - f_{\text{ctk},0.05}\right)/1.64}{f_{\text{ctm}}} \tag{2.31}$$

Assuming that, according to EC2, $f_{\text{ctk},0.05} = 0.7 f_{\text{ctm}}$, the equation simplifies to:

$$\text{COV} = \frac{(f_{\text{ctm}} - 0.7 f_{\text{ctm}})}{1.64 f_{\text{ctm}}} = \frac{0.3}{1.64} = 0.183 \tag{2.32}$$

Meaning that the coefficient of variation according to EC2 is independent of the concrete class and is approximately 18%.

JCSS probabilistic model code

The JCSS probabilistic model code for concrete (JCSS, 2001) gives coefficients of variation for multiple material properties. These are given in table 2.2. It can be observed that the COV for the tensile strength is 30% as compared to 18% according to EC2.

2.5.2. Stochastic variation in FRC

Soetens and Matthys (2014) reported coefficients of variations for the residual tensile strengths of 6 different concrete mixtures. These were in the range between 11 and 33%. This corresponds to the

Table 2.2: Stochastic properties of concrete according to JCSS (2001)

Material property	COV	Distribution type
Compressive strength	0.06	Log-normal
Tensile strength	0.30	Log-normal
E-modulus	0.15	Log-normal
Ultimate strain	0.15	Log-normal

values for the standard deviation of the tensile strength of regular concrete that were found in the previous paragraph.

3

Underwater concrete floors

3.1. Construction

3.1.1. Construction method

The most commonly used method for construction below the groundwater table in the Netherlands, is the application of underwater concrete (W. van der Woerdt & Bouwmeester - van den Bos, 2011). UWC projects include tunnels, parking garages, rail and road construction, building pits, basements and more. The construction technique has been applied for more than 60 years. The UWC functions as a temporary seal of the building pit, so the structural top floor can be constructed in a dry environment. The three main types of construction with UWC have been explained in section 1.1. The general construction process is quite similar for all of these types.

The construction method of UWC floors is illustrated in Figure 3.1. The general steps are described in this list.

1. Sheet piles or slurry walls are installed in the ground, which forms the walls of the building pit.
2. Installation of anchors or struts, in order to prevent the walls from step 1 from caving in during excavation.
3. The soil is excavated until the desired depth. The first part can be done with excavators, but when the groundwater table is reached, this changes to wet excavation from barges or cranes.
4. Installation of foundation piles. These are tension piles or anchors and prevent the UWC floor from bursting up due to upwards water pressure when the building pit is drained.
5. After installation, connections have to be made at the top of the piles, which will connect the UWC floor with the piles. This is done by divers by stripping the upper part of the pile so the reinforcement is exposed.
6. The bottom of the building pit will be levelled to ensure a uniform thickness of the UWC floor.
7. UWC is poured by making use of a so-called ”hop-dobber” or a pipe with a valve.
8. The UWC floor has time to set and develop enough strength.
9. The building pit can be drained. The UWC floor in combination with the anchors prevents the soil from bursting up due to upward water pressure (Figure 3.2).
10. After draining, the building pit is checked for leaks (especially at the connection between the sheet piles and the UWC floors), which are repaired when necessary.

11. The building pit is completed and the rest of the construction work can be executed.

3.1.2. Construction phasing

After casting, the UWC floor will have time to harden, whilst being submerged, before the building pit is drained. During this period the water level is kept equal to the surroundings so no upward water pressure acts on the floor. When the floor develops sufficient strength, the building pit will be drained and due to the head difference, an upward load will be introduced to the floor. The construction phase can roughly be divided into two phases. Phase A is where the concrete is poured and hardens under water before the load is introduced. Phase B starts when the building pit is drained and external forces are introduced on the floor. A conservative assumption for the transition point between phases A and B can be taken as the moment when the floor is fully cooled down to the external temperature of the environment, and no changes in thermal stresses due to the hydration process will occur anymore. In practice, draining might occur earlier in time, as long as enough strength is already developed. As mentioned in the scope, the focus will lie on crack formation in phase A.

It has to be noted that if separation cracks form, they will form in phase A. In phase B the cracks might either grow or partially close due to bending and the subsequent occurring compression zone. During phase B, the construction will reach an equilibrium situation where the crack widths are stabilised and do not grow. However, seasonal temperature changes might still lead to cracking and the formation of water-leaking separation cracks, where there were non at first, especially when the construction occurred during the summer. This is also taken into account in the building codes and it is taken into account in section 4.1.3.

3.2. Structural behaviour

The first step after (partial) hardening of the floor will be draining the building pit. In this stage, the main load on a UWC floor will be the upward water pressure. This force will be resisted by the self-weight of the UWC floor and the tension piles that keep the floor down. This means that the resistance of the floor against upwards forces is mainly determined by the tension piles and the spacing between them. Currently, it is advised to dimension UWC floors in such a way that the transverse direction of the floor is governing (CUR-Aanbeveling 77:2014, 2014). This is achieved by choosing a larger intermediate spacing between the tension piles in the transverse direction.

For an equal thermal strain, UWC floors with a longer span will elongate more than shorter spans for a similar thermal strain ($\varepsilon_T = \Delta L \cdot L$). At first glance, this is not obvious when looking at Equation 2.12. When applying this formula, an equal thermal strain would lead to a similar stress development. However, it is known that longer spans will lead to higher stresses. The reason behind this is that longer spans will have a larger elongation, which will exert more force on the boundary conditions. Due to the nonlinear character of these boundary conditions, the degree of restraint will be larger for longer-span floors. Taking this into account, Equation 2.12 does indeed explain why longer floors will lead to a higher stress.

The sheet piles on all four sides of a rectangular building pit will deform inward due to active soil pressure (see Figure 3.2). This force is smaller than the force that may develop due to passive soil pressure. Passive soil pressure occurs when the UWC slab expands (due to thermal variations) and pushes against the sheet piles. These sheet piles will restrain this deformation and a strut force will develop. This compressive normal force on the UWC floor acts as a prestress force (Figure 3.2). This strut force will be present in the short transversal direction, but in the longitudinal direction, these forces will quickly be dissipated through other types of restraint in that direction such as the restraint from the horizontal resistance of the tension piles and the restraint from the parallel sheet piles[1]. Together

[1]The definition of parallel sheet piles is that they are parallel in the longitudinal direction. See Figure 4.1 for illustration.

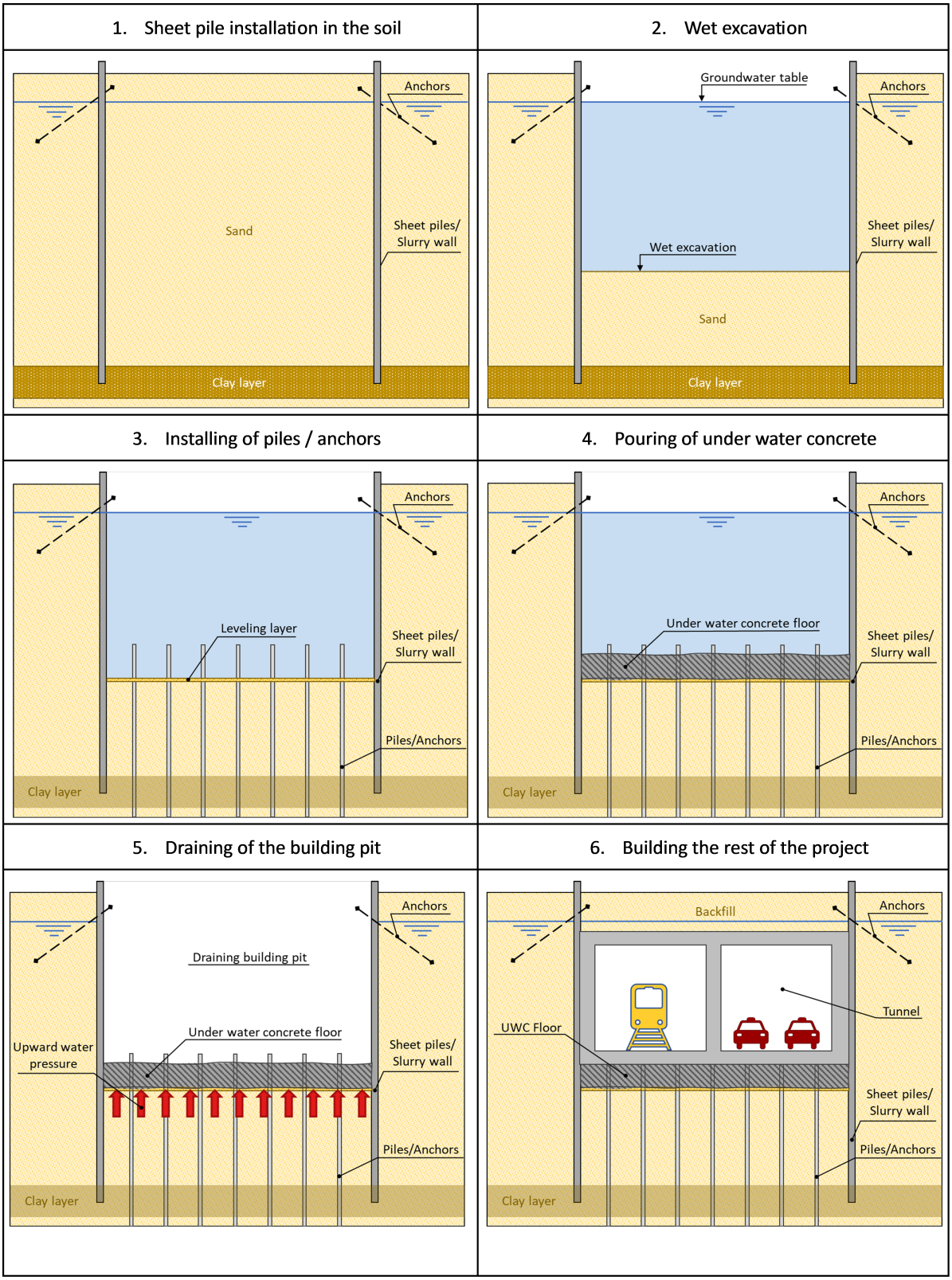

Figure 3.1: Building process of underwater concrete floors

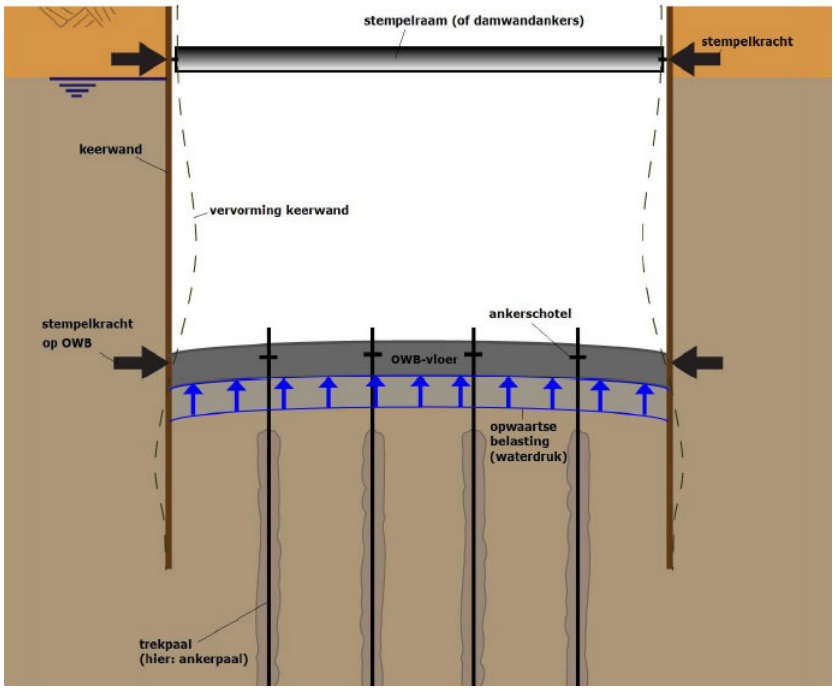

Figure 3.2: Passive soil pressure will cause the sheet piles to deform which will introduce an (eccentric) strut force on the UWC floor. Adapted from Arkesteijn, 2012

with the conclusion from the previous paragraph, it can be concluded that the longitudinal direction is governing for the crack width calculations. This is also supported by the recommendations from the CUR-77 (2014).

With this in mind, it can be assumed that adding fibres to limit crack width is especially beneficial in shallow, long narrow building pits. Sheet piles of shallow building pits will tend to deform less in a horizontal way, leading to lower strut forces, which is especially relevant for the transverse direction. Additionally, the addition of steel fibres also increases the resistance to punching shear in the slab (Arkesteijn & Menting, 2013), which is important for the anchors/tension piles that are used in UWC floors.

3.3. General cracking in different UWC floor types

Underwater concrete can generally be assumed to act as mass concrete. Due to the large thickness of the UWC floors, it is almost certain that some cracking will occur in UWC floors during the hardening process. Even before external forces are applied to the construction, cracking can be expected. This is typical for mass concrete. Especially in long and narrow building pits as was explained in Section 3.2.

Therefore, crack width limitation is especially important for UWC slabs. The formation of separation cracks that might cause leakage is a problem that occurs regularly in this type of construction. It is not an immediate problem when the drainage capacity is larger than the leakage flow rate, because the building pit remains dry. However, it does cause additional problems and risks for the durability and quality of the concrete and the performance of the structural top floor. In the user's phase, crack formation in the UWC concrete is less critical when a reinforced concrete structural top floor is used since the top floor will function as a second barrier to prevent leaks. But applying a structural top floor directly on top of the UWC floor brings other challenges. Casting new concrete on existing concrete causes cracking in the top floor due to the restrained deformation by the existing UWC floor. In this

case, the second barrier is less effective as a watertight structure. This was also observed by den Boef (1996), who has shown that leaking separation cracks in structural top floors cast on UWC floors are caused by restrained deformations during the hardening process. Climatological fluctuations such as temperature and humidity also play a significant role. In 2001 guidelines were set up for the construction of temporary unreinforced UWC floors, which were updated in 2014 (CUR-Aanbeveling 77:2014, 2014). However, these guidelines are only intended for structural safety but do not include extensive crack width calculations.

Practically it is not possible to create a floor that is entirely uncracked. Moreover, the amount of leakage is mainly determined by the crack width and not by the number of cracks. When the crack width is limited, these cracks might not even be a risk for leakage, since self-healing can occur (van Breugel, 2003). Self-healing can be caused by specific mechanisms when both the crack width and water pressure are sufficiently small, as was explained in section 2.3. Nonetheless, many uncertainties exist in the circumstances under which self-healing can occur.

The apparently unavoidable formation of cracks in UWC floors is the cause of discussion in the construction industry (W. van der Woerdt & Bouwmeester - van den Bos, 2011). Without a structural top floor, the UWC floor functions as the permanent structural floor (design type: permanent UWC floor) and it needs to ensure the whole structure's water tightness, as explained in the introduction (Ch. 1.1). In the permanent UWC floor design type, crack width limitation and leakage prevention become even more critical than in the traditional design types. Determining the maximum occurring crack width beforehand is still somewhat imprecise. Reasons for this are that there is a large spread in the temperature loading, and determining the degree of restraint depends on quite some uncertain assumptions. Additionally, the stress that develops in the hardening phase is not always taken into account, but it does significantly influence the stress in the final state of the floor (W. van der Woerdt & Bouwmeester - van den Bos, 2011). The practice of not taking stress development during the hardening phase into account led to the occurrence of water-leaking cracks in several projects in which UWC floors were used (W. van der Woerdt & Bouwmeester - van den Bos, 2011). For this reason, attention has to be paid to the development of calculation methods that consider temperature loads and stress development during the hardening phase. Van der Woerdt (2010) presented a method and FE models to calculate the stress in structural top floors on top of UWC that take these effects into account. These calculations are suitable for insight into the measures that can be taken to reduce the stresses caused by restrained deformation as much as possible.

As opposed to the traditional temporary UWC floor with a separate structural top floor described in the previous paragraphs, the integrated UWC floor is a significant improvement. In this construction method, the UWC floor does not only have a temporary function but also contributes to the load-carrying capacity in the final phase. This is achieved by making the UWC floor and top floor work together by means of using dowels and extending the piles and tension anchors into the top layer (middle panel figure 1.1). This method is characterised by the addition of steel fibres to the UWC mix, making it a SFRUWC floor. Adding steel fibres reduces the risk of large separation cracks and leakage. This is important because the UWC floor must have a dry surface to ensure good bonding between the UWC floor and the top floor. In this integrated floor, the combined bottom and top floor's full height results in a large bending moment capacity because both floors work together. The structural performance and the water tightness seem superior to the traditional construction method (van Tilburg et al., 2021).

3.4. Hardening and thermal shrinkage cracking in UWC floors

3.4.1. Temperature difference in young concrete

During the hardening process, heat is produced due to the hydration reaction of cement (Chapter 2.1). After reaching a certain maximum temperature, the concrete slab will cool down until it reaches the

environmental temperature. Hence, the whole process can be divided into a heating and a cooling phase. Where the concrete is heated to a maximum temperature T_{max}, followed by a cooling phase until the temperature reaches the temperature of the environment T_{external}.

$$\text{Heating phase:} \quad t_0 < t \leq t_{T=T_{\text{max}}}$$
$$\text{Cooling phase:} \quad t_{T=T_{\text{max}}} < t < t_{T=T_{\text{external}}}$$

Heating phase

The crack formation due to restrained thermal strains is mainly caused by a temperature difference over the height of the slab. Heat will be produced uniformly in the concrete, but it is only dissipated at the top and bottom edges. This causes a temperature differential, where the temperature in the middle will be higher than the temperature at the boundaries of the slab. This becomes obvious when looking at the temperature distribution in Figure 3.3. The temperature distribution can be divided into an average temperature and an Eigen temperature. In some cases when the rate of heat dissipation is unequal, there will also be a linear component as displayed in Figure A.2 in the appendix. The average (and potential linear) temperature change will only be translated into stresses when the deformation is restrained, while the eigen temperature distribution will always lead to internal stresses (van Breugel et al., 2016). The average temperature component will lead to extension, the linear component to bending and the Eigen temperature will lead to internal strain differences. When looking at the temperature distribution in Figure 3.3 it can be seen that the middle will indeed become hotter than the outer zones.

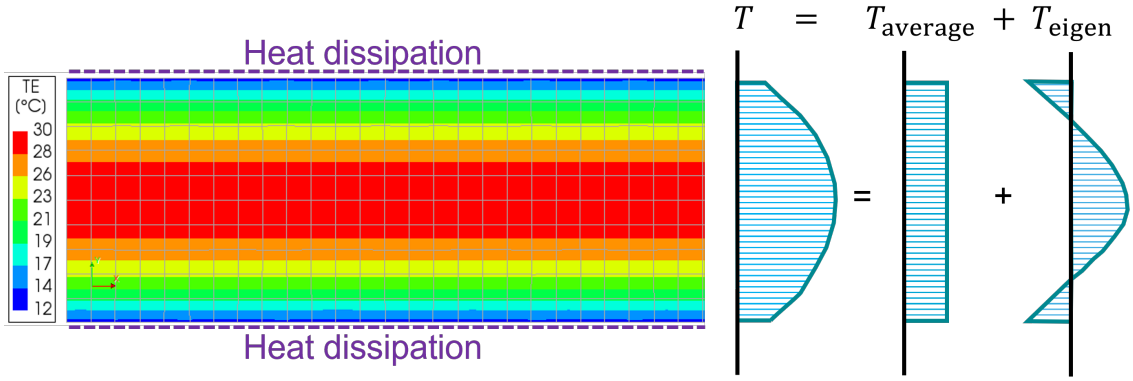

Figure 3.3: Temperature distribution over the height of the slab. The middle becomes hotter than the boundaries. The temperature can be divided into an average temperature and an Eigen temperature.

This temperature differential causes an Eigen temperature component which will lead to the ”middle zone” expanding more than the outer zones. In this case, the outer zones restrain the middle zone where the middle zone will experience compressive stresses and the outer zones will experience tensile stresses. This is also called the internal restraint of the Eigen Stresses and is elaborated in section 2.1.5. The tensile stresses at the slab’s top and bottom surfaces will lead to surface microcracking in the edge zones during the heating phase. As explained in Section 3.2, there is also restraint from the sheet piles, which is depicted in Figure 3.4.

Cooling phase

After reaching the maximum temperature, the cooling phase starts. Since the middle strip reached a higher temperature than the top and bottom boundaries during the heating phase, it must also cool down more to reach the environmental temperature. This implies that the process is reversed, where the outer strips will constrain the middle strips from shrinking. This leads to tensile stress in the middle strip. This is combined with the restrained average component of the Temperature during the cooling phase, which will cause the micro-cracks that formed in the outer zones during the heating phase to grow towards the middle zone. At a given time, the cracks at the bottom and the top of the slab might

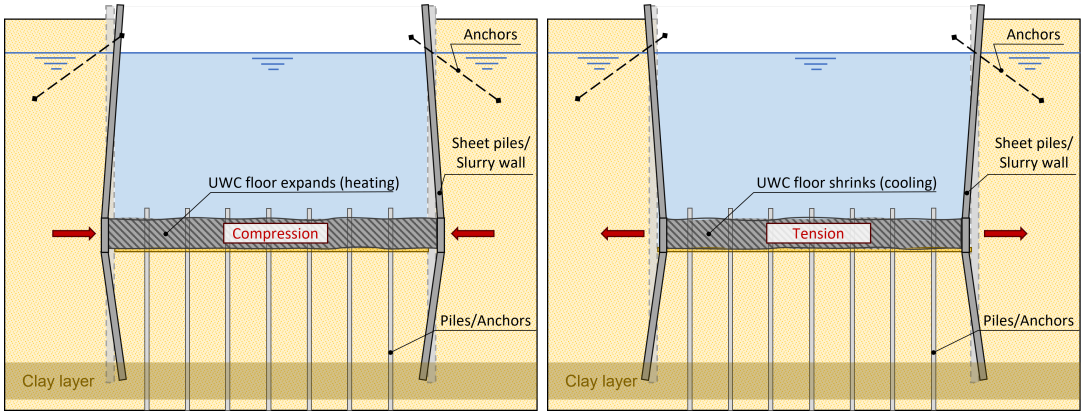

(a) Expansion of the UWC floor leads to compressive stresses

(b) Shrinkage of the UWC floor leads to tensile stresses

Figure 3.4: Schematic overview of restrained deformations of the UWC floor and subsequent forces. Displacements are exaggerated for illustrative purposes.

connect in the middle, forming separation cracks. These cracks can cause leakage. This process is schematically illustrated in Figure 3.5.

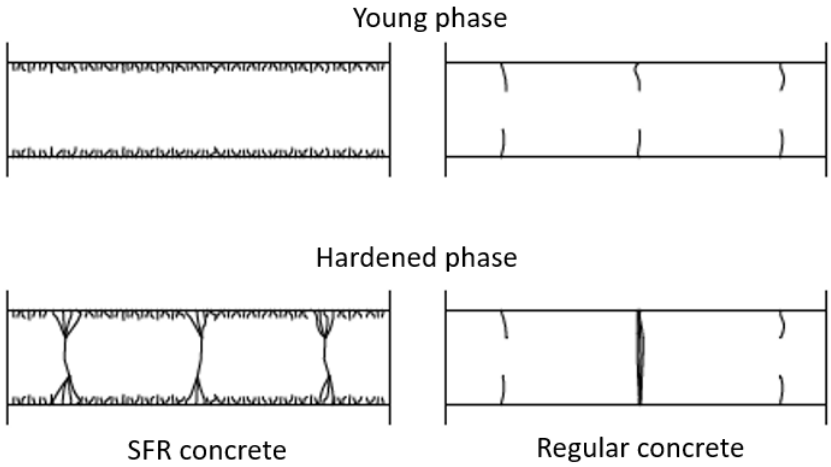

Figure 3.5: Crack pattern in SFR concrete and regular concrete. From Arkesteijn and Menting, 2013

In practice, the heat dissipation at the top and bottom will not be equal. The top boundary of the slab borders an open building pit, filled with water that is in contact with the air. The bottom boundary is adjacent to the soil in which there is groundwater with a constant temperature. Also the soil itself at the bottom acts as an insulating layer. In most cases, the heat transfer coefficient at the top boundary will be larger than the coefficient at the bottom. This will introduce a linear component in the temperature distribution as shown in Figure A.2 in the appendix. Heat dissipation might even be more substantial in the case of flowing water, which will increase the gradient of the linear component.

3.4.2. Development of strength and stiffness over time

The temperature change from the previous section will lead to thermal strains, which lead to stresses when restrained. Shrinkage during the cooling phase due to the temperature decrease will lead to tensile stress. Cracking will occur if the tensile stress becomes more significant than the tensile strength. However, the strength also needs time to develop. Concrete strength and stiffness properties develop as the hydration reaction progresses, as explained in Section 2.1.4. For example, the modulus of elas-

ticity will be larger during the cooling phase after the peak temperature has been reached than in the pre-peak heating phase. As can be observed from Equation 2.12, the magnitude of the stress that develops, given a certain thermal strain and degree of restraint also depends on the Young's modulus. This means that for a similar temperature difference, the absolute stress development is higher during the cooling phase than during the heating phase because the Young's modulus is higher during the cooling phase due to the increased maturity. This can also be concluded from Figure 2.6. The compressive stress increases during the heating phase to a certain maximum. This stress maximum corresponds with the moment when the maximum temperature is reached, which also denotes the start of the cooling phase. It can be seen that all of the developed compressive needs to be overcome before tensile stress can develop. So the absolute stress development is larger during the cooling phase.

3.5. Fibre reinforced underwater concrete floors

According to Arkesteijn and Menting (2013), an average steel fibre dosage of 35 kg/m^3 is generally applied in current projects. This corresponds to approximately 0.45% by volume of the concrete mixture. Underwater concrete is often a significant part of the material used in a project (Bouwmeester - van den Bos & Galjaard, 2013). Therefore, generally, concrete of normal strength classes is used. Moreover, it is usually not feasible to achieve a high concrete quality due to the construction underwater. In the case of a SFRUWC floor, this will almost always lead to a fibre-reinforced concrete that shows tension-softening behaviour as illustrated in Section 2.2.

As discussed in section 3.3 and in 1.1, multiple studies and examples from practice show that using fibres is a considerable improvement in crack width control and overall strength as opposed to unreinforced UWC. Adding fibres to the concrete mixture also increases the material's toughness, which increases the redistribution of forces and the slab's resistance. The main reason for a better maximum crack width control is that the residual tensile strength of FRC can divide the shrinkage strain over multiple cracks, preventing the formation of large localised cracks. This is illustrated in Figure 3.5. This crack width dispersion positively affects the water tightness of the floor. Results have been reported where leakage through FRC specimens (1% steel fibres by volume) occurs at a strain that is 1.5 to 2 times greater than for ordinary concrete (Arkesteijn & Menting, 2013). Evidently, the amount of leakage is dependent on the crack width. As was observed in section 2.3.2, the equation (Eq.2.16) that gives an estimate of the flow rate through a crack has the crack width to the third power in it. Making this the most important parameter influencing the leakage. Figure 3.6 shows lower flow rates in FRC than ordinary concrete for similar crack widths.

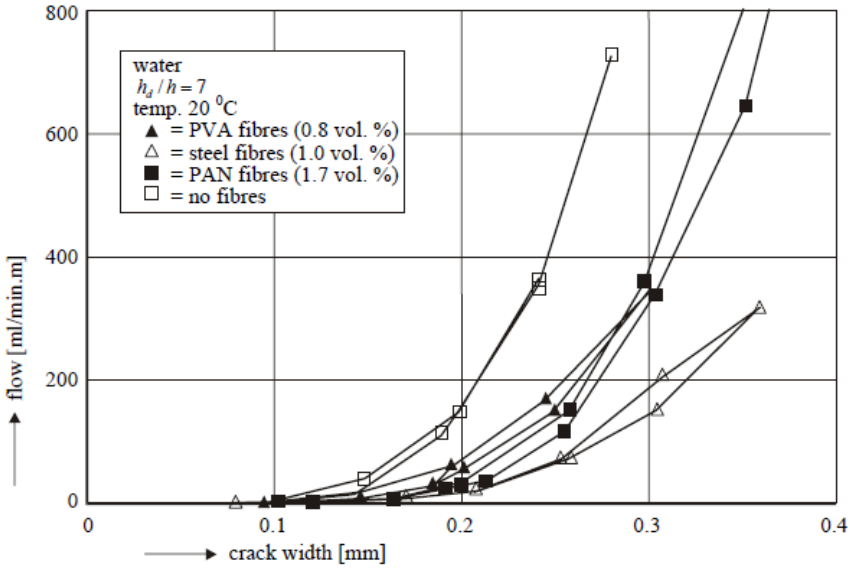

Figure 3.6: Water Permeability of ordinary concrete and as a function of crack width. From Tsukamoto and Wörner, 1991

3.6. Uncertainties and tolerances

Since the construction of the floor takes place underwater, and often at large depths, it is accompanied by quite some uncertainties in geometry and quality (CUR Rapport 102, 1981). There is simply no easy and clear way of checking the placement of the concrete and if the required final thickness of the actual floor is achieved everywhere. This tolerance is dependent on the type of soil, the excavation method, the presence of a filling layer and the method of casting. The Dutch guidelines CUR 77 (2014) illustrate these tolerances, shown in Figure 3.7. Furthermore, the CUR 77 states that the average thickness $(h_{average})$ of the floor should be used to calculate the stiffness and the minimum thickness (h_{min}) should be used with stress and strength calculations. The minimum thickness should also be used in crack width calculations. CUR 77 states that common tolerances for the bottom are in the range of 150 to 350 mm, depending on the soil condition. While for the top, they are in the range of 75 to 150 mm, depending on the pouring method.

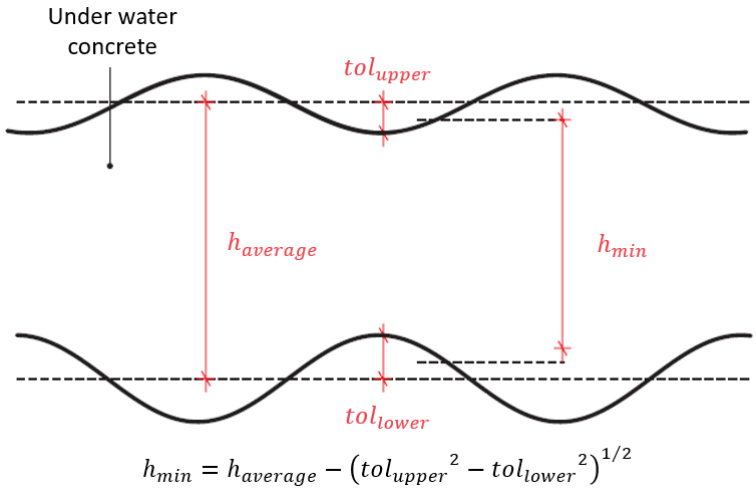

Figure 3.7: Tolerances in the geometry of UWC floors. From CUR 77, 2014

The material properties such as strength and stiffness also cause additional uncertainty. This is even the case for regular concrete beams made in a controlled environment in a factory. Entrapped air or water caused by underwater casting may cause local weak spots in the slab. If these weak spots coincide with the sections where the floor is much thinner than the average, these effects will amplify each other. Specifically for FRC, the placement and local distribution of the fibres is also unsure. Concrete is poured through a long chute, which might affect these properties. fibres might align or cluster due to the pouring process, while they should be randomly oriented, and dispersed evenly through the concrete.

Environmental circumstances are also a cause for uncertainty. The heat boundary transfer coefficients heavily depend on the water temperature, flow and groundwater conditions. These coefficients determine how much heat the slab can dissipate to the environment, which influences the stress development during the hardening process and therefore also the crack formation. Values for these heat transfer coefficients vary between 111 $Wm^{-2}K^{-1}$ for stagnant water to 695 $Wm^{-2}K^{-1}$ for flowing water, according to (van Breugel et al., 2016). The wide spread of these values indicates the uncertainty of these assumptions. Besides the transfer coefficients, the actual external temperature is also of great influence. Dependent on the internal heat development, the larger the difference between the maximum temperature reached during hardening and the external temperature of the environment, the larger the stress development will be. One can imagine that this is completely different when the construction is cast in winter or in summer. The soil conditions are also included in the uncertain environmental properties. These also influence the properties of the sheet pile walls and therefore boundary conditions of the slab, as is explained in chapter 3.2.

In conclusion, it shows that most of these properties are hard to capture in one specific deterministic value and can better be modelled as ranges. This can be achieved by a probabilistic analysis that considers these variables as stochastic distributions with a certain mean and standard deviation.

3.7. Existing design recommendations

Several (Dutch) recommendations about UWC floors or separate aspects already exist. The most relevant is the CUR 77, which covers the design rules of ordinary UWC floors. From the other standards, some relevant concepts are briefly summarised in this section. The general structural behaviour is already described in Section 3.2 and therefore it will not be repeated in this section. Only the relevant general concepts and design philosophies of the guidelines will be discussed. Details from these guidelines such as the prescribed partial safety factors are not presented in this Section.

CUR 77 - Design rules for underwater concrete floors

The CUR 77 (2007) contains design rules for unreinforced UWC floors with a temporary function. The design rules are based on the presence of the tension elements as depicted in Figure 3.1 which are the main resistance against the upwards water pressure. Cur 77 rules mainly focus on the floor's structural safety but do not guarantee water tightness. It states that leakage is almost unavoidable due to the restrained thermal shrinkage strain in the building pit's longitudinal direction or bad seals with the sheet piles. The CUR-77 presents a precise, convenient overview of all the design checks that have to be performed. The main design checks are split up between the longitudinal and transversal directions and are discussed in the following sections.

Longitudinal direction

The design philosophy is that the centre-to-centre distance between the tension piles is smaller in the longitudinal direction than in the transversal direction. This ensures that the ULS check is always governing in the transversal direction. To ensure this, there is a SLS check for the longitudinal direction. When this check is satisfied, the ULS in the longitudinal direction will not be governing. The spans

between the tension piles in the longitudinal direction will be modelled as a simply supported beam. The tensile stress caused by the bending moment may not exceed 1.25 times the concrete design tensile strength. If a strut force is present, this may not be taken into account for this check.

Transversal direction

There is no SLS check in the transversal direction because leakage will almost always be the result of the forces in the longitudinal direction due to restrained thermal deformations. The ULS check considers two failure mechanisms: failure due to the exceedance of either the tensile strength or compressive strength in the compression arch in the UWC floor. For the ULS check for the tensile strength, the UWC floor needs to be modelled continuous beam with spring supports. In this case, the horizontal strutting force from the sheet piles does need to be taken into account. CUR 77 prescribes all the details of this calculation. In this case the compressive strength may not be exceeded by the occurring compressive stress caused by the bending moments in combination with a normal force (strut force). The ULS check for the transversal direction is similar to the check for the longitudinal direction.

CUR 2007-3 - Cracks in underwater concrete

The goal of this report was to set up guidelines regarding the crack width limitation in structural top floors cast on UWC (Integrated design). The report includes some relevant observations from practice:

- The cracks that occurred were primarily full through-cracks
- Additional cracks would form after a cold period in the winter, while no cracks were present before this period.
- The above-mentioned crack formation also occurred in floors that were artificially cooled during the hardening process. Cooling during the hardening phase is beneficial for crack formation during this phase, but it does not rule out crack formation in later stages.
- An intermediate layer of sand between the UWC and structural floor showed better results, and in some cases, there were no cracks at all.

Furthermore, it is suggested that the critical phases for crack formation are between 5 and 20 hours after mixing and 2 to 10 days after casting. Also, it is recommended to use the equivalent age concept in combination with the Eurocode formula (2.9) to determine the tensile strength of hardening concrete at a particular time.

A similar model compared to the model from Chapter 4 was set up and some relevant conclusions from the calculation are that:

- The probability of cracking is higher when a floor is cast in the summer
- The probability of cracking is higher for thicker floors
- The influence of the strut force from the sheet piles in the floor is small

4

Finite element model of a UWC floor

4.1. Model

The objective of this thesis is to investigate the influence parameters on thermal shrinkage cracking. By only considering cracking in one direction, the results can be interpreted better compared to cracking in two directions. Therefore, a tension bar model was chosen to consider cracking in one direction. In this case the long direction in a rectangular building pit. The justification for only considering cracking in this direction was elaborated in section 3.2. This section also argued that the probability of separation cracking becomes larger for increasing length, which will lead to a conservative result. Besides that, the probability of cracking in the short direction will be smaller due to strut action. A strip in the middle of the building pit will be selected (Figure 4.1) to exclude edge distortion effects from the parallel sheet piles and purely focus on the shrinkage behaviour of the FRC.

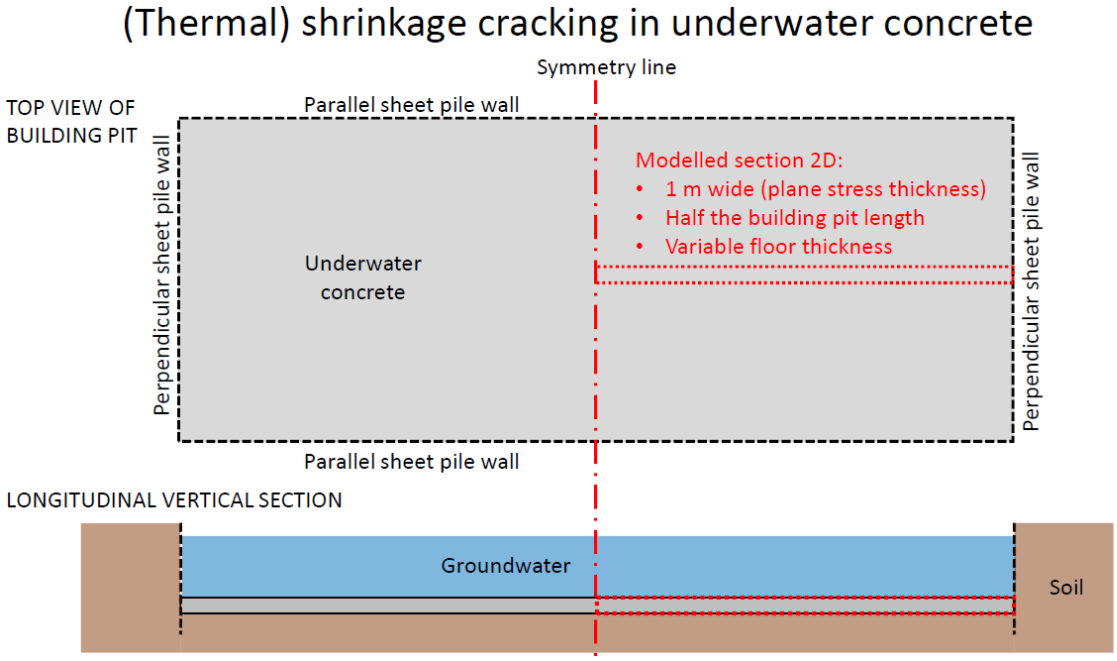

Figure 4.1: Overview of the model and building pit.
Adapted from internal document (van der Meer, 2022)

In this thesis, the influence of certain model parameters and assumptions is investigated. These variations will always be based on a standard case, that is described in this chapter. A complete concise overview of all parameters and assumptions can be found in appendix section C.1.

4.1.1. Geometry and mesh

As explained in the previous paragraph, a one-meter wide strip in the middle of the floor will be considered, as illustrated in Figure 4.1. The model will be a 2D longitudinal vertical cross-section of the floor with a variable height (standard height of 1 meter) and a length of 25 meters. By taking symmetry into account, only half of the building pit will be modelled and a standard length of 50 meters will be halved to 25 meters. The length will be varied in a later stage to check if the results do not depend on the length of the model.

The model uses quadratic plane stress elements, which require a thickness, despite the model being in 2D. A standard thickness of 1 meter is chosen. The FE model of this strip is displayed in Figure 4.2, with a height of 1 meter and a length of 25 meters. Elements with quadratic interpolation are chosen over linear elements, as advised by the RTD 1016-1 (Hendriks & Roosen, 2022). These quadratic elements are considered to be better suited because they can describe more deformation modes. The elements that are used are 100 x 100mm. The maximum element size that is advised by the RTD 1016-1 (2022) is 166 mm (height / 6), so the chosen element size fulfils this requirement. A mesh refinement study was done in appendix Section C.2. It was found that halving the element size does not influence the results, meaning that the assumed element sizes can be used. The top and bottom boundaries are modelled with linear heat flow boundary elements in order to model the heat transfer coefficients. The types of elements that are used are described in appendix table C.6.

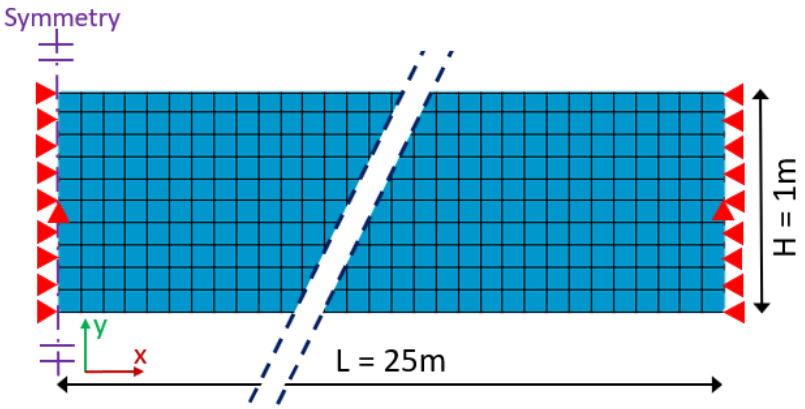

Figure 4.2: Finite element model with variable length L and height H

Symmetry

The validity of the use of symmetry can be argued when stochastic spatial variation in the material properties is used. Strictly speaking, a strip of 25 meters on the left of the building pit is not symmetrical to a strip on the right in figure 4.1, when considering these material properties. So there is symmetry in geometry, but not exactly in the material properties. However, the separation cracks that occur in this tensile bar model primarily depend on the model's spatial variation and using symmetry does not influence these results. A model of 25 meters long is also long enough to include this spatial variation. When looking at the behaviour of the building pit, the horizontal displacement in the middle is zero, which also justifies the use of symmetry.

4.1.2. Mechanical boundary conditions

The model is in fact a tension bar, where the tensile stress develops due to thermal shrinkage. In Figure 4.2 the boundary conditions are shown. The midpoint on the left (symmetry side) and right side are both fixed in the y-direction. The left edge of the beam is fully restrained in the x-direction. Two scenarios exist for the right side, which are explained in this section.

In Section 3.2, it was explained that during the heating phase the material will expand and is restrained by the edges of the building pit. These restraints are not fully fixed, since the sheet pile walls will be able to deform and therefore act as springs, which is illustrated in Figures 3.2 and 3.4. In the cooling phase, the concrete will shrink, but the sheet piles' horizontal deformation will follow this shrinkage due to the active soil pressure. As defined in the scope, the model does not include the sheet pile behaviour and deformation from the soil pressure. Moreover, considering the goal of investigating the cracking behaviour of this construction type, it is more useful to look at the extreme cases instead of individual cases with different properties of the surrounding soil. Therefore, only fully fixed and fully free boundary conditions will be considered in this model.

Two boundary conditions are defined, in which the distinction is made between the heating and the cooling phase, as is illustrated in Figure 4.3. For boundary condition A, the slab is free to extend (on the right side) in the heating phase and constrained in the cooling phase, which is called the "free-fixed" boundary condition. In this thesis, free-fixed indicates the state of the right support in respectively the heating and cooling phase. For boundary condition B, the right support is fixed in both the heating and cooling phase. This is called the fixed-fixed boundary condition.

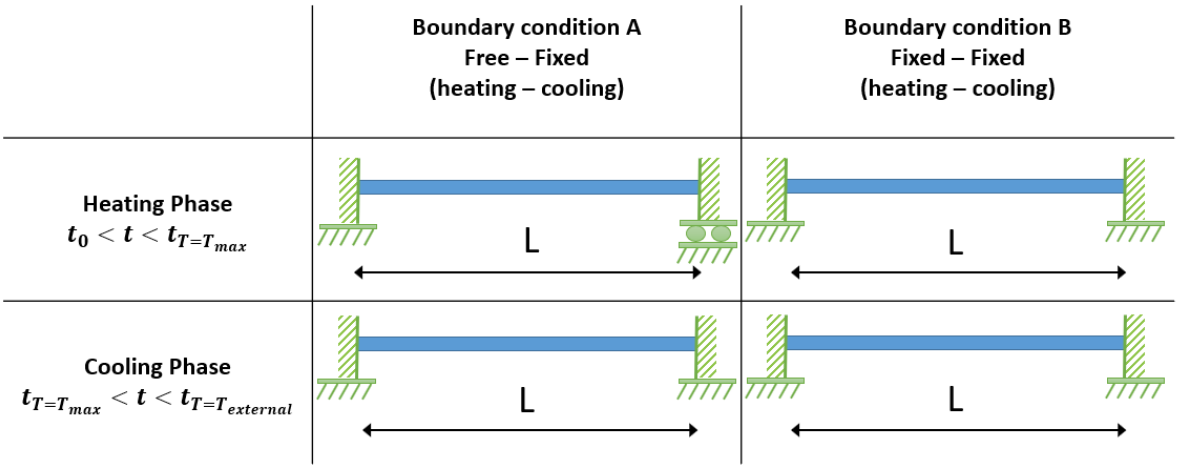

Figure 4.3: Two types of boundary conditions that differ in the heating phase and are similar in the cooling phase

With boundary condition A (free-fixed), the slab is free to extend in the heating phase and will be fixed when the maximum temperature is reached. In the cooling phase, the degree of restraint is 1, meaning that the beam will experience a maximum thermal strain ε_T from cooling from T_{max} to T_{external}, which can be calculated with the formula 2.11.

With boundary condition B (fixed-fixed), the slab is not free to extend in the heating phase and therefore compressive stresses occur during this phase. After T_{max} has been reached, tensile stresses start to develop in the cooling phase. However, the existing built-up compressive stress will cancel out part of these stresses. A net absolute tensile stress will only occur when all compressive stresses are cancelled out. This is explained in Section 3.4.2 and is illustrated in Figure 2.6. Besides the fact that the boundary conditions actually act like springs (because of the sheet pile action), this extreme case will not occur in practice, because stress relaxation plays an important role in this, as was explained in section 2.1.5. In practice, this will lead to lower compressive stress development in the heating phase

than in the theoretical case that this thesis considers in boundary condition B. Stress relaxation is not taken into account in the model. In short, the possibility of building up compressive stress in the heating phase with boundary condition B will act favourable and prevent cracking in this phase. Therefore this boundary condition will lead to an underestimation of the crack widths. In contrast, boundary condition A can be considered as a worst-case scenario, which will lead to conservative results.

The stress development in the slab for both boundary conditions is discussed in the results in Section 4.3.4. The statements made in this current section are visually presented in these results.

4.1.3. Thermal boundary conditions

The thermal boundary conditions are essential, since these are, together with the adiabatic heat development and degree of restraint, the main influences on the thermal stress development. They have been discussed in section 2.1.3. To model the heat dissipation to the environment, the heat transfer coefficients and the external temperature for each boundary are needed. These can differ for the top and bottom boundary since the slab rests on soil with groundwater and there is only water at the top boundary. Values for the heat transfer coefficients vary between 5.6 $Wm^{-2}K^{-1}$ according to the ROK 1.4 ROK 1.4 (2017), to 111 $Wm^{-2}K^{-1}$ for stagnant water or 695 $Wm^{-2}K^{-1}$ for flowing water according to (van Breugel et al., 2016). The value of 5.6 defined by the ROK 1.4 is probably a value for convection through air only, but this is not explicitly mentioned. However, this is in line with other values that were found in the literature, which are given in appendix section E. The heat transfer coefficients between concrete and air are quite commonly described in other research, but almost no values between concrete and water are reported. From the wide spread of these values found in the literature, it can be concluded that it is important to look at the influence of the heat transfer coefficient when modelling a UWC floor. This is done in section in section 5.5.3. The uncertainty in these values indicates the importance of a probabilistic analysis.

It is assumed that the values for the heat transfer coefficients, can therefore vary between 100 and 700 $W\,m^{-2}K^{-1}$ for contact with water. A value of 100 can be used for stagnant water and higher values for flowing water. For the standard case, a value of 100 will be used.

The casting and environmental temperatures (for the Netherlands) are obtained from the ROK 1.4 (2017). The temperatures are defined per season. The casting temperature is 10 °C for the winter, 17 °C for spring and autumn and 26 °C for summer. The external air temperature is defined as 5, 12 and 21 °C and the external water temperature is defined as 7, 12 and 16°C respectively. The values for contact with water will be chosen since the UWC floor will be surrounded by water. Different combinations of the starting and external temperatures will be investigated in the sensitivity analysis. Table 4.1 summarises the assumptions for the standard case.

Table 4.1: Thermal boundary conditions, the value column represents the values for the standard case

Property	Value	Range	Unit	Source
Heat transfer coefficient top $h_{c,top}$	100	5-700	$W\,m^{-2}K^{-1}$	van Breugel et al., 2016
Heat transfer coefficient bottom $h_{c,bottom}$	100	5-700	$W\,m^{-2}K^{-1}$	van Breugel et al., 2016
Casting temperature T_0	12	10-26	°C	ROK 1.4, 2017
External temperature top $T_{ext,top}$	12	7-16	°C	ROK 1.4, 2017
External temperature bottom $T_{ext,bottom}$	12	7-16	°C	ROK 1.4, 2017

4.1.4. Material properties

Material properties plain concrete

There is a general trend in the construction industry in the Netherlands to use higher concrete classes than was usually done before in UWC floor construction such as C30/37 or sometimes even C35/45 (Bouwmeester - van den Bos & Galjaard, 2013). Therefore, this model assumes concrete class C30/37. In table 4.2, the material properties of the standard case of the model are given. More info on the conductivity and expansion coefficient and the specific heat capacity is given in section 2.1.3 of the literature review. Different values obtained from the literature study were reported in appendix E. For this model, the values from the guideline ROK 1.4 (2017) were used.

Table 4.2: Material properties

Property	Value	Unit	Source
Concrete Class	C30/37	-	EC2
Young's modulus E	33000	N/mm^2	EC2
Tensile strength f_{ctm}	2.9	N/mm^2	EC2
Density ρ	2300	kg/m^3	ROK 1.4
Poisson Coefficient μ	0.2	-	ROK 1.4
Thermal expansion coefficient α_c	$1.2 \cdot 10^{-5}$	$°C^{-1}$	ROK 1.4
Conductivity coefficient λ_c	2.6	W/(m°C)	ROK 1.4
Specific heat capacity c_c	1.0	kJ/(kg°C)	ROK 1.4

An adiabatic curve is needed to model the heat development during hydration. Three variations of adiabatic curves are shown in Figure 4.4. The standard model assumes the Adiabatic curve CEM I + CEM III. This theoretical curve corresponds with a concrete based on a combination from CEM I and CEM III cement with fly ash, which is commonly used in the Netherlands for UWC floors. In the next chapter, variations will be made, using the other adiabatic curves.

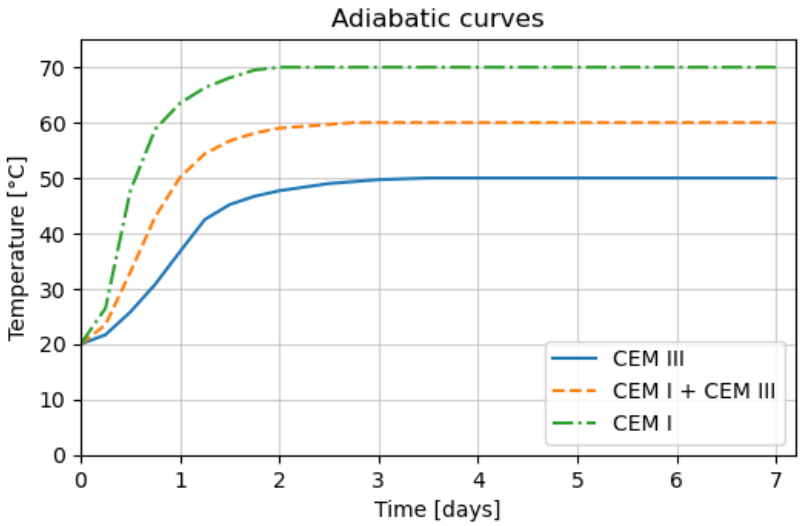

Figure 4.4: Fictitious adiabatic curves. Adapted from van der Meer (2022)

Material properties FRC

As explained in chapter 2.2, the main property that classifies FRC is the residual flexural tensile strength. These values are usually determined from 4-point bending tests with notched beams[1], as was described in Section 2.2.3. Different models can be used to define the residual tensile strength characteristics of FRC. The Model Code 2010 FRC tensile strength model for case 1 (figure 2.14) will be used according to section 5.6.5 of the Model Code (MC 2010, 2010). The residual tensile strength is defined in two factors f_{R1k} and f_{R3k}. FRC with fibre classification 4c is used for the standard case according to section 5.6.3 of the MC2010. This classification leads to the following values for the residual tensile strength:

$$4 \leq f_{\mathrm{R1k}} < 5$$

$$0.9 \leq f_{\mathrm{R3k}}/f_{\mathrm{R1k}} < 1.1$$

Where f_{R1k} denotes the flexural strength for serviceability limit state and f_{R3k} for the ultimate limit state. With these conditions, the following values are assumed:

$$f_{\mathrm{R1k}} = 4.0\ \mathrm{N/mm^2} \text{ and } f_{\mathrm{R3k}} = 3.6\ \mathrm{N/mm^2}$$

The Model Code defines two constitutive laws to translate the residual flexural strength to residual tensile strength, or just residual strength (section 5.6.4, MC 2010, 2010). The linear model is chosen over the rigid-plastic model, since this can describe hardening and softening behaviour. Two values f_{Fts} and f_{Ftu} can be determined for the SLS and ULS according to the following equations:

$$f_{\mathrm{Fts}} = 0.45 f_{\mathrm{R1}} = 0.45 \cdot 4.0 = 1.8\ \mathrm{N/mm^2}$$

$$f_{\mathrm{Ftu}} = f_{\mathrm{Fts}} - \frac{w_u}{CMOD_3}\left(f_{\mathrm{Fts}} - 0.5 f_{\mathrm{R3}} + 0.2 f_{\mathrm{R1}}\right) \geq 0$$

$$f_{\mathrm{Ftu}} = 1.8 - \frac{2.5}{2.5}\left(1.8 - 0.5 \cdot 3.6 + 0.2 \cdot 4.0\right) \approx 1.00\ \mathrm{N/mm^2} \text{ for a } w_{cr} = 2.5\mathrm{mm}$$

With these values, a stress-strain/crack width diagram can be set up, as is shown in Figure 4.5. Two simplifications are made, compared to the MC2010.

- Line segment AB from Figure 2.14 is not modelled. Instead, only one straight line between the origin and point B is used. Model Code uses this line segment A-B for crack localisation, but this is not desired for FRC in combination with a smeared crack calculation approach. A smeared cracking model is able to capture micro cracking as well, therefore crack localisation is not needed.
- Instead of the mean values f_{R3} and f_{R1}, the characteristic values for the residual strength f_{R3k} and f_{R1k} are used to determine f_{Ftu} and f_{Ftus}. There is no factor to transform these values in the MC2010, but by using the characteristic values, it will lead to a conservative approach.

In order to give the FRC tensile strength graph a spatial variation and a development in time (explained in the next sections), the finite element model uses a ”FRC factor”. This multiplication factor scales the y-coordinate (stress) of all the points in the tensile strength graph, i.e. from Figure 4.5, by the same value. This factor is also denoted as ”FRCFAC” and indicates the tensile strength of fibre-reinforced concrete in this model.

Research (Soetens & Matthys, 2014) has shown that in some cases, the tensile behaviour of FRC can better be modelled with a ”dip” in the material model. Figure 4.5 shows a material with and without a dip. The idea behind this dip is explained in Section 2.2.3, but by following the graph of regular concrete longer it also makes sure that the fibres are properly activated and therefore also utilised. According to recent internal research by NLyse and ABT, a dip is especially needed when numerical results have

[1] An analysis about these 4-point bending tests on notched FRC beams is performed in Appendix G. For more information on these tests, the reader is referred to this appendix.

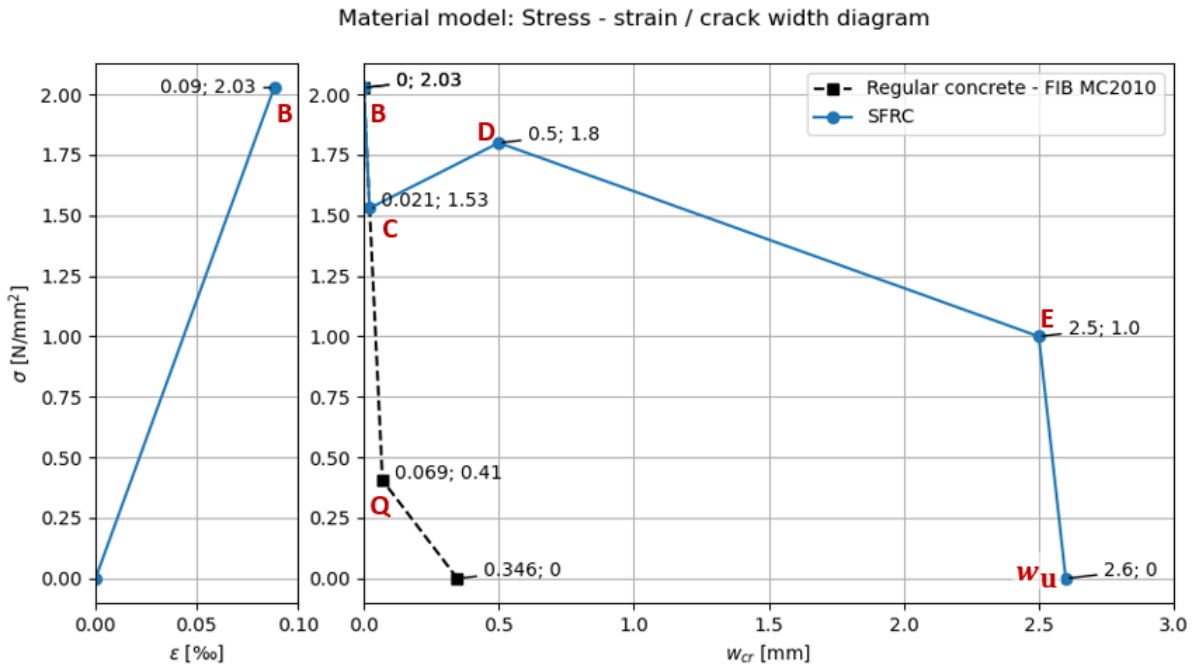

Figure 4.5: FRC properties: stress-strain / stress-crack width diagram. Regular material model from MC2010, including a "dip" where $f_C = 0.85 f_D$. The points are indicated with capital letters.

to be validated with experimental results. The dip in the standard model is constructed by setting the value of $f_C = 0.85 f_D$.

Since the characteristic values for the residual tensile stress are used, it can be argued that the characteristic value of the tensile strength (f_{ctk}) also has to be used instead of the mean value. Considering these two changes, the standard fib model is transformed into the material model used in the standard case, which is displayed in Figure 4.5.

Time dependent properties

The need for modelling time-dependent properties is explained in chapter 2.1. In the FE model, the Young's modulus and tensile strength are time-dependent properties that are calculated from the degree of reaction. For this time dependence, EC2 section 3.1.2 can be used. It defines the time dependence for the tensile strength and Young's modulus for regular concrete as:

$$\beta_{cc}(t) = \exp\left\{s\left[1 - \left(\frac{28}{t}\right)^{1/2}\right]\right\} \tag{4.1}$$

$$f_{cm}(t) = \beta_{cc}(t) \cdot f_{cm} \tag{4.2}$$

$$f_{ctm}(t) = \beta_{cc}(t)^{\alpha} \cdot f_{ctm} \tag{4.3}$$

$$E_{cm}(t) = \left(f_{cm}(t)/f_{cm}\right)^{0.3} \cdot E_{cm} \tag{4.4}$$

$s = 0.25$ for class N cement, $\alpha = 1$ for $t < 28$ and $\alpha = 2/3$ for $t \geq 28$

Where t is in days. Research by Fu et al. (2014), has shown that both the tensile strength and the residual strength of FRC both show an increase in time during the hardening phase. For the development of the residual strength in time, the multiplication factor FRCFAC will be used which is explained earlier in this section. In order to incorporate time dependence in the residual strength, this FRCFAC will use the $\beta_{cc}(t)$ function from equation 4.1, similarly to the tensile strength for regular concrete as in equation 4.3. This will lead to:

$$\text{FRCFAC}(t) = \beta_{cc}(t)^{\alpha} \cdot \text{FRCFAC} \tag{4.5}$$

Since these formulas are used for modelling the maturity of the material, the FE model will use the equivalent age in these formulas, so that $t = t_{eq}$. This concept was explained in chapter 2.1. The equivalent age can be determined with equation 2.7. The value for the activation energy of the reaction is assumed to be constant and the value from the EC2 and MC2010 is used, which is 33.5 kJ/mol. This leads to $E_a/R \approx 4000$. The finite element software will determine the equivalent age with a numerical method.

4.1.5. Loading

No external loading is taken into account in phase A (before draining of the building pit) of the construction (Section 3.1.2). The only forces that develop are caused by thermal expansion and shrinkage in combination with the restraint of these deformations. In phase B, when the building pit is drained, there will be an upward water pressure from the groundwater. In phase A, this upward pressure was counteracted by the weight of the water in the building pit and resulted in a net force of (almost) zero. However, there is a distributed net upward force in phase B because the building pit is drained, which is displayed in Figure 3.2. This has to be counteracted by the weight of the slab and the anchors, which means there will be a distributed upward force and several concentrated downward forces from the tension piles. As defined in the scope this research primarily focuses on phase A, and therefore no loading will be taken into account in the standard model.

4.1.6. Analysis

Phased analysis

First of all, a random field is generated for the spatially stochastic material properties, which will be elaborated upon in Section 4.2. Secondly, a transient heat analysis is executed to determine the time when the maximum temperature is reached $t_{T_{\max}}$. When this time is known, the complete analysis can be divided into a heating and cooling phase and corresponding time steps can be determined. As explained in section 4.1.2, the right boundary condition changes from free to fixed when this maximum temperature is reached. After this, the actual analysis starts. Both phases consist of two coupled analyses: a transient heat (thermal) analysis followed by a nonlinear structural analysis. There is only a one-way coupling, which means that the transient heat analysis influences the structural analysis, but not the other way around. First, the transient heat analysis calculates the temperature distribution and development with the Fourier differential equation and the maturity and corresponding strength development are derived from these temperatures as was explained in Section 2.1.4. With this data, the nonlinear structural analysis calculates the resulting thermal strain and displacements, stress and crack widths. This whole process is illustrated in Figure 4.6.

The parameters that influence the actual time when the maximum temperature is reached are the initial and external temperature, the heat transfer coefficients and the adiabatic temperature development. If all these parameters are not stochastic or are not varied and thus take the values described in the standard case (section 4.1.4), the initial transient heat analysis 0 does not have to be executed. In this case, the time step $t_{T_{\max}}$ is fixed, and for the standard case, specified time steps are used for this.

Time steps

The time steps should be sufficiently small, especially in the heating phase where they are in the order of hours. At a given moment, there is no crack growth anymore when the internal temperature reaches the external temperature. When reaching this point, the time steps can be increased. The time steps of the transient heat and nonlinear structural analyses should be equal to avoid interpolation issues. The time steps for the standard case are reported in Appendix C.1. A time-step dependency analysis was done in appendix Section C.2. It was found that halving the time steps does not influence the results, meaning that the assumed time steps can be used.

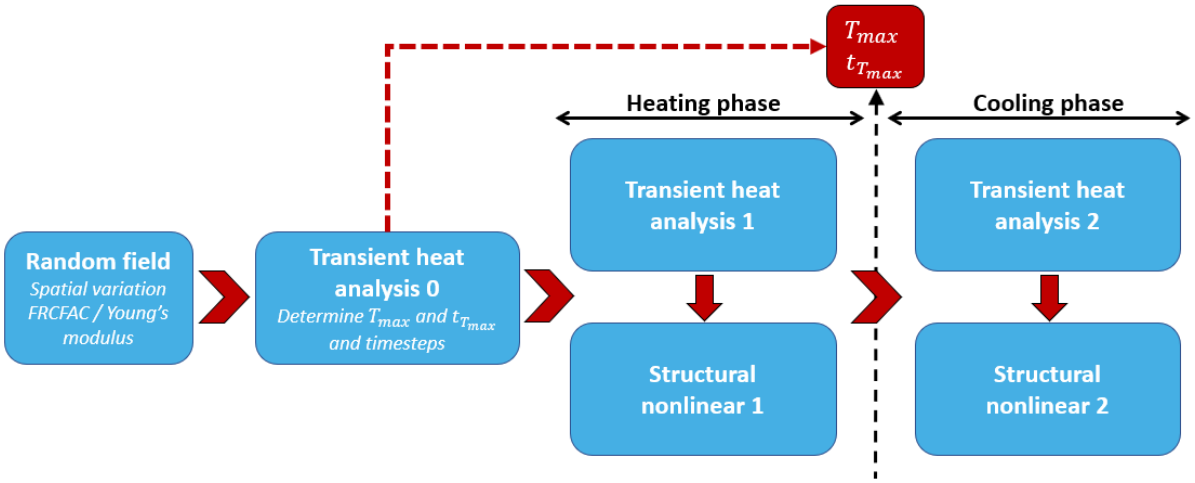

Figure 4.6: Analysis procedure

Iteration method and convergence

For the iteration method and convergence criteria, the guidelines from the RTD:1016-1:2022 (Hendriks & Roosen, 2022) will be adopted. The Newton-Rhapson iteration scheme will be used with convergence criteria for force and energy simultaneously. The convergence criteria are set to 0.01 and 0.001 respectively. The arc-length method as advised by the RTD is not used, since the FE calculation uses time steps only, and there is no external loading. Additional settings are reported in Appendix C.1.

4.2. Random fields

This chapter describes the regular model without probabilistic properties. However, the model is a so-called tensile bar that needs some local weak spots in the material properties at certain locations to determine where cracks are initiated. If it does not have these weak spots so that there is a uniform strength, the software does not ”know” where to crack first. Compare this to a simple case of a bending beam on two supports, the point of maximum stress is in the middle, which is the location where the first cracks will be initiated. For this tensile bar model, the stress is uniformly distributed over the length of the slab. Because of this, the choice was made to include some weak spots in the material properties in the form of spatially stochastic properties. This is also realistic, given the geometrical variations in the thickness, which will also introduce weak spots in the slab. These spatially stochastic properties can be modelled with a random field. A random field is the introduction of a spatial variation in certain properties in the form of a function. An example of a 1D random field is displayed in Figure 4.7 and in Figure D.1a in the appendix. 2D and even 3D random fields are also possible. An example of a 2D random field is shown in Figure D.1b in the appendix. For the plane stress FE-model either a 1D or 2D random field can be used, and the effect of this will be elaborated upon later in Section 5.5.1.

The relevant material properties that can be modelled with a random field are the Young’s modulus and the tensile strength of FRC, which is described with the FRC-factor (FRCFAC). A varying Young’s modulus also means that thermal strains lead to varying thermal stresses, as is indicated in Equation 2.12. In order to purely study the effect of the residual tensile strength of fibre-reinforced concrete on the crack pattern, only the FRC factor is modelled with a Random field at first. In the next chapter, the influence of modelling both the FRC-factor and Young’s modulus with a random field will be discussed. How random fields are generated, is extensively discussed in appendix Section D.4. The use of random fields also introduces a new set of input parameters. The meaning of these parameters and how they result in different random fields, is all explained in Appendix D. The properties used in the standard model for random fields are given in Table 4.3.

The random field mesh is chosen so that it corresponds with the FE mesh and there is only stochastic variation in the length direction and not over the height. The choice was made to only consider stochastic variation in the X-direction, so the cracks present themselves clearly as separation cracks, and the results can be interpreted more easily. The difference between 1D and 2D stochastic variation is displayed in Figure D.1a. More information on this is given in section D.2.

Since the FRC-factor is a multiplication factor for the tensile strength of FRC, the mean is 1.0 by definition. The log-normal distribution is used since this is more appropriate for the tensile strength of concrete (JCSS, 2001). For the standard deviation of the tensile strength, two values were determined. The JCSS model code advises 30%, and the Eurocode uses 20% of the mean as described in section 2.5.1. For the standard case, 20% was chosen and the effect this has on the results will be investigated.

An example of a random field for the FRCFAC is displayed in Figure 4.7. Since the FRCFAC is a scaling factor, the mean is 1.0 by definition.

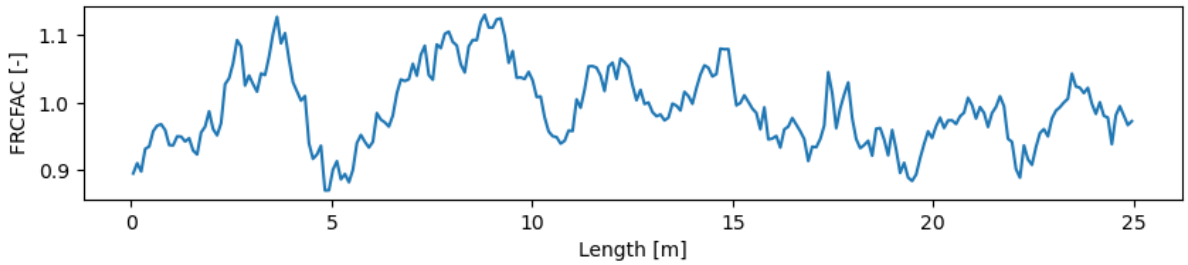

Figure 4.7: Possible graph of the spatial multiplication factor over the length. In this case the property that is made stochastic is the FRCFAC, which has a mean of 1.0

Table 4.3: Random field properties

Random field property	Value
Algorithm	Covariance Matrix Decomposition
Correlation matrix decomposition	Cholesky
Random field mesh	N_x = 251, N_y = 1, N_z =1
Correlation function	Regular exponential
Treshold	0.0
Correlation length l_c	1 m
Property	FRCFAC
Distribution	Log-normal
Mean	1.0 [-]
Standard deviation	0.20 [-]
Correlation with other properties	-

4.3. Results

4.3.1. Temperature development and maturity

The basics of temperature development, corresponding maturity and the development of the strength properties have been discussed in Section 2.1. The temperature distribution over the height and how this influences the crack initiation and development has been explained in section 3.4. The resulting temperature development over time for the standard case is plotted in Figure 4.8. This figure shows

that the middle zone of the beam reaches a higher temperature than the boundaries, as was explained in section 3.4. It can also be observed that the slab reaches the maximum temperature around 1.5 days and that after 10 to 12 days, the temperature is practically equal to the external temperature. After this time, no change in the crack formation is expected in this model. The degree of reaction and the maturity that result from the temperature development are plotted in Figure 4.9. The maximum FRCFAC is 1.0 at 28 days following equation 4.5. It can be verified that the FRCFAC develops slower in the top and bottom boundaries, which indicates that the equivalent age is indeed used in determining this factor.

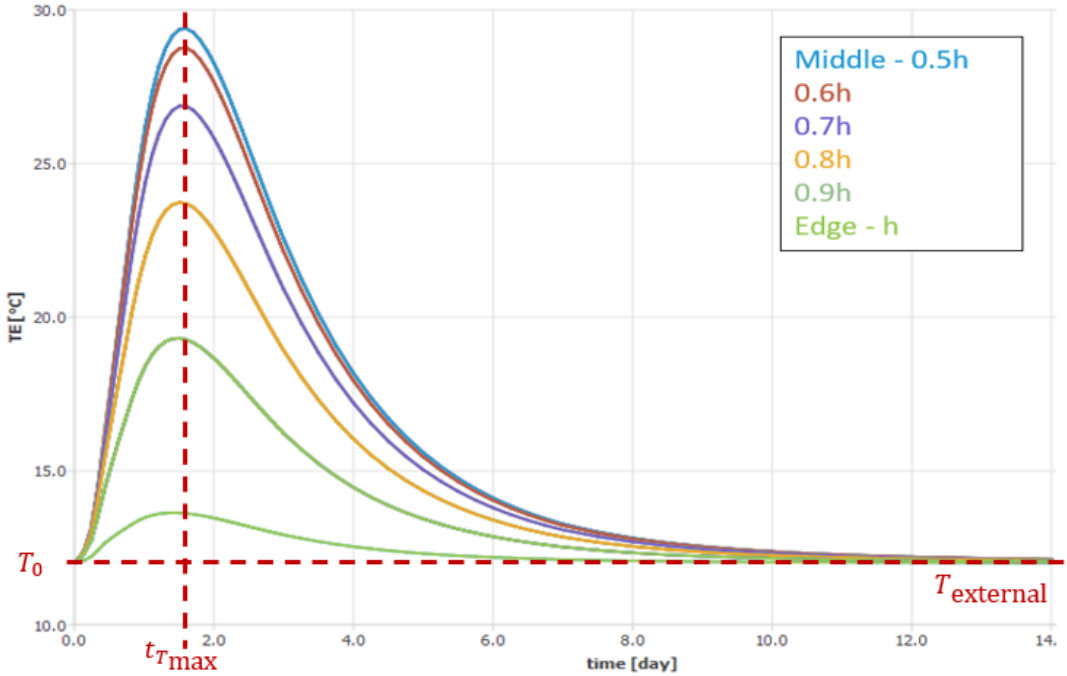

Figure 4.8: Temperature development over time. The different lines indicate different positions in the beam, where $0.5h$ is the middle and h is the top boundary. The middle zone (centre) reaches a larger temperature than the boundaries. The time when the maximum temperature is reached in the centre is denoted with $t_{T_{max}}$

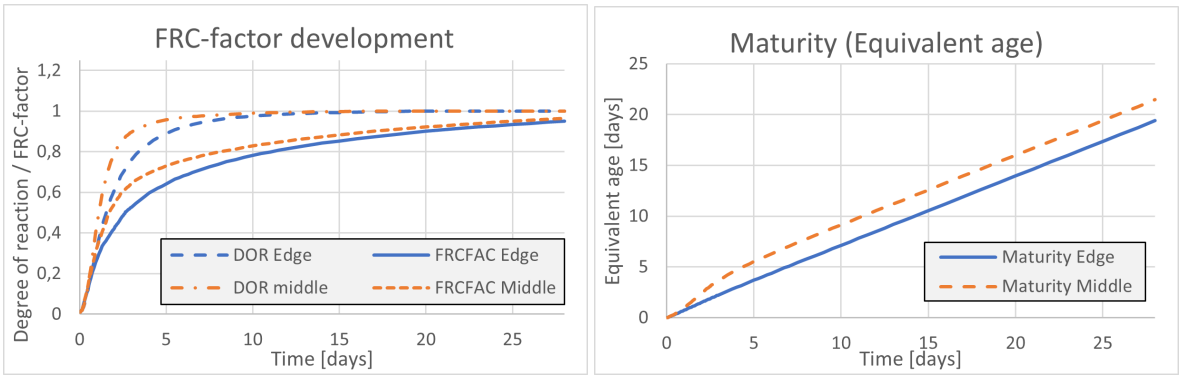

(a) Maturity (equivalent age)

(b) Degree of reaction and FRC-factor development

Figure 4.9: Maturity of the slab and the corresponding FRC-factor (tensile strength) development

4.3.2. Crack development

For the crack width results from the FE-model, the element averaged values are used. This compensates for the crack bandwidth that has to be used when elements are only cracked on one side, which was observed in the FE-results. In section 3.4, it was explained that micro-cracks start to occur in the top and bottom zones during the heating phase and that these might grow and connect in the middle zone during the cooling phase, which will lead to separation cracks. This crack development is shown in Figure 4.10. The panels in this figure indicate the following time steps:

Upper panel: Time when the maximum temperature is reached, micro-cracks have formed in the upper and lower edge zones during the prior heating phase.

Middle panel: During the cooling phase, the existing micro-cracks start to ”grow” towards the middle. At a given point, the top and bottom cracks might connect to form separation cracks.

Lower panel: When the complete structure has cooled down, the final crack pattern might look like this.

This process is illustrated in a graph that shows the tensile stress vs the developing tensile strength over time in Figure A.1 in the appendix.

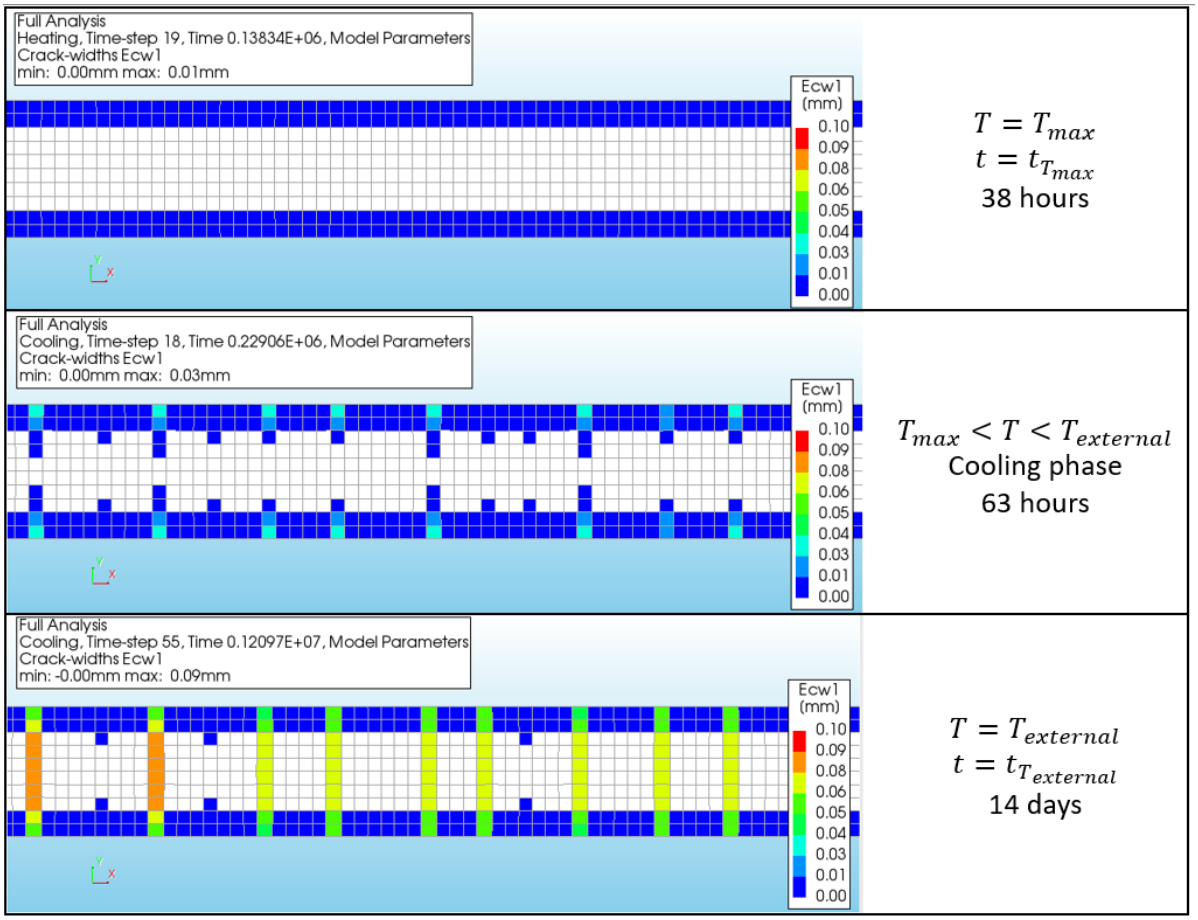

Figure 4.10: Crack development during the cooling phase in a (enlarged) part of the slab of a 10m model. The figures show crack widths in mm. White squares are uncracked elements, and dark blue squares indicate micro cracks.

The crack development as a function of time is plotted in the graph in Figure 4.11. This figure displays five cracks that form in a model that is 25 meters long. As can be seen in Figure 4.10, a lot more cracks appear for a 25-meter model. A graph with all the separation cracks that occur is shown in Figure A.3

in the appendix. From these graphs it can be observed that the largest crack appears first, followed by the second largest crack and so on. It turns out that there is an absolute maximum crack width of approximately 0.18 mm. After 12 days, the cracks are stabilised. No more cracks form and the existing cracks do not grow in time anymore. This is the point where the internal temperature is close to the external temperature and no shrinkage is to be expected anymore, which is confirmed by the results from the temperature graph in Figure 4.8.

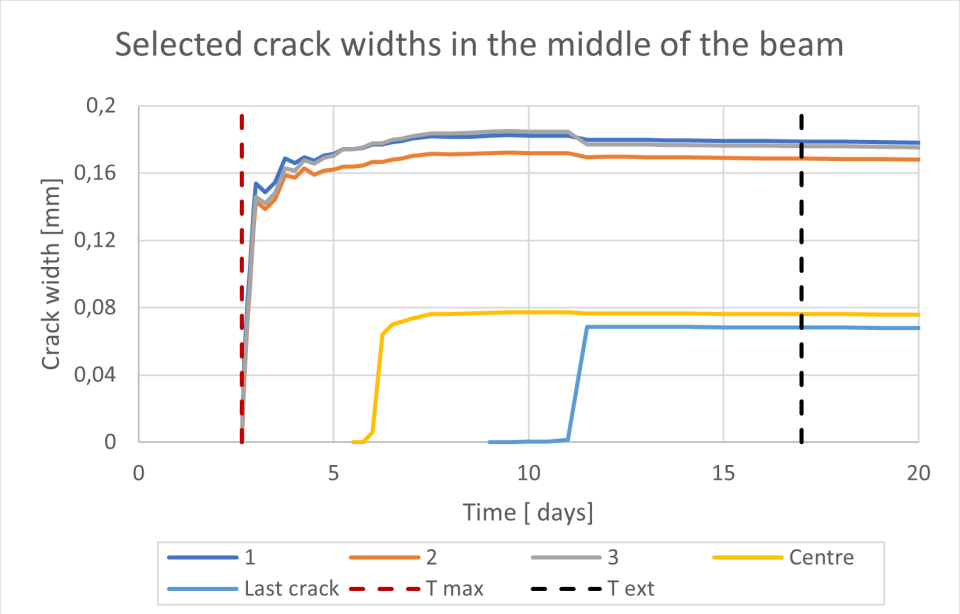

Figure 4.11: Crack development over time for a model with a length of 25 meters. The first three cracks that occur are plotted, one crack that occurs halfway through the analysis and the last crack that occurs during the analysis are also plotted. The times where T_{max} and $T_{external}$ are reached are indicated in red and black respectively

4.3.3. Crack pattern

It was observed that the model shows two types of results, which are shown in Figure 4.12. This was expected from the literature review, and this phenomenon is illustrated in Figures 2.15 and 3.5. Result type A shows multiple distributed smaller cracks (second panel) and result type B shows one single localised crack (fourth panel). These two different types of results can be explained by looking at the material behaviour. The distributed crack result follows from FRC which has a tension hardening behaviour, while the localised crack result follows from tension softening behaviour.

Looking at the appearing crack widths and the info from the section about fluid-tightness (2.3), behaviour A can possibly be watertight, depending on the maximum allowable crack width (<0.2 mm). As opposed to behaviour B, which will definitely experience leakage since there is a crack of 4 mm wide. This phenomenon of two different result types and its importance will be discussed in the next chapter. During the analyses for this chapter it was observed that for the standard case, small standard deviations (<0.05) of the FRCFAC random field lead to a distributed crack pattern, while a larger standard deviation (>0.15) results in a localised crack type result. This will be further investigated in Chapter 5.

It is verified for these results that the summation of the crack widths of all the separation cracks can be determined from the total elongation of the slab in the heating phase:

$$\sum_{i=1}^{m} w_{cr,i} = \Delta L_{pot} - \sum_{j=1}^{n} \left(\varepsilon_j \cdot l_{el}\right) \tag{4.6}$$

In which:

- i indicates the cracked m elements in the centre row of the slab
- $w_{cr,i}$ is the crack width for each cracked element i
- ΔL_{pot} is the total potential shrinkage when the slab is not restrained at the boundary conditions
- j indicates the uncracked n elements in the centre row of the slab
- ε_j is the linear elastic strain in each uncracked element j
- l_{el} is the element width

The absolute maximum crack width of the localised crack in the corresponding crack pattern can be determined with this formula and it is a fixed value for different samples with different random fields.

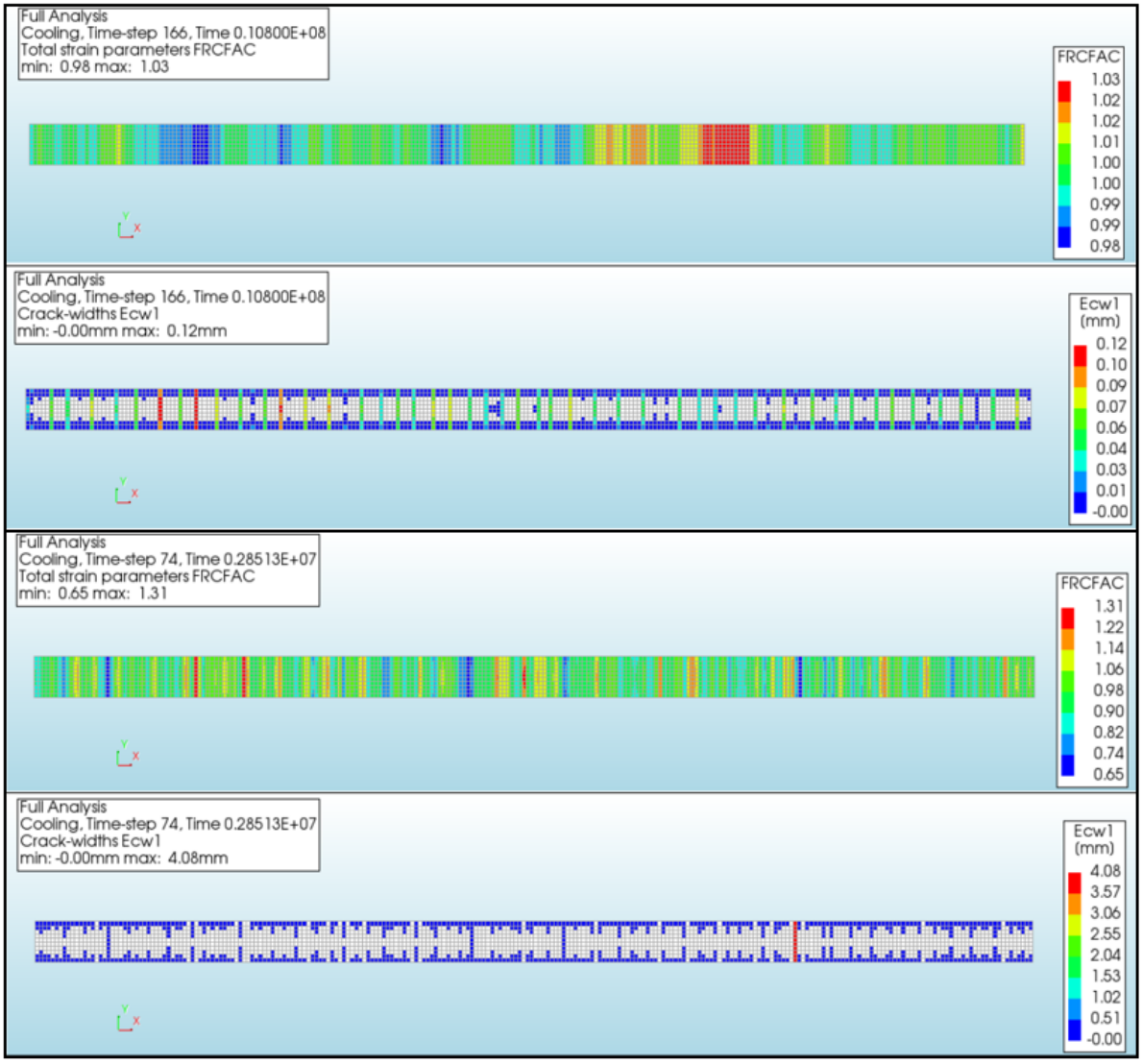

Figure 4.12: Example results, a similar random field with a different standard deviation (σ) displays two types of behaviour. Multiple distributed smaller cracks (upper panel, $\sigma = 1\%$) or a single localized large crack (lower panel, $\sigma = 15\%$)

4.3.4. Influence of the boundary conditions

Strictly speaking, the right boundary condition should be activated when the model is at its maximum expansion, right before it starts to cool down. When looking closely at Figure 4.8, it can be observed

that the maximum temperature at the boundaries is reached earlier than in the middle. This means that the moment in time when there is maximum expansion does not necessarily correspond exactly with the moment where the centre reaches the maximum temperature. This can be observed when very small time steps are used. However, it turns out that in practice the moment when the middle reaches the maximum temperature is a very good indicator for the moment when maximum expansion occurs. Moreover, when the regular time steps of the model are used, this effect is not noticeable because the times when the maximum temperature is reached in the middle or boundary zones occur in the same time step.

Free-fixed boundary condition

The difference between these two boundary conditions that is described in Section 4.1.2, is shown in the graph of Figure 4.13. In the graph, it can be seen that for the free-fixed boundary condition, tensile stress will occur immediately in the edge zones, but the middle will first experience compressive stress. This is due to the fact that the middle wants to expand more than the outer zones, which causes the middle zone to experience internal compressive stress from the outer zones. After the maximum temperature is reached, the compressive stresses will have to be cancelled out first. After some time, tensile stress also develops in the middle zone.

Fixed-fixed boundary condition

For the fixed-fixed boundary condition, it can be seen that both in the middle and at the boundary zones, compressive stresses develop. They also grow larger than in the case with boundary condition A. The final magnitude of the tensile stress is quite similar in both cases but it can be observed that the tensile stress develops later in time for boundary condition B. Since in boundary condition B, the tensile strength has already developed more at that time when tensile stresses start to occur, fewer cracks will form. An added factor is that no micro cracks form in the outer zones during the heating phase. Due to the absence of these, there are no crack inducers for crack growth towards the middle zone. These different results in crack formation due to these different boundary conditions are displayed in Figure 4.14.

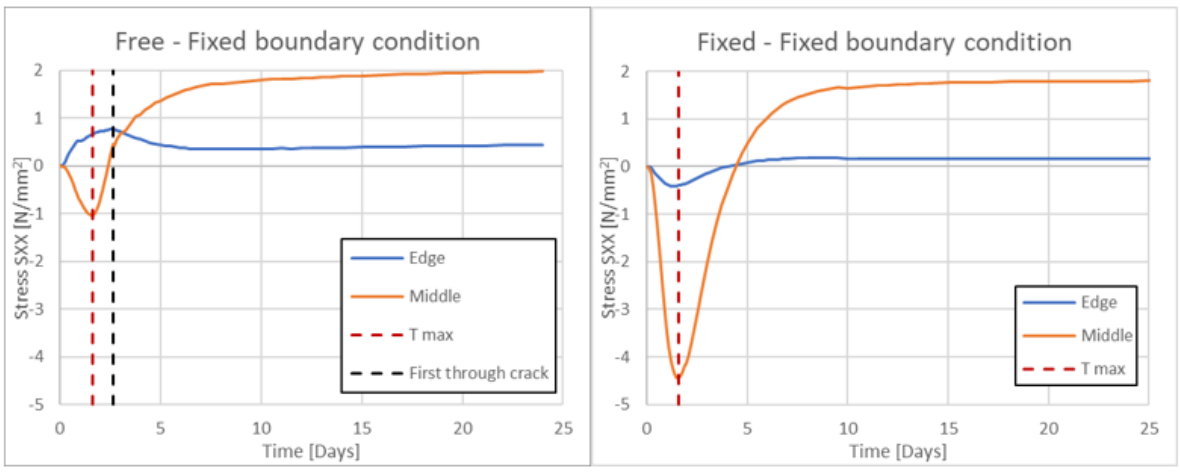

Figure 4.13: Stresses at the lower/upper edge and the middle of the slab for different boundary conditions (in uncracked sections).

These two theoretical cases can be seen as the extremes, where boundary condition A leads to the most and largest cracks and boundary condition B leads to the smallest and least amount of cracks. A realistic scenario in which the sheet piles act as springs and where stress relaxation in the concrete and horizontal resistance from the tensile piles are taken into account, will be somewhere between these two theoretical boundary conditions. Nevertheless, the scenario with boundary condition A can be considered as the absolute worst-case scenario for crack development and water tightness in a UWC

floor. The philosophy behind this is that, when the worst-case scenario satisfies the maximum allowable crack width criterion, a realistic scenario will definitely satisfy this criterion. As stated in section 4.1.2, the result of the fixed-fixed boundary condition does not have micro-cracks in the boundary zones. In this case, there is no crack induction from the lower and upper edges, and the cracks start from the middle of the slab.

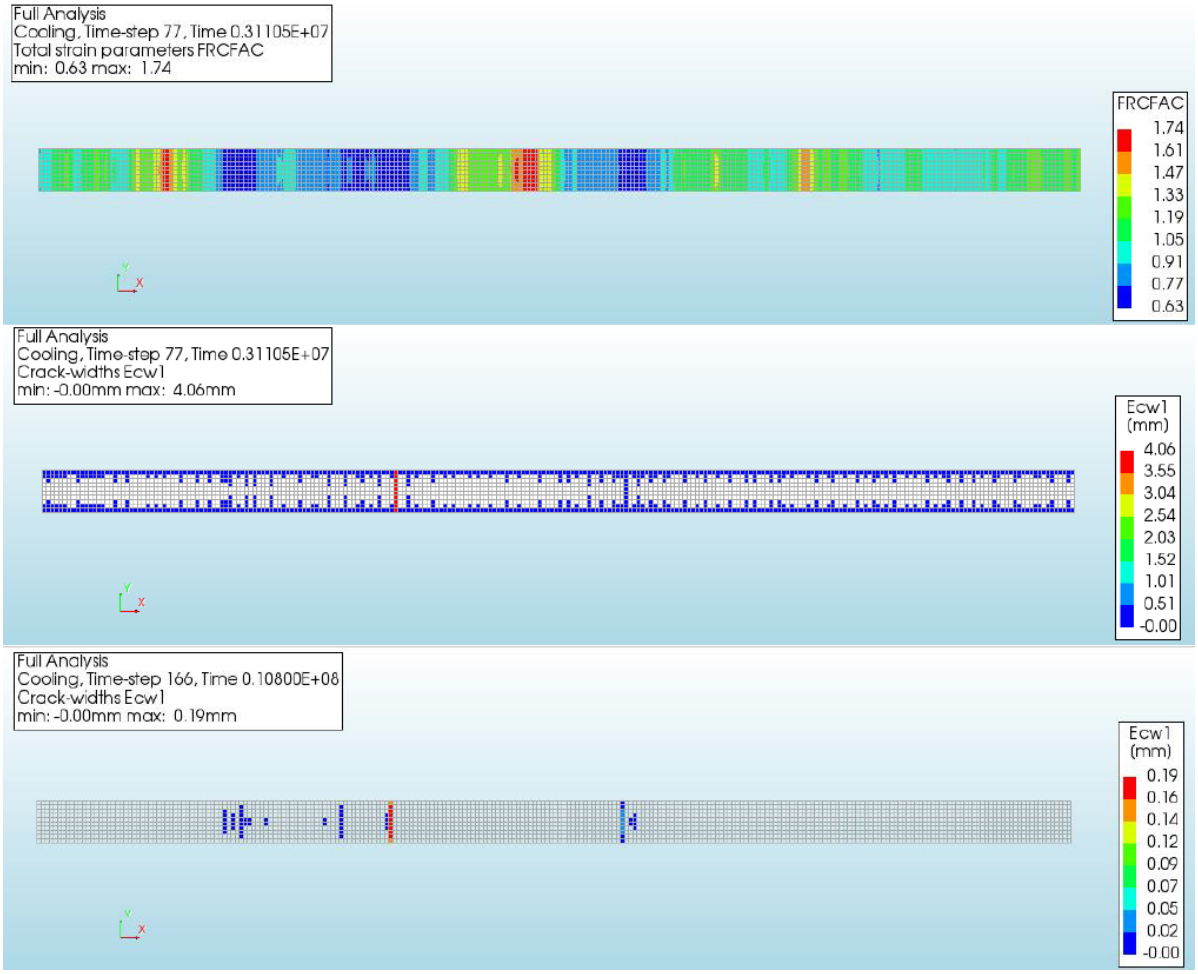

Figure 4.14: Results with the free-fixed boundary condition (middle panel), or for the fixed-fixed boundary condition (lower panel). The models are both based on the same random field (upper panel).

4.4. Discussion

Quite some assumptions and simplifications were made in this model, which will be discussed in this section. For starters, it was defined in the scope that only construction phase A (before draining the building pit) would be considered. This leads to the exclusion of perpendicular and eccentric loading. In practice, these loads will be there and influence the final crack width result positively or negatively, which will have to be investigated. Due to an additional load, cracks might grow, or separation cracks might reduce when a concrete compression zone occurs and no longer cause leakage. In this case, the floor is not necessarily considered as failing. However, the choice was made to only look at phase A because when crack widths are limited in phase A, it is less likely that they will cause problems during phase B. It has to be noted that some examples from practice exist where UWC floors start leaking several months after construction. This can especially happen when the floor is cast in a hot summer, followed by a severe winter. This is also included in the building codes. It is prescribed that a sudden

temperature drop to -10°C (absolute value) has to be taken into account for a certain time after casting, depending on the season in which the floor was cast. There are more reasons to only consider phase A. The objective of this thesis is not to determine exact accurate crack widths, but it is to qualitatively look at the different influence parameters, and identify which ones are the most important to realise a watertight design.

The FE-model does not take the state of matter of concrete into account. In reality, the concrete will still be a slurry directly after casting. This means that the slab cannot develop strength or stress directly from time t_0. From the moment of initial set which is later than t_0, strength ans stress can develop in the UWC floor. This is not taken into account in the model. Besides that, the Eurocode model for the time development of the strength properties also assumes a strength development right after casting. It is expected that this simplification will not drastically change the results.

Another model uncertainty results from the simplification of the boundary conditions. Neglecting the horizontal resistance of the tensile piles and parallel sheet piles also introduces model simplifications. It seems that the influence of fixing the boundary conditions results in a too conservative approach, comparing it to the described behaviour in the literature. In Section 3.2 it was concluded from the literature, that the influence of restrained deformation from the perpendicular sheet piles quickly diminishes in the long direction. By only looking at the theoretical boundary conditions, little can be said about the prediction of realistic crack widths. However, this model can be used to compare the effect of different parameters. Moreover, by choosing the same ”worst-case” boundary condition for every variation of the model, it can be concluded that the crack width for a realistic design, will always be lower.

There is no consensus about the correct input parameters that should be used for a FE model of a SFRUWC floor. The assumptions that were made to choose certain values for this, were also influenced by the choices made in the CROW committee to some extent. For these properties, it was convenient to keep them similar to the CROW model, so this thesis can be used to compare certain results. Nonetheless, the assumptions for these values are in the range of the values found in the literature. The model that was used in this thesis was not experimentally validated. However, the CROW model will be validated, which can later be compared to the results that are presented in this thesis.

Besides a wide spread in the material properties, Section 3.6 also discusses the uncertainty in geometry, caused by the underwater casting process. Because a fixed thickness is assumed, this is not taken into account in the current model. Locally thinner spots in the UWC floor have the same effect as the weak spots in the spatially variational material properties, which are modelled by random fields. It can be argued that by including the local variations in floor height, the standard deviation of these random fields should be increased. Looking ahead to the next chapter, the choice of the standard deviation in the rest of this thesis will even be more arbitrary. It does not make sense to increase the standard deviation by a couple of percentage points when a standard deviation of 5% is assumed in the rest of this thesis. Consequently, the effect of locally varying thickness will be assumed to be included in the spatial variation of the tensile strength.

The tensile behaviour of fibre-reinforced concrete is an important parameter to determine the crack width. The maturity effects and stochastic variation are introduced by using a multiplication factor (FRCFAC) that scales all the points in the material model. It can be argued if this is realistic. The first point in the model depends on the tensile strength of concrete while the other points depend more on fibre properties, such as fibre dosage, distribution and the type of fibre. It should be investigated what the effect of scaling the entire graph is, instead of scaling separate points. However, the FRC factor is currently the only option in DIANA FEA to include time dependency and stochastic variation in the finite element model.

4.5. Conclusions

In order to determine thermal shrinkage cracking in SFRUWC floors, a tensile bar model was proposed. This chapter presented the finite element model that models a strip of a UWC floor in a building pit. All the assumptions and choices for the geometry, boundary conditions and material properties are described and explained. The procedure and parameters of the FEA were also discussed. The FE model's intermediate results were presented and compared to the predictions from Chapters 2 and 3. The results for the temperature and strength development were in line with expectations. The influence of simplifying the boundary conditions was discussed and the validity of other assumptions was reflected in the discussion.

By interpreting the results of the finite element model, some intermediate conclusions can be drawn which are divided into primary conclusions and secondary conclusions.

Primary conclusions

- The crack width results produced by the finite element model can either show tension-softening behaviour in some cases while it shows tension-hardening behaviour in others. These two different types of behaviour can lead to a localised crack or a distributed crack pattern respectively, which is in line with the expectations that were formed in the literature review. It was observed that for the standard case, both result types can occur. This is caused by a different realisation of the random field for every calculation.
- The input standard deviation of the FRC-factor (FRC tensile strength behaviour) random field properties heavily influences the occurrence of either a localised crack or a distributed crack pattern. Small standard deviations will result in more distributed crack patterns, while large standard deviations result in more samples that show a single localised crack.
- Random field properties heavily influence the results of the model. Most of the random field settings cannot be determined from physics or literature and are therefore considered model parameters. The effect that these model parameters have on the results will be evaluated in the next chapters.
- The boundary conditions determine the degree of restraint, which make them a crucial parameter in the model. However, it is challenging to determine the exact degree of restraint. A boundary condition that is free to extend in the heating phase, but restrained in the cooling phase results in larger crack widths than the boundary condition which is fixed in both phases. Therefore the free-fixed boundary condition will lead to a conservative result. As a simplification, only this worst-case scenario with full restraint (DOR = 1) is considered during the cooling phase. If this situation satisfies the maximum crack width criterion, a realistic scenario (0 < DOR < 1) will also satisfy the criterion.
- A non-uniform temperature distribution over the height of the slab causes eigen stresses. These eigen stresses cause surface cracking at the lower and upper boundary zones during the heating phase. These micro-cracks will act as crack-inducers during the cooling phase. In the cooling phase, the slab is restrained and the average component of the Temperature distribution will also result in stress development. This will cause the cracks to grow into the centre and at a certain time, the bottom and top cracks will connect, forming through cracks. Surface shrinkage cracking will occur in any case due to the internal restraint but additional restraint from the boundary conditions is needed for the occurrence of through cracks.

Secondary conclusions

- The non-uniform temperature distribution also leads to a difference between the strength development in the middle and the outer zones.
- The magnitude of the maximum crack width in a localised crack pattern can be determined with

equation 4.6. The maximum crack width of the distributed crack pattern is needed to answer the research questions, but no way of determining this based on an equation has been found yet.

- In both result types, the first crack will be the largest crack in the model. The location of the largest crack corresponds to the lowest value (weak spot) in the random field of the tensile strength (FRCFAC for FRC).
- There are no changes in the crack pattern and widths after approximately two weeks for the standard case. This means that the analysis can be shortened to two weeks when only considering construction phase A before drainage of the building pit.
- In the heating phase, the Young's modulus is lower than in the cooling phase. Meaning that for the case where the boundary conditions are fixed in both phases, the absolute stress difference in the cooling phase will be larger than in the heating phase, which will result in a nett tensile stress.
- The size of the random field mesh does not influence the correlation between different points in the random field. It can be seen from the mathematical definitions in chapter D that the correlation is scaled to the physical distance between points and not to the mesh size. Therefore, the resulting random fields are independent of the mesh size.

Some of these points lead to additional questions besides the research questions. These will be taken into consideration in the next chapter:

- How do the random field properties influence the results and what are appropriate choices?
- In the results, different crack patterns (localised or distributed) are observed. When does the FRC material model result in either one of these crack patterns?
- Why does the standard deviation of a random field influence the crack pattern type?

5

Probabilistic analysis

5.1. General

As mentioned before, due to the uncertainty and wide range of the input parameters, that come with the design of a UWC floor, a probabilistic approach is required. In the previous chapter, section 4.1.4, it was determined that using a random field in the non-probabilistic model was already necessary. Meaning that the standard model already has a probabilistic component built in. So, because of the random field, every time the finite element model is run, it will generate different results. Therefore a Monte Carlo analysis could already be performed with the standard model. Instead of looking at only one result of the model, multiple results will be considered, which is the probabilistic aspect of this chapter. The term sample(s) is used throughout this chapter to discuss the different results caused by different realisations of the random fields. This chapter investigates the influence of various input parameters on the results.

In this chapter, the variations are done by only varying the considered parameter with respect to the standard model with a dip in the material model as described in appendix section C.1.

Terminology

As seen in the previous chapter (section 4.3.3), a distinction has to be made between results that show the distributed crack pattern or a localised crack. In this chapter the following terms are used interchangeably, all considered as synonyms for the same concept:

- **D**istributed **C**rack **P**attern/result (DCP), distributed crack cluster, left cluster in Figure 5.1. These results are associated with tension hardening behaviour.
- (**S**ingle) **L**ocalised **C**rack pattern/result (SLC), localised crack cluster, right cluster in Figure 5.1. These results are associated with tension softening behaviour.

When looking at FRC, not only is the concrete tensile strength important, but the complete tensile behaviour with the residual strength included must be considered. Therefore, the tensile behaviour of FRC is modelled with multiple points (4.1.4). As introduced in Chapter 4, this material model could be varied with a FRC multiplication factor, that scales all the points in the graph by multiplying them with a certain factor. This factor is called the FRC-factor or FRCFAC. In this chapter, the term FRCFAC is the main parameter that indicates the complete ”tensile strength behaviour” inherent to FRC.

5.2. Stochastic properties

5.2.1. General

In Chapter 4, the properties for the standard case of the finite element model were determined. These included thermal and material properties and boundary conditions. Chapter 4 discussed using only the boundary condition that provides the worst-case scenario for the crack width results, which is a fixed situation. This leaves the thermal and material properties that can be varied in this chapter. The shrinkage cracking model also uses a random field to model some material properties with a spatially stochastic character. It is interesting to investigate how different types of random fields influence the results. Therefore, these properties are also varied in this chapter. The properties that are used for a sensitivity analysis in this chapter can be divided into three categories. The results and conclusions will also follow this division:

1. Random field properties
2. Material properties
3. Thermal properties

Properties that are less relevant for thermal shrinkage cracking are kept as deterministic properties. These include the density, Poisson coefficient and the compressive strength, which do not change the model significantly when considering thermal shrinkage cracking. On the other hand, there is no added value in making properties like the thermal expansion coefficient and conductivity stochastic, since the results would be difficult to compare if these properties are stochastic. These properties are intentionally kept deterministic.

Even though the height is an interesting parameter to vary, it is difficult to make stochastic, as this requires a different geometry for each sample. This means a different model would have to be constructed for each sample. Instead, a model with a standard thickness of 1 meter was considered in all cases. Afterwards, the thickness can be varied while keeping all the other properties the same to map the change in results. Local variations in thickness also play an essential role in the construction of UWC floors, as pointed out in section 3.6. Considering the tolerances that occur during the pouring of a UWC floor, it would be appropriate to model local variations in the thickness. However, the effect of these local variations reduces to having weak and strong slices over the length, which is already modelled in the spatially stochastic material properties (Figure D.1a). When including local variations in thickness and a spatially stochastic tensile strength, these effects can cancel each other out or add up. It can be argued that the combination of both these effects can be modelled by increasing the standard deviation of the spatially stochastic material properties. However, since the influence of the magnitude of the standard deviation will already be investigated in this chapter, the result of a locally varying thickness will not be modelled explicitly. It is considered to be already included in this standard deviation analysis.

5.2.2. Random field properties

A distinction must be made between spatially stochastic and random field properties. The spatially stochastic properties signify the material properties that are modelled with a random field, whereas the random field properties define the 'shape' of the random field. These include the correlation length, correlation function, distribution type and the standard deviation of the modelled property. The random field properties of the standard case are given in Table 4.3. How these properties influence the characteristics of the random field is analysed in appendix D. The random field properties that are varied in this chapter are given in the following list:

- Standard deviation of the modelled property

- Spatial correlation of the modelled property which is indicated with the correlation length
- Correlation function
- Distribution type

5.2.3. Material properties

As discussed in section 4.2, the Young's modulus and the FRC tensile strength (FRC factor, FRCFAC) are modelled with a spatially stochastic behaviour by using random fields. It should be emphasised that initially, only random fields with stochastic variation in one direction are used. As explained in section 4.1.4, initially only the tensile strength will be considered spatially stochastic, while the Young's modulus is kept as a fixed deterministic value. Results show that the Young's modulus has a limited effect on crack formation compared with the tensile strength. In section 5.5.2, the influence of the combination of including spatial variation in both parameters will be investigated. Parameters that can be varied such as the standard deviation and the correlation length of the FRC-factor, are included in section 5.2.2. The material parameters of interest that are investigated are the:

- Tensile strength and residual strength of FRC (FRC-factor)
- Young's modulus
- General FRC tensile behaviour: mean or characteristic tensile strength, combinations of tensile and residual strength
- Dip in the FRC tensile behaviour graph (after the tensile strength)
- Fibre classification

5.2.4. Thermal properties

The properties that influence the heat development, described in section 4.1.3 include the heat transfer coefficients, external temperatures, the casting temperature and the adiabatic heat development. These properties do not vary in space, but these may take on different values at the top or bottom boundaries of the slab (except the casting temperature). Therefore these properties are not modelled in a random field but are two fixed values per sample for the upper and lower boundary. The thermal parameters of interest that are investigated are:

- Heat transfer coefficients
- Adiabatic heat development (cement type)
- Casting temperature
- External temperature

5.3. Failure definition

To differentiate between failing and non-failing samples, the definition of failure must be clear. The failure definition for UWC floors can be formulated as a maximum allowable amount of leakage, which can be transformed into a maximum crack width criterion. As proposed in chapter 2.3, the maximum allowable crack width should be between 0 and 0.2 mm. The failure definition can be formulated as a limit state in the following form:

$$Z = R - S = w_{\text{cr,lim}} - w_{\text{cr,max}} > 0 \tag{5.1}$$

Where:

- Z is the limit state with resistance R and load S

- $w_{cr,lim}$ is the maximum allowable crack width criterion [mm]
- $w_{cr,max}$ is the maximum occurring crack width in the calculation [mm]

This equation means that failure is defined when the maximum occurring crack width in a sample is larger than the maximum allowable crack width. It has to be checked whether the crack is actually a separation crack. Practically, the $w_{cr,max}$ is determined in the centre of the slab, implying that it is a full through crack.

In Chapter 4 it was concluded that two different crack pattern types might occur: a distributed crack pattern (DCP) or a single localised crack (SLC). In practice, the crack width of a SLC will always be larger than 0.2mm for the standard model. As a result, a sample with one localised crack will always fail according to the limit state. This was pointed out in Section 4.3.3. The samples that do show a distributed crack pattern, might either fail or not, depending on the exact maximum allowable crack width and the maximum occurring crack width. For the standard case, this is approximately 0.2 mm (see figure 5.1), which corresponds to the largest value of the maximum allowable crack width criterion. Therefore, it is expected that when multiple samples with different random fields are considered, part of the samples that show distributed crack behaviour fail, and another part does not. Examples of samples that show a DCP or SLC are displayed in appendix B.1.

By taking this into account, the problem can be split up into two parts. First, it has to be checked when samples show either a distributed crack pattern (sometimes failing) or a single localised crack (always failing). After this, only DCP results are considered. Then it has to be checked whether the maximum occurring crack width for samples with a distributed crack pattern is small enough to meet the failure criterion. So, the questions are:

1. When do samples show either a single localised crack or a distributed crack pattern?
2. Does the maximum crack width for samples that show a DCP meet the failure criterion?

5.4. Approach

In every variation, one input parameter is varied which can be any of the parameters described in section 5.2. Each sample will produce a different result because a different random field of the tensile strength (FRCFAC) will be generated for each sample. Every sample requires a separate FE analysis.

When multiple (150) samples are considered, this division between the two result types can be plotted in Figure 5.1. Where a distributed crack result corresponds with the left cluster in the histogram and a single localised crack result corresponds with the right cluster. The relative size of these clusters to each other varies depending on input parameters. In some cases, more results might fall into the SLC cluster, and for certain cases, all results fall entirely into either one of the clusters.

Looking at Figure 5.1, and setting the maximum allowable crack width to 0.2 mm, the failure probability is determined by the fraction of samples that fall on the right side of this line. For illustrative purposes, the failure probability was calculated as a function of a varying limit state ($w_{cr,lim}$), which is shown in Figure 5.2. This graph takes the form of a step function where the failure probability can be defined as:

- $P_f \approx 1.0$, when the maximum allowable crack width is lower than the minimum of the maximum occurring crack widths of cluster A ($w_{cr,lim}$ < 0.15 mm)
- $P_f \approx 0.126$, when the maximum allowable crack is in between both clusters (0.25 < $w_{cr,lim}$ < 3.9 mm)
- $P_f = 0.0$, when the maximum allowable crack is higher than the maximum occurring crack width in cluster B ($w_{cr,lim}$ > 4 mm)

In chapter 4, it was observed that the different types of behaviour can be triggered by changing the standard deviation of the random field. For a small coefficient of variation (<5%), most of the results

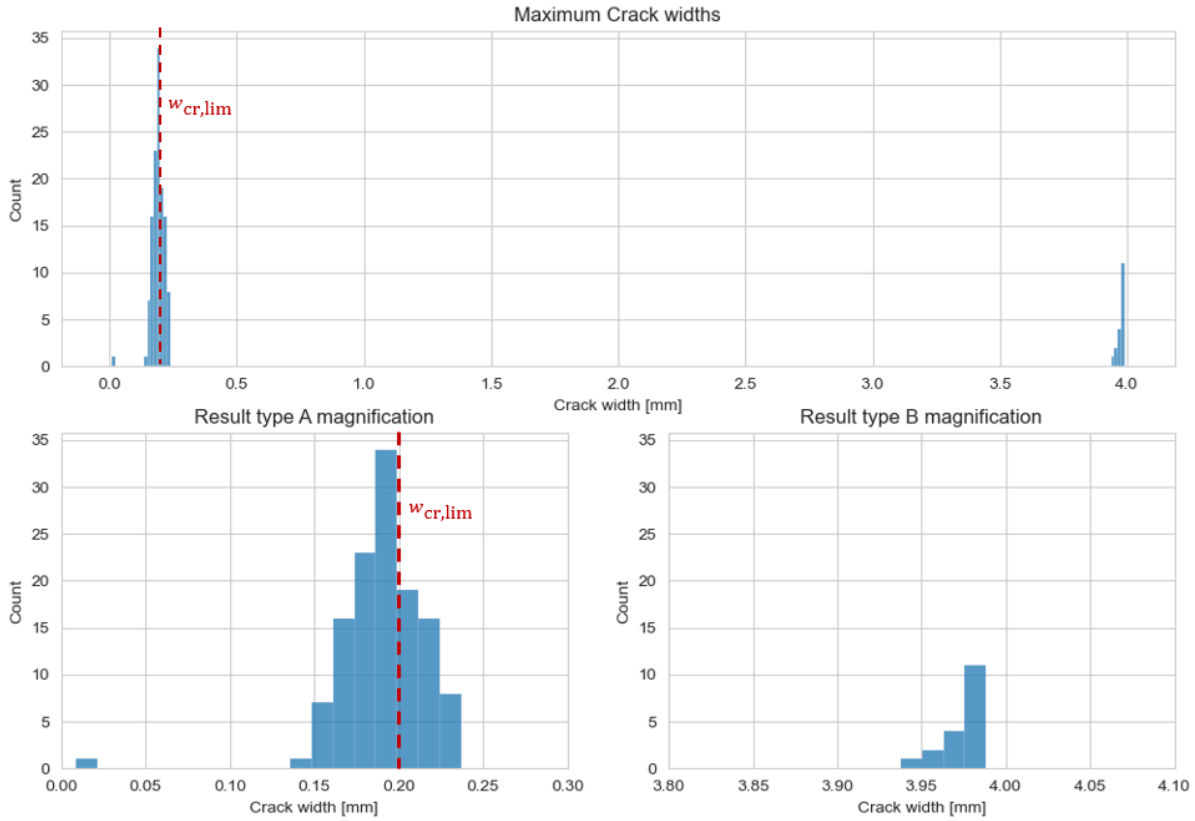

Figure 5.1: Magnitude of the maximum occurring crack widths. It can be observed that two clusters are formed, the left cluster around 0.2 mm corresponds to a distributed crack result and the right cluster around 4 mm corresponds to a single localised crack. The bottom graphs are magnifications of the clusters in the upper graph.

show a distributed crack pattern. For a coefficient of variation of 10%, there is a certain division between type A and type B behaviour. When the coefficient of variation of the random field is larger than 20%, all results will show a single localised large crack. If all of the samples show a SLC, the results of the influence parameters cannot be compared. For this reason, the standard deviation of the FRC-factor in the standard case is assumed to be 5%, as opposed to the 20% which was presented in Section 4.2. The consequences and reasoning behind this choice are further discussed in Section 5.7.

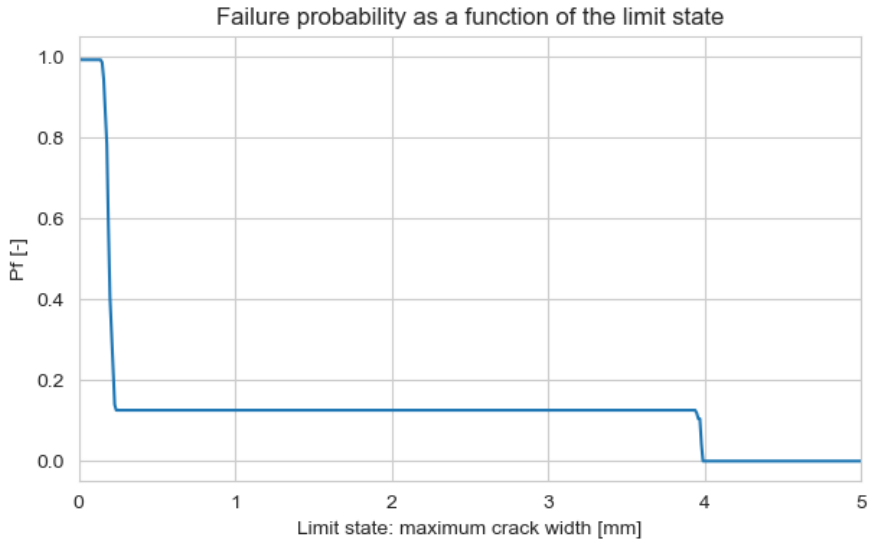

Figure 5.2: Failure probability as a function of the maximum allowable crack width to prevent leaking trough cracks.

5.5. Results

The results are split into three categories:

1. Influence of the random field properties
2. Influence of the material properties
3. Influence of the thermal properties

The starting point is the standard case described in appendix C.1. For each analysis, one input parameter will be varied. A table displays the value of that parameter, the percentage of samples that show a distributed crack pattern type result, the mean of the left cluster (distributed crack pattern) and the mean of the right cluster (single localised crack). For most analyses, at least 100 samples were generated, from which the results were obtained. For the results regarding the random field properties, 150 samples were generated.

5.5.1. Influence of Random field properties

To clarify how the random field parameters influence the characteristics of a random field, examples are presented in Section D.5 in the appendix.

Influence of the standard deviation

From Table 5.1, it can be seen that the standard deviation of the random field has a large influence on the results, where a smaller standard deviation means a larger percentage of distributed crack results. It can be seen that the mean of the maximum crack widths of the DCP cluster increases with increasing standard deviation, but it cannot be determined if this is significant. There are no samples with a distributed crack pattern for standard deviations larger than 0.15. The mean crack width for the SLC samples is a constant value as is shown with Equation 4.6. These results will not be presented in the rest of this section[1].

[1] The "Mean $w_{cr,max}$ SLC cluster" result is only presented once in Table 5.1a. In the rest of this section, the results of the SLC cluster are omitted, because they are similar for all variations. This can be explained by looking at equation 4.6, which produces the same crack width when there is only one large through-crack.

The same analysis was also done in which the random fields were generated with the squared exponential correlation function. Similar behaviour can be observed compared to the regular exponential function but larger standard deviations will also show a small percentage of samples that show a DCP.

Table 5.1: Influence of the standard deviation on the crack width results, expressed as the coefficient of variation (COV = standard deviation / mean).

(a) Exponential correlation function

COV	% Distributed crack pattern	Mean $w_{cr,max}$ DCP cluster	Mean $w_{cr,max}$ SLC cluster
0.05	80	0.19	3.98
0.10	20	0.23	3.98
0.15	0	-	3.97
0.20	0	-	3.97

(b) Squared exponential correlation function

COV	% Distributed crack pattern	Mean $w_{cr,max}$ DCP cluster
0.05	95	0.19
0.10	35	0.22
0.15	12	0.23
0.20	4	0.23

After interpreting the (individual sample) results, it was hypothesised that the percentage of DCP results depends on the relative magnitude of the weak spots in the FRC-factor random field. A larger standard deviation means a lower minimum in the random field than for a small standard deviation, which is supported and illustrated in Figure D.12 in the appendix. A possible explanation for a distributed crack pattern could be that consecutive weak spots[2] (weakest spot, second weakest spot, third etc.) must have sufficient tensile strength to initiate another crack. A distributed crack pattern forms when this process is repeated multiple times. An indicator for this is the ratio between the weakest spot and second weakest spot. These ratios are plotted, and it was indicated whether a sample led to a DCP or SLC.

The hypothesis can be verified when there is a well-defined division line between DCP and SLC results. If this line exists, it can be predicted, based only on the random field, whether a sample will show either type of behaviour. The two most promising results are shown in Figure 5.3:

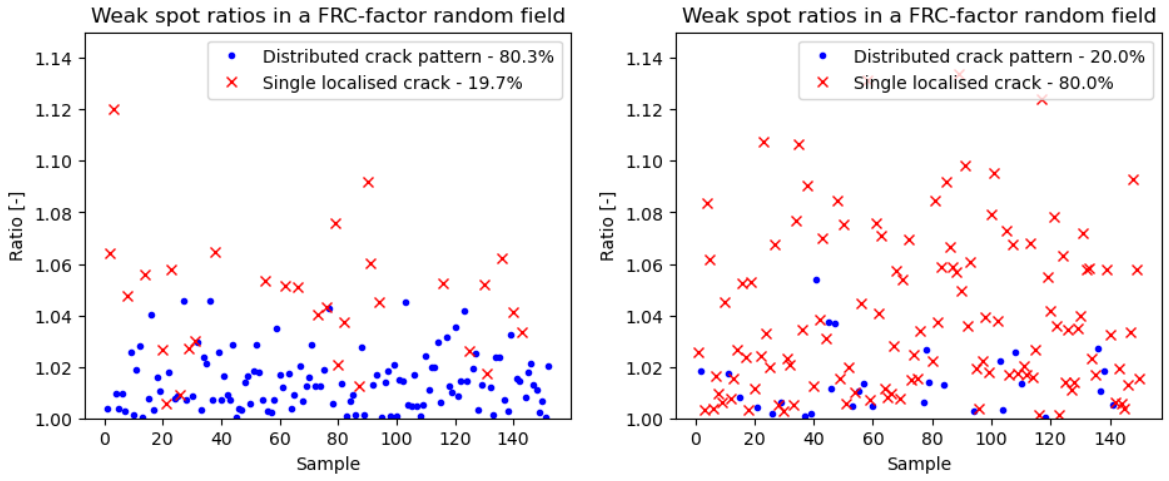

(a) COV = 0.05 (b) COV = 0.10

Figure 5.3: Ratios between the weakest spot and second weakest spot of the FRC-factor random field (Standard case with a varying standard deviation). Blue dots indicate a DCP and red dots indicate a SLC.

It can be seen that the SLC results in Figure 5.3 are generally higher than the DCP results according to the hypothesis, but an exact well-defined division line between a SLC and the DCP results cannot be

[2]The weak spot is defined as the largest negative peak in the random field. The second weak spot is the negative peak with the largest value (in absolute sense) after the first weak spot.

observed. It was also observed that the absolute value of the minimum in the random field is generally lower for SLC results which are displayed in Figure 5.4. The division line for Figure 5.3a is better defined than the results of the ratios, but also not perfect. It must be noted that the absolute weakest values in the random field are also used in the determination of the ratios in Figure 5.3.

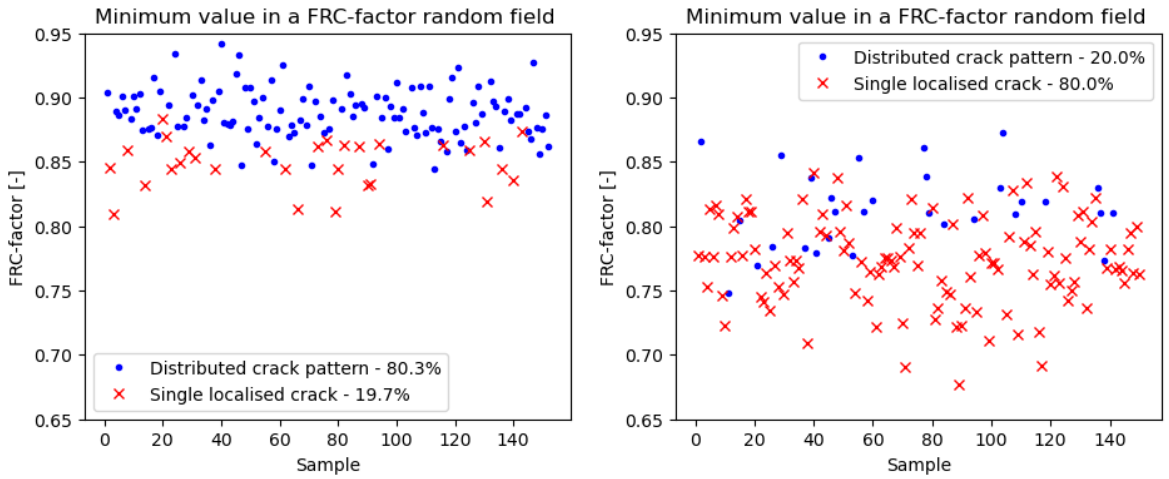

(a) COV = 0.05 (b) COV = 0.10

Figure 5.4: Minima (weak spots) of the FRC-factor random field (Standard case with a varying standard deviation). Blue dots indicate a DCP and red dots indicate a SLC.

From the comparison between Figures 5.4a and 5.4b and the results from Table 5.1a, it can be concluded that higher absolute minima in the random field will not only result in more samples with a DCP but also in a decrease in the mean $w_{cr,max}$. To further explore this an analysis with a random field with a standard deviation of 0.01 was performed and the results are given in Table 5.2. A significantly smaller $w_{cr,max}$ is observed while the average number of cracks is similar to the results in Table 5.1a. Moreover, this is the only analysis that would completely satisfy a maximum allowable crack width criterion of 15mm, which is the best result that was observed in this thesis. It seems that the maximum crack width is influenced by the absolute value of the minimum in the random field.

% DCP	Mean $w_{cr,max}$	Min $w_{cr,max}$	Max $w_{cr,max}$
100	0.13 mm	0.10 mm	0.15 mm

Table 5.2: Crack width results of the standard case with a standard deviation of 0.01

Influence of the correlation length

It has to be noted that, as stated in the previous section, the standard deviation of the standard case is 5% from now on. Except for the uncorrelated random field ($L_c = 0$), it is observed from Table 5.3 that a higher correlation length (L_c) corresponds with a higher percentage of DCP results. This can be explained when we consider the correlation length as another parameter that influences the random field standard deviation. A large correlation length means a large correlation over a greater section of the random field, resulting in neighbouring data points in the random field being more similar in magnitude. This means that the influence of the correlation length and the standard deviation are inversely proportional. The effect of a larger correlation length corresponds to a random field with a smaller standard deviation. And as was shown in the previous section, a small standard deviation results in a high percentage of samples that show a DCP. In summary, a large correlation length means high correlation, which indicates a smaller standard deviation, resulting in a larger percentage of the distributed crack type.

Table 5.3: Influence of the correlation length

(a) Exponential correlation function

L_c [m]	% Distributed crack pattern	Mean $w_{cr,max}$ DCP cluster
0	96	0.19
0.5	79	0.20
1	80	0.19
2	92	0.19
5	98	0.18

(b) Squared exponential correlation function

L_c [m]	% Distributed crack pattern	Mean $w_{cr,max}$ DCP cluster
0	-	-
0.5	83	0.19
1	95	0.19
2	99	0.17
5	100	0.15

Influence of the correlation function

The influence of the correlation function was presented in the previous two sections in Tables 5.1 and 5.3. In section D.3 of the appendix, the difference in the resulting random fields from the exponential and squared exponential function are discussed and examples can be found in Section D.5. Even though these functions produce significantly different random fields, the crack width results are comparable. This can be explained because function type does not influence the standard deviation, which was observed to be the main influence. Examples of crack patterns for both functions are presented in appendix B.1.

Influence of the distribution type

Varying the distribution type of the FRC-factor between a normal and a log-normal distribution does not result in significant differences in results. When looking at the corresponding generated random fields from these distributions, it can be concluded that no difference in results was also expected. These two distributions produce approximately the same random fields, as is displayed in Figure 5.5.

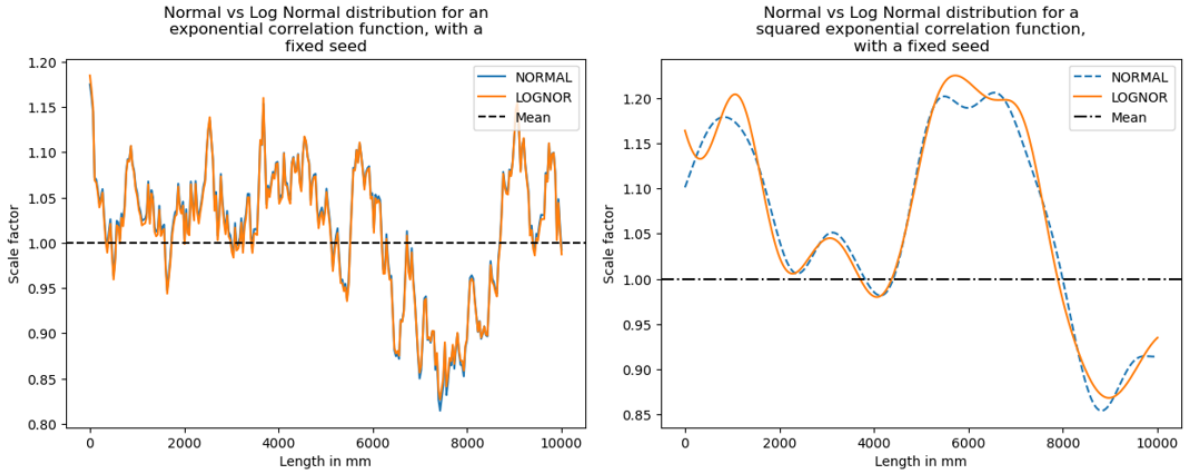

Figure 5.5: Random fields with a fixed seed, generated from a Normal and Log-normal distribution. Left: exponential correlation function. Right: squared exponential function

2D random field mesh

The influence of random fields with a 2D stochastic character instead of 1D was also examined. The difference between 1D and 2D stochastic variation in random fields is shown in Figure D.1. An example of the development of such a random field and the corresponding crack width is presented in Appendix B.3. These results show a similar cracking behaviour in which the first large separation cracks are formed at the locations of the weak spots. However, it is observed that growing surface cracks do not necessarily connect in the centre of the slab, but they have to grow completely from top to bottom or

the other way around. From the results in Table 5.4, it can be seen that the use of 2D random fields leads to a higher percentage of DCP results. A possible explanation for this is that the weak spots over the entire height of the slab (Figure D.1a) in a 1D random field present a discrete weak slice in the slab. On the other hand, 2D random fields might have a weak spot in the upper half of the slab, which might be counteracted by a strong spot in the lower half. This effect can be observed in Figure D.1b at around 4/5 from the left side. This means that averaged over the height; the slice does not behave as a weak slice. It can be concluded from this that in general, 1D random fields will produce (more) weaker slices than 2D random fields, meaning that the percentage of samples that show a DCP is lower for 1D random fields.

For the analysis with a 2D random field and standard deviation of 20%, 6 samples showed unique behaviour. Instead of a single localised crack of approximately 4mm, two localised cracks occurred with a width of 2mm. This phenomenon can also be explained by the previous paragraph's reasoning that a weak spot in a 2D random field does not necessarily mean a weak slice over the entire height. When a through crack only forms from one edge (either top or bottom), this may lead to a second crack developing before the first crack formed a full separation crack.

Table 5.4: Comparison of results where the FRC-factor is modelled in a 1D or 2D random field

(a) 1D FRC-factor random field

COV	% Distributed crack pattern	Mean $w_{cr,max}$ DCP cluster
0.05	80	0.19
0.10	20	0.23
0.15	0	-
0.20	0	-

(b) 2D FRC-factor random field

COV	% Distributed crack pattern	Mean $w_{cr,max}$ DCP cluster
0.05	97	0.21
0.10	45	0.28
0.15	6	0.275
0.20	0	-

5.5.2. Influence of Material properties

All results in this section are based on 100 samples per variation. When the first 50 samples only showed either a DCP or SLC, the analysis was stopped, and it was assumed that the result would either be 100 or 0%. The same notation as in the Model Code 2010 will be used to indicate the points in the material graph, which can be seen in figure 2.14. The points are indicated with the letters B, C, D and E, which is displayed in figure 4.5. For example, f_C is the tensile strength at point C with the corresponding crack width $w_{cr,C}$.

Influence of the FRC tensile strength material model

The assumption of the standard model was a FRC-tensile model according to fib Model code 2010 based on C30/37 concrete with fibre classification 4c. As discussed in section 4.1.4, it can be argued that the FRC tensile behaviour should be modelled with a dip and that the characteristic tensile strength should be used instead of the mean value because the characteristic residual strengths are also used. These adaptations are displayed in Figure 5.6. The orange-dotted graph denotes the standard model as defined by the MC2010 and the blue graph denotes the material model with a dip and the characteristic value of the tensile strength. The influence of these assumptions will be looked at in this subsection. The "dip" in the material model is indicated as a fraction η of the tensile strength at point D, f_D. So this means $f_C = \eta \cdot f_D$. A dip where $\eta = 0.85$ shows good results when calibrating test results from internal research done by ABT, but there is no general consensus on what this value should be.

The result of these variations on the standard case are displayed in table 5.5. Table 5.5a shows the results for the material models with a characteristic and mean strength, both with and without a dip. It can be observed that there are results with a distributed crack pattern only when the characteristic

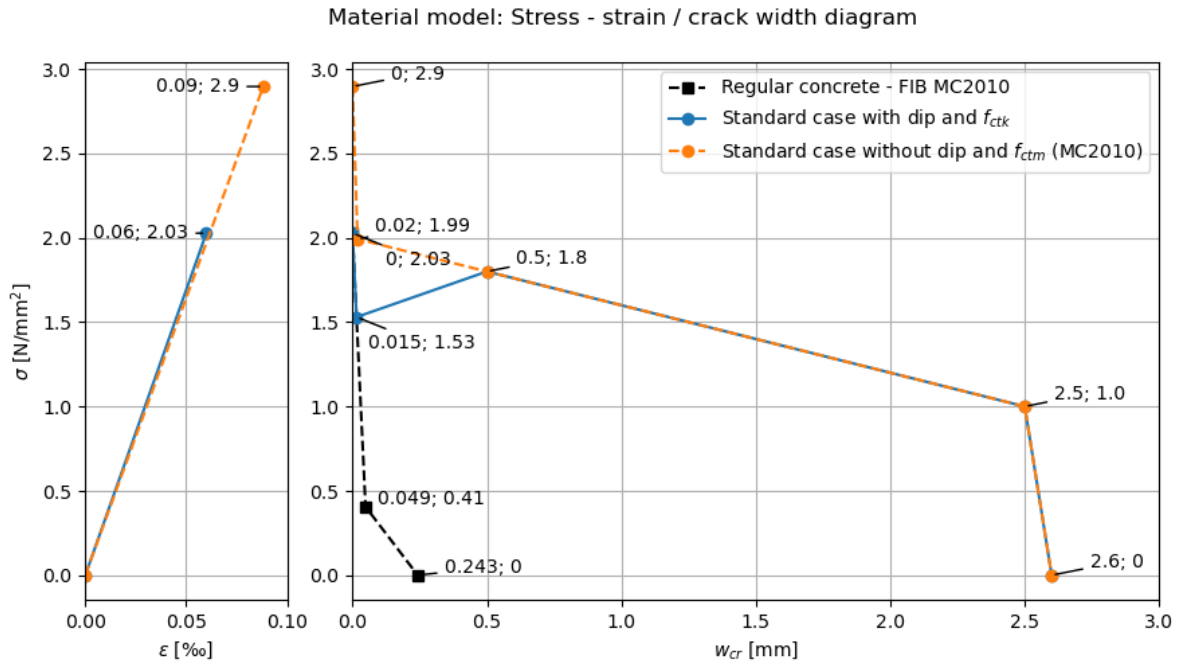

Figure 5.6: FRC properties: stress-strain / stress-crack width diagram. Regular material model from MC2010 compared to a model with a ”dip” where $f_c = 0.85 f_D$

Table 5.5: Results of different material models based on standard case

(a) Influence of material model

Tensile strength	Dip (η)	% Distributed crack pattern
f_{ctm}	-	0
f_{ctm}	0.85	0
f_{ctk}	-	0
f_{ctk}	0.85	87

(b) Influence of the dip

Tensile strength	Dip (η)	% Distributed crack pattern	Mean $w_{\text{cr,max}}$ DCP cluster
f_{ctk}	1.0	0.0	-
f_{ctk}	0.95	11	0.22
f_{ctk}	0.90	63	0.21
f_{ctk}	0.85	87	0.19
f_{ctk}	0.8	99	0.18

tensile strength and a dip are used. Table 5.5b shows the results when the size of the dip is varied. It can be concluded that the larger the dip is, the more samples show a distributed crack pattern.

These results are surprising since a lower residual tensile strength causes a more favourable result, which is against expectations. It seems that a dip is required in any case to obtain a distributed cracking pattern and the difference in stress between the tensile strength and the stress at point C (f_c) may not be too large. To investigate this observation, a fictitious material model is made that uses the mean tensile strength with approximately the same shape as the standard case model but scaled. In order to obtain this shape, the value for f_d is chosen as 2.25 MPa and the model is plotted in Figure 5.7.

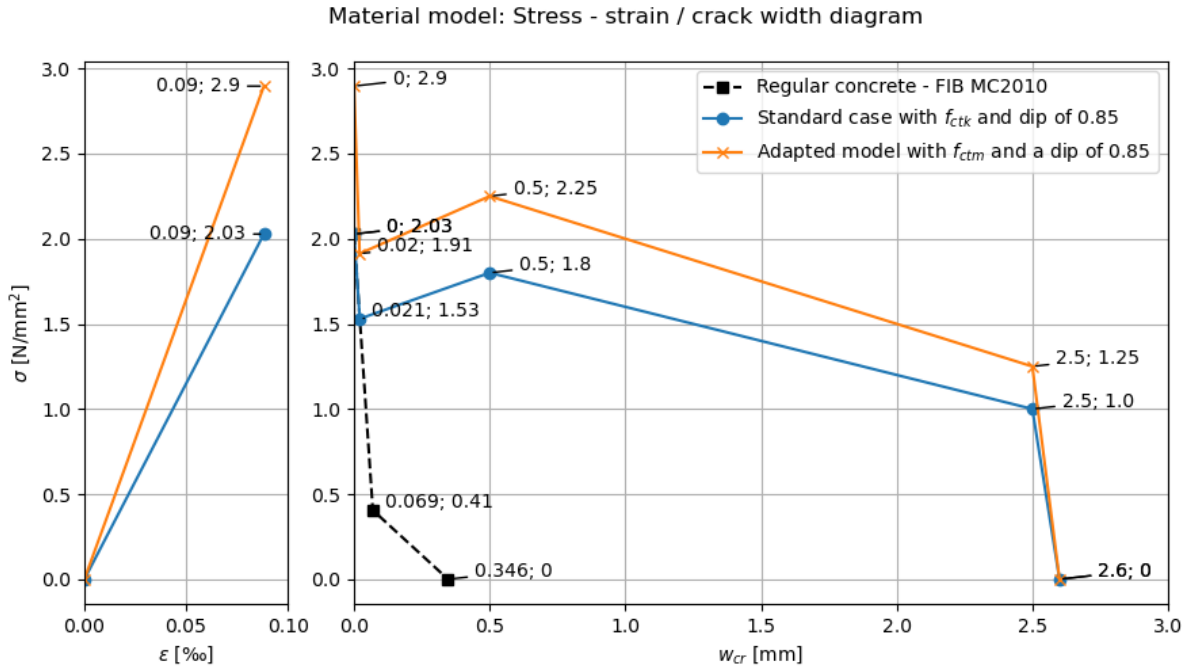

Figure 5.7: Standard case with f_{ctk} compared to an fictive model with approximately the same shape, but with f_{ctm}. Both with a dip of 0.85

The results are displayed in Table 5.6, where the column on the right compares the result to those of the standard case with f_{ctk}. Looking at the results, it seems that the shape of the material model graph is indeed the determining factor, especially the ratio between the tensile strength and the stress at point C. A possible explanation is that the fibre strength ”needs to match” the concrete tensile strength (in a relative sense). For example, when weak fibres are used in strong concrete, this concrete will take all the tensile stress, and the fibres might not be activated. When the tensile strength is reached, a large crack will occur directly in the concrete since the fibres are not contributing. This is in line with the philosophy behind the dip. Another observation is that there is a trend in the mean of the maximum occurring crack widths in a DCP. The larger the dip, the smaller the maximum occurring crack width will be.

Table 5.6: Results of a fictious material model with f_{ctm} and f_d = 2.25.
The final column displays the results from the standard case with f_{ctk} (Table 5.5b)

Dip	% Distributed crack pattern	Mean $w_{cr,max}$ DCP cluster	Comparison % Standard case
-	0.0	-	0
0.85	4	0.22	87
0.7	98	0.20	100
0.5	100	0.19	-
0.3	100	0.18	100

Figure 5.8 shows different combinations of the dip and standard deviation. In this figure, the influence of the standard deviation is plotted for three different magnitudes of the dip. As seen before, a larger dip and a smaller standard deviation will result in a higher percentage DCP.

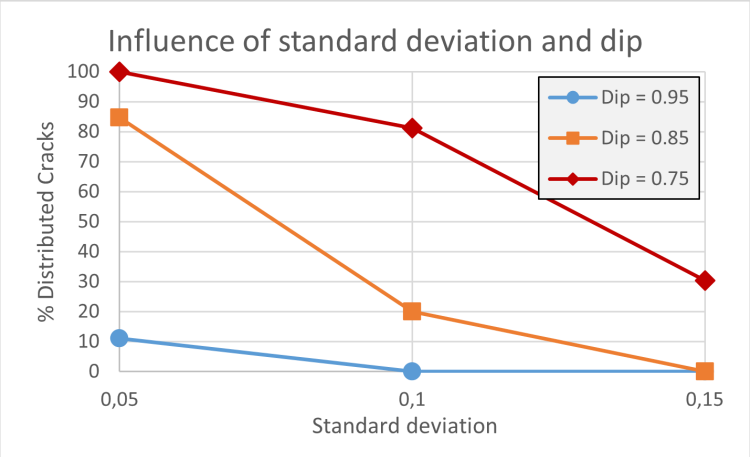

Figure 5.8: Influence of the standard deviation for different values of the dip

Influence of fibre classification

The standard case includes fibres with classification 4c. Different classifications were modelled (4a,4b, 4d and 4e) with the same C30/37 concrete, which is also the standard case. In these models, the mean value of the tensile strength was used, both with and without the dip. All 8 of the models resulted in 0% DCP results. This is in line with the results from Table 5.5a. To try to get results with a distributed crack pattern, two options can be investigated:

1. Use the characteristic tensile strength instead of the mean tensile strength
2. Look at a higher fibre strength class 5 ($f_{R1k} = 5$).

The results of both options are presented in Table 5.7. The corresponding input graph of option one is displayed in Figure A.4 and the input graph of option two is displayed in Figure 5.9. From these figures, it becomes clear that the number in the fibre classification influences point C and D, and the corresponding letter that indicates the ratio f_{R3k}/f_{R1k} changes point E.

Looking at the results, there are distributed crack patterns for both options. Where a higher fibre classification (letters) corresponds with more samples showing a DCP. Again it has to be noted that the combination f_{ctm} with fibre class 4 does not result in any distributed crack patterns. This is in line with the observations from the previous subsection that the stress at points C and D in the FRC tensile graph has to be close enough to the tensile strength in a vertical sense while point E seems to have less influence on the occurrence of distributed crack patterns.

Table 5.7: Influence of different fibre classifications for the two options

Tensile strength	Fibre Classification	% Distributed crack pattern	Mean $w_{cr,max}$ DCP cluster
f_{ctk}	4a (0.5)	93	0.19
f_{ctk}	4c (0.9)	87	0.19
f_{ctk}	4e (1.3)	100	0.20
f_{ctm}	5b (0.8)	39	0.22
f_{ctm}	5c (1.0)	54	0.22
f_{ctm}	5d (1.2)	69	0.24

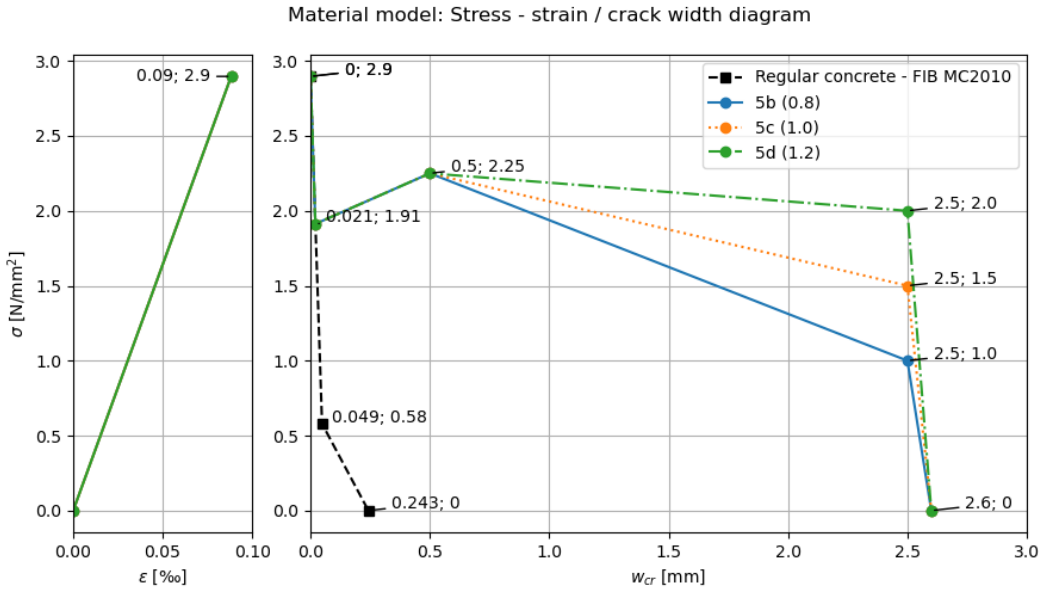

Figure 5.9: Influence of different fibre classifications in combination with the mean tensile strength where $f_{R1k} = 5$ N/mm² and the ratio f_{R3k}/f_{R1k} is indicated with the number between brackets

Influence Young's modulus

As discussed in section 4.2, initially only the FRC-factor is modelled with a random field in the standard case and the Young's modulus is kept as a constant value over the length. This section will discuss the influence of modelling both properties with a random field. The results in Table 5.8 do not show a significant difference in crack widths when the Young's modulus is included as a random field.

Table 5.8: Comparison of results where only the FRC-factor is modelled in a random field or both the FRC-factor and Young's modulus are modelled with a random field. The varying variable is the standard deviation

(a) FRC-factor only

COV	% Distributed crack pattern	Mean $w_{cr,max}$ DCP cluster
0.05	80	0.19
0.10	20	0.23
0.15	0	-
0.20	0	-

(b) FRC-factor + Young's modulus

COV	% Distributed crack pattern	Mean $w_{cr,max}$ DCP cluster
0.05	84	0.20
0.10	20	0.23
0.15	1	0.19
0.20	0	-

An analysis was also done in which only the Young's modulus was modelled with a random field. The results for this always show that all samples lead to a DCP. It must be noted that this model's maximum crack widths were around 0.1 mm. In Figure B.7 in the appendix, a result of a sample of this analysis is shown. It can be seen that all crack widths are approximately equal and that there is no largest crack at the minimum of the random field. It can be concluded from this that the Young's modulus has an inferior influence on crack development compared to the FRC factor.

When applying two random fields for both the Young's modulus and FRC-factor, there is also a certain correlation between these random fields, which is denoted by the correlation coefficient ρ. The correlation is a different property than the earlier discussed correlation length. The correlation length L_c defines the correlation within one random field and the correlation coefficient ρ defines the correlation between two random fields of two different material properties. When the correlation between these two random fields is 1, exactly the same random field shape will be used for both material properties.

When the correlation is 0, two completely different random fields will be used with peaks at different locations. The value of the correlation can be varied between 0 and 1, where the two random fields will vary from being completely different to being completely the same. Table 5.9 shows that varying this correlation does not significantly influence crack width development.

Table 5.9: Influence of the correlation between the FRC-factor and the Young's Modulus

Correlation	% Distributed crack pattern	Mean $w_{cr,max}$ DCP cluster
0	77	0.20
0.5	82	0.19
1.0	84	0.20

5.5.3. Influence Thermal properties

In this section 100 samples were used for all variations. The results are compared by looking at the percentage of samples that show a DCP, the average maximum crack width that occurs and how much the slab will need to cool down. It has to be noted that the conclusions are drawn based the input parameters of the standard case and that these conclusions might nog be generally applicable for any combination of parameters.

Influence of the heat transfer coefficients

From Table 5.10 it can be concluded that the heat transfer coefficients do not play a big part as long as they are larger than 100 W/(m^{2}K). All three of these results where the coefficients are larger than 100, are pretty similar. The result does change drastically when very small values (5 W/(m^{2}K) for the heat transfer coefficients are used. In this case, much heat will be accumulated combined with insufficient heat dissipation. This will lead to a large temperature increase, meaning that there will be a large restrained shrinkage, which can also be seen from the crack width of SLC. This also means that higher tensile stresses can develop, which leads to a small percentage of type A results for this variation compared to the other cases. As presented in Section 4.1.3, the coefficient of 5 is for air convection and the values of 100 and 700 are for stagnant and flowing water respectively. In the case of UWC floors, the hardening of concrete will happen underwater, meaning that the variation with the heat transfer coefficients of 5, will generally not occur in practice. Therefore, this variation can be disregarded in the rest of this section and further probabilistic analyses. The value of 100 can be assumed to be a minimum for completely stagnant water because in practice there will always be some form of flow in the water on top of the floor. The groundwater at the bottom of the floor might be completely still and the heat transfer coefficient might be close to 100 W/(m^{2}K).

From the literature study, it was expected that these parameters would have a significant influence, which seems not to be the case. Also, the variation in which the top and bottom coefficients are unequal gives similar results to the standard case. It appears that a heat transfer coefficient of 100 W/(m^{2}K) can dissipate more heat than the hydration reaction can produce, meaning that larger coefficients do not have any additional effect. This can also be seen from the fact that the temperature change for these three cases is almost similar. In conclusion: for UWC floors the minimum heat transfer coefficient that will be used is 100 W/(m^{2}K), which results in this parameter only having a minimal effect on the crack width.

Internal research by ABT and the CROW committee has shown that the heat transfer coefficient at the bottom should be significantly lower than 100 W/(m^{2}K) to match the experimental results. The reason behind this is that the soil at the bottom acts as an insulating layer, leading to lower heat transfer coefficients. If this is the case, the conclusion that the heat transfer coefficients are not very influential under the conditions in this thesis and in UWC floors might not hold. To verify this one result was

added where the heat transfer coefficient at the bottom was assumed to be 50 W/(m^{2}K). However, these results are similar to the rest.

Table 5.10: Influence of the heat transfer coefficients. T_0 = 12 °C, T_{ext} = 12 °C. Crack widths are given in mm. The table is split into two parts. S.D. is the abbreviation of standard deviation.

$h_{tr,top}$ [W/(m^{2}K)]	$h_{tr,bottom}$ [W/(m^{2}K)]	% Distributed crack pattern	Mean $w_{cr,max}$ DCP cluster	Mean # Cracks	Mean $w_{cr,max}$ SLC cluster	ΔT [°C] cooling
5	5	4	0.27	40	7.24	39.3
100	50	90	0.19	47	4.19	29.9
100	100	91	0.19	43	4.03	29.4
300	100	89	0.20	45	3.91	29.0
700	700	94	0.18	43	3.75	28.4

$h_{tr,top}$ [W/(m^{2}K)]	$h_{tr,bottom}$ [W/(m^{2}K)]	Min $w_{cr,max}$ DCP cluster	Max $w_{cr,max}$ DCP cluster	S.D. $w_{cr,max}$ DCP cluster
5	5	0.25	0.31	0.028
100	50	0.15	0.29	0.026
100	100	0.145	0.24	0.020
300	100	0.139	0.38	0.052
700	700	0.133	0.26	0.021

Influence of the adiabatic heat development

The results from the variation of the adiabatic heat development are in line with expectations. CEM III, which produces the least amount of heat also has the lowest temperature difference during cooling and CEM I has the highest. Despite the low temperature development, the DCP maximum crack width results do not indicate that the type of cement is an important parameter for the maximum crack width, which is against expectations. It can be observed that the amount of cracks does increase to accommodate for the larger shrinkage, which is spread out over more cracks. The Mean $w_{cr,max}$ of approximately 0.2 mm is also observed in these results, implying that the thermal properties do indeed not influence the maximum crack width but only the number of cracks.

Table 5.11: Influence of the adiabatic heat development. T_0 = 12 °C, T_{ext} = 12 °C. Crack widths are given in mm.

Adiabatic heat development	% Distributed crack pattern	Mean $w_{cr,max}$ DCP cluster	Mean # Cracks	Mean $w_{cr,max}$ SLC cluster	ΔT [°C] cooling
CEM I	92	0.20	62	6.24	25.5
CEM I + III	91	0.19	43	4.03	17.4
CEM III	93	0.19	20	2.64	12.2

Influence of the casting and external temperatures

The crack width results are given for different combinations of initial and external temperatures in Table 5.12. There are no real obvious outliers for these results. The results are comparable to those of the adiabatic heat development and heat transfer coefficient variations. High initial and low external temperatures will lead to the largest shrinkage. A similar result regarding the number of cracks can be observed as in the previous paragraph.

When the final temperature is higher than the initial temperature, the edges of the slab will heat up quicker than the middle at the very beginning as can be seen in Figure 5.10. This is exactly reversed

Table 5.12: Influence of the casting temperature and external temperature. Crack widths are given in mm.

T_0 [°C]	$T_{ext,top}$ [°C]	$T_{ext,bottom}$ [°C]	% Distributed crack pattern	Mean $w_{cr,max}$ DCP cluster	Mean # Cracks	Mean $w_{cr,max}$ SLC cluster	ΔT [°C] cooling
12	12	12	91	0.19	43	4.03	17.4
10	7	7	93	0.19	43	3.70	16.4
17	12	12	93	0.20	52	4.79	20.4
26	16	16	91	0.20	64	6.53	27.0
26	7	7	93	0.20	73	7.59	30.4
10	16	16	97	0.18	-	3.81	16.3
10	16	12	99	0.20	-	3.83	16.4
10	16	7	92	0.28	-	3.90	16.4

from the regular process from all the other analyses. The reason behind this is that the hydration reaction needs a little while before it picks up speed, but the external temperature is applied immediately. This results in the edge zones expanding more than the centre, which means a (small) tensile stress develops in the middle, together with a still very low tensile strength. This will lead to micro-cracking in the centre before micro-cracking in the edge zones. After the temperature in the centre becomes higher than the temperature in the edge zones, the regular process takes over. However, this result can be disregarded because the model does not take into account that during these very early stages, the concrete will not be solid yet. In reality micro-cracking in the centre will most likely not occur. Nonetheless, because every element in the centre was cracked, this is the reason why the number of cracks is not given in Table 5.12 for the variations where $T_{ext} > T_0$.

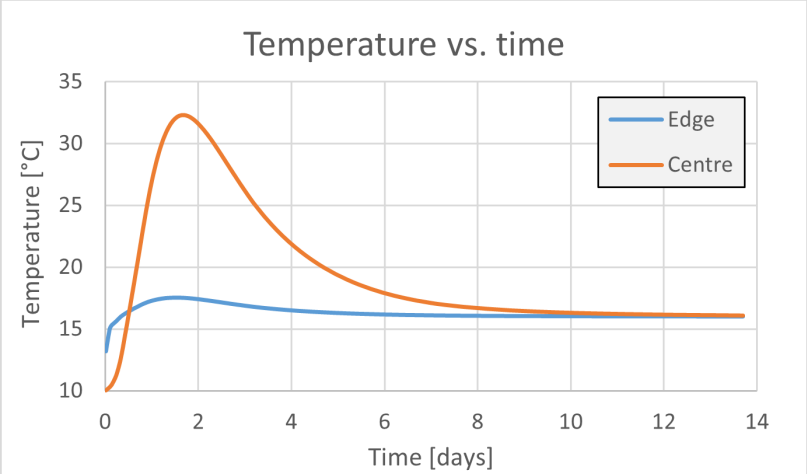

Figure 5.10: Temperature development in the centre and edges over time. $T_0 = 10$°C and $T_{ext} = 16$°C

5.5.4. Influence Geometry

The results for a varying thickness of the slab are presented in Table 5.13. It can be observed that thicker slabs can develop a larger temperature. The reason behind this is that there is more concrete which will hydrate, and the heat not be dissipated as well as thinner slabs. This can be concluded from the temperature drop and the maximum crack width of the SLC. Remarkably the maximum crack width results and the percentage of samples that show a DCP are very similar for the slabs that are 1 and 1.5 metres thick. The slab of 2 metres performs a little bit worse, with a larger maximum crack width of 0.29 mm, but the difference is not very significant as was expected.

Table 5.13: Influence of the slab thickness. All other properties are from the standard case. Crack widths are given in mm.

Thickness [m]	% Distributed crack pattern	Mean $w_{cr,max}$ DCP cluster	Mean # Cracks	Mean $w_{cr,max}$ SLC cluster	ΔT [°C] cooling
1	91	0.19	43	4.03	17.4
1.5	97	0.21	53	6.03	38.2
2	75	0.29	58	7.72	43.5

5.6. Full probabilistic analysis

This chapter aims to provide example calculations as proof of concept of how the failure probability can be calculated when multiple stochastic parameters are considered simultaneously. Additionally, the results can be compared to the previous section in which only one parameter was varied at one time. In this way the influence of different combinations of parameters can be observed. One analysis will be done in which all the parameters are chosen as realistically as possible and in a second analysis, the parameters will be chosen to be optimised for the crack width results.

5.6.1. Parameters

The stochastic parameters that are selected for the model with realistic parameters are summarised in Table 5.14.

Table 5.14: Realistic input properties for the case study

Category	Input parameter	Distribution	Mean	Standard deviation	Source
Random field properties	Correlation length [m]	Normal	2	0.5	Ch.5
	FRC-factor [-]	Log-Normal	1	0.20	2.5.1
	Young's modulus [N/mm^2]	Log-Normal	32836	4925 (15%)	2.5.1
	Correlation between properties ρ [-]	Deterministic	1	-	
Material properties	Tensile strength f_{ctk}	Deterministic	2.0	-	
	Compressive strength f_{cm}	Log-Normal	38	2.28 (6%)	2.5.1
Thermal properties	Heat transfer coefficient top	Normal	200	50	4.1.3
	Heat transfer coefficient bottom	Normal	125	25	4.1.3
	Casting temperature	Normal	17	3	4.1.3
	External temperature top	Normal	12	2	4.1.3
	External temperature bottom	Normal	12	0.5	4.1.3

5.6.2. Results

From the results it can be concluded that both a dip and low standard deviation are required for the occurrence of a distributed crack pattern. This is in line with the results that were observed before. It can be concluded that the standard deviation and the dip are so dominant, that the effect of the other stochastic variables cannot be studied. Because these influences are that big, it is not possible to make a optimized design with a realistic standard deviation of 20%.

Table 5.15: The parameters are based on Table 5.14. All other parameters that are not included are based on the standard case. The second result includes a standard deviation of 5% and no dip. The third result includes a standard deviation of 5% and a dip as in the standard case

Model	% Distributed crack pattern	Mean $w_{cr,max}$ DCP cluster	Min $w_{cr,max}$ DCP cluster	Max $w_{cr,max}$ DCP cluster	Mean # Cracks	Mean $w_{cr,max}$ SLC cluster
Realistic Dip $0.85\ f_D$	0	-	-	-	-	4.70
Realistic $\sigma = 0.05$	3	0.68	0.53	0.98	101	4.67
Realistic $\sigma = 0.05$ Dip $0.85\ f_D$	99	0.21	0.09	0.35	68	4.44

5.7. Discussion

This section includes an evaluation of the assumptions and the model's limitations. Possible explanations of the results is already included in the previous section.

Analyses where the percentage of samples with a distributed crack pattern is close to either 100 or 0% do not need as many samples to reach the desired accuracy as analyses where the failure probability is somewhere in the middle of this range. Nevertheless, due to time constraints, a practical value of 100 samples for each analysis was chosen. Because of this, some results might not be entirely accurate but the focus is more on the change in results between the varied parameters. An estimate for the accuracy can be based on 100 samples of the standard case (80.3%) with an analysis of 1000 samples of the standard case (83.6%). This is a difference of 3.3%. It is estimated that results can maximally differ by 5%. The mean value of the maximum crack width is exactly the same. The expected possible error for this result is very small.

In Chapter 4, a standard deviation of 20% was assumed, but at the beginning of this chapter, it turned out that using this standard deviation resulted in a single localised crack in all the samples. Since it was not useful to continue with this because all of the samples failed all the time, it was decided to change the standard deviation in the standard case to 5%, which does show both crack patterns. Nevertheless, this is a very low standard deviation compared to the values given in the Section 2.5.1. As discussed in Section 4.4, the local variations in geometry could also be included in the standard deviation of the random field of the FRC-factor. And the simplification from a 3D stochastic character to a 1D stochastic random field also influences the local variation in material properties. In conclusion, the standard deviation is a rather arbitrary choice when it is used with a simplified model. When considering the objective of this thesis, which is to determine a suitable probabilistic method, it is the most convenient to choose the standard deviation such that increasing or decreasing the value can be seen in the results. 5% is a suitable value for this objective.

Research by ABT and the CROW committee on thermal shrinkage has shown that using the mean value of the residual tensile stress shows a better correspondence with results from already realised FRC projects. With this in mind, the assumptions to use the characteristic values for the residual tensile strength and the tensile strength of concrete from section 4.1.4 can be questioned. However, the results show that the ratio between the tensile strength and residual strength is the important factor, and the absolute value (mean or characteristic values) is of minor importance. The most important aspect is that either the characteristic or mean values are used for both the tensile and residual strength.

This chapter investigates the input parameter's influence on the result by varying them separately and

reporting the resulting crack widths. However, this method excludes the combined effects of varying multiple parameters simultaneously. For example, one parameter might be beneficial for crack width limitation while another is disadvantageous. If both these parameters are used simultaneously, the effects might cancel each other out, which means that the conclusions might only be valid for this specific set of input parameters. Therefore, it has to be noted that the conclusions drawn in this chapter may not be generally applicable.

The assumed boundary conditions in the model and the exclusion of external forces lead to very conservative crack width results. This choice was made with the idea of obtaining an upper limit for the maximum crack width so that a realistic model will result in smaller maximum crack widths. In this way, when the conservative approach satisfies the maximum allowable crack width criterion, the more realistic model will also satisfy this criterion. This decision results in the conclusion that determining the exact failure probability is not meaningful from a scientific standpoint. A more extensive model is required for this.

The dip in the FRC tensile graph is modelled with linear line segments, which causes an acute angle at the location of the dip, which might lead to problems in a finite element analysis. When the time steps are not sufficiently small enough, the exact behaviour of this dip might not be adequately modelled in the FEA. In appendix Section C.2 this effect was investigated and it can be concluded that this is not a problem.

5.8. Conclusions

5.8.1. Summary

A failure definition was formulated based on a maximum allowable crack width that should be lower than 0.2 mm. The crack width results showed either a localised crack or a distributed crack pattern. This is important for the failure definition because a distributed crack pattern might show multiple smaller cracks that are small enough so the construction will not fail, whereas a single localised crack will always be too large and lead to failure. Therefore the main indicator that was used in this chapter was the percentage of samples that showed a distributed crack pattern as a result. A secondary criterion was to look at the maximum crack width that occurred in the distributed crack pattern. Together, these criteria were the main indicators for the sensitivity analysis that was carried out in this chapter.

A distinction was made between three categories of stochastic properties: random field properties, material properties and thermal properties. Especially the standard deviation of the random field and the characterisation of the FRC tensile behaviour were of interest because these parameters influenced the results the most. Most of the results can be explained when looking at the material model or making the connection to how the random field properties influence these material properties. Against expectations from previous chapters, the thermal properties turned out to be of minor importance for the given, fixed structural properties that were used in these analyses.

5.8.2. General

The standard deviation of the random field and the inclusion of a dip in the FRC tensile graph are the most important influence parameters for the maximum crack width. For the combinations that were considered in this thesis, these parameters overshadow the other parameters. Meaning that the other parameters have a negligible influence compared to these two. By tweaking either one of them, the results can be manipulated to show either 100% DCP or SLC. The thermal properties mainly influence the number of occurring cracks. The conclusions per influence parameter category are discussed hereafter.

5.8.3. Random field properties

It was confirmed that the random field properties heavily influence the results, as was previously noticed in Chapter 4.

- The lower the standard deviation in the random field, the more samples show a distributed crack pattern and the maximum crack width is also lower. A small standard deviation influences the absolute value of the minimum (weakest spot) of the FRCFAC random fields. These are generally larger, which can explain the better crack width results. The standard deviation is a property that has a physical interpretation, but there is no consensus on what a representative value for the standard deviation should be. It can be argued that based on the model assumptions in this thesis, the standard deviation can be reduced with respect to the values found in the literature. While on the other hand, it could be increased when considering the added effect of the tolerances in geometry which are not modelled.
- The correlation function and correlation length do have a physical interpretation but they have no experimental foundation, which primarily makes these properties model uncertainties. However, a higher correlation length means a higher percentage of samples with a distributed crack pattern. This can be explained because the correlation length influences the standard deviation of a random field, where a larger correlation length means a lower standard deviation.
- To model the material properties with a random field, a normal and a log-normal distribution were considered. The crack width results are not influenced by using different distributions. This is backed up when looking at the random fields. Both of the distributions produce similar random fields for the material parameters that were considered in this thesis (FRCFAC and Young's modulus).

5.8.4. Material properties

- It can be argued that FRC can better be modelled with a dip in the tensile behaviour as is discussed in Section 2.2.4 because this is a better resemblance to the combined behaviour of concrete and steel fibres. In order to obtain the required distributed crack patterns, the results show that such a dip in the material model seems to be a prerequisite. A similar material model without a dip shows mostly localised crack results, while models with a dip show mostly distributed crack patterns. The magnitude of the dip also plays a role in this. A possible explanation of these results could be that the dip introduces a hardening branch in the FRC tensile behaviour, and tension-hardening is generally associated with a distributed crack pattern.
- The occurrence of distributed crack results is more dependent on the relative stress difference between the tensile strength and the location of the location (y-coordinate) of the hardening branch in the tensile behaviour graph (Figure 5.6) than on the absolute magnitude of the points. For example, a high concrete class with an average fibre classification does not necessarily result in the desired crack width results. In comparison, lower-quality concrete in which the tensile strength is closer to the dip, can show the desired results of a distributed crack pattern.
- Also modelling the Young's modulus with a random field is of negligible influence for the crack width results. This means that the correlation between the FRC-factor and Young's modulus is also of minor importance.

5.8.5. Thermal properties

Generally, the conclusions pertaining to the thermal influences are all based on a singular set of structural parameters. The conducted variations were exclusively based on the standard case. It is important to note that the conclusions might be different when considering alternative structural parameters.

- The thermal influence parameters turn out to be less important than was expected from previous chapters and the literature review. They do have a large influence on temperature development and the magnitude of expansion and shrinkage, but they do not have a large influence on the maximum crack widths in a distributed crack pattern. However, they do significantly influence the number of cracks that occur in a DCP. It was observed that the mean of the $w_{cr,max}$ in distributed crack patterns is around 0.2 mm (dependent on the standard deviation). So for the variations where the total expansion (and therefore shrinkage) is larger, the total shrinkage has to be divided over more cracks.
- As long as the heat transfer coefficients are above 100 W/(m^{2}K), which is the literature value for stagnant water, there is no significant difference in crack width results. Results only start to differ when the heat transfer coefficients are significantly lower than 100 W/(m^{2}K). For the application of UWC floors, the lowest probable heat transfer coefficients are not in the range where they significantly influence the crack width results. So within the scope of this thesis and the topic of UWC floors, the heat transfer coefficients do not have a large influence. The heat transfer coefficient at the bottom is generally lower than at the top because the soil insulates the UWC floor.
- Varying the adiabatic curve of the model does influence the temperature development a lot and also the maximum crack width for a localised crack. The maximum crack width for a distributed crack pattern and the fraction of results with a DCP, do not differ significantly. Therefore, the adiabatic heat development does not have a big influence on the results of interest for the structural parameters of the standard case.
- Similar observations are made for varying the casting and external temperature and all possible combinations of this.
- When considering the distribution of the maximum crack widths of the distributed crack patterns in combination with varying thermal properties, the lowest and highest maximum crack widths can differ significantly between different analyses. However, a low minimum of the $w_{cr,max}$ is usually accompanied by a high maximum of the $w_{cr,max}$. This indicates that mainly the standard deviation of the maximum crack widths is increased or decreased and it does not change the mean value of the crack widths. Therefore, not any specific temperature case can be indicated that is beneficial for crack width limitation.

6

Conclusion

Summary

The two main chapters 4 and 5 ended with specific conclusions regarding the finite element model and the probabilistic analysis. The main findings of these chapters are summarised in the following paragraph.

Certain combinations of input parameters will lead to a distributed cracking pattern, consisting of multiple small cracks which are more likely to satisfy the crack width criterion as opposed to a single large separation crack which does not satisfy the maximum allowable crack width. It was found that the tensile behaviour of FRC and modelling this with a random field are the two major factors that influence the crack width and the occurrence of a distributed crack pattern. The main influence parameter of the random fields was the standard deviation, which influences the absolute minimum (weak spot) in the random field. A lower minimum will result in higher maximum crack widths and more samples that show a single localised crack. Looking at the tensile behaviour, the main conclusion was that a drop and a rise after cracking (dip) in the tensile stress-CMOD diagram was the governing influence factor. Both these factors affect the relation/ratio between the tensile strength of the concrete and the residual tensile strength of the fibre-reinforced concrete.

In the rest of this chapter, the research questions formulated in Chapter 1 will be addressed. First, the sub-questions will be answered and after this, the main research question can be answered. Finally, the follow-up questions are addressed.

Sub questions

- **What does the structural behaviour of a young hardening UWC floor look like, and how can this be modelled?**

It is important to include the hardening phase of concrete in the design of UWC floors. One of the main causes of crack formation is restrained thermal deformations. Heat is produced during the hydration reaction, and the temperature distribution over the thickness of the slab can be divided into an average, sometimes a linear and an Eigen component. The Eigen stresses caused by the Eigen temperatures will cause a difference in thermal strain over the thickness, resulting in internal restraint. This will lead to micro-cracking in the upper and lower edge zones during the hardening phase. During the cooling phase, there will be an additional restraint of the average temperature component, which will cause

the micro-cracks to grow from the edge zones and connect in the centre of the slab to form through cracks which may cause leakage. When considering thermal shrinkage cracking in young hardening concrete, the development of the tensile strength and Young's modulus over time also play a prominent role in crack development and initiation. Besides that, the boundary conditions greatly influence the structural behaviour of a young hardening UWC floor.

A finite element model was developed that can be used to calculate the temperature distribution and determine the strength development and the resulting crack pattern and development over time in UWC floors. This FE-model is set up as a tension bar. The most conservative crack width results are obtained by setting the degree of restraint of the boundary conditions to zero (no restraint) in the heating phase and to one in the cooling phase (full restraint). This will lead to a "worst-case" scenario for crack development, leading to conservative crack width results. In the model, spatial variation in the Young's modulus and the FRC tensile behaviour is introduced by using random fields. Spatial variation in the FRC tensile behaviour or development over time can be introduced by making use of a FRC-factor, which scales the strength of all the points in the FRC tensile strength graph (in the y-direction).

The use of random fields leads to different crack results every time the FE-model is evaluated. The consideration of multiple analyses (samples) confirmed the expectation that FRC can show two types of behaviour: a single localised crack, which is associated with tensile softening behaviour or a distributed crack pattern resulting from tension hardening behaviour in FRC. Tension hardening is defined as such that the tensile strength increases after cracking. However, a combination of softening and hardening in the shape of a drop and a rise after cracking (dip) can also result in a distributed crack pattern. The distinction between a distributed crack pattern and a single localised crack is important because a single localised crack will have a crack width approximately equal to the magnitude of the shrinkage, whereas a distributed crack pattern will divide this over multiple cracks, leading to smaller maximum crack widths. The larger cracks can become water leaking when they grow into separation cracks, which leads to the next question.

- **How is the failure of the SFRUWC floor defined when looking at thermal shrinkage cracking?**

When looking at the entire building pit and considering the scope of this thesis, the main criterion for failure is the amount of leakage through separation cracks in the SFRUWC floor. Separation cracks will only cause leakage when the crack widths exceed a certain criterion. This maximum allowable crack width to prevent leaking can be determined by taking the self-healing capacity of the concrete into account. By taking this mechanism into account, the maximum allowed leakage can be translated into a maximum crack width criterion. When considering only cracking, a failure limit state can be defined in which the maximum occurring crack width should be smaller than the maximum allowable crack width. In practice, the Lohmeyer diagram is used to determine this value. Assuming a hydraulic head of 10 m, this will lead to a maximum allowable crack width of 0.10 mm. This value decreases for deeper building pits.

As mentioned in the previous question, it is only possible to satisfy the maximum allowable crack width criterion when the results show a distributed crack pattern. Therefore, the failure definition can also be expanded to include the crack pattern that occurs. The limit state will then be satisfied when there is a distributed crack pattern and the individual crack widths are smaller than the maximum allowable crack width.

- **What is a suitable probabilistic method that takes the uncertainties of SFRUWC floor construction into account and is compatible with FEA?**

First of all, random fields are a great tool to model uncertainty in this type of construction. Moreover, it is an essential aspect of the tensile bar FE-model. It was observed that multiple samples have to be evaluated before conclusions can be drawn about which crack pattern will occur with what certainty. Although random fields proved to be a very useful tool to model uncertainty, the standard deviation

of these fields (FRC-factor) was found to be a very dominant input parameter that heavily influences the crack width results. In order to obtain samples that show a distributed crack pattern, a standard deviation lower than approximately 10% has to be used, which is lower than the values prescribed in the guidelines.

While random fields provide a valuable means to incorporate stochastic variation in parameters that possess a spatially stochastic nature, their utilisation presents a substantial challenge in implementing advanced and faster Monte Carlo algorithms. The computation times of a complex FEA analysis in combination with a probabilistic analysis still remain the main obstacle. A regular Monte Carlo approach is possible but this excludes the benefits of possible faster calculations that other algorithms can provide by requiring fewer samples. Besides that, regular Monte Carlo is the most straightforward algorithm. Especially when a problem with a complex structural behaviour is considered, this transparency is crucial to investigate the differences between individual results and why a model produces certain results. In the end, a probabilistic method must be able to calculate the failure probability of a particular design, but it is equally important to obtain insight into the behaviour of the structure to understand why it is failing or not. It is essential to look at individual samples and have control over the steps of the probabilistic analysis.

- **What are appropriate stochastic definitions for the input parameters, and which of these parameters influence the results the most?**

The stochastic definitions of the input parameters are very important when including uncertainty in the model. It was observed that the random field properties, such as the standard deviation and correlation, greatly influence the crack width results but these properties are still quite ambiguous. Additional input parameters are introduced by including random fields in the model, which adds to the model uncertainty. Moreover, values obtained from the literature span a significant range. The stochastic properties of specific material properties such as the tensile strength and Young's modulus can be obtained or deduced from building codes. Especially the recommended standard deviation seems relatively high (>20%) when using it in this FE model. For the model in this thesis, lower standard deviations (<10%) are required to obtain distributed crack patterns. The reason for this lies in the simplifications and assumptions of the FE-model that was used.

The influence of three categories of input parameters was investigated: random field properties, material properties and thermal properties. As discussed in the conclusion to the previous question, the influence of the standard deviation of the random field or other properties that influence the standard deviation is significant. A possible explanation is that the standard deviation influences the magnitude of the absolute minimum (weak spot) in a random field that describes the tensile strength. The lower this minimum, the less resistance against cracking, which will result in larger crack widths and more samples that show a single localised crack.

From the material properties, the FRC tensile behaviour significantly influences the crack width results. It was observed that a drop after reaching the tensile strength, followed by a small rise (the drop and rise is defined as a "dip") in the FRC material graph positively influences the crack width results. The suspected reason for this is the introduction of a small hardening branch when a dip in the tensile behaviour of FRC is used. Against expectations from the literature, the thermal input parameters only had little effect on the maximum crack widths for the set of structural input parameters that was considered in this thesis. However, the thermal properties do heavily influence the total potential restrained shrinkage in the slab, but it was observed that a larger potential shrinkage results in more cracks, but not necessarily in larger crack widths.

- **How can the failure probability of a particular design be determined?**

Three analyses were performed in which all the relevant parameters were made stochastic simultaneously so that a proper Monte Carlo analysis could be performed. However, it was found that the most influential input parameters, which were discussed in the answer to the previous question, completely

dictate the crack width results. This results in the outcome that determining the exact failure probability with this FE-model is not meaningful from a scientific standpoint. Moreover, the simplification of the boundary conditions and assumptions regarding the stochastic parameters result in a very conservative model. It can only be concluded that an improved FE-model is required before possible realistic failure probabilities can be determined. This will be included in the recommendations.

Main research question

- **How can the failure probability of a SFRUWC floor subjected to thermal shrinkage cracking be determined, and which factors influence this failure probability?**

The restrained thermal deformations, tensile strength development, and boundary conditions are the most important factors in modelling the structural behaviour of a young hardening steel fibre-reinforced underwater concrete floor. A tension bar finite element model which uses random fields to model spatially stochastic material properties was developed. This FE-model is able to determine the aforementioned most important factors and the corresponding crack pattern and widths. To calculate the failure probability, a limit state has to be set up. Failure of a SFRUWC floor subjected to thermal shrinkage cracking is defined by leakage through separation cracks, which can be translated into a maximum allowable crack width criterion.

To include uncertainties in SFRUWC floors, a suitable probabilistic method is required that is compatible with finite element analysis. Random fields are a useful tool for this but introduce additional model input parameters and uncertainties. The stochastic definitions of input parameters significantly influence the crack width results, with the standard deviation of the random field properties and a dip in the FRC tensile behaviour being the most influential input parameters. Thermal properties have a limited impact on crack widths (for the considered structural parameters) but they do have an impact on the number of cracks that may occur.

Determining the exact failure probability using the current FE-model is not scientifically meaningful because the model assumptions lead to very conservative results. This emphasises the importance of improving the FE-model to incorporate realistic boundary conditions and additional concepts such as relaxation in order to obtain an accurate estimate of the failure probability. Nevertheless, the current FE-model and approach provide valuable insights into the impact of the input parameters and it is able to identify the most influential factors. The results of this thesis may serve as a basis for future advancements and refinements in determining the failure probability of a SFRUWC floor subjected to thermal shrinkage cracking.

Follow up questions

- **How can shrinkage cracks be limited or mitigated, and what are the most important input parameters for mitigation?**

The main parameters that can limit the crack width are identified by looking at the influences that were considered in this thesis. The random field properties are considered to be more like model properties than material properties, meaning that these are unlikely to be varied in different designs. The properties that can be adjusted in a design are the material and thermal properties, of which the material properties are the most impactful, but adjusting the thermal properties is the most obvious. This is because these properties can be influenced by keeping the concrete cool by applying curing methods and using cement with a low hydration heat, which are relatively easy solutions. A practical solution is to induce an artificial flow in the building pit, which increases the cooling capacity and the thermal boundary coefficient at the top of the floor, meaning that heat can be dissipated more quickly and the floor will expand and shrink less. While these are the most straightforward solutions, it was

concluded that the thermal properties only influence the number of cracks but have a minor impact on the crack width.

The most influential parameters are the material input parameters, but contradictory to expectations, the results from this thesis did not show that higher fibre strength and better concrete quality drastically decrease crack widths. This can be because of the limited number of combinations with the considered parameters, but another possible cause can be that the slab is subjected to (almost) pure tension, which is a very extreme case for determining crack widths. The dip in the FRC tensile behaviour does have a large influence on the crack width results but this is not a parameter that can easily be varied in designing a FRC mixture. Moreover, it can be argued whether it is realistic to have a part of the diagram show tension hardening.

7

Recommendations

The recommendations are divided into the following sections: extension of this research, additional research and recommendations for the CROW committee. The section ”extension of this research” describes the most important points that should be considered if this topic is continued in future research. The section ”additional research” describes the knowledge gaps that could not be answered or because of a lack of experimental data. It also describes critical assumptions that would be useful to verify with experimental data to check whether these assumptions are valid for the topic of shrinkage cracking in UWC floors. Finally, the section ”Crow committee” describes the recommendations on how the info and conclusions from this thesis can be used in the development of the new guidelines for permanent SFRUWC floors.

Extension of this research

The research in this thesis assumed two ”extreme” boundary conditions from which the most conservative one was used to obtain the results. During the research, it turned out that the boundary conditions caused by the horizontal resistance of the anchors in the building pit are more important for the crack width results than the boundary conditions at the edges. These were not modelled in this thesis. It is necessary to look at the influence of boundary conditions that are more realistic and less theoretical. When looking at the results from chapter 5.6, none of the analyses provided crack widths in the range of 0.1 mm, which would be a realistic maximum allowable crack width criterion. It is expected that when a spring is modelled during the heating phase instead of a fully free boundary condition, these maximum crack widths can be achieved in the model. To properly model the boundary conditions, the interaction between the UWC floor and the surrounding soil and sheet piles must also be modelled.

Crack width mitigation is an aspect that must be addressed during the entire service life of a UWC floor. However, this thesis focuses on crack formation during the hardening process caused by thermal shrinkage. Therefore only the first two weeks after casting are considered in which no external loading was present. When external loading is introduced, this can lead to a compression zone in a part of the slab, which would be beneficial for crack width limitation, but it must be verified if crack widths do not grow when introducing external loading. Besides this, the seasonal changes during the service life will introduce additional thermal deformations after the hardening phase. From practice, it is known that UWC floors can still crack years after casting. This could be investigated with a prescribed temperature development in a FE-model.

This research was purely focused on shrinkage cracking in the concrete slab, but the connections to the surrounding sheet piles are an important factor in preventing leakage in practice. Additional research

is necessary on what the bonding capacity with the sheet piles is, and how this can be modelled in an extended FE-model.

Regarding the material assumptions, relaxation and autogenous and drying shrinkage are important aspects for calculating restrained deformations in young hardening concrete, which should be included in future improvements of the model. Autogenous and drying shrinkage may worsen the crack width results, while relaxation can be a mitigating factor. It will have to be investigated if the combined result of these phenomena would be beneficial or disadvantageous for the maximum occurring crack widths.

A 2D plane stress FE-model was used in this thesis to model a 3D construction. This thesis only considered cracks with a certain width (in the longitudinal direction), but with an infinite length (in the transversal direction). Normally these cracks are surrounded by concrete in multiple directions, and the length will not be infinite. It is expected that taking this into account by using a 3D model will result in additional resistance against cracking. This effect will have to be investigated. Also, it has to be investigated whether the stochastic properties need to be corrected for the simplification to a 1D random field from a 3D reality.

Additional research

Despite extensive literature research, it seems that there is not a lot of experimental data available regarding the stochastic properties of FRC, such as the standard deviation. These input parameters can be obtained/deduced from standards by looking at the tensile strength variation in regular concrete, but experimental data regarding FRC is generally lacking. For future research, it would be a good addition to contact concrete companies to ask for data regarding FRC, so assumptions about the standard deviation can be validated. Fib has recently started a database with FRC properties, but this database is not very extensive yet. This also holds for the correlation within one concrete specimen.

The crack width criterion in this thesis is based on the Lohmeyer diagram, which determines until what crack width self-healing is possible. The research on which these graphs are based was performed under laboratory conditions (van Breugel, 2020). It would be of added value to do experimental research on the self-healing capacity of SFRUWC floors under representative conditions. It could then be concluded if the self-healing criterion is a valid criterion to use or if it might be too optimistic.

Weak spots can be introduced in FRC due to an uneven fibre distribution caused by the casting process. This might potentially be a risk for UWC floor applications since the concrete is usually poured through a long pipe which can align or unevenly distribute the fibres in the concrete, which is undesired. Research on how the fibre distribution / orientation can cause weak spots in a UWC floor would be very valuable.

The tensile characteristics of FRC are generally determined from the flexural residual strength that is obtained from bending tests. After which it is converted to residual tensile strength. This conversion uses a simplified constitutive relation. It would be good to also directly determine the residual tensile strength by performing pure tension tests to validate the FRC tensile behaviour that is used in this thesis. With these tests, the validity of the dip can also be investigated.

CROW Committee

- **How can the results from the probabilistic approach contribute to the development of guidelines regarding permanent SFRUWC structural floors?**

This thesis shows that uncertainties can be adequately modelled with random fields, but this does introduce additional input parameters. The effect that these different random field parameters have on the shape of the random fields is discussed. With the results presented in Appendix D, an informed choice can be made on what random field properties to use. I would suggest a random field with a

regular correlation function and mesh size which is twice the size of the FE-mesh. In my opinion, these settings are adequate, but the squared exponential function produces random fields with insufficient variation, which results in artificial (non-random) crack patterns. The influence of the standard deviation and correlation length will have to be evaluated. Covariance matrix decomposition in combination with the Cholesky method is the fastest method for large random fields, but for certain fields that use a squared exponential function, the Cholesky decomposition results in problems with setting up the lower triangular correlation matrix. The Eigen decomposition can be used as an alternative. Both decomposition methods will result from random fields with equal characteristics.

It was also concluded that it is necessary to consider multiple samples of one FEA because it cannot be anticipated if the model produces a single localised crack or a distributed crack pattern. A singular maximum crack width result from a model that uses random fields can be unreliable and may not show the whole picture. Either multiple samples will have to be performed for the variations in the sensitivity analysis or it has to be investigated a priori if the input parameter combinations of these variations will always lead to either a single crack or a distributed crack pattern.

Finally, this thesis has identified the most influential input parameters (under the assumption of the input parameters of the standard case), which are the standard deviation (correlation length also changes the standard deviation) and the FRC tensile behaviour, and especially the dip in this graph. These findings can be used to define the focus points in the work of the CROW committee and can be used to compare whether similar results regarding the most influential parameters are obtained.

References

Works Cited

ABT. (2016). Innovaties in keldervloeren: Niet stapelen maar integreren! https://www.abt-belgie.eu/blog/innovaties-in-keldervloeren-niet-stapelen-maar-integreren.aspx

ABT. (2018). Keldervloeren vergeleken: Duurzaamheid en kosten gaan hand in hand. https://www.abt.eu/actueel/blog/keldervloeren-vergeleken-duurzaamheid-en-kosten-gaan-hand-in-hand.aspx

Achenbach, M., Lahmer, T., & Morgenthal, G. (2017). Identification of the thermal properties of concrete for the temperature calculation of concrete slabs and columns subjected to a standard fire—methodology and proposal for simplified formulations. *Fire safety journal*, *87*, 80–86. https://doi.org/10.1016/j.firesaf.2016.12.003

ACI 544.1R-96. (2001). *Report on fiber reinforced concrete* (Standard). ACI.

Aniskin, N., & Nguyen, T.-C. (2019). Influence factors on the temperature field in a mass concrete. *E3S Web of Conferences*, *97*. https://doi.org/10.1051/e3sconf/20199705021

Arkesteijn, R. (2012). *Dimensionering van onderwaterbetonvloeren* (Master's thesis). Delft University of Technology. TU Delft Repository. http://resolver.tudelft.nl/uuid:894f9135-0edc-4a8d-9d0e-324b0adc5bf9

Arkesteijn, R., & Menting, M. (2013). Staalvezelversterkt onderwaterbeton. *Cement*. https://www.cementonline.nl/artikel/staalvezelversterkt-onderwaterbeton

Arregui-Mena, J. D., Margetts, L., & Mummery, P. M. (2016). Practical application of the stochastic finite element method. *Archives of computational methods in engineering*, *23*, 171–190. https://doi.org/10.1007/s11831-014-9139-3

Asadi, I., Shafigh, P., Hassan, Z. F. B. A., & Mahyuddin, N. B. (2018). Thermal conductivity of concrete–a review. *Journal of Building Engineering*, *20*, 81–93. https://doi.org/10.1016/j.jobe.2018.07.002

ASTM - C1074. (2004). *Standard practice for estimating concrete strength by the maturity method* (Standard). ASTM. https://www.astm.org/c1074-17.html

Balaguru, P. N., & Shah, S. P. (1992). *Fiber-reinforced cement composites*. McGraw-Hill, Inc.

Beghini, A., Bažant, Z. P., Zhou, Y., Gouirand, O., & Caner, F. C. (2007). Microplane model m5f for multiaxial behavior and fracture of fiber-reinforced concrete. *Journal of engineering mechanics*, *133*(1), 66–75. https://doi.org/10.1061/(ASCE)0733-9399(2007)133:1(66)

Benjamin, J. R., & Cornell, C. A. (2014). *Probability, statistics, and decision for civil engineers*. Dover publications. https://app.knovel.com/hotlink/toc/id:kpPSDCE00M/probability-statistics/probability-statistics

den Boef, E. M. (1996). *Scheurvorming in tunnelvloeren* (Master's thesis). Delft University of Technology. TU Delft Repository. http://resolver.tudelft.nl/uuid:5d45db8e-ad7a-44ce-bd35-c783386a3e2f

Bomhard, H. (1992). Concrete and environment - an introduction. *FIP symposium*, *Vol. 1*, p. 51–59.

Bouwmeester - van den Bos, J., & Galjaard, H. (2013). De praktijk van onderwaterbeton voor ontwerp, uitvoering en technologie. *Cement*. https://www.cementonline.nl/artikel/balanceren-voor-gevorderden

van Breugel, K. (2003). Self-healing en vloeistofdichtheid. *Cement*. https://www.cementonline.nl/artikel/self-healing-en-vloeistofdichtheid

van Breugel, K., Braam, C. R., van der Veen, C., & Walraven, J. C. (2016). *Concrete structures under imposed thermal and shrinkage deformations*.

van Breugel, K. (2020). Fluid tightness - transport mechanisms through concrete (chapter from lecture notes).

Charpin, J., Myers, T., Fitt, A., Fowkes, N., Ballim, Y., & Patini, A. (2004). Piped water cooling of concrete dams. *Proceedings of the Mathematics in Industry Study Group*, *Vol. 1*, pp. 69–85.

CROW-CUR Aanbeveling 111:2018. (2011). *Staalvezelbeton-bedrijfsvloeren op palen* (Standard). CROW-CUR. https://www.cur-aanbevelingen.nl/cur-aanbeveling-111

CUR Rapport 102. (1981). *Gewapend onderwaterbeton* (Standard). CUR.

CUR Rapport 2007-3. (2007). *Scheurgedrag en berekening van constructievloeren van gewapend beton* (Standard). CUR.

CUR rapport 245. (2012). *Staalvezelbeton kennis en kennisleemten* (Standard). CUR.

CUR rapport 246. (2012). *Staalvezelbeton inventarisatie van regelgeving* (Standard). CUR.

CUR-Aanbeveling 77:2014. (2014). *Rekenregels voor ongewapende onderwaterbetonvloeren* (Standard). net, SBR CUR. https://www.cur-aanbevelingen.nl/cur-aanbeveling-077

D'aloia, L., & Chanvillard, G. (2002). Determining the "apparent" activation energy of concrete: Ea—numerical simulations of the heat of hydration of cement. *Cement and Concrete Research*, *32*(8), 1277–1289. https://doi.org/10.1016/S0008-8846(02)00791-3

Deák, I. (1980). Three digit accurate multiple normal probabilities. *Numerische Mathematik*, *35*(4), 369–380. https://doi.org/10.1007/BF01399006

Deltares. (2021). *Probabilistic toolkit user manual* (Vol. Version 2.0). https://www.deltares.nl/nl/software/probabilistic-toolkit-ptk-2/

DIANA FEA. (2022). Diana documentation - release 10.5. https://manuals.dianafea.com/d105/Diana.html

Ditlevsen, O., Bjerager, P., Olesen, R., & Hasofer, A. M. (1988). Directional simulation in gaussian processes. *Probabilistic Engineering Mechanics*, *3*(4), 207–217. https://doi.org/10.1016/0266-8920(88)90013-6

Evangeliou, P. (2016). *Probabilistic nonlinear finite element analysis of reinforced concrete beams without shear reinforcement* (Master's thesis). Delft University of Technology. TU Delft Repository. http://resolver.tudelft.nl/uuid:366ddd80-6da2-4c3c-9fec-4b05b06e357b

fib Bulletin 105. (2022). *Fib bulletin 105 - fibre reinforced concrete* (Standard). fib. https://doi.org/10.35789/fib.BULL.0105

Fu, C. Q., Ma, Q. Y., Jin, X. Y., Shah, A. A., & Tian, Y. (2014). Fracture property of steel fiber reinforced concrete at early age. *Computers and Concrete*, *13*(1), 31–47. https://doi.org/10.12989/cac.2014.13.1.031

Girolami, M., Febrianto, E., Yin, G., & Cirak, F. (2021). The statistical finite element method (statfem) for coherent synthesis of observation data and model predictions. *Computer Methods in Applied Mechanics and Engineering*, *375*, 113533. https://doi.org/10.1016/j.cma.2020.113533

Guo, L., Guo, L., Zhong, L., & Zhu, Y. (2011). Thermal conductivity and heat transfer coefficient of concrete. *Journal of Wuhan University of Technology-Mater. Sci. Ed.*, *26*(4), 791–796. https://doi.org/10.1007/s11595-011-0312-3

Haldar, A., & Mahadevan, S. (2000). *Reliability assessment using stochastic finite element analysis*. John Wiley & Sons.

van der Have, R. (2015). *Random fields for non-linear finite element analysis of reinforced concrete* (Master's thesis). Delft University of Technology. TU Delft Repository. http://resolver.tudelft.nl/uuid:25780e9a-49c4-4085-9a65-af73119d97a7

Hendriks, M. A. N., & Roosen, M. A. (2022). *Guidelines for nonlinear finite element analysis of concrete structures* (Report RTD 1016-1:2022). Rijkswaterstaat Centre for Infrastructure. https://standaarden.rws.nl/link/standaard/1335

JCSS. (2001). *Probabilistic model code, part 3, resistance models* (Report). Joint Committee on Structural Safety. https://www.jcss-lc.org/jcss-probabilistic-model-code/

Jonkman, S. N., Steenbergen, R. D. J. M., Morales-Nápoles, O., Vrouwenvelder, A. C. W. M., & Vrijling, J. K. (2017). *Probabilistic design: Risk and reliability analysis in civil engineering (lecture notes)*. Delft University of Technology.

Kada-Benameur, H., Wirquin, E., & Duthoit, B. (2000). Determination of apparent activation energy of concrete by isothermal calorimetry. *Cement and concrete research*, *30*(2), 301–305. https://doi.org/10.1016/S0008-8846(99)00250-1

Katsuki, S., & Frangopol, D. M. (1994). Hyperspace division method for structural reliability. *Journal of Engineering Mechanics*, *120*(11), 2405–2427. https://doi.org/10.1061/(ASCE)0733-9399(1994)120:11(2405)

Kim, K.-H., Jeon, S.-E., Kim, J.-K., & Yang, S. (2003). An experimental study on thermal conductivity of concrete. *Cement and concrete research*, *33*(3), 363–371. https://doi.org/10.1016/S0008-8846(02)00965-1

Lee, Y., Choi, M.-S., Yi, S.-T., & Kim, J.-K. (2009). Experimental study on the convective heat transfer coefficient of early-age concrete. *Cement and Concrete Composites*, *31*(1), 60–71. https://doi.org/10.1016/j.cemconcomp.2008.09.009

Ma, Y., Zhang, Y., Hu, Z., Yu, Z., Huang, Y., & Zhang, C. (2019). Experimental study of the heat transfer by water in rough fractures and the effect of fracture surface roughness on the heat transfer characteristics. *Geothermics*, *81*, 235–242. https://doi.org/10.1016/j.geothermics.2019.05.009

MC 1990. (1990). *Ceb-fip model code 1990* (Standard). fib.

MC 2010. (2010). *Model code 2010 - first complete draft, volume 1* (Standard). fib. https://doi.org/10.35789/fib.BULL.0055

van der Meer, L. J. (2022). CROW werkgroep staalvezel onderwaterbeton SG4 - uitgangspunten EEM studie krimpscheurmodel V4. *(Internal document)*.

Meijdam, J., Gereveling de Vos, M., & Ramkema, A. (2017). Ronde owb-vloer met staalvezels. *Cement*. https://www.cementonline.nl/ronde-owb-vloer-met-staalvezels

Melchers, R. E., & Beck, A. T. (2018). *Structural reliability analysis and prediction*. John wiley & sons. https://doi.org/10.1002/9781119266105

NEN-EN 14651. (2007). *Beproevingsmethode voor staalvezelbeton - meten van de buig-treksterkte (proportionaliteitsgrens (lop), reststerkte)* (Standard NEN-EN 14651:2005+A1:2007 en). NEN. https://www.nen.nl/nen-en-14651-2005-a1-2007-en-120650

NEN-EN 1992-1-1+C2. (2011). *Eurocode 2: Design of concrete structures – part 1-1: General rules and rules for buildings* (Standard NEN-EN 1992-1-1+C2). NEN. https://www.nen.nl/nen-en-1992-1-1-c2-2011-nl-159356

Nielsen, C. V., & Kaasgaard, M. (2020). Activation energy for the concrete maturity model–part 1: Compressive strength tests at different curing temperatures. *Nordic Concrete Research*, *62*(1), 87–106. https://doi.org/10.2478/ncr-2020-0002

Poole, J. L., Riding, K. A., Folliard, K. J., Juenger, M. C., & Schindler, A. K. (2007). Methods for calculating activation energy for portland cement. *ACI Materials Journal*, *104*(1), 303–311. https://doi.org/10.14359/18499

ROK 1.4. (2017). *Richtlijnen ontwerp kunstwerken 1.4* (Standard). Rijkswaterstaat. https://standaarden.rws.nl/link/standaard/991

Roy, A. (2019). *Efficient reliability analysis of concrete structures on the basis of non-linear finite element analysis under numerical noise* (Doctoral dissertation). Delft University of Technology. https://doi.org/10.4233/uuid:389bbb4d-141d-425f-bc0f-b7e37918720c

Soetens, T., & Matthys, S. (2014). Different methods to model the post-cracking behaviour of hooked-end steel fibre reinforced concrete. *Construction and Building Materials*, *73*, 458–471. https://doi.org/10.1016/j.conbuildmat.2014.09.093

Stefanou, G. (2009). The stochastic finite element method: Past, present and future. *Computer methods in applied mechanics and engineering*, *198*(9-12), 1031–1051. https://doi.org/10.1016/j.cma.2008.11.007

van Tilburg, S., Arkesteijn, R., & Wagner, C. (2021). Grensverleggende parkeergarage. *Cement*. https://www.cementonline.nl/grensverleggende-parkeergarage

Torrenti, J. M., Pijaudier-Cabot, G., & Reynouard, J. M. (2013). *Mechanical behavior of concrete*. John Wiley & Sons. https://doi.org/10.1002/9781118557587

Tsukamoto, M., & Wörner, J. (1991). Permeability of cracked fibre-reinforced concrete. *Darmstadt Concrete - Annual Journal on concrete and concrete structures*, *6*, 123–135.

Waarts, P. H. (2000). *Structural reliability using finite element analysis - an appraisel of dars: Directional adaptive response surface sampling* (Doctoral dissertation). Delft University of Technology. TU Delft Repository. http://resolver.tudelft.nl/uuid:6e6d9a76-fd12-4220-9dc1-36515b3f638d

van der Woerdt, W. H. (2010). *Crack formation in structural slabs on underwater concrete* (Master's thesis). Delft University of Technology. http://resolver.tudelft.nl/uuid:0e77748e-5fab-47df-a433-ed76ddffaa4e

van der Woerdt, W., & Bouwmeester - van den Bos, J. (2011). Constructievloeren op onderwaterbeton. *Cement*. https://www.cementonline.nl/artikel/constructievloeren-op-onderwaterbeton

Yang, J.-K., Lee, Y., & Kim, J.-K. (2011). Heat transfer coefficient in flow convection of pipe-cooling system in massive concrete. *Journal of Advanced Concrete Technology*, *9*(1), 103–114. https://doi.org/10.3151/jact.9.103

Ye, G. (2020). Portland cement. *Concrete science and technology - Lecture slides*, Delft University of Technology.

Works Consulted

ACI 544.4R-18. (2018). *Guide to design with fiber-reinforced concrete* (Standard). ACI.

Arkesteijn, R. (2014). Rekenen aan onderwaterbeton met vezels. *Cement*. https://www.cementonline.nl/artikel/rekenen-aan-onderwaterbeton-met-vezels

Bentur, A., & Mindess, S. (2007). *Fibre reinforced cementitious composites* (2nd Edition). Taylor & Francis.

Braam, R., van der Veen, C., & de Boer, A. (2013). Trekelementen in onderwaterbetonvloeren. *Cement*. https://www.cementonline.nl/artikel/trekelementen-in-onderwaterbetonvloeren

Carino, N. J., & Lew, H. S. (2001). The maturity method: From theory to application. In *Structures 2001: A structural engineering odyssey* (pp. 1–19). https://doi.org/10.1061/40558(2001)17

CUR-Aanbeveling 36:2011. (2011). *Ontwerpen van elastisch ondersteunde betonvloeren en -verhardingen* (Standard). CUR. https://www.cur-aanbevelingen.nl/cur-aanbeveling-36

Józsa, Z., & Fenyvesi, O. (2010). Early age shrinkage cracking of fibre reinforced concrete. *Concrete structures*, *11*, 61–66. https://www.researchgate.net/publication/265541910

Naaman, A. E. (2008). High performance fiber reinforced cement composites. In C. Shi & Y. L. Mo (Eds.), *High-performance construction materials* (pp. 91–153). World Scientific Publishing Co. Pte. Ltd. https://doi.org/10.1142/9789812797360_0003

Narin, F., & Wiklund, O. (2012). *Design of slabs-on-ground regarding shrinkage cracking* (Master's thesis). Chalmers University of Technology. Chalmers Open Digital Repository. https://hdl.handle.net/20.500.12380/165126

van Waarde, F., & Bolhuis, J. (2018). Onderwaterbeton na 72 uur belast. *Cement*. https://www.cementonline.nl/stationsgebied-driebergen-zeist-2

Wolsink, G., & Zeilmaker, A. (2003). Definitieve ongewapende onderwaterbetonvloeren i.c.m. definitieve damwanden. *Cement*. https://www.cementonline.nl/artikel/def-ongewapende-onderwaterbetonvloeren-icm-def-damwanden

A

Additional Images

This appendix includes supporting figures for the thesis. Figure A.1 shows the tensile stress and strength development in the same graph for two locations. The centre of the slab and the top and bottom edges. It can be observed, when the stress becomes larger than the strength, cracking occurs. For the top and bottom boundaries, microcracking immediately starts from the beginning. In the centre of the slab, first compression develops due to the temperature differential over the heigth. When the cooling phase starts, the compressive stress reaches a maximum and starts to reduce before changing into a tensile stress. When the tensile strength is reached, immediately a large through crack is formed. In the graph that shows the top and bottom boundaries, it this moment can also be seen, when the crack width makes a sudden jump.

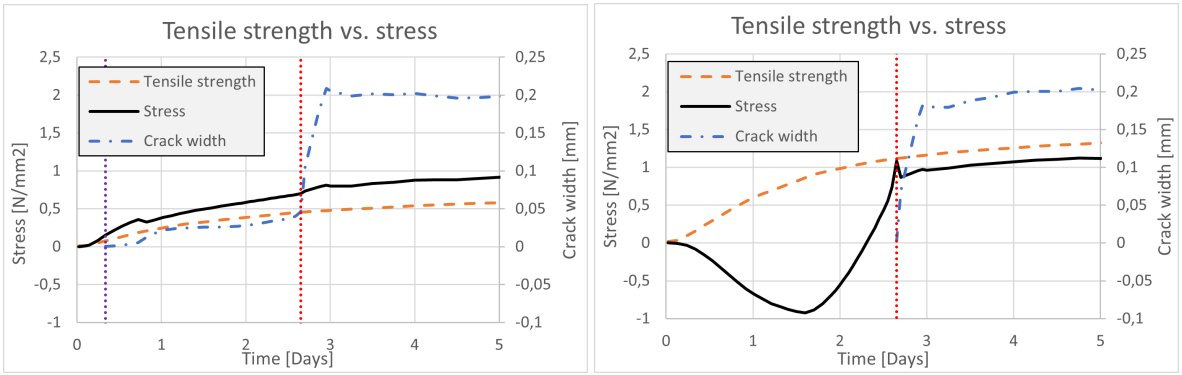

(a) Top and bottom boundaries

(b) Centre of the slab

Figure A.1: Stress vs strength development and the corresponding crack width. The moment where micro-cracking in the boundaries starts is indicated with the purple dotted line, the moment where the crack connects in the centre and a through crack is formed is indicated with the red dotted line.

Figure A.2 is an extension of Figure 3.3 that includes a linear component. A linear component can be present because the heat transfer coefficient at the top and bottom are unequal. In this case, the heat transfer coefficient at the top is 100 $\mathrm{W\,m^{-2}K^{-1}}$ and at the bottom it is 5 $\mathrm{W\,m^{-2}K^{-1}}$. When the linear component is restrained, this will result in bending, as was discussed in Section 3.4

Figure A.3 shows all through cracks formed in one sample of the standard case over time. It can be seen that more through cracks are initiated over time and all crack widths are stable at a given point. Generally, the first cracks will have the largest crack widths.

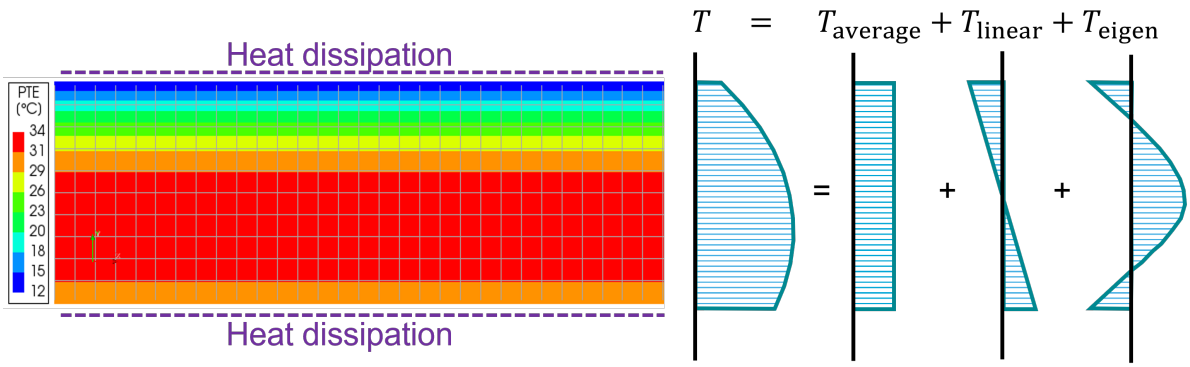

Figure A.2: Temperature distribution over the height of the slab where the dissipation is higher at the top edge than the bottom edge. The temperature can be divided into an average component, a linear component and the Eigen temperature.

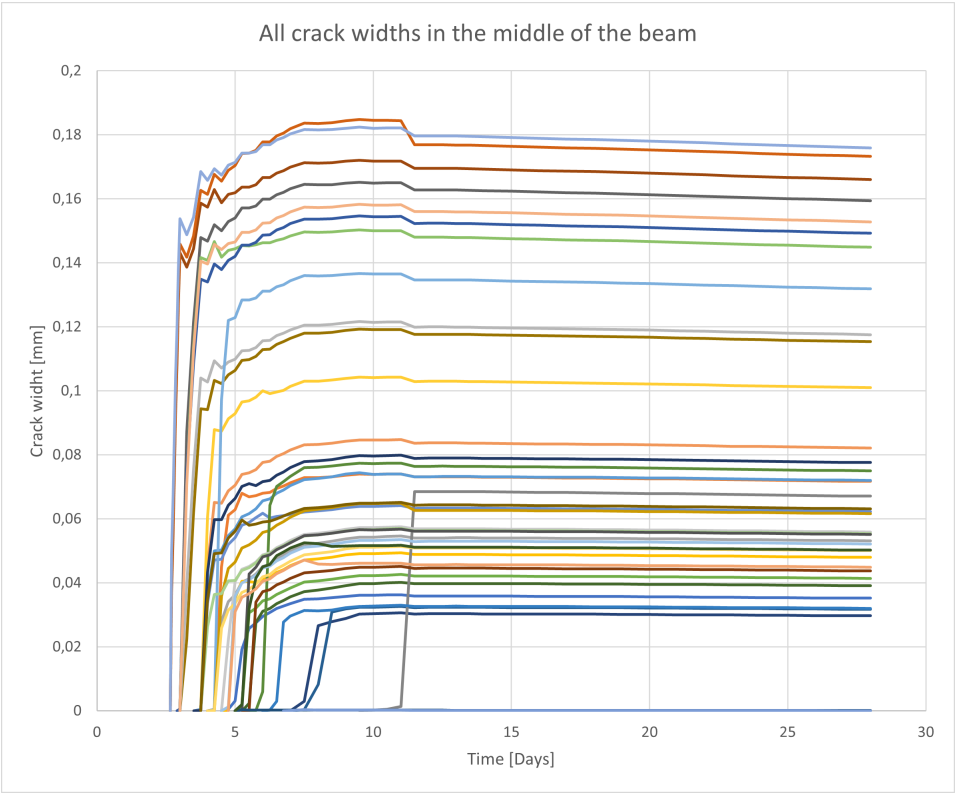

Figure A.3: Crack development in the centre of the slab over time for a model with a length of 25 meters where every line indicates a separate through crack.

Figure A.4 shows the different tensile behaviour models when the fibre classification is varied according to the model from the Model Code 2010.

Figure A.5 shows that tension softening behaviour might lead to either softening or hardening behaviour in bending. Whilst tension hardening behaviour will always lead to hardening behaviour in bending.

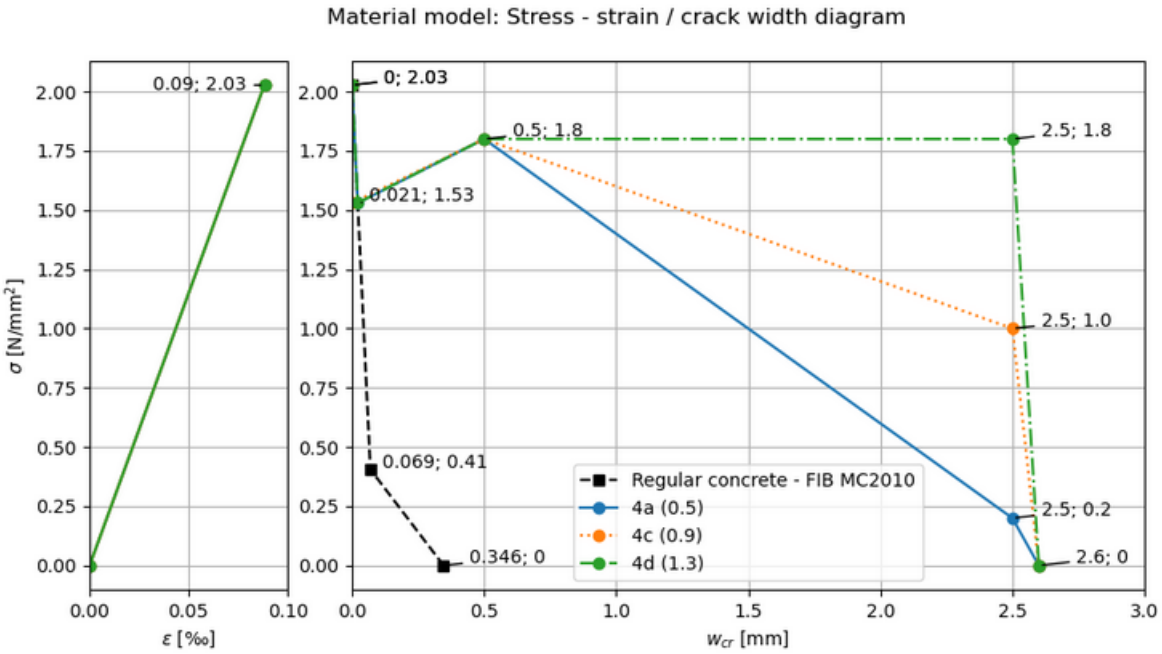

Figure A.4: Influence of different fibre classifications in combination with the characteristic tensile strength where $f_{R1k} = 5$ N/mm^2 and the ratio f_{R3k}/f_{R1k} is indicated with the number between brackets

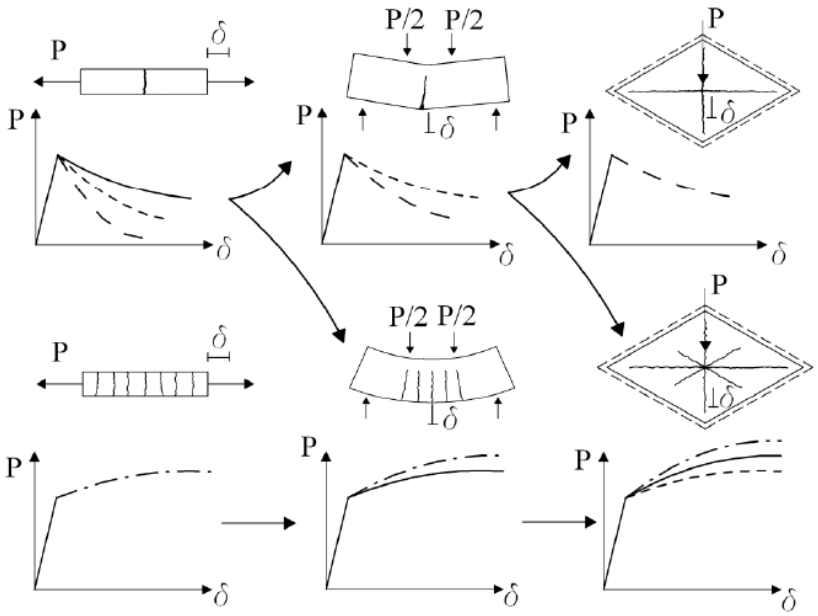

Figure A.5: Response of different FRC structures under axial tension or bending. In pure tension, either softening or hardening behaviour can be observed. Softening behaviour that occurs under axial tension may cause hardening behaviour in bending for the same FRC mixture. From MC 2010, 2010

B

Additional results

B.1. Single sample results

This appendix shows some examples of a crack width result of a single sample. The FRC-factor random field is displayed in the bottom panel of the figures, in which the locations of the cracks are indicated. The top panel of the figures display the actual magnitude of the crack width per crack. There is also an indication of the random field minimum and the location of the maximum crack width. The two minima that are used for the calculation of the weak spot ratios in section 5.5.1 are also indicated. Underneath the figures, data is provided about the number of cracks, the maximum crack width and the data of the realisation of the random field such as the minimum, maximum, mean and standard deviation.

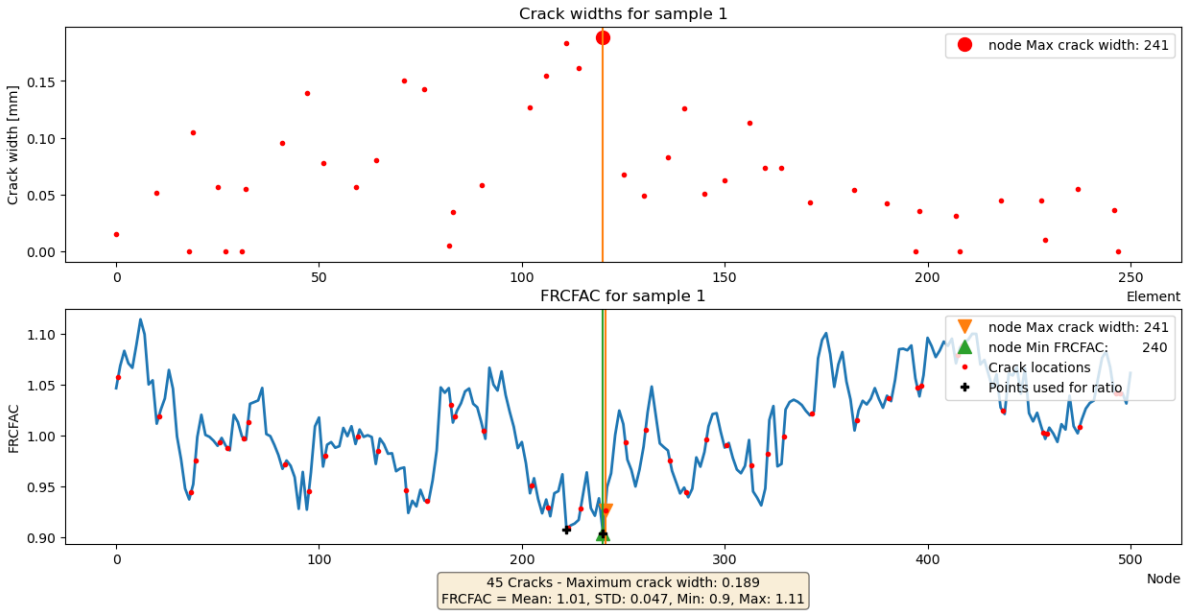

Figure B.1: Standard case with a distributed crack pattern

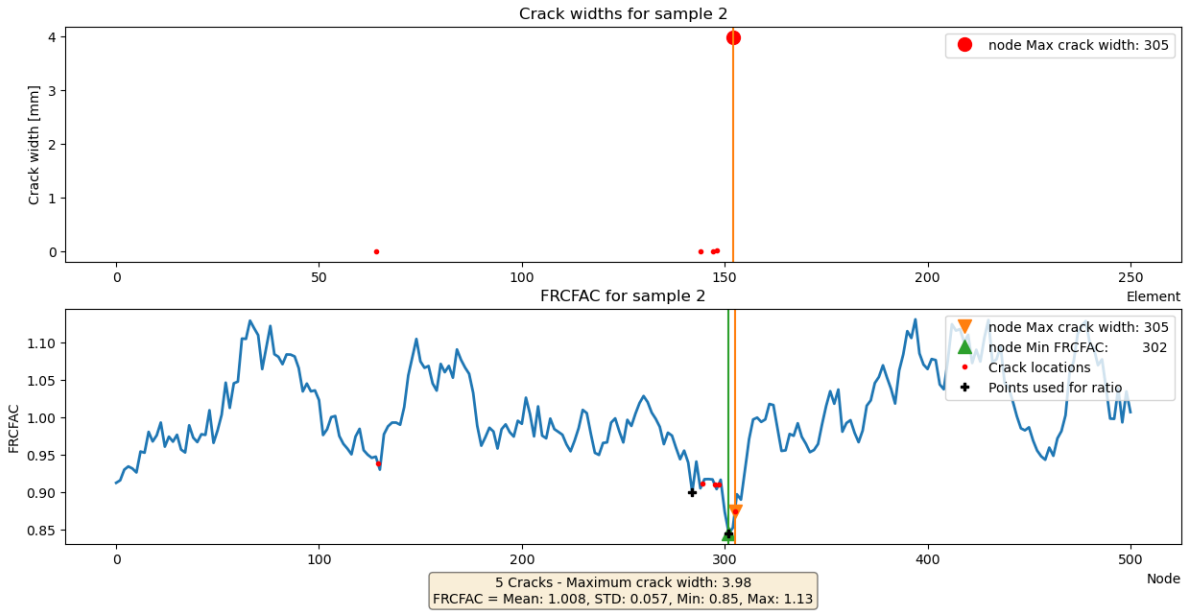

Figure B.2: Standard case with a single localised crack

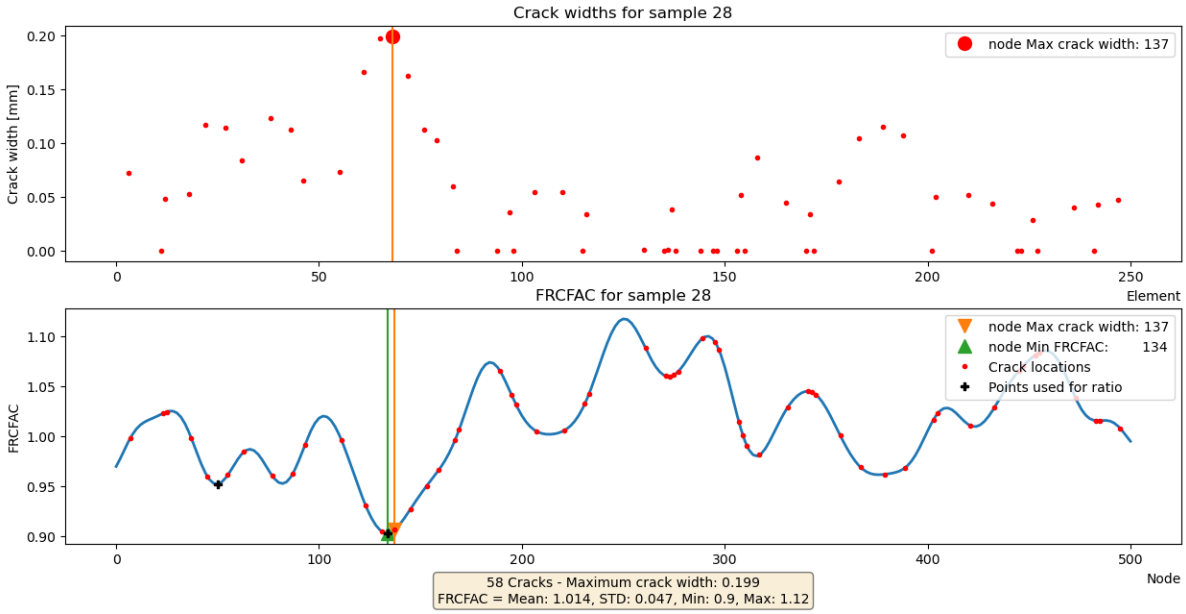

Figure B.3: Standard case with a squared exponential correlation function - distributed crack pattern

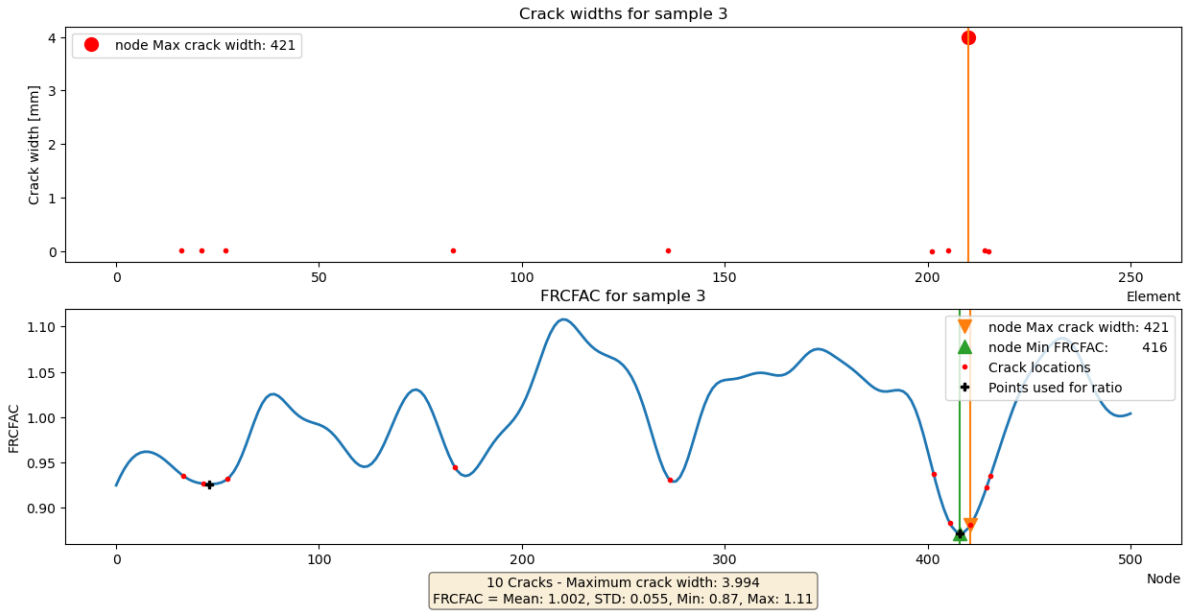

Figure B.4: Standard case with a squared exponential correlation function - single localised crack

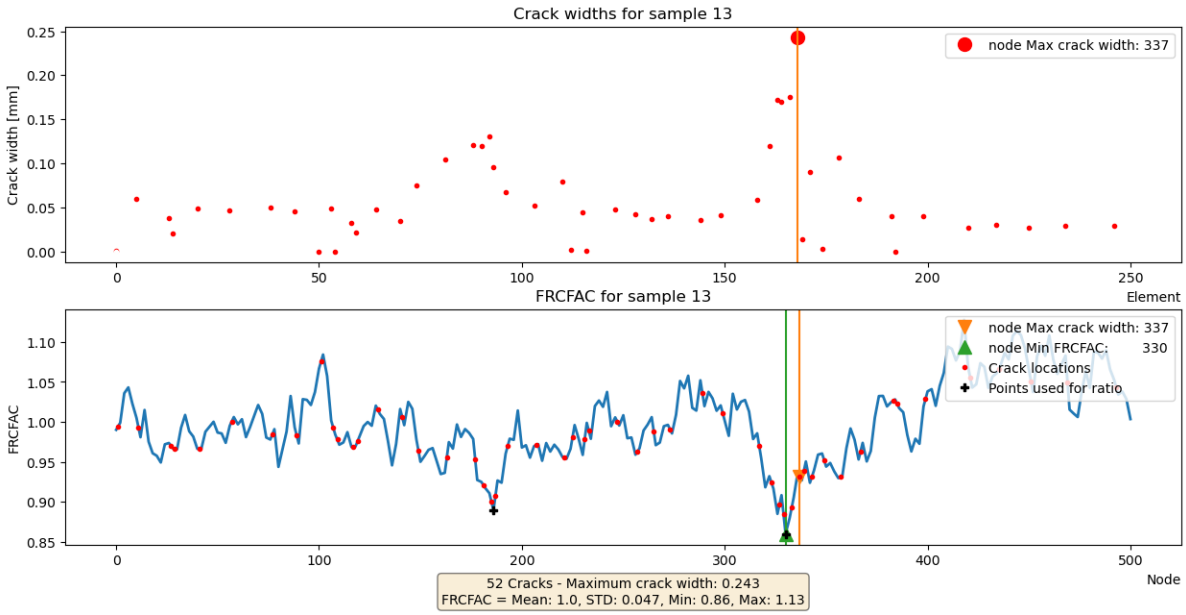

Figure B.5: Standard case with a 2D random field - distributed crack pattern. The random field in this picture is a slice from the centre of the beam at half the height.

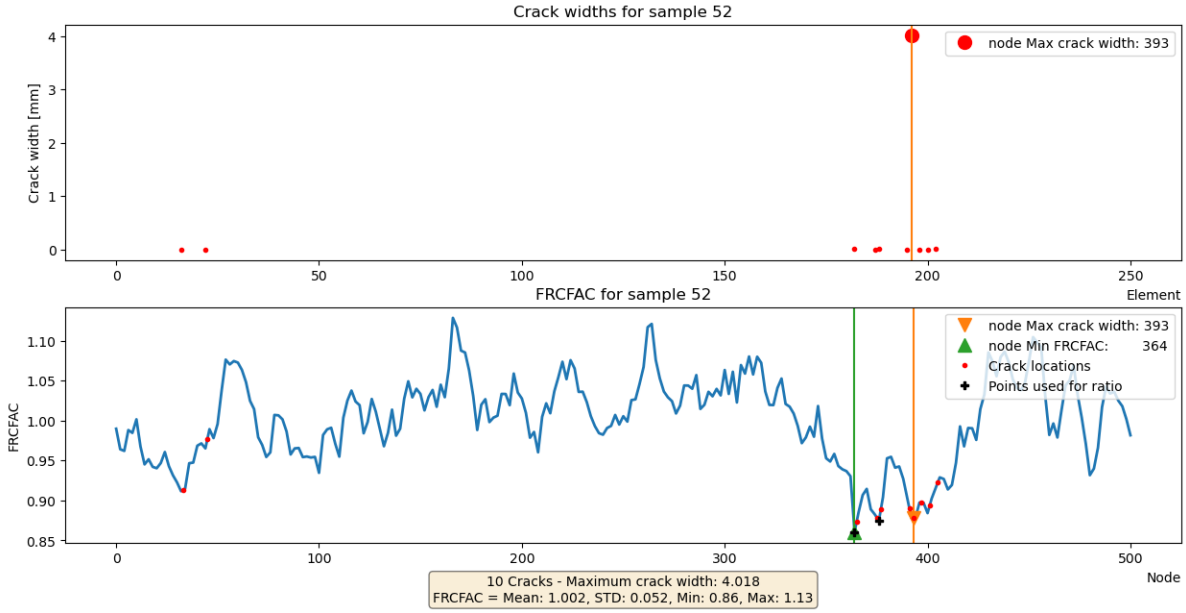

Figure B.6: Standard case with a 2D random field - single localised crack. The random field in this picture is a slice from the centre of the beam at half the height.

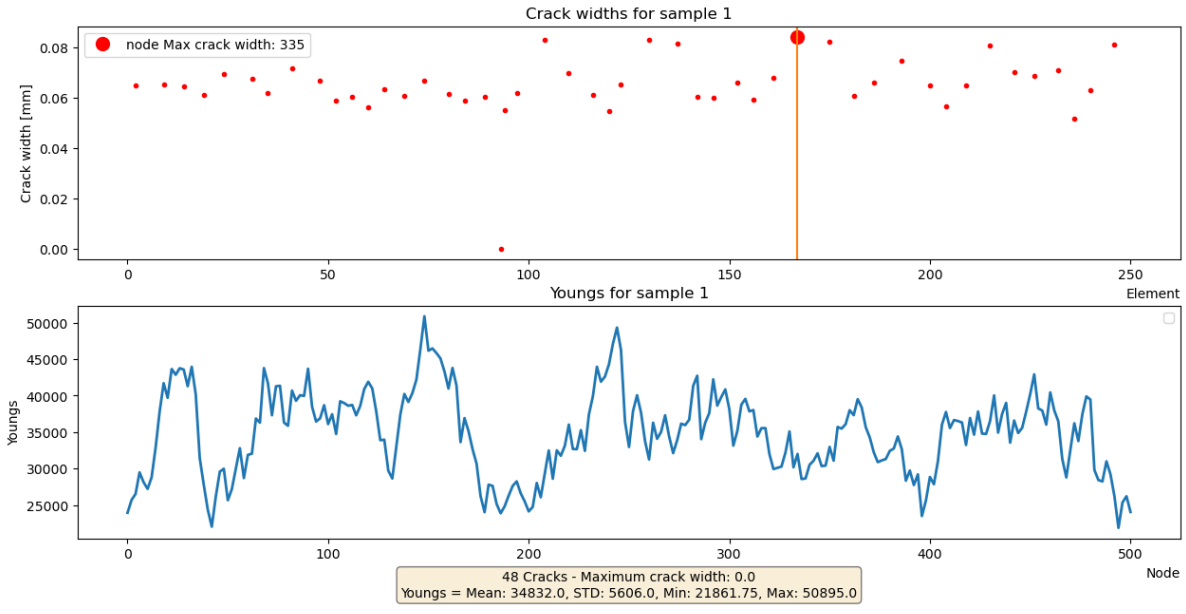

Figure B.7: Model where only the Young's modulus is modelled with a random field

B.2. Supporting results

Figure B.8 shows a crack pattern for a sample where $T_{\text{external}} > T_0$. This figure shows micro-cracking in the centre of the beam. This phenomenon is explained in section 5.5.3.

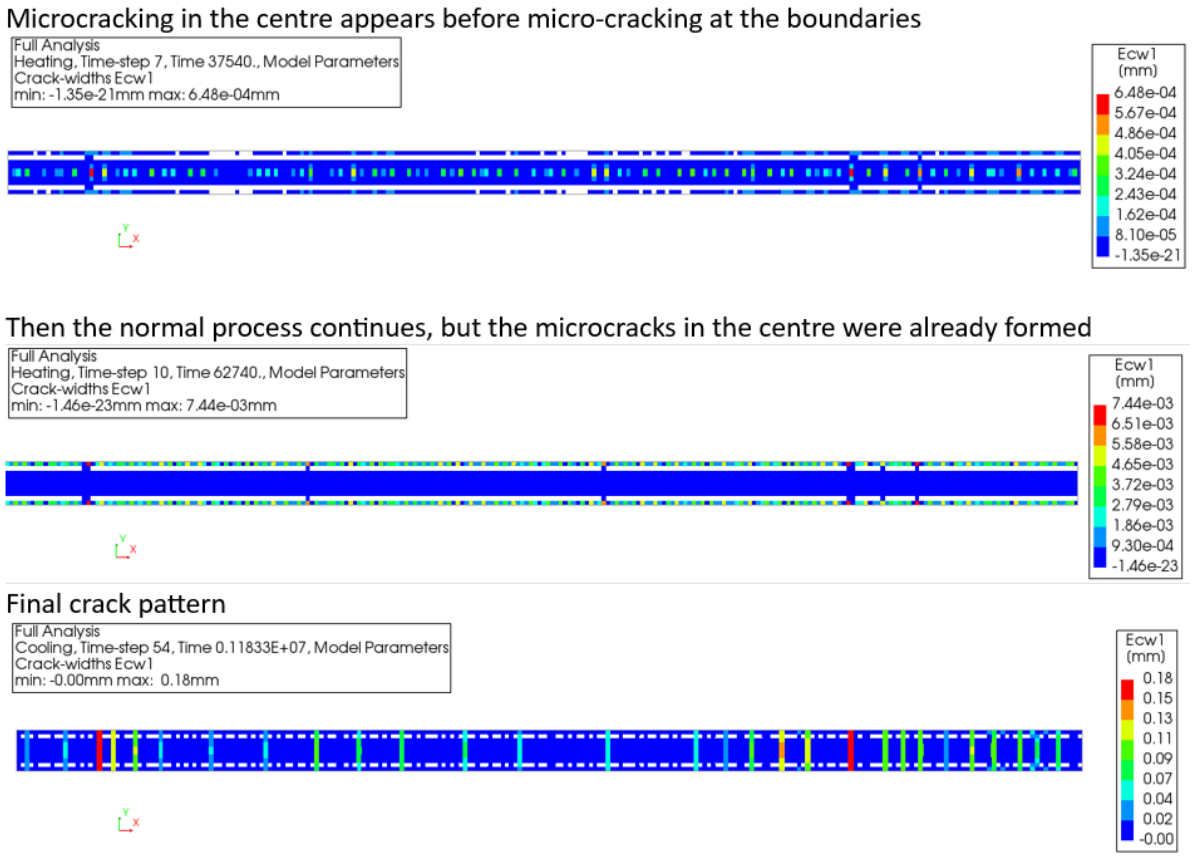

Figure B.8: Resulting crack pattern when the final temperature is higher than the initial temperature

B.3. 2D random field and crack widths

The next page shows the development of the FRC-factor in a 2D random field over time. The first panel shows the input random field. The following 5 panels show the development of the random field with a fixed scale. On the page after this, the crack development corresponding to this random field is displayed.

Random field development and corresponding crack width development of the standard case with a 2D random field

Input random field FRCFAC

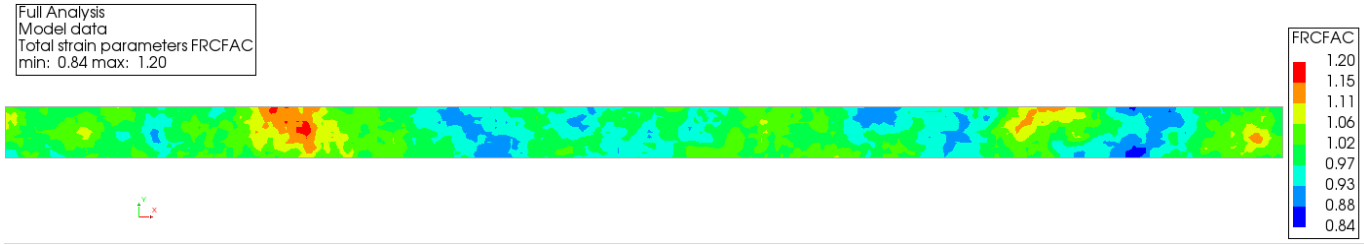

Random field FRCFAC step 1

Random field FRCFAC at transition heating/cooling phase - T_{max}

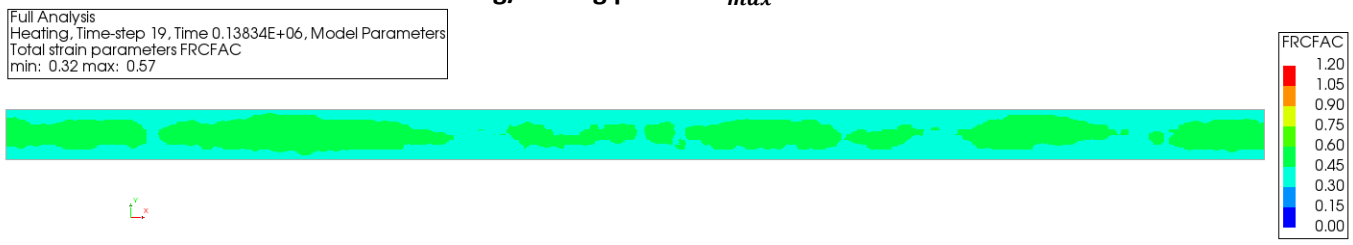

Random field FRCFAC cooling phase step 40

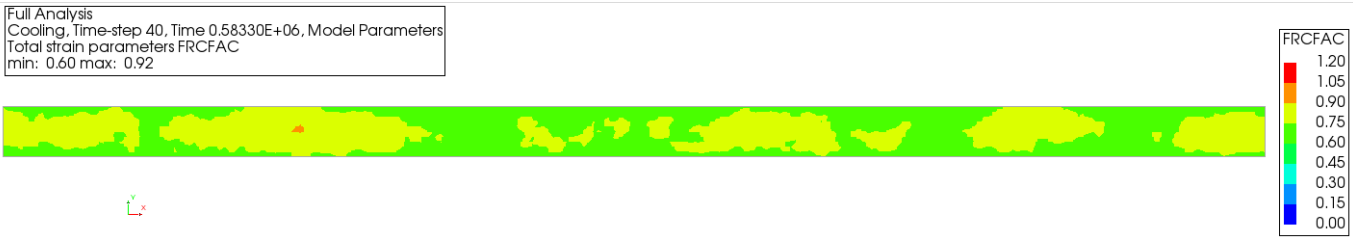

Random field FRCFAC cooling phase step 55 (2 weeks)

Random field FRCFAC at degree of reaction = 1

Crack width heating phase – first micro cracks

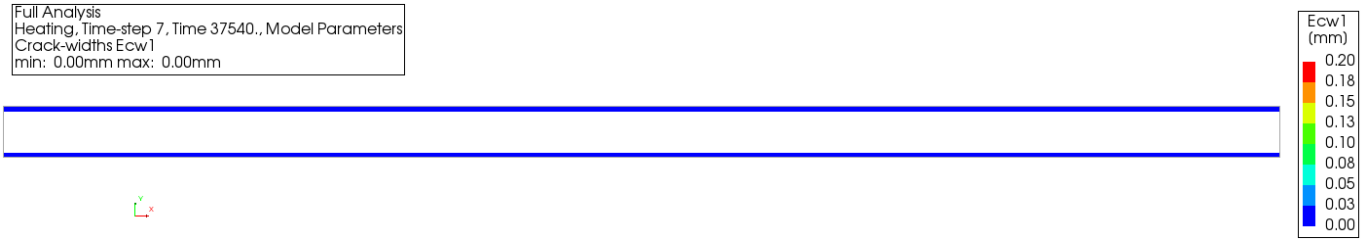

Crack width heating phase at transition heating/cooling phase - T_{max}

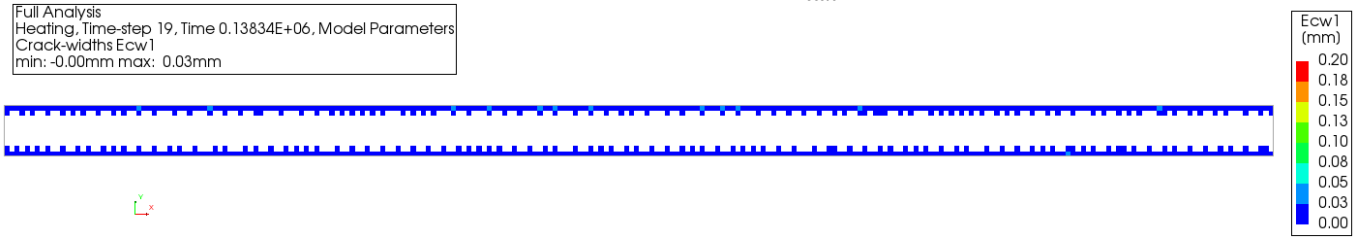

Crack width cooling phase step 17 – Cracks start to grow

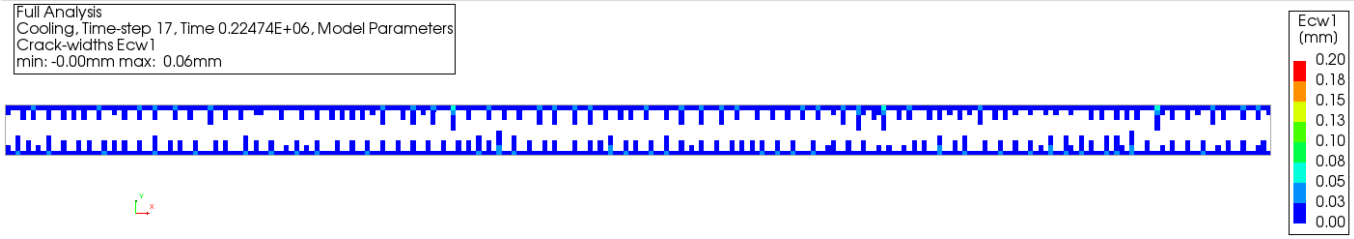

Crack width cooling phase step 21 – Cracks connect – formation of separation cracks

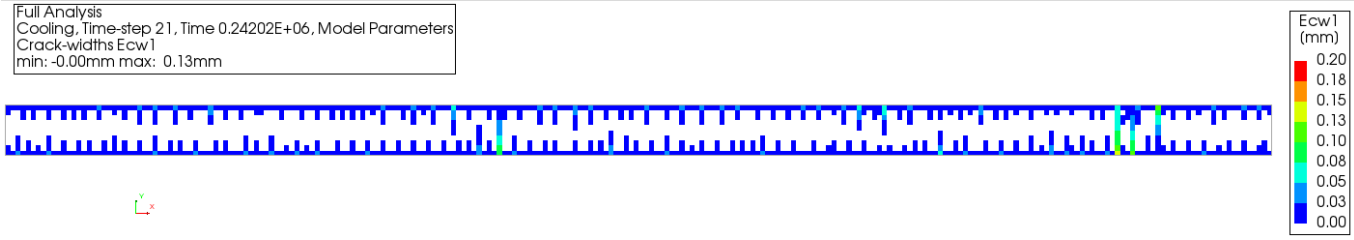

Crack width cooling phase step 30 – More separation cracks

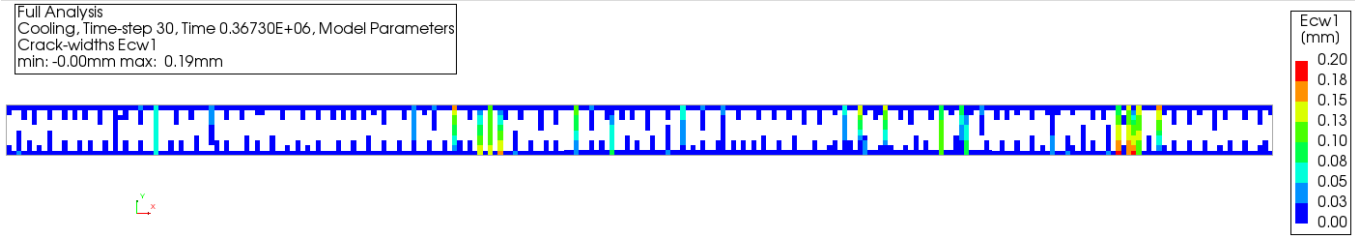

Crack width cooling phase step 55 – Final cracking pattern (2 weeks)

C

Finite element model

C.1. Standard case

This appendix is a summary of all the material properties and settings that are used in DIANA FEA for the standard case.

C.1.1. Material properties and settings

Table C.1: Material properties of the standard case

Property	Value	Unit	Source
Concrete Class	C30/37	-	EC2
Young's modulus E	32836	N/mm^2	EC2
Tensile strength f_{ctm}	2.9	N/mm^2	EC2
Density ρ	2300	kg/m^3	ROK 1.4
Poisson Coefficient μ	0.2	-	ROK 1.4
Thermal expansion coefficient α_c	$1.2 \cdot 10^{-5}$	$°C^{-1}$	ROK 1.4
Conductivity coefficient λ_c	2.6	W/(m°C)	ROK 1.4
Specific heat capacity c_c	1.0	kJ/(kg°C)	ROK 1.4

The fracture energy that is necessary to construct the FRC tensile behaviour graph is assumed as $G_F = 0.073 \cdot f_{cm}^{0.18}[N/mm^2]$. The crack opening for the tensile behaviour for regular concrete (MC2010 figure 5.1-4) is calculated as $w_1 = G_F/f_{ctm}$ and $w_2 = 5w_1$. The value of w_1 is needed to construct the FRC material model. The values that are used in the DIANA settings can be obtained from Figure C.1.

Table C.2: Material properties FRC of the standard case

Property	Value	Unit
f_{R1k}	4.0	N/mm^2
f_{R3k}	3.6	N/mm^2
f_{Fts} or f_d without dip	1.8	N/mm^2
f_{Ftu} or f_e	1.0	N/mm^2
f_d with dip	0.85 $\cdot f_c$	N/mm^2
Crack width SLS $w_{cr,d}$	0.5	mm
Crack width ULS $w_{cr,e}$	2.5	mm
Ultimate crack width w_u	2.6	mm
Constitutive law	Linear model	-
FIB MC 2010 frc model	Case (I)	-

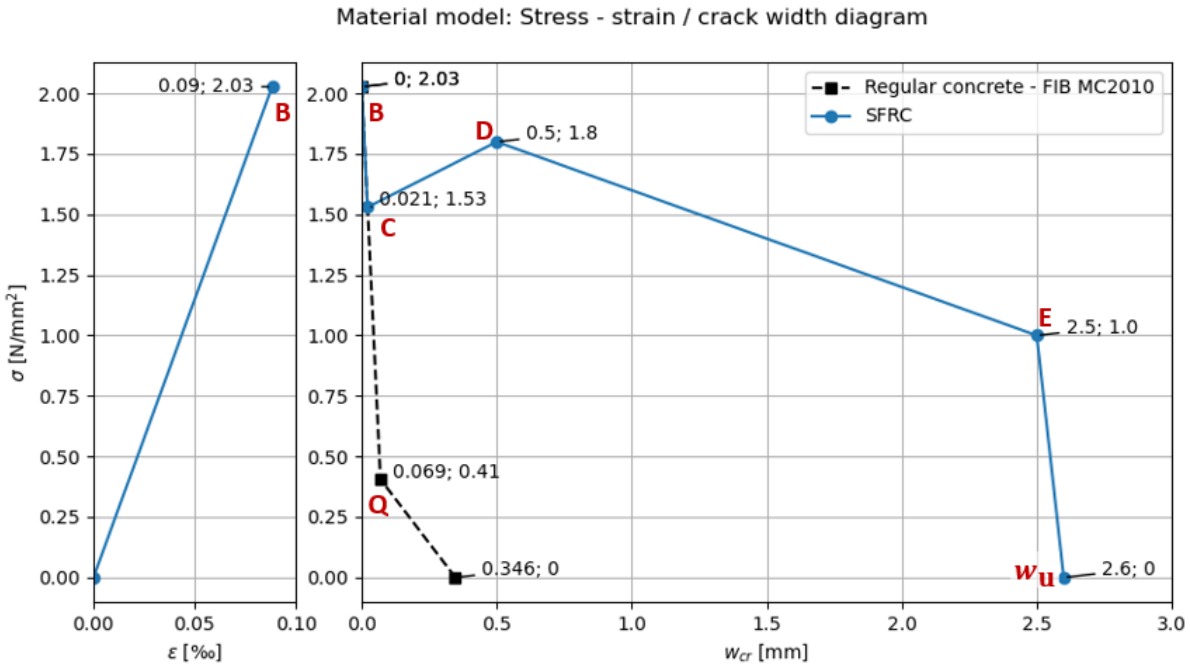

Figure C.1: FRC tensile behaviour

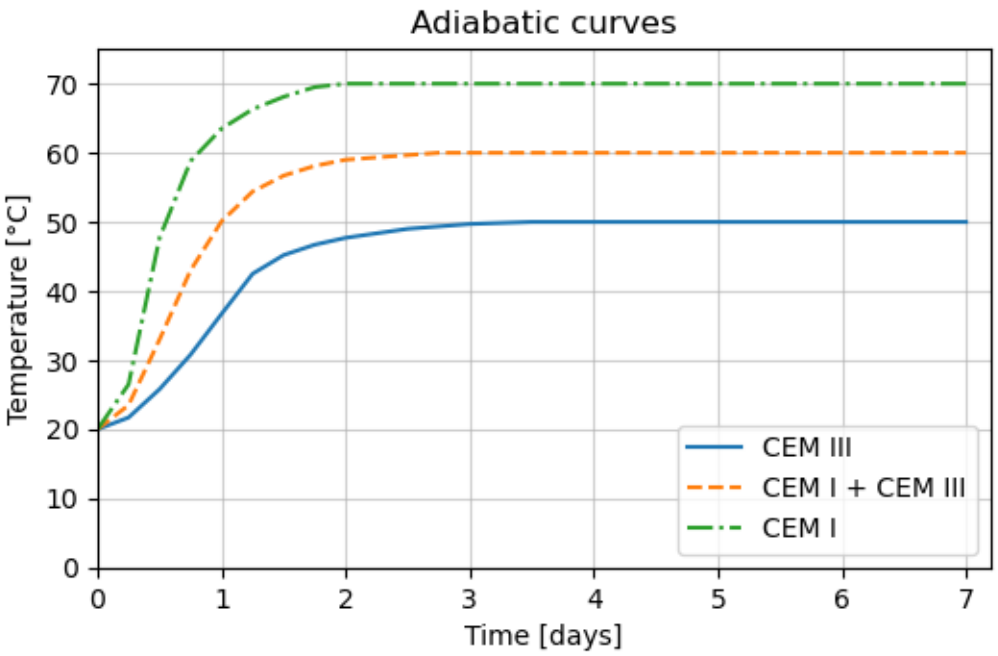

Figure C.2: Adiabatic curves, the curve for CEM I + CEM III is used in the standard case

Table C.3: Material FE settings of the standard case

Property	Option
Total strain based crack model	Rotating
Tensile behaviour	
Tensile curve	fib FRC, CMOD based
Crack bandwidth specification	Rots
Poisson's ratio reduction	Damage based
Compressive behaviour	
Compression curve	Elastic
Heat flow	
Heat of hydration calculation	Preprocessing from adiabatic heat development
Preprocessing type	Based on degree of reaction
Equivalent age calculation	Arrhenius
Reference temperature	20 °C
Arrhenius constant (E_a/R)	4000 °C^{-1}

C.1.2. Thermal properties

Table C.4: Thermal boundary conditions of the standard case

Property	Value	Variation	Unit	Source
Heat transfer coefficient top $h_{c,top}$	100	5-700	$W\,m^{-2}K^{-1}$	van Breugel et al., 2016
Heat transfer coefficient bottom $h_{c,bottom}$	100	5-700	$W\,m^{-2}K^{-1}$	van Breugel et al., 2016
Casting temperature T_0	12	10-26	°C	ROK 1.4, 2017
External temperature top $T_{ext,top}$	12	7-16	°C	ROK 1.4, 2017
External temperature bottom $T_{ext,bottom}$	12	7-16	°C	ROK 1.4, 2017

C.1.3. Random field properties

Table C.5: Random field properties for the standard case

Random field property	Value
Algorithm	Covariance Matrix Decomposition
Correlation matrix decomposition	Cholesky
Random field mesh	N_x = 251, N_y = 1, N_z =1
Correlation function	Regular exponential
Treshold	0.0
Correlation length l_c	1 m
Property	FRCFAC / Young's modulus
Distribution	Log-normal
Mean	1.0 [-] / 32836 N/mm^2
Standard deviation	5% / 15%
Correlation between properties	1.0

C.1.4. Mesh

Table C.6: Mesh settings of the standard case

Property	Option
Plane stress elements	CQ16M
Heatflow boundary elements	B2HT
Element size	100 x 100 mm
Mesher type	Hexa/Quad

C.1.5. Iteration scheme and convergence

Table C.7: Iteration scheme and convergence settings of the standard case

Property	Option
Transient heat analysis	
Iteration method	Newton regular
Maximum iterations	25
Initial degree of reaction	0.01
Nonlinear structural analysis	
Initial degree of reaction	0.01
Initial equivalent age	0.0
Iteration method	Newton-Raphson regular
Convergence criteria	Energy and Force simultaneously
Tolerance Energy / No convergence	0.001 / continue
Tolerance Force / No convergence	0.01 / continue

C.1.6. Analysis settings

Phased Analyses

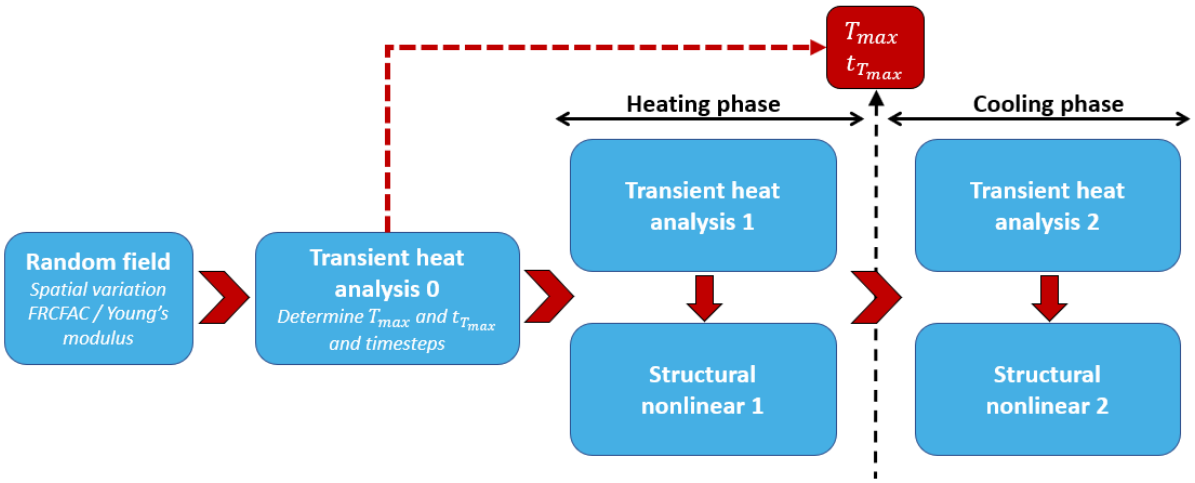

Figure C.3: Phased Analysis procedure

Time steps

Table C.8: Time steps of the standard case

Heating phase		Cooling phase	
Time step [s]	Times	Time step [s]	Times
1728	1	8640	3
6912	1	4320	22
3600	1	21600	16
100	1	43200	14
8400	15		
Total: 138,340		Total: 1,071,360	
1.6 days		12.4 days	

C.2. FEM checks

This section presents a comparison of the results of a mesh refinement analysis and a time-step refinement analysis. All results are based on the standard case in combination with a fixed random field. The mesh refinement analysis was performed to investigate if the choice of 100x100mm elements was valid. In the mesh refinement, half-size elements of 50x50mm were used. In the time-step analysis, all the time steps were halved to check if the results are not time-step dependent. Finally, a special time step analysis was performed where the time steps during the first through crack development were made very small (300 seconds). This was done so the process of the first crack formation can be studied and the effect of the sharp angle in the dip in the FRC-tensile behaviour graph.

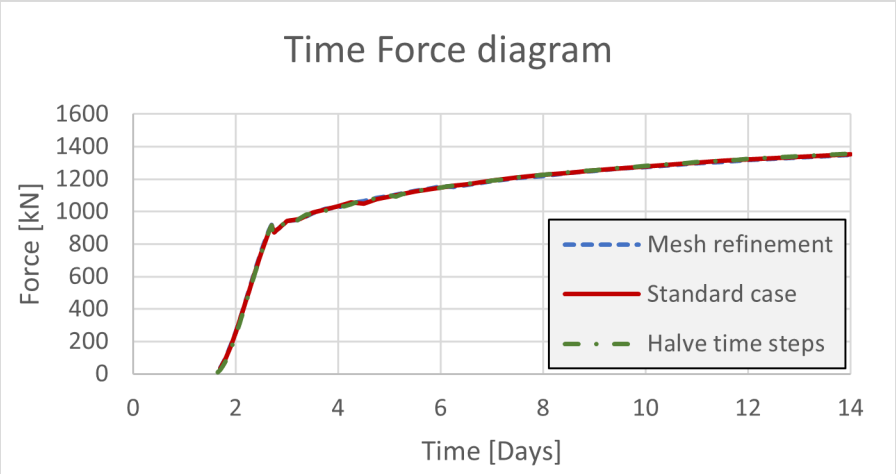

Figure C.4: Comparison of the time-force graphs of the mesh refinement, time-step dependency analysis and the standard model.

Figure C.4 shows exactly the same force diagram for all three analyses. Figure C.5 shows a similar crack pattern for all 4 analyses. The mesh refinement study showed just a slightly larger maximum crack width, but overall the results are very similar. The total extension during the hardening phase was 4.08, 4.12 and 4.17 mm for the standard case, mesh refinement and time-step analysis respectively. It is safe to conclude that the assumptions for both the time steps and element sizes are okay and do not significantly influence the results.

Figure C.5: Comparison of the crack width results of the mesh refinement, time-step dependency analysis, the special time-step analysis and the standard model

D

Random Fields

D.1. Basics of random fields

Random fields (RFs) can be used to introduce a spatial stochastic character in engineering problems. This is useful because in reality, concrete will also have quality differences in e.g. one and the same beam. Reality can therefore be better approached in numerical modelling by using random fields. An example of a spatial stochastic parameter is the tensile strength in a concrete beam. When this beam is split into several smaller cubes, the experimental results for each cube's tensile strength will be different. By combining all of these results, the average tensile strength can be determined of the concrete beam. In Figure D.1, an example of two random fields can be seen for a cross-section of a beam. In this example, the Tensile strength of concrete is the stochastic property, but other properties that have a spatial stochastic character are for example the Young's modulus, compressive strength and fracture energy. Figure D.1a shows two-dimensional spatial characteristics, which better approximates reality. However, for the tension bar model that determines separation cracks in this thesis, it is helpful to only model the slab with a one-dimensional stochastic property, as is shown in Figure D.1b. In this case it is easier to interpret the crack width results and understand the behaviour of the slab. Afterwards, the transition to 2D stochastic properties can be made.

Random fields can heavily influence the results of a numerical analysis. Therefore, careful attention has to be given to selecting the parameters and settings of the random field. Each random field needs specific input parameters such as the mean, variance and covariance. The variance describes the spread in the material properties and the covariance describes the correlation between certain positions in the random field for one certain property.

D.2. Correlation function and correlation length

The correlation is a measure of how much the property at point A is related to point B in the same random field. It is logical that values for a specific property closer together in space, are also similar in magnitude. In other words, a point on $x = 1/10$L of the beam is more strongly correlated to a point on the left side ($x = 0$) of the beam than a point on the right side ($x =$ L). For random fields, this measure of spatial correlation within one random field is called the correlation length. In reality, this spatial correlation is influenced by the construction process. Underwater concrete is cast from one side to the other side, where the full height of the floor is cast before gradually moving to the next position. This means that spaces close together over the width are more heavily correlated than spots

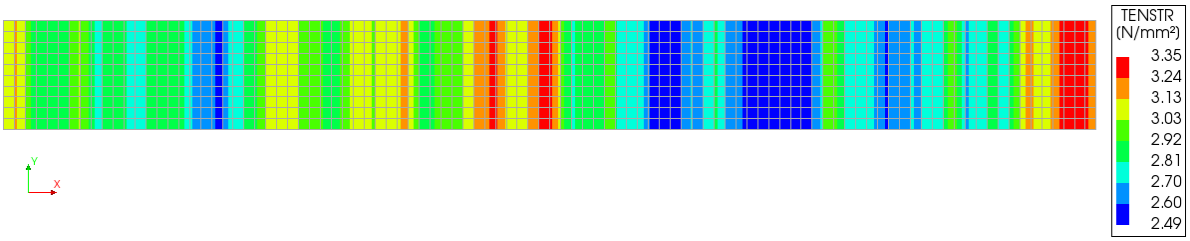

(a) 1D stochastic spatial variation

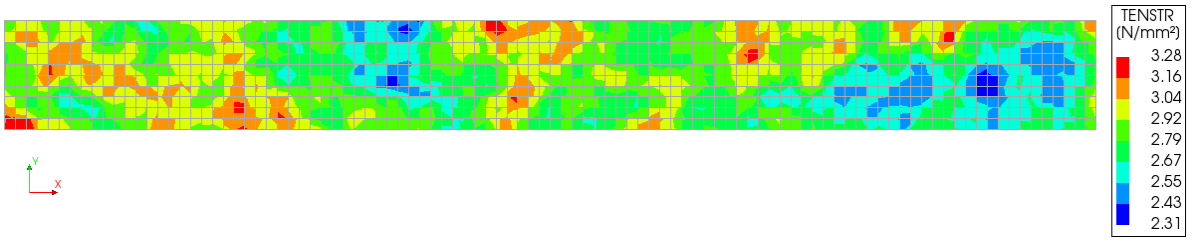

(b) 2D stochastic spatial variation

Figure D.1: Example of random fields for the tensile strength of a concrete beam of 10m length. For both examples, the mean of the tensile strength is $2.9\ \mathrm{N/mm^2}$ with a COV. of 10%.

that are far apart. Different locations over the height have a very high correlation. Compare this to a 3D-printed structure that is cast in layers. These layers will almost have no correlation with each other. Nonetheless, there is no experimental data available that has verified these expectations. The mean and variance of a particular property can be determined from actual material properties from literature or experiments. These material properties can also be modelled with different probabilistic distributions, such as the normal or log-normal distribution. Contrarily, the correlation length is a model property chosen by the engineer. There is literature that advises values for the correlation length for some instances, but the influence of this parameter on the results will always have to be assessed retrospectively.

The correlation between two different points in space can be determined with correlation functions. Common examples of correlation functions are the exponential and squared exponential function:

$$\rho\left(\Delta x\right) = \rho + (1-\rho)\cdot \exp\left(-\frac{\Delta x}{l_c}\right) \tag{D.1a}$$

$$\rho\left(\Delta x\right) = \rho + (1-\rho)\cdot \exp\left(-\frac{\Delta x^2}{{l_c}^2}\right) \tag{D.1b}$$

Where:

- $\rho\left(\Delta x\right)$ is the measure of correlation between points with a distance Δx
- Δx is the distance between two points in space
- ρ is a certain threshold value for a minimum measure of correlation in the random field
- l_c is the correlation length, which is a scaling parameter for the correlation function

The difference between the two types of correlation functions is displayed in the upper graphs of Figure D.2. The squared exponential function is steeper than the regular exponential function. Both correlation functions with a threshold are displayed in the top right graph. The threshold value makes sure that there is always a minimum correlation in the random field. In the bottom panels, the influence of the correlation length can be seen for both correlation functions. It can be concluded that a larger correlation length means that points that are further away from each other have more correlation. In comparison, a smaller correlation length means faraway points are almost entirely not correlated. The

correlation length is the main scaling parameter to investigate the influence of correlation on the results. The correlation length denotes the x-coordinate where the tangent of the exponential function at $x = 0$, intersects the x-axis. It also indicates the x-coordinate where both the exponential and squared exponential functions intersect.

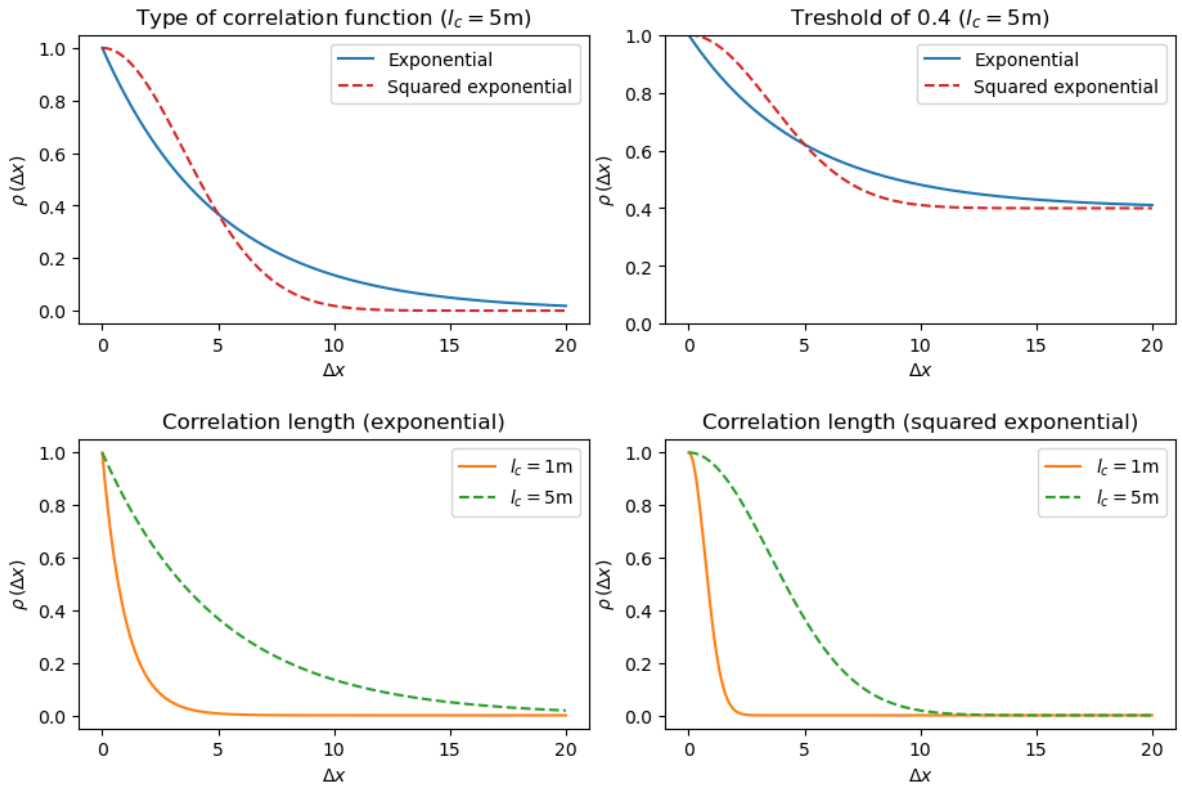

Figure D.2: Influences of parameters on the correlation function

It can be observed that there are quite some parameters that influence the correlation of a material property. All of these parameters are model parameters, meaning that a choice for these has to be made by the engineer. The outcome of different choices will have to be evaluated and if possible, calibrated with experiments.

The measure of correlation denoted by the correlation length (within one random field) must not be confused with the correlation between different material properties (between two different random fields). When for example, both the tensile strength and the Young's modulus are modelled with a random field, it is likely that a weak spot in the random field of the tensile strength coincides with a weak spot in the random field of the Young's modulus. In this case, a correlation exists between two parameters and is often denoted with a correlation coefficient that takes values between 0 (no correlation) and 1 (full correlation).

D.3. Influence of correlation properties on random fields

This paragraph shows examples of random fields, and how different parameters in the correlation function (introduced in Figure D.2) influence the random fields. All random fields in this section are based on a scale factor which has a mean of $\mu = 1$ and a standard deviation of $\sigma = 0.1$. In Figure D.3, the difference between the exponential and squared exponential is displayed and how this affects the random fields. It can be observed that a squared exponential function gives a much smoother function compared to the regular exponential function. The influence of the threshold parameter (Figure D.4)

is unclear from the corresponding random field. Still, the threshold parameter guarantees a certain minimum correlation between all the points in the random field. The difference between a correlation with and without a threshold is given in section D.3. Figure D.5 and D.6 display the influence of the correlation length for the regular exponential and squared exponential functions. It has to be noted that this is only one realisation of a random field, but a pattern emerges when multiple random fields are observed. For the random field with a high ($l_c = 5$) correlation length, the graph has a smaller spread than the random field with a low correlation length. This can be explained by the fact that points in the field are more heavily correlated, meaning they are situated closer together in the y-direction. This is even more clear when the squared exponential function is used. Ultimately, this also influences the standard deviation of the realisation of the random field, leading to different standard deviations than what was chosen as the standard deviation from the input parameters. If 1000 random fields are generated from the same input properties, the mean of all these 1000 standard deviations should be close to the input standard deviation. This is not the case for a high correlation. This effect is elaborated in Section D.6.

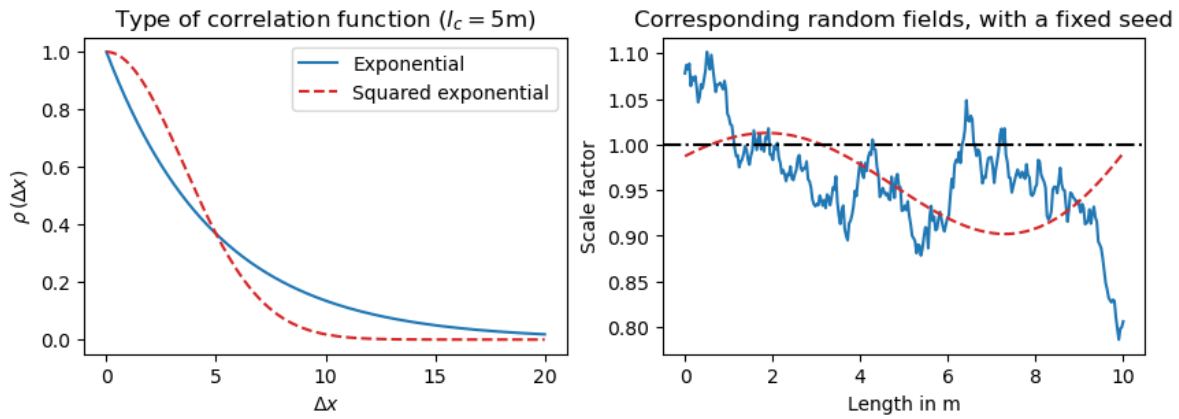

Figure D.3: Influence of the type of correlation function on random fields

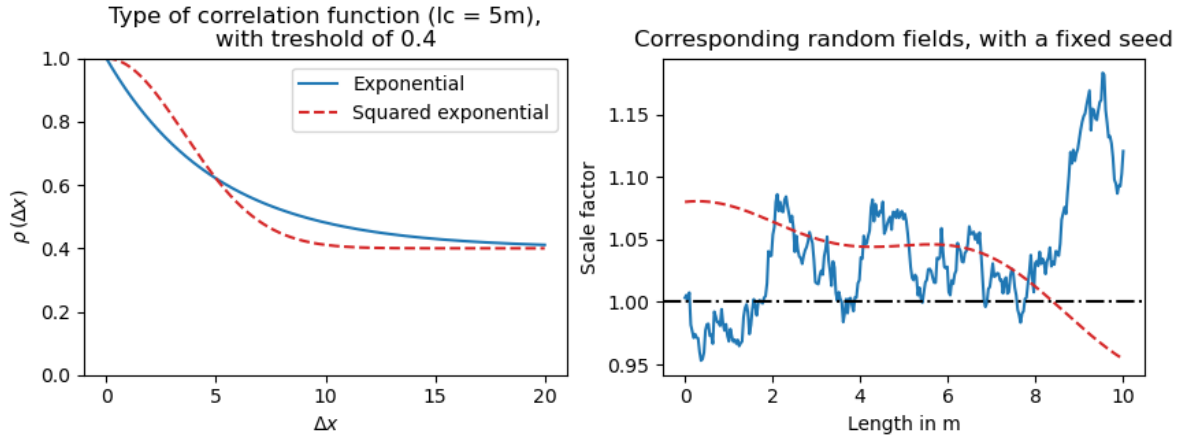

Figure D.4: Influence of the threshold on random fields

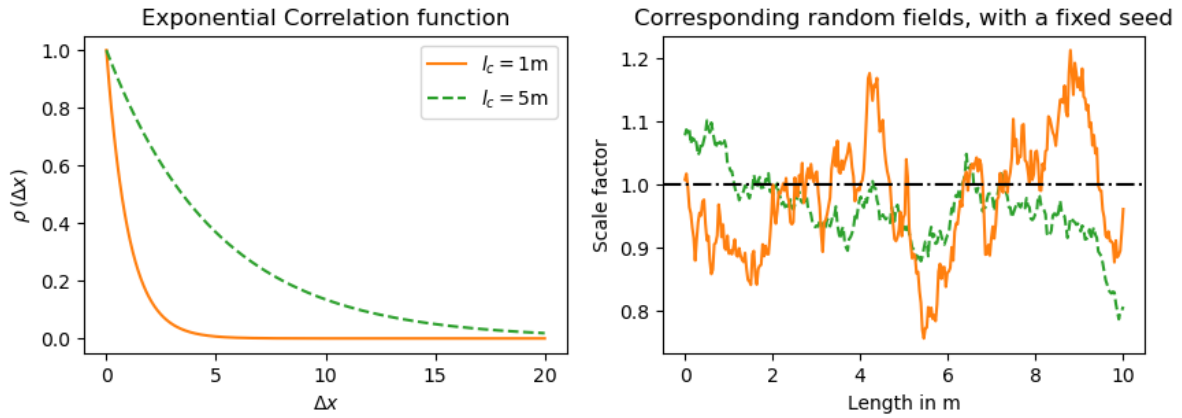

Figure D.5: Influence of the correlation length for an exponential correlation function. The random field with l_c = 5 corresponds with the random field with the exponential function in figure D.3

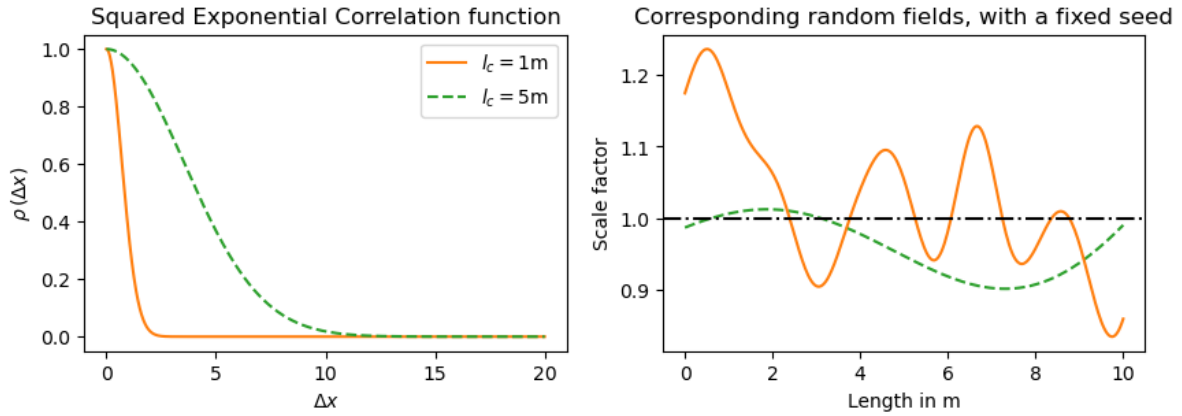

Figure D.6: Influence of the correlation length for a squared exponential correlation function. The random field with l_c = 5 corresponds with the random field with the squared exponential function in figure D.3

D.4. Generation of random fields

D.4.1. Method

The five steps to generate a random field are:

1. Determine statistical properties of a material property (mean and variance)
2. Define a random field mesh
3. Generate uncorrelated random numbers from the standard normal distribution (zero mean and unit variance)
4. Transform random numbers into (correlated) random variables
5. Transform random numbers into random field points with the correct statistical properties from point 1

As observed from step 2, a mesh for the random field is needed to generate the random field points. This mesh might be the same as the FE mesh, but the random field mesh should generally be smaller than the FE mesh. In any case, the two meshes are separated so that the same random field can be used in the case when alterations to the FE mesh are made. In step 3, uncorrelated random numbers are drawn from the standard normal distribution with a mean of 0 and a standard deviation of 1. Finally,

these points are transformed into random correlated random variables. There are different methods to achieve this which are called:

- Covariance Matrix Decomposition (CMD)
- Local Average Subdivision (LAS)
- Expansion Optimal Linear Estimation (EOLE)
- Fast Fourier Transform (FFT)

All of these algorithms have their own accuracy and efficiency regarding computation time. Van der Have (2015) concluded in his thesis that, when looking at accuracy, the covariance matrix decomposition performs the best. From personal experience, there are no notable issues with computation time regarding the generation of fields with CMD. Therefore, the chosen method used in this thesis to generate random fields is CMD.

D.4.2. Algorithm to generate random fields

Normal distribution

An algorithm to generate 1D random fields will be given where the modelled property will be sampled from a normal distribution. With CMD, a series of correlated random variables can be generated:

$$\mathbf{\Phi} = \mathbf{L}\boldsymbol{n} \tag{D.2}$$

Where:

- $\mathbf{\Phi}$ is a vector containing the correlated random variables of length n
- $\mathbf{L}$ is the lower triangular matrix of the decomposed correlation matrix
- $\boldsymbol{n}$ is a vector with uncorrelated random variables from the distribution N(0,1) of length n

In order to determine $\mathbf{L}$, the correlation matrix must first be constructed. The n by n correlation matrix is symmetric and is defined as:

$$\mathbf{P}_{ij} = \begin{bmatrix} 1 & \rho(x_1,x_2) & \dots & \dots & \rho(x_1,x_n) \\ & 1 & & & \rho(x_2,x_n) \\ & & 1 & & \vdots \\ & & & 1 & \rho(x_{n-1},x_n) \\ & & & & 1 \end{bmatrix} \tag{D.3}$$

Where $\rho(x_1,x_2)$ can be determined with the correlation functions from equation D.1. And Δx can be determined by subtracting $j-i$ in each element of the matrix $\mathbf{P}_{ij}$. To transform Δx into the actual difference in length when looking at a beam with length L the following formula can be used: $\Delta\mathrm{L} = \Delta x/n \cdot \mathrm{L}$. This transforms equations D.1 into:

$$\rho(\Delta\mathrm{L}) = \rho + (1-\rho)\cdot\exp\left(-\frac{\Delta\mathrm{L}}{l_c}\right) \tag{D.4a}$$

$$\rho(\Delta\mathrm{L}) = \rho + (1-\rho)\cdot\exp\left(-\frac{\Delta\mathrm{L}^2}{{l_c}^2}\right) \tag{D.4b}$$

A similar correlation matrix as in D.3 can be constructed by using equations D.4 that take the actual length into account. This matrix has to be decomposed by either using Cholesky decomposition or Eigen decomposition. The Cholesky decomposition is defined as:

$$\mathbf{P} = \mathbf{L}\mathbf{L}^{\mathsf{T}} \tag{D.5}$$

Where **L** is a lower triangular matrix. A similar approach with eigendecomposition is also possible. First, the matrix is decomposed in the eigenvectors (**E**) and eigenvalues (λ_i). After this, the same lower triangular matrix **L** as in equation D.5 can be determined by:

$$\mathbf{L} = \mathbf{E}\boldsymbol{\Lambda} \tag{D.6}$$

Where:

- **E** is a matrix containing the eigen vectors
- $\boldsymbol{\Lambda}$ is a diagonal matrix, composed of the square roots of the eigenvalues, $\boldsymbol{\Lambda} = \text{diag}(\sqrt{\lambda})$

Both Cholesky and eigendecomposition produce similar random fields. It was observed that Cholesky decomposition does not work when the correlation matrix is constructed with the squared exponential function. The reason is that sometimes the correlation matrix is not positive definite, in which case the matrix cannot be decomposed with Cholesky decomposition. In these cases, eigendecomposition does not result in these problems, and it provides similar results.

After obtaining the decomposed correlation matrix, determined by either of the two methods, it can be filled into equation D.2 to obtain a vector with correlated random variables $\boldsymbol{\Phi}$. Finally, this vector can be scaled with the predetermined statistical properties of a material property according to the formula:

$$\mathbf{X} = \mu \cdot \boldsymbol{i} + \sigma \cdot \boldsymbol{\Phi} \tag{D.7}$$

Where:

- μ is the mean of the material property
- $\boldsymbol{i}$ is a unit vector of the same length as $\boldsymbol{\Phi}$
- σ is the standard deviation of the material property
- $\boldsymbol{\Phi}$ is a vector containing the correlated random variables of length n
- $\mathbf{X}$ is a vector containing the random field data points

Log-normal distribution

In order to make use of the log normal distribution, the previous statistical properties will have to be transformed according to:

$$\sigma_{\text{Ln}} = \sqrt{\log\left(1 + \left(\frac{\sigma_{\text{N}}}{\mu_{\text{N}}}\right)^2\right)} \tag{D.8}$$

$$\mu_{\text{Ln}} = \log(\mu_{\text{N}}) - \frac{1}{2}\sigma_{\text{Ln}}^2 \tag{D.9}$$

Where the subscript "Ln" indicates the properties of the log-normal distribution and the subscript "N" denotes the normal distribution. Also, the correlation values$\rho\left(x_i, x_j\right)$ from matrix $\mathbf{P}$ have to be transformed with the Nataf transformation (van der Have, 2015) according to:

$$\rho_{\text{Ln}}(\Delta x) = \frac{\exp\left(\sigma_{\text{Ln}}^2\, \rho(\Delta x)\right) - 1}{\exp\left(\sigma_{\text{Ln}}^2\right) - 1} \tag{D.10}$$

The final scaling, when sampling from the log-normal distribution is defined as:

$$\mathbf{X} = \exp\left(\mu_{Ln} \cdot \boldsymbol{i} + \sigma_{Ln} \cdot \boldsymbol{\Phi}\right) \tag{D.11}$$

Where:

- $\boldsymbol{i}$ is a unit vector of the same length as $\boldsymbol{\Phi}$
- $\boldsymbol{\Phi}$ is a vector containing the correlated random variables of length n
- $\mathbf{X}$ is a vector containing the random field data points

The exponent operation in this equation has to be performed on all the individual components in the resulting vector. The mathematical algorithm from this section was coded in Python. In section D.4.3, pseudo code elaborates the practical steps that have to be scripted to program this random field generation algorithm.

D.4.3. Random field generation script

The code follows the steps of the algorithm in section D.4.2, but it is split up into three separate blocks. Where the output of a previous block is needed for the next block. Some operations refer to equations from the previous chapter. This code is only applicable for 1D random fields as displayed in Figure D.1a. The input properties that are needed for the script are defined as:

Random field input properties:

- Mean, μ
- Standard deviation, σ
- Distribution type: Normal (NORMAL) or Log-Normal (LOGNRM)
- Correlation function: exponential (EXPONE) or squared exponential (SQTYPE)
- Correlation length, L_c
- Decomposition method: CHOLESKY, EIGEN
- 1D random field mesh. This is the number of points of which the 1D random field consists, N_x
- Length of the model, L
- Treshold, η

Algorithm 1: Creating the correlation matrix

Input: N_x, L, η, L_c
Output: N_x by N_x correlation matrix **P** scaled to the physical length

```
Construct empty correlation matrix P_ij of size N_x by N_x ;
for i = 0 to N_x do
    for j = 0 to N_x do
        if i = j then
            P_ij(i,j) = 1.0
        else if i > j then
            dx = i − j ;
            begin Subroutine: fill correlation matrix
                dL = (dx/N_x) · L ;
                if Correlation function = EXPONE then
                    ρ = η + (1 − η) exp(−dL²/L_c²)
                else if Correlation function = SQTYPE then
                    ρ = η + (1 − η) exp(−dL/L_c)
                P_ij(i,j) = ρ
            end
        else if i < j then
            dx = j − i ;
            Execute Subroutine: fill correlation matrix
```

Algorithm 2: Correlation matrix decomposition

Input: Correlation matrix **P**, Distribution type, Decomposition method
Output: Decomposed lower triangular correlation matrix **L**

if *Distribution type* = *NORMAL* **then**
  begin Subroutine: Matrix decomposition
    if *Decomposition method* = *CHOLESKY* **then**
      Use Cholesky decomposition to obtain matrix **L** (Eq. D.5);
      $\mathbf{P} = \mathbf{L}\mathbf{L}^{\mathsf{T}} \rightarrow \mathbf{L}$
    else if *Decomposition method* = *EIGEN* **then**
      Use Eigen decomposition to obtain matrix **L** (Eq. D.6);
      $\mathbf{L} = \mathbf{E}\boldsymbol{\Lambda}$
  end
else if *Distribution type* = *LORNRM* **then**
  Use equations D.8 and D.9 to transform μ and σ to corresponding lognormal properties μ_{Ln} and σ_{Ln}. ;
  Use equation D.10 to transform all the individual items of the correlation matrix ;
  Execute Subroutine: Matrix decomposition

Algorithm 3: Creating the random field data points

Input: N_x, μ, σ, Decomposed lower triangular correlation matrix **L**, Distribution type
Output: Vector $\mathbf{X}$ with correlated random field datapoints

Generate random vector $\boldsymbol{n}$, sampled from standard normal distribution of length N_x ;
$\boldsymbol{\Phi} = \mathbf{L}\boldsymbol{n}$ (Inner product) ;
Scale the vector $\boldsymbol{\Phi}$ with the material properties ;
  if *Distribution type* = *NORMAL* **then**
    $\mathbf{X} = \mu \cdot \boldsymbol{i} + \sigma \cdot \boldsymbol{\Phi}$ (Eq. D.7)
  else if *Distribution type* = *LORNRM* **then**
    $\mathbf{X} = \exp\left(\mu_{Ln} \cdot \boldsymbol{i} + \sigma_{Ln} \cdot \boldsymbol{\Phi}\right)$ (Eq. D.11)

D.5. Influence of random field settings

In this section, the effect of some additional random field properties is shown as an addition to the influences discussed in section D.3. The following properties are explored:

- Correlation length (more in-depth)
- Standard deviation of the sample distribution
- Sample distribution type
- Threshold in the correlation function
- Correlation matrix decomposition method

For every property, both the regular and squared exponential function are discussed and the random fields have the same mesh (number of data points). In some comparisons, the seed is fixed, which means that the same random draws from the normal distribution (step 3 from section D.4.1) are used for each field. This section only shows a couple of random fields per topic, but multiple random fields were studied in order to come to conclusions in this section.

Correlation length

First, random fields with correlation and uncorrelated fields are displayed in Figure D.7. It can be observed that the uncorrelated field ”jumps” all over the place because the data points have no correlation with each other. Compared to that, two correlated fields are shown, both the regular and squared exponential functions. It can be concluded that the points in the correlated fields are closer to each other on the vertical axis. It can also be observed that a random field with a regular correlation function is much more erratic than a random field with a squared exponential function. Figure D.8 demonstrates this effect. It can be seen that the absolute difference between the lowest and highest point in each of the random fields is smaller for the field with a lower correlation length. Figure D.11, also shows the same effect for random fields without a fixed seed. A similar effect can also be observed for random fields that use a squared exponential correlation function such as in Figure D.10. This effect is magnified when two extremes for the correlation length are used, as shown in Figure D.9.

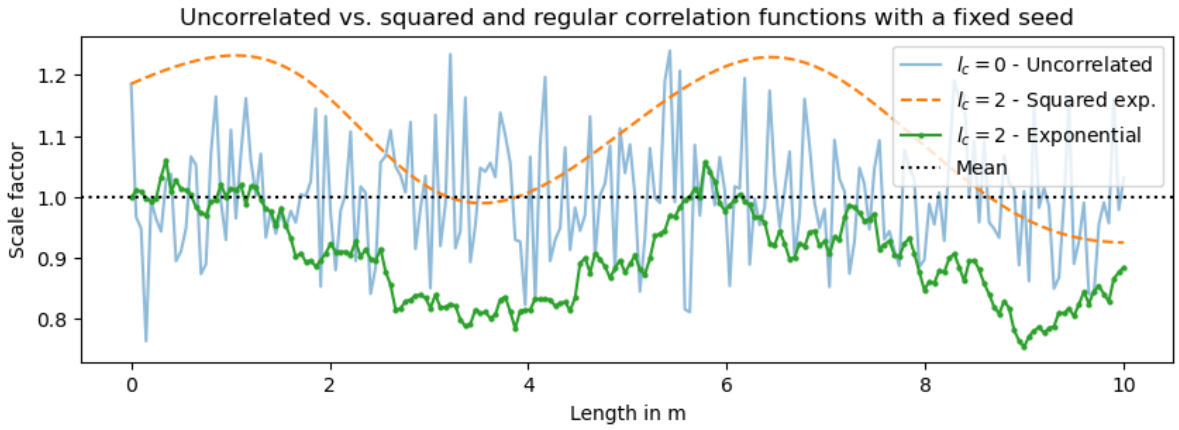

Figure D.7: Correlated random field compared to correlated random fields - 200 data points

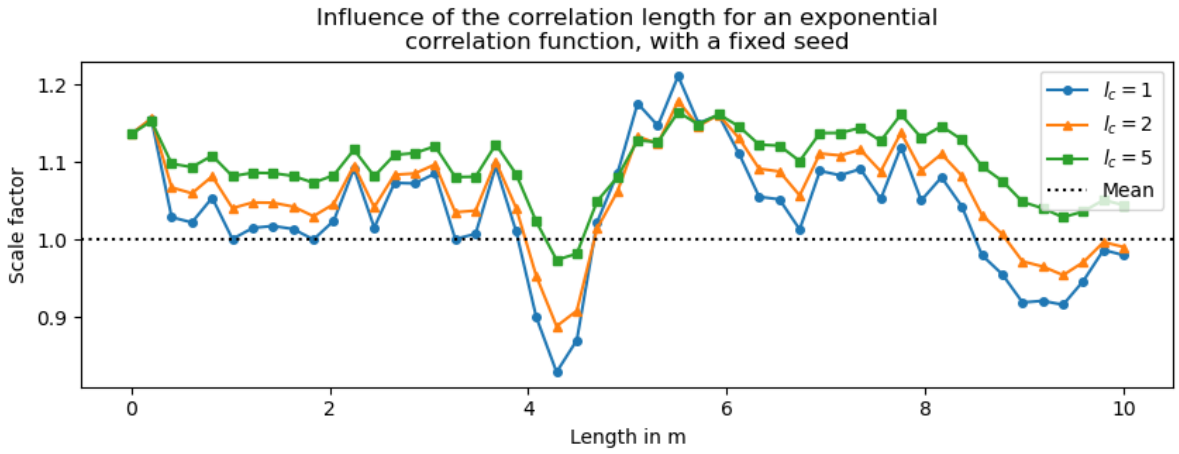

Figure D.8: Influence of the correlation length 1 - 50 data points

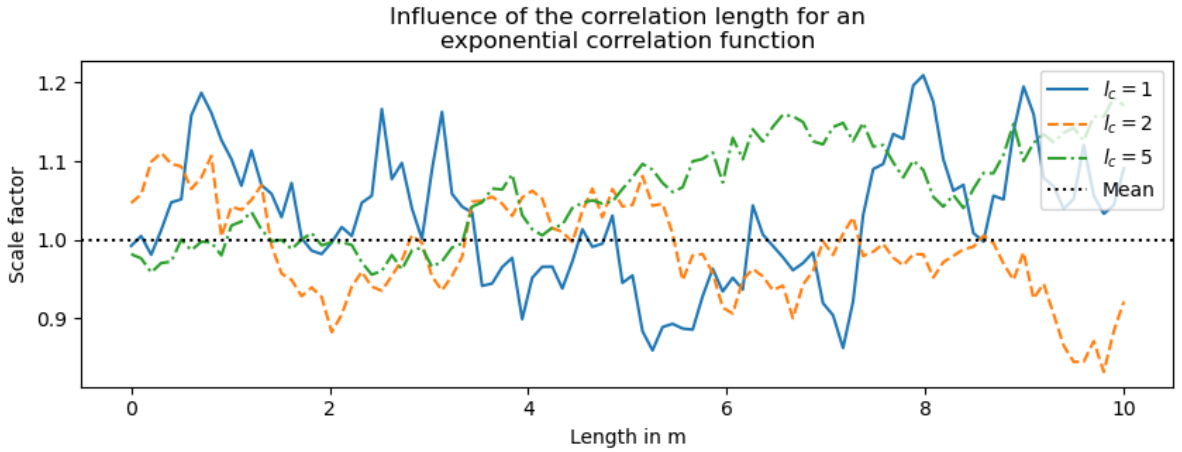

Figure D.9: Large vs small correlation length - 100 data points

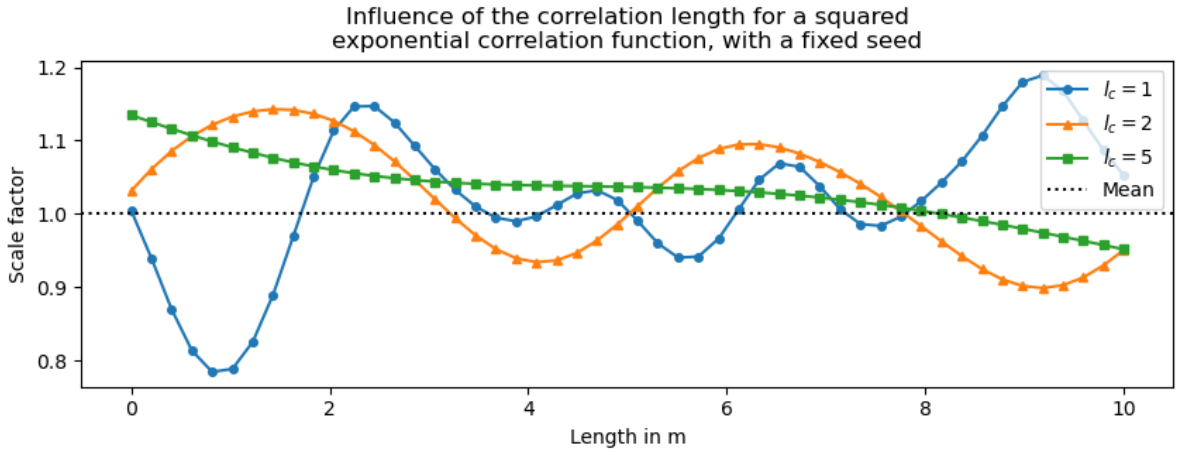

Figure D.10: Influence of the correlation length 2 - 50 data points

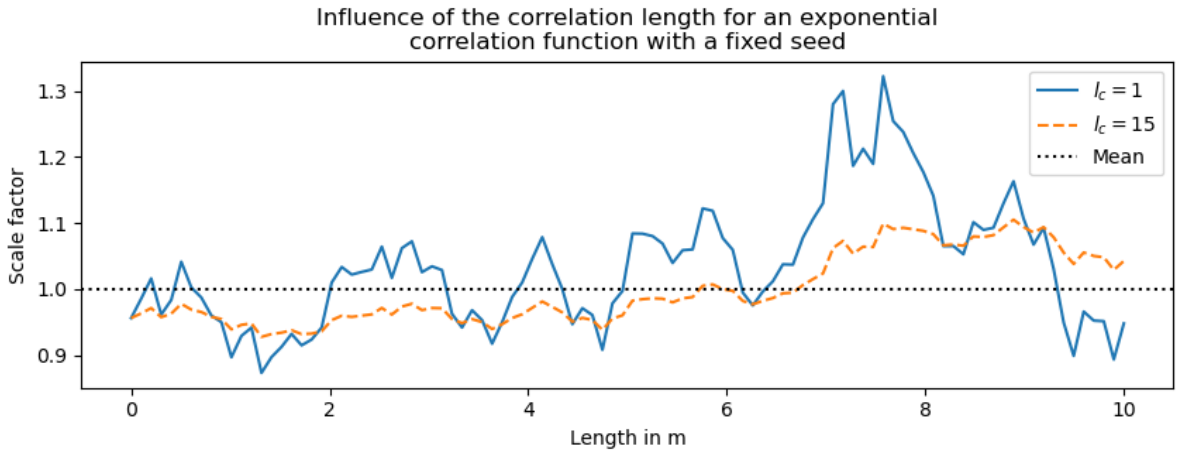

Figure D.11: Influence of the correlation length 3 - 100 data points

Standard deviation

In the previous section, it was explained that a larger correlation length corresponds with a smaller absolute difference between the minimum and maximum in a random field. A similar effect is also

observed for varying the standard deviation, which is more straightforward than the correlation length. A higher standard deviation means a higher absolute difference. This is observed in all three figures D.12, D.13 and D.14. These figures show random fields with an exponential correlation function with and without a fixed seed and a squared exponential function with a fixed seed.

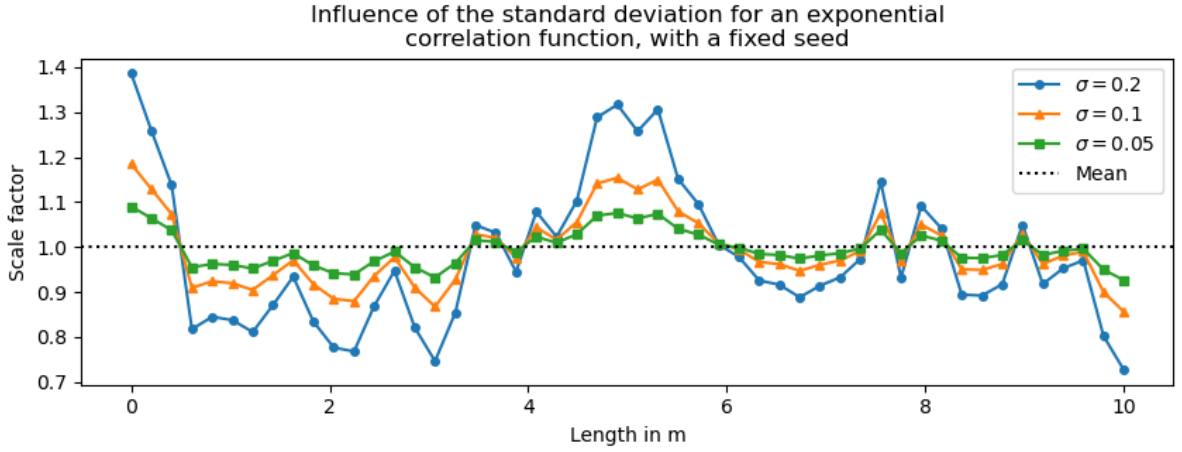

Figure D.12: Influence of the standard deviation 1 - 50 data points

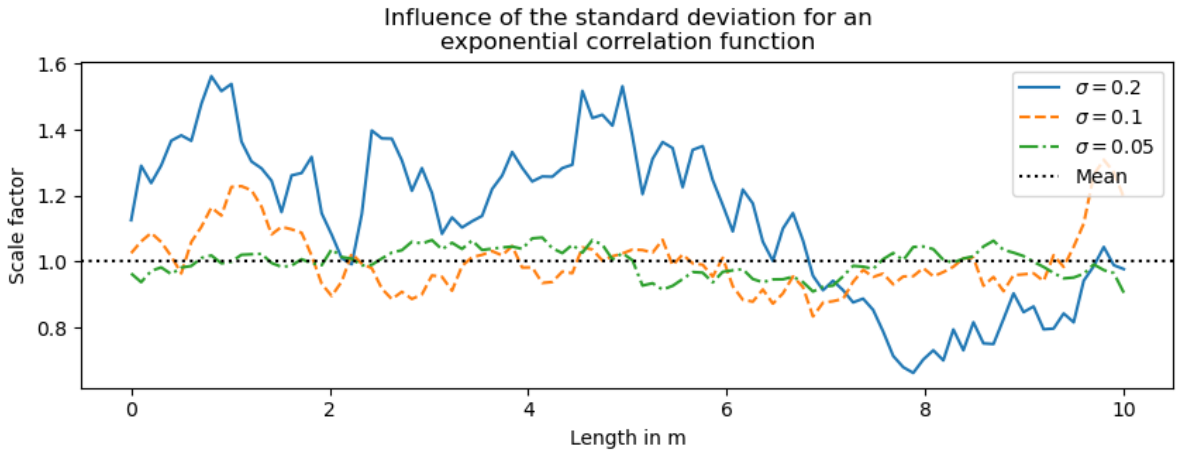

Figure D.13: Influence of the standard deviation 2 - 100 data points

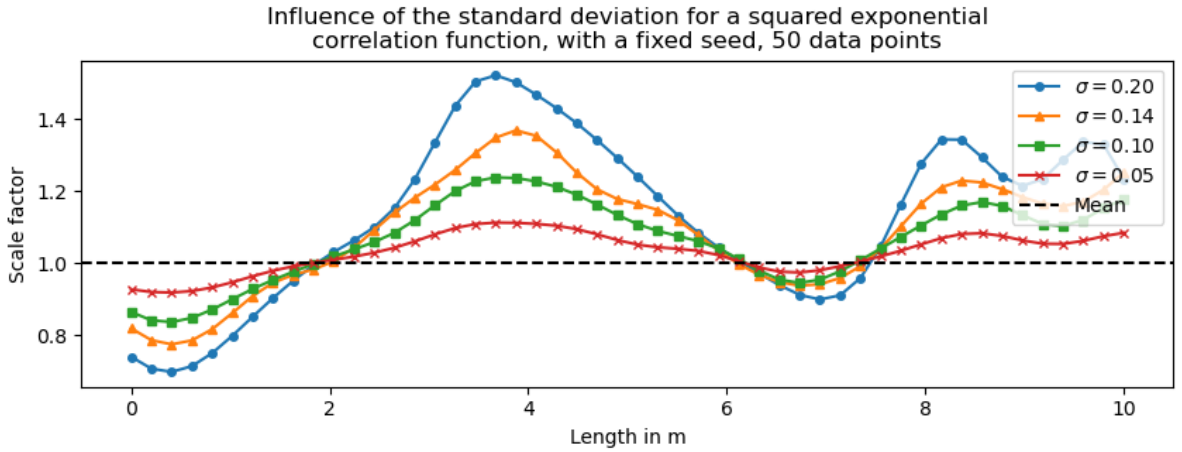

Figure D.14: Influence of the standard deviation 4 - 50 data points

Sample distribution

It was observed from Figures D.15 and D.16 that the generation of random fields is almost not influenced by the sample distribution. The behaviour of some material properties can better be modelled with the log-normal distribution since this is closer to reality, but it does not influence the random fields. Except when a material property is close to zero. The log-normal distribution can only sample positive values, which is useful when sampling small values, such as for instance the tensile strength of concrete. Dependent on the standard deviation, if this value is close to zero, a random field from the normal distribution would also sample negative values, which is impossible for the tensile strength. The log-normal distribution can be used to prevent this, which is shown in Figure D.17.

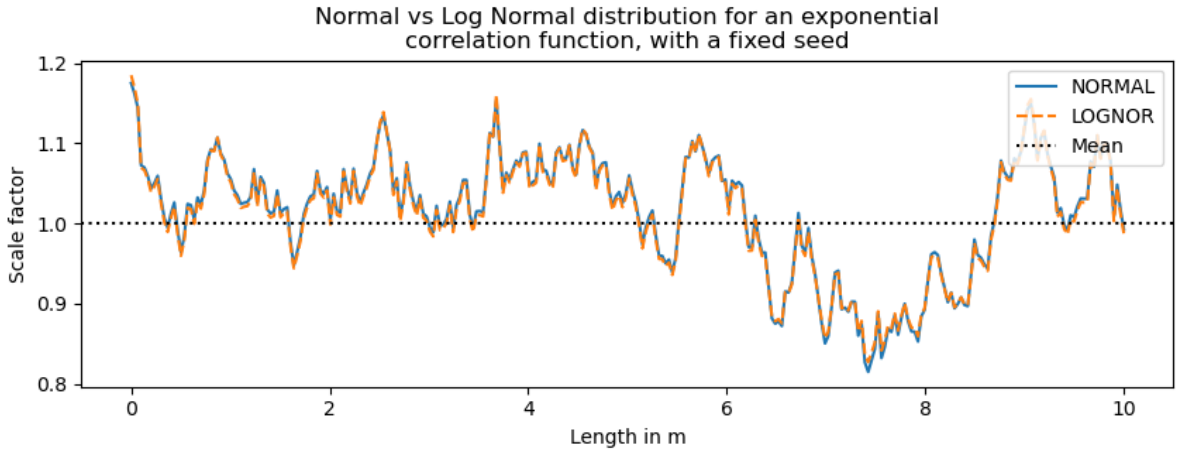

Figure D.15: Normal vs Log-normal distribution 1

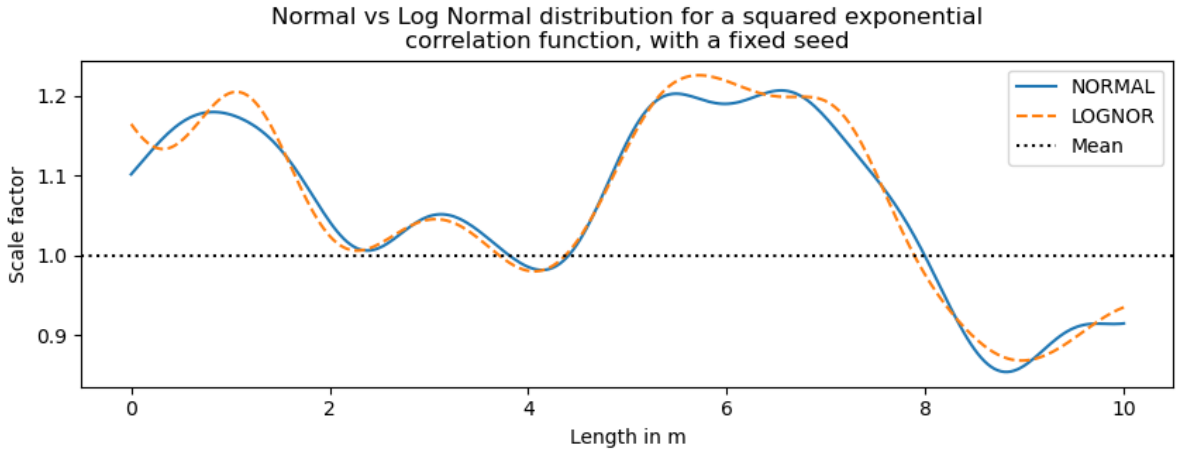

Figure D.16: Normal vs Log-normal distribution 2

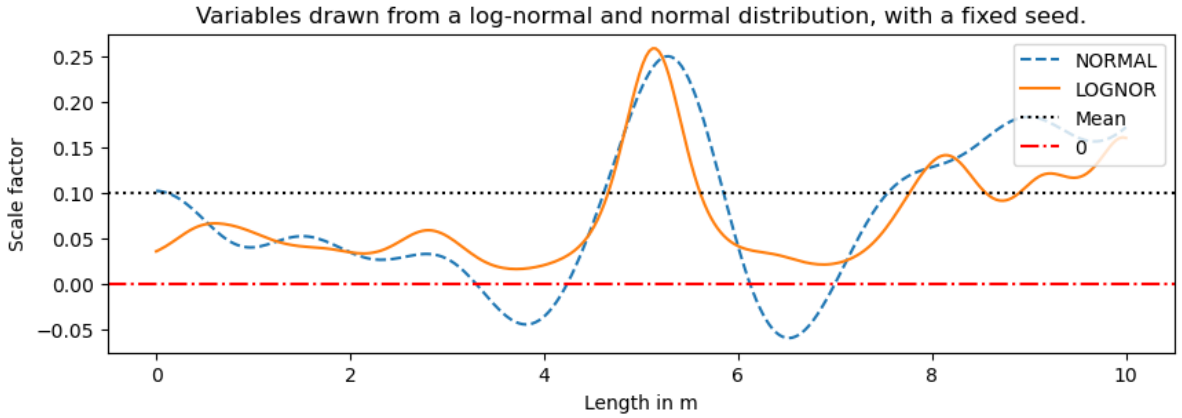

Figure D.17: Normal vs Log-normal distribution with a mean close to 0

Size of the random field mesh

Figures D.18 and D.19 show that the general resulting random fields are independent of the mesh size. The only exception is that random fields generated with the exponential correlation function are more erratic when more data points are used. However, it can be seen that the general correlation within the fields is similar.

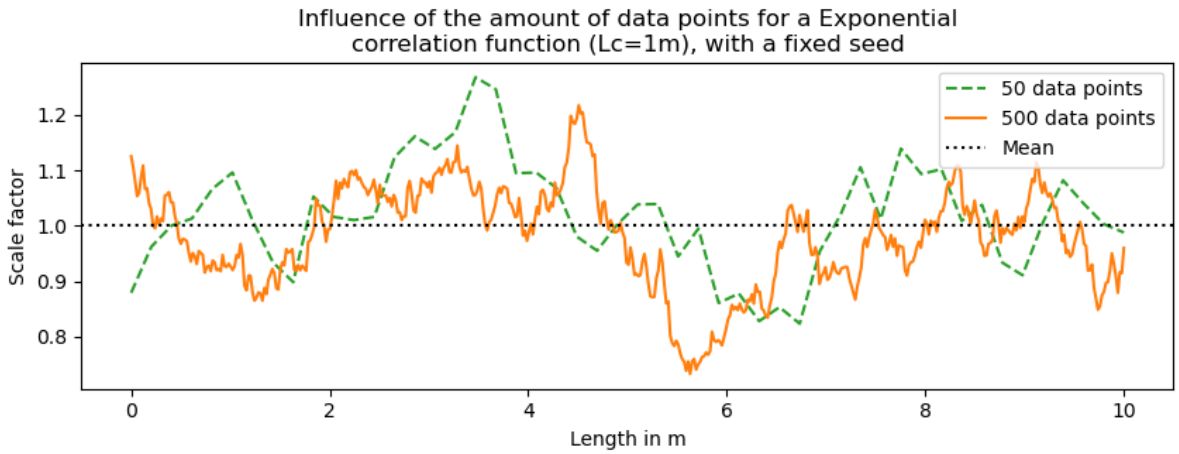

Figure D.18: Influence of the random field mesh size - Exponential correlation function

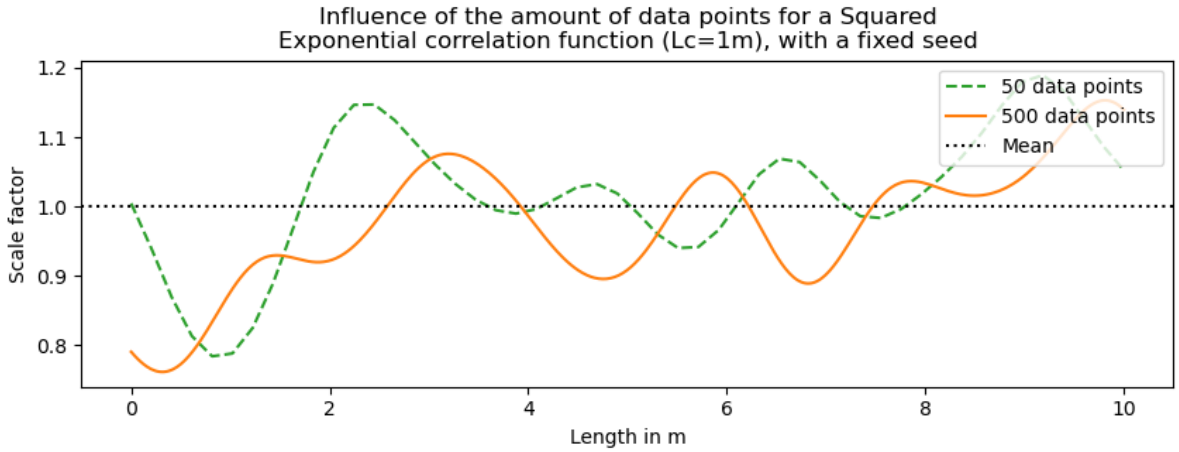

Figure D.19: Influence of the random field mesh size - Squared exponential correlation function

Threshold

The influence of the correlation threshold does not become apparent from Figures D.20, D.21 and D.22.

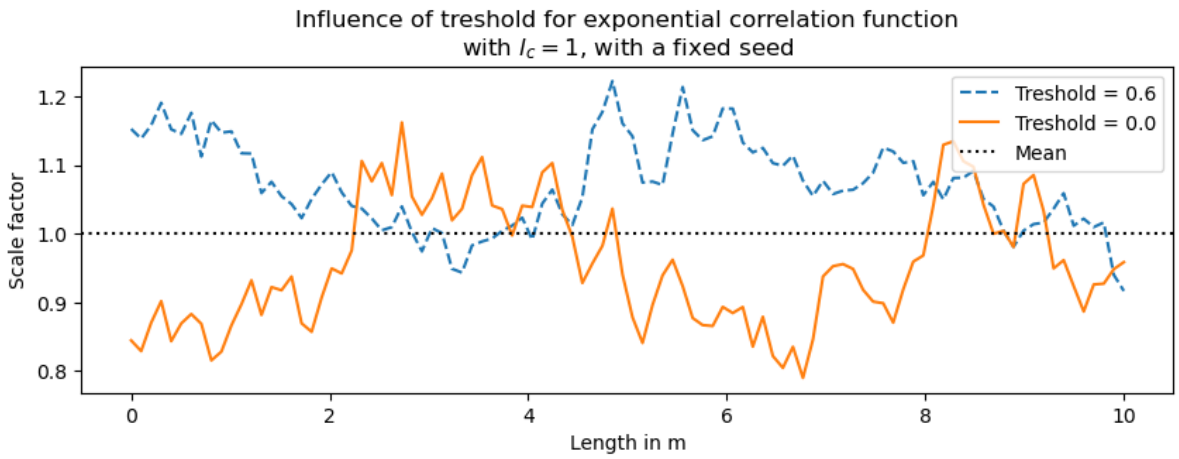

Figure D.20: Influence of the threshold option 1

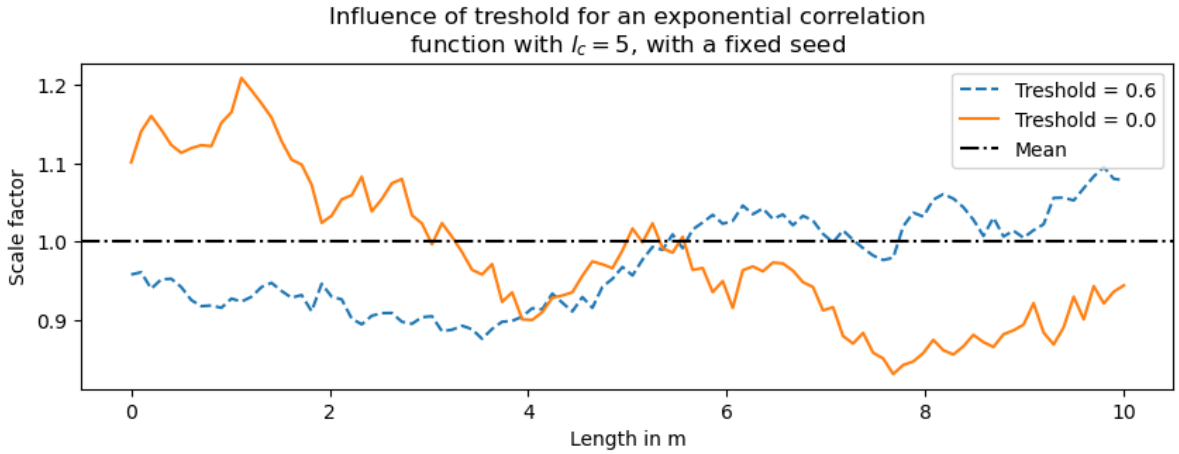

Figure D.21: Influence of the threshold option 2

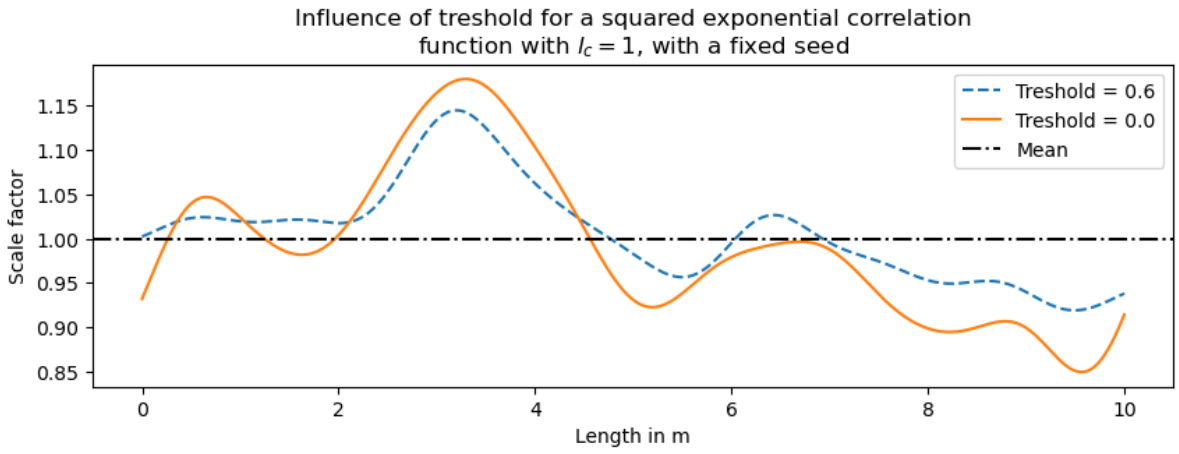

Figure D.22: Influence of the threshold option 3

Decomposition method

Figures D.23 and D.23 show that the decomposition method in the random field generation algorithm does give different random fields for a fixed seed. However, when you look at multiple realisations of the random fields, the general results all look similar. This was checked by generating 1000 random fields with both decomposition methods. The average mean (averaged over these 1000 random fields) and average standard deviation was equal for both decomposition methods. Therefore it can be concluded that the decomposition method does not influence the results when multiple samples are considered.

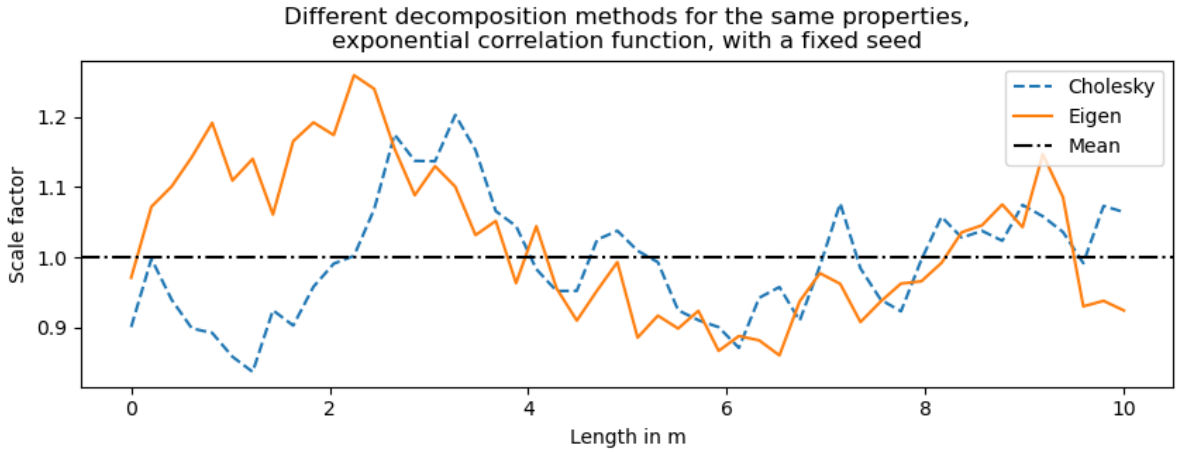

Figure D.23: Influence of the decomposition method 1

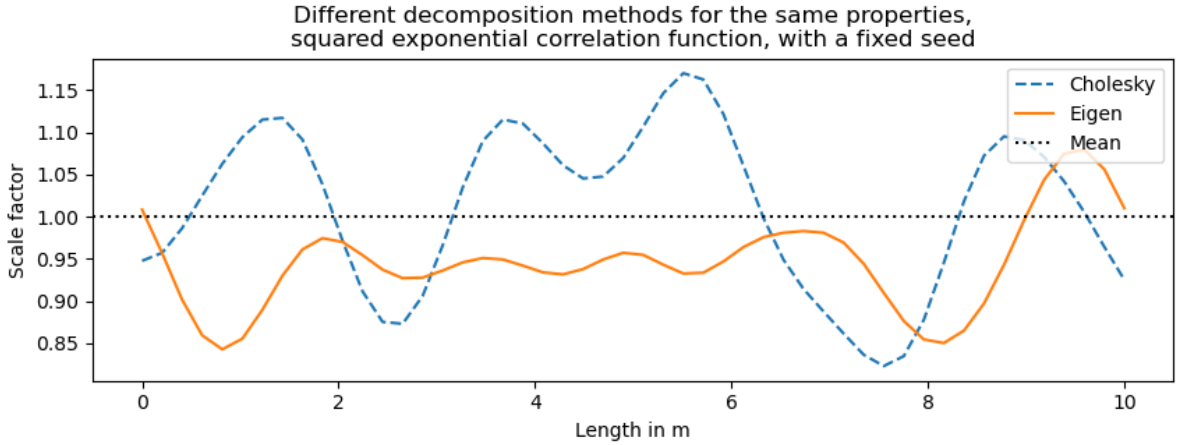

Figure D.24: Influence of the decomposition method 2

D.6. Input and output standard deviation

Table D.1 shows the average standard deviation of 10,000 random fields. The input standard deviation is 0.2 in all cases. Columns two and three report the average standard deviation of 10000 random fields, for different correlation lengths for a 3D and 1D random field. It can be seen that for small correlation lengths, the output standard deviation is closer to 0.2 than for larger correlation lengths. This is expected behaviour. Uncorrelated random fields will return exactly the input standard deviation of 0.2. There is no difference between 1D and 3D random fields.

A correction factor can be calculated by dividing the input standard deviation (0.2) by the output standard deviation. The corrected input standard deviation in column 6, can be calculated by multiplying the correction factor with the regular input standard deviation of 0.2. These adapted input standard deviations will result in an output standard deviation of 0.2. For example, an input standard deviation of 0.251 for a random field with a correlation length of 5m, will result in an average standard deviation of 0.2 when multiple random fields are generated.

Table D.1: Mean ouput standard deviation of 10000 random fields

Correlation length [m]	3D RF $\sigma = 0.2$	1D RF $\sigma = 0.2$	Difference	Correction factor (0.2 / 1D RF column)	Adapted input standard deviation
0.5	0.201	0.195	97%	1.025	0.205
1	0.194	0.190	98%	1.049	0.210
2	0.184	0.181	99%	1.100	0.220
5	0.159	0.159	100%	1.256	0.251

E

Thermal properties of concrete from literature

Conductivity values of concrete

Table E.1: Conductivity values of concrete found in literature in [$Wm^{-1}K^{-1}$]

Nr.	Value	Notes	Source
1	1.4 - 2.5	Depending on different concrete mixtures	Guo et al. (2011)
2	2.6	Guidelines	ROK 1.4 (2017)
3	2 - 3	Strongly depend on mix composition and aggregates	van Breugel et al. (2016)
4	1 - 2.5	Range for different types of concrete at different ages in wet conditions. Paper explorers all type of different influences on the Conductivity.	Kim et al. (2003)
5	2.65	Assumed in the research	Aniskin and Nguyen (2019)
6	1.7 - 2.3	Assumed in the research	Lee et al. (2009)
7	1.4 - 2	Eurocode concrete structures and fire	NEN-EN 1992-1-2
8	0.2 - 3.9	Wide literature review of values (low values are for very lightweight concrete)	Asadi et al. (2018)
9	3.5	Steel fibre concrete with high dosage	Asadi et al. (2018)
10	2 - 2.5	-	Achenbach et al. (2017)

Table E.2: Heat transfer coefficients found in literature in [$W\,m^{-2}K^{-1}$]

Nr.	Value [range]	Type	Flow / wind speed [m/s]	Notes	Source
1	13 - 22	Wind	1.8 - 3.6	Depending on different concrete mixtures and different wind speeds	Guo et al. (2011)
2	5.6 - 17.6	Wind	0 - 3	Guidelines	ROK 1.4 (2017)
3	111 - 695	Water	Stagnant - Flowing	Only values are given, no flow speeds. Values for free convection, states that for forced convection, values can get as high as 11000.	van Breugel et al. (2016)
4	5.6 - 83	Wind	0 - 25	Also gives formula for coefficient depending on wind speed.	van Breugel et al. (2016)
5	12	Air	0	Research is about cooling pipes in mass concrete, coefficient is for concrete and surroundings though	Aniskin and Nguyen (2019)
6	90 - 1050	Wind	0.1 - 1.3	Research is about air through cooling pipes, coefficient is between concrete and pipes.	Yang et al. (2011)
7	8.1 - 29.3	Wind	0 - 4.3	Article gives an extensive overview of measured coefficients. Also gives values for curing methods with blankets (not included in this table)	Lee et al. (2009)
8	4 - 25	Wind	-	Based on exposure to fire	Achenbach et al. (2017)
9	1000	Water	Pipe flow	Assumed in research, coefficients between concrete and a cooling pipe with flowing water	Charpin et al. (2004)
10	50 - 250	Water	5 - 20 ml/min	Research on the influence of surface roughness on heat transfer characteristics, water under pressure through a crack.	Ma et al. (2019)

F

PROBAB

F.1. Outline

- Outline
- General: explain what was done with PROBAB and why we stepped away from it
- PROBAB explanation: document all the things that were learned from working with PROBAB, and what the issue is with the current model with random fields
- Recommendations: Give possible solutions and fixes
- Exercise with PROBAB and verification

F.2. General

Initially, the aim was to use the built-in probabilistic analysis of the FE package DIANA, which is called PROBAB. At a given point, it turned out that the package's functionality was not yet developed enough to combine it with the FE model, so we switched to a separate probabilistic analysis in Python. The main issues were the combination of random fields and the time aspect with the PROBAB module. The parts that were already done with this module are included in this thesis, so it might function as a starting point for someone who wants to use the PROBAB module. This also includes a part of the literature review. Sections 2.4.4 and 2.4.5, which are about directional sampling (with a response surface) explain the algorithms that are used in the PROBAB module, which are based on a Monte Carlo algorithm.

Some of the problems we encountered were fixed by the team from DIANA, but other problems remained. An exercise with a simply supported steel beam was done in order to verify the results produced by PROBAB with an analytical solution for the failure probability. A second exercise was done to get familiar with fibre-reinforced concrete and how this could be optimised for use in combination with PROBAB.

F.3. PROBAB verification: Steel beam - Linear static

In this appendix, the PROBAB module in DIANA will be explored. It is important to investigate the influence of different settings and how to program the module in the DIANA text files. Moreover, the module has not yet been fully verified and the steps the module takes are a bit of a ”black box”. There-

fore some verification is needed, which is done by creating two simpler models that can be verified. The first model is a steel beam with a linear static calculation with an analytical solution that lends itself to a relatively simple verification with a Monte Carlo analysis. These results can be compared to the software Probabilistic Toolkit from Deltares (PTK), which is capable of running MC analysis given certain stochastic properties and a particular limit state. The second model is a notched FRC beam. This model is more difficult to verify since it already uses a nonlinear calculation, making it impossible to verify the results with the PTK. This model was chosen since it consists of FRC, which will also be the case in the final model and the standardised notched beam tests have a lot of references in literature.

F.3.1. Model

General

The model is a simply supported beam with span $L = 5$m and a distributed load q.

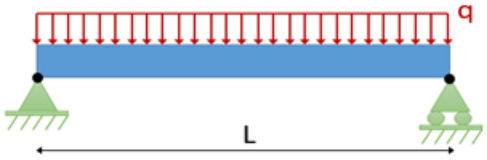

Figure F.1: Mechanics Scheme

Material properties

Table F.1: Material Properties Steel S355

Material property	Symbol	Value	Unit	DIANA value	Unit
Yield strength	f_y	355	MPa	$3.55 \cdot 10^8$	N/m^2
Young's modulus	E	210	GPa	$2.10 \cdot 10^{11}$	N/m^2
Poisson's ratio	ν	0.3	-		
Mass density	ρ	7800	kg/m^3		

A steel IPE200 profile is being used in this example, which has a height of 200 mm. and a moment of inertia of $I_y = 1.846 \cdot 10^7 mm^4$.

Analytical calculation

$$u = \frac{5}{384}\frac{qL^4}{EI_y} = \frac{5}{384} \cdot \frac{20 \cdot 10^3 \cdot 5000^4}{210000 \cdot 1.846 \cdot 10^7} = 41.99\text{mm}$$

Some characteristic parameters for the model are:

- A load of 21 kN will lead to a stress of 355.57 MPa, which is the yield stress.
- A load of 20 kN will lead to a displacement of 41.99 mm.

F.3.2. FEM

Ten elements along the length of the beam were used. This model returns the same result as the analytical solutions for the stress and the displacement. Class-II beam elements were needed to define the yield strength in the material property. Since Class-I beams elements are evaluated analytically in a linear manner, the yield strength is not a property for these elements.

The DIANA model was verified with hand calculations, the results are given in the table below.

Table F.2: Mesh properties

	Class-I beams 2D	Class-II beams 2D
Element type	L6BEN	L7BEN
Mesh order	Linear	Linear
Mesh size	0.5 m	0.5 m
Integration	Analytical	Numerical

Table F.3: Verification of DIANA model

Property	DIANA Class-1	DIANA Class-2	Hand Calculation	Unit
Maximum moment	31.25	31.25	31.25	KNm
Maximum stress	169.32	170.45	169.32	N/mm^2
Displacement	21.00	21.00	20.997	mm

F.3.3. Limit states

DIANA has different limit state (LS) options: a direct limit state and an inverse limit state. The limit state is always defined as $Z = R - E$, where R indicates the resistance of the model and E indicates the loading of the model. The limit state is considered as failing when $Z < 0$, or in other words when the loading exceeds the resistance.

As mentioned there are two options in DIANA, you can assign either the R or the E to a calculated value from the DIANA FE model and the respective other parameter is defined in the probabilistic module, which is called the critical parameter. This can either be a stochastic distribution or a deterministic value. These two options are indicated as a direct or an inverse limit state.

Direct	Inverse
$Z = R\{X\} - E$	$Z = R - E\{X\}$
(Calculated - Critical)	(Critical - Calculated)

In this table, ”calculated” means that it is an output from the DIANA FE model, and the critical parameter is a user-defined parameter.

So for example, when the requirement of a structure is the maximum stress in the structure and that may not exceed the yield stress, this would result in the following limit state:

$$Z = R - E\{X\} = f_y - \sigma_{max} \tag{F.1}$$

So when the maximum stress would exceed the yield stress this would for example lead to:

$$Z = R - E\{X\} = f_y - \sigma_{max} = 355 - 400 = -45 < 0$$

Which would lead to a failing limit state. In this case the maximum stress is the result from the FE model and is therefore called the calculated parameter, while the yield stress is a user defined value, which is called the critical parameter. From the table above, one can see that this is the inverse limit state.

The stochastic vector $\{X\}$ indicates that this calculated parameter can be a result of different stochastic input parameters. For example the maximum stress can vary between samples, when a stochastic load or for example a stochastic moment of inertia is chosen. The critical parameter, which is the other

one, can be a deterministic value or it can be a stochastic distribution, such as the normal distribution for instance. In the latter case, there also will be a different value for every sample for the critical parameter.

F.3.4. Probabilistic Analysis and Results

For the first models a displacement limit state is adopted in the following (inverse) form:

$$Z = R - E\{X\} = u_{max} - u\{X\} \tag{LS.A}$$

Where u_{max} is the maximum allowable displacement and u is the calculated displacement of the model. In this configuration both u_{max} and u should be positive values.

Stochastic critical limit state parameter

The most simple model is the steel beam model described in section F.3.1 with only a stochastic critical parameter, where u_{max} has a normal distribution with a certain mean and a certain standard deviation, which is indicated as $N(\mu;\sigma)$. For these variations the standard deviation was set to 4 mm. and the mean was varied. The results are given in figure F.2. The parameters of the probabilistic calculation are given in table F.4.

Table F.4: Probabilistic calculation settings

Method	Coefficient of variation C_v	LS Convergence criterion	LS type
Directional sampling	0.1	0.01	Inverse

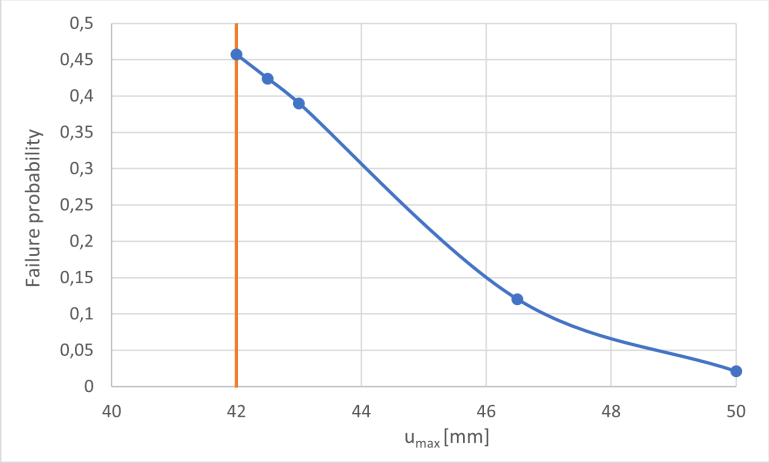

Figure F.2: Failure probability as a function of a different u_{max}

It can be seen that only results are obtained for $u_{max} > 42$, below this value DIANA only returns an error that the initial limit state must be positive and greater than the convergence criterion. Remember that the calculated parameter, which is the actual deflection results in 41.99 mm. It turns out that for values $u_{max} < 42$, DIANA is unable to produce results. This happens when the LS is negative, for instance:

$$Z = R - E\{X\} = u_{max} - u\{X\} = 40 - 41.99 = -1.99$$

Furthermore, it can be concluded that these results are logical results, because a larger maximum allowable u_{max} leads to a lower failure probability.

The failure probability can be calculated analytically in the following way. First the limit state has to be transformed to one single standard normal distribution by the method given in equation F.2.

$$z = \frac{X - \mu}{\sigma} \tag{F.2}$$

Following this procedure the following results are obtained:

$$u_{max} - u = N(40, 4) - 41.99 \rightarrow \frac{40 - 40}{4} - \frac{41.99 - 40}{4} = 0 - 0.4975 = -0.4975 \tag{F.3}$$

The failure probability of the limit state $Z < 0$ can then be calculated with:

$$P(Z < 0) = P(z < -\beta) = P\left(z < -(0.4975)\right) = 0.6906 \tag{F.4}$$

Figure F.4 shows more or less the same failure probability for this u_{max}, that is obtained with the PTK.

Errors and lessons learned

The approach in the previous chapter is the second generation of models, first a different approach was tried. Because the displacement of the model is negative, the limit state above would never result in a value lower than 0 with a negative calculated value ($u_{max} - -u = u_{max} + u$), this would never lead to a failing limit state, and this has to be solved. In the first iterations of the model the limit state was switched around to LS. B (direct) and negative values were adopted for the critical parameter, resulting in:

$$Z = E\{X\} - R = u\{X\} - u_{max}, \text{ where } u \text{ and } u_{max} < 0 \tag{LS.B}$$

Which results in (for the characteristic values from section F.3.1 and for example a maximum displacement of 40 mm.):

$$Z = u\{X\} - u_{max} = -41.99 - -40 = -1.99$$

This results in a failing limit state, which is correct, because the absolute value of the maximum allowable deflection is smaller than the actual calculated deflection. However, this is actually a wrong limit state, since the E and R are switched around. This leads to the confusion if DIANA is now calculating the failure probability P_f or the 1-P_f. The results of this approach are given in figure F.3. The problem seemed to be fixed, but DIANA produces some weird results. So for the second generation of models, the model was made in such a way that it would result in a positive deflection and LS. A was adopted, which results in a more logical limit state which can be seen in section F.3.4.

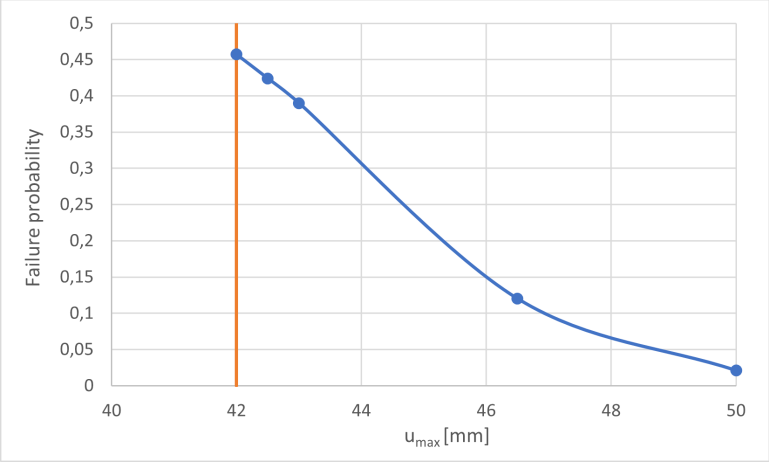

Figure F.3: Failure probability as a function of a different u_{max}

From this figure it can be seen that the smaller the absolute value of u_{max} is, the lower the failure probability is, while one might expect exactly the opposite. Therefore one might expect that with this

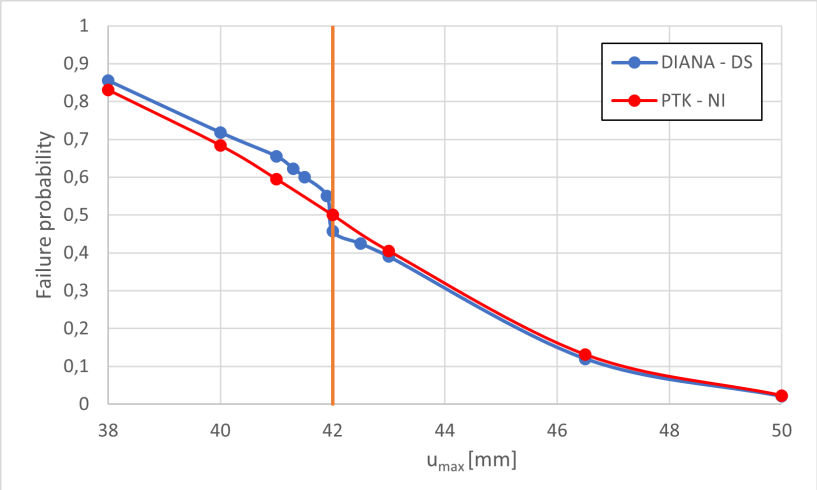

Figure F.4: Failure probability as a function of a different u_{max}.
The results of $u_{max} < 42$ are the complementary results $(1 - P_f)$ of F.3

configuration, actually the complement of the failure probability 1-P_f is calculated. When these graphs are plotted back to back, a weird jump in the line can observed, as can be seen in figure F.4.

The error that is returned is as follows: *"ERRORMSG.W: Initial calculation gives an invalid result for limit state (g). Initial limit state must be positive and greater than convergence criterion."*. Since the error occurs when the failure probability reaches 0.5, it is suspected that this causes the error, because a failure probability of 0.5 is expected when the limit state function evaluation (LSFE) is 0. This can also be seen from the LSFE's below.

Table F.5: LSFE's for different u_{max} with LS. Conv. = 10^{-5}

u_{max}	u_{calc}	LSFE	P_f
46.5	41.99	4.51	0.119
43	41.99	1.01	0.367
42	41.99	0.01	0.457
41	41.99	-0.99	Error
40	41.99	-1.99	Error

Later on this is confirmed by the DIANA help desk that this is the case, because for a $P_f > 0.5$, the corresponding reliability index β becomes negative. For normal structural applications, this is not a problem, since we are most of the time only interested in very small failure probabilities, but for a limit state based on crack width, failure probabilities of 1 should also be expected.

Influence of probabilistic settings

The standard settings of the PROBAB calculation are given in table F.4. In this section, we look at different variations of these properties. The failure probability for a $u_{max} = 43$ should converge to 0.4003, which is the exact analytical solution. Throughout this chapter the force is kept constant to 20 kN.

Coefficient of variation

The coefficient of variation of the failure probability is defined as:

$$C_v = \frac{\sigma(P_f)}{P_f} \tag{F.5}$$

In which:

$$\sigma\left(P_{\mathrm{f}}\right)=\sqrt{\frac{1}{N(N+1)}\sum_{i=1}^{N}\left(P_i-P_{\mathrm{f}}\right)^2} \tag{F.6}$$

Where N is the number of samples, P_i is the failure probability for each sample and P_{f} is the total probability of failure, which is expressed as:

$$P_{\mathrm{f}}=\frac{1}{N}\sum_{i=1}^{N}P_i \tag{F.7}$$

The coefficient of variation of the failure probability is a measure of convergence. When it drops below a certain maximum user-defined value, the calculation is considered as converged and will be terminated, provided that the maximum number of samples (user-defined) has not been reached. As can be seen from table F.6a, the failure probability does not necessarily monotonically converge to a certain value when reducing the maximum allowable C_v. This is indicated by the fact that the failure probability corresponding to a C_v 0f 0.01, which is considered to be the most precise, is closer to the P_{f} corresponding to a C_v of 0.2 than the one corresponding to a C_v of 0.1. This convergence behaviour is illustrated in figure F.5, in which it can be seen that the failure probability dangles around a certain value for a decreasing $\sigma(P_{\mathrm{f}})$ (and thus C_v). This behaviour is also shown in figure F.6b.

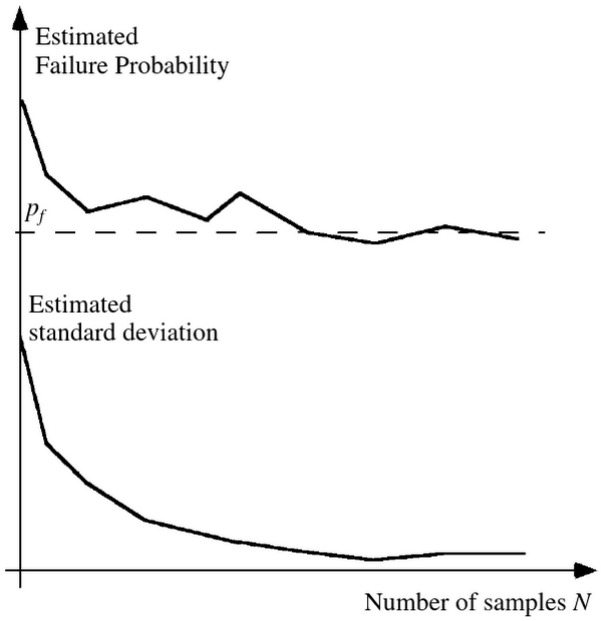

Figure F.5: Convergence of the failure probability for an increasing sample size N.
From Melchers and Beck, 2018, p. 71

Limit state convergence criterion

The limit state convergence criterion (LSCC) is another setting that can be changed. The probabilistic methods are searching for points that lie on the limit state function, which are the points where the limit state (Z=R-E) equals 0. In practice it is not possible to find the exact point of 0, but this will always be a very small number where it is considered 0. The tolerance criterium for how much the actual value can differ from 0 is called the LSCC. In table F.6b, similar analyses were done with a varying limit state convergence criterion. This table shows that for small failure probabilities, it does not matter to decrease the failure probability, since the results will be approximately equal. However, for larger failure probabilities a difference of around 2% occurs. For a $u_{max}=42$, the lower LSCC does produce

Table F.6: Variations of different PROBAB settings with directional sampling (DS)

C_v	P_f	Samples	Run time
0.35	0.569	4	< 1 min.
0.3	0.474	10	1 min.
0.2	0.418	24	3 min.
0.1	0.390	119	10 min.
0.05	0.409	435	23 min.
0.01	0.427	9985	28 hours

(a) Failure probability for different coefficients of variation (C_v) for $u_{max} = 43$ with corresponding run time. The exact value is $P_f = 0.400$

	LSCC.			
u_{max}	10^{-2}	10^{-3}	10^{-5}	Analytical
41	Error	Error	Error	0.598
42	Error	Error	0.457	0.499
43	0.390	0.367	0.367	0.400
46.5	0.120	0.120	0.119	0.130
50	0.021	0.021	0.021	0.023

(b) Failure probability for different LS convergence criteria (10^{-2} or 10^{-5}) and the exact value. $C_v = 0.1$

a result, since the other one produces an error. This has to do with the fact that the higher accuracy of the calculation produces a limit state that is just larger than 0 and the other one does not. The result should be 0.01. When taking the extra run time in consideration, which is around 1.5 to 1.8 times as long, it can be concluded that in general it is not necessary to reduce the LSCC lower than 10^{-2}.

Methods

The method of Directional Sampling (DS) has mostly been used, since the more advanced Directional Adaptive Response Surface (DARS) method does not work with such simple models. For these models with a linear static analysis it is not necessary to create a response surface, since the linear analysis is equally quick. When you use the DARS procedure it basically reduces to regular DS. The other option that was tried is the First Order Reliability Method (FORM). Firstly it can be seen that the failure probability which is found with DS ($p_f = 0.427$, table F.6a) with $C_v = 0.01$ corresponds with the failure probability that is found with the FORM (table F.7a). There is however a big time difference, since the DS took over 28 hours, while FORM took less than one minute to run.

From table F.7a, it can be seen that either decreasing the C_v or increasing the number of samples does not change the failure probability. This is because FORM uses a linear approximation of the limit state function in the design point, which is not dependant on these factors for this model. It can however be seen that when the LSCC is decreased, that it does change the failure probability. As can be seen from table F.7b, the failure probability seems to converge to 0.401. Which is a good result since the analytical solution is 0.4003.

Table F.7: Variations of different PROBAB settings with FORM

C_v	# samples	P_f
0.1	10	0.427
0.1	200	0.427
0.1	5000	0.427
0.01	200	0.427
0.01	5000	0.427

(a) Results for FORM with different C_v and # of samples for $u_{max} = 43$

LSCC.	P_f
10^{-2}	0.427
10^{-3}	0.404
10^{-4}	0.401
10^{-5}	0.401
10^{-7}	0.401

(b) Results for FORM with different LS. Convergence criteria for $u_{max} = 43$

Comparison with the probabilistic toolkit

With DS and a C_v of 0.1, a comparison was done with the Probabilistic Tookit (PTK) of Deltares. The results are displayed in table F.8.

Table F.8: Different Probab settings for $u_{max} = 43$

u_{max}	DIANA	PTK
38	Error	85.6
41	Error	63.7
42	Error	54.8
42.5	42.4	49.3
43	39.0	45.7
46.5	12.0	14.8
50	2.10	2.60

(a) Failure probability as a function of u_{max}

C_v	DIANA	PTK
0.1	39.0	45.7
0.01	42.7	40.5
0.001	-	40.0

LSCC	DIANA	PTK
10^{-2}	39.0	45.7
10^{-5}	36.7	45.7

(b) Failure probability in %, DIANA compared with PTK

The PTK is a toolkit in which analytical limit states can be entered together with certain probabilistic distributions for certain variables, which then calculates the failure probability with different methods. The nice thing about the PTK is that it includes the options to do DS, DARS and FORM. The results in table F.8a show quite large differences.

Figure F.6a shows a converging failure probability for a decreasing coefficient of variation, while figure F.6b shows that this convergence behaviour is not monotonic for a decreasing coefficient of variation.

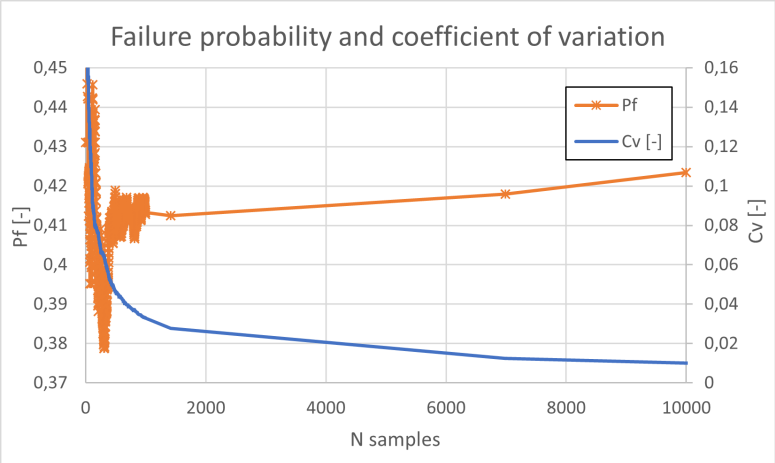

(a) Failure probability and coefficient of variation as a function of N samples

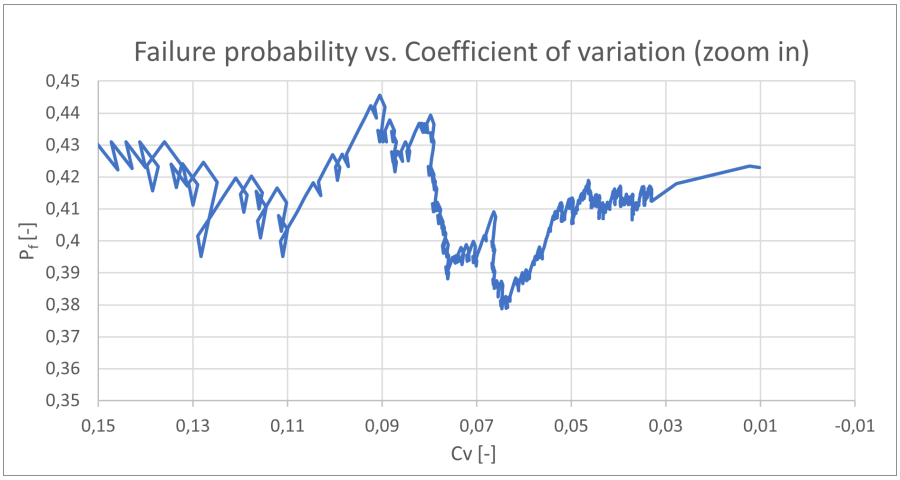

(b) Failure probability as a function of a decreasing coefficient of variation

Figure F.6: Failure probability for the PTK results

Table F.9 shows the different failure probabilities for $u_{max} = 43$ and $C_v = 0.01$. Numerical integration is considered to be an exact calculation of the failure probability. It can be seen that DS and DARS return the exact same results with less samples needed than Crude Monte Carlo and importance sampling. This is also the reason that these methods together with the FORM are implemented in DIANA. The FORM returns almost the exact results with very few samples. The failure probability that was acquired with FORM corresponds exactly to the converged value of table F.7b.

Table F.9: Comparison of PTK methods

Method	p_f	Samples
Numerical integration	0.405	-
Crude Monte Carlo	0.404	14773
Importance Sampling	0.398	27055
Directional Sampling	0.405	9815
DARS	0.405	9815
FORM	0.401	4

Multiple stochastic properties

To get a more realistic model, the force can also be made stochastic, whilst keeping a deterministic value for u_{max}. The results are given in the table F.10a. Everything else is kept constant with $C_v = 0.1$.

Table F.10: Failure probability calculated with DIANA vs PTK (Directional Simulation and Numerical Integration)

u_{max}	DIANA - DS	PTK - DS	Anaytical
42	-	0.504	0.500
43	0.445	0.428	0.405
45	0.260	0.250	0.236
47	0.128	0.123	0.116
50	0.031	0.030	0.028

(a) Failure probability as a function of u_{max}, with stochastic force $N(20, 2)$

Force	DIANA - DS	PTK - DS	Analytical
$N(15, 2)$	0.003	0.003	0.003
$N(17, 2)$	0.045	0.043	0.041
$N(19, 2)$	0.252	0.242	0.229
$N(20, 2)$	0.445	0.428	0.405
$N(21, 2)$	-	0.607	0.602

(b) Failure probability as a function of a stochastic force, normally distributed with $N(\mu, \sigma)$

Table F.10b shows the comparative results for a changing stochastic force and a constant $u_{max} = 43$. In these graphs the solution that is produced by numerical integration are considered to be exact. It can be seen that DIANA consistently returns higher failure probabilities. It should be noted that when PTK-DS with a $C_v = 0.01$ is done, these values tend to the values given by PTK-NI. This can also be seen from table F.11. In this table multiple stochastic properties are defined.

Table F.11: Failure probability calculated with DIANA vs PTK for multiple stochastic properties

u_{max}	Force	DIANA	PTK - DS $C_v = 0.1$	PTK - DS $C_v = 0.01$	PTK - NI
$N(43, 4)$	$N(20, 2)$	0.517	0.505	0.437	0.431
$N(42, 2)$	$N(20, 2)$	Error	0.540	0.500	0.507

For a $u_{max} = N(43, 4)$ and a $q = N(20, 2)$, the following images are obtained from the PTK. In figure F.7, the realisations of the directional simulation are given. The limit state line can clearly be observed. For this calculation four notes are made:

- The FORM calculation in PTK returns the exact same value as Numerical integration (exact value).
- The FORM calculation in DIANA returns a failure probability of 0.453, which is closer to the exact value than the failure probability that is obtained with DIANA-DS. From literature, generally a level 3 method such as DS should be more accurate than a level II method such as FORM but this is dependent on the settings of both analyses and the amount of samples in DS. It is to be expected that for a more complex model with enough samples, DS is the more reliable method.
- The FORM calculation in DIANA is besides more accurate for this particular problem, also significantly quicker (<1 min.) as opposed to the DS in DIANA (6 min.).

Figure F.8 shows the influence factors that are determined from the analysis. The design point consists of a contribution per stochastic variable and a reliability index. The contribution in standard normal space (u-space) is denoted with a α_f and it can be obtained from:

$$u_f = -\beta \alpha_f \tag{F.8}$$

Where u_f is the value of the variable in the u-space. The sum of all alpha values squared should equal to 0 (Deltares, 2021). Which for the example in figure F.8 is true. The influence factors that are given in figure F.8 are simply the α_f values squared.

The sign of the alpha values is important, since it indicates whether an increase of that parameter causes the result to move more towards the failure area or the non failure area (Deltares, 2021).

- Positive a_f: A higher value of the corresponding variable would go into the non failure area (Z > 0) and thus the failure probability will decrease.
- Negative a_f: A higher value of the corresponding variable would go into the failure area (Z < 0) and thus the failure probability will increase.

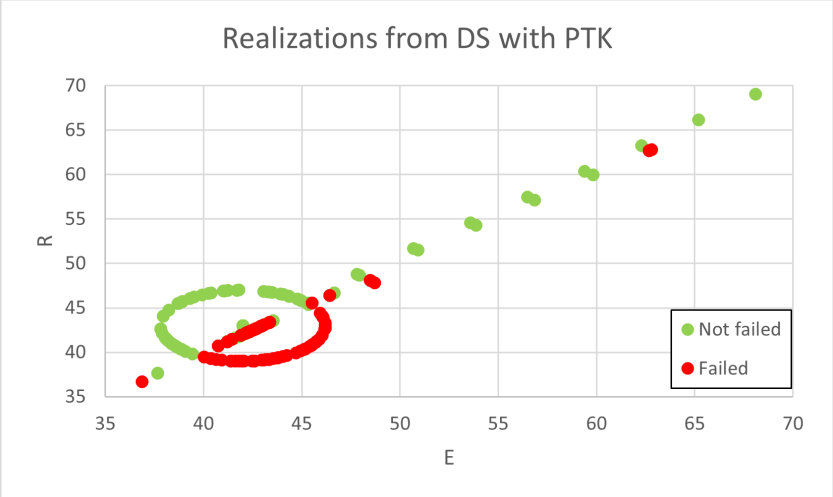

Figure F.7: Directional simulation in PTK

Variable	Alpha [u]	Influence factor [%]	Physical value [x]	Limit state value [x]
q	-0,667	44,523	19,984	20,232
u_max	0,745	55,477	43,035	42,482

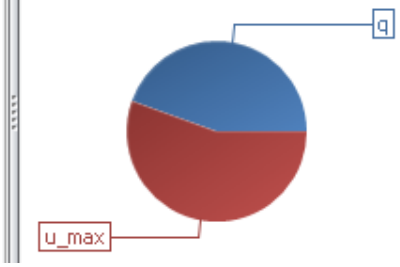

Figure F.8: Influence factors obtained with PTK

G

Notched fibre reinforced concrete beam

The modelling of a standard Notched FRC beam (standard testing method according to Model Code 2010) in DIANA FEA was done as an introductory exercise for this thesis. This analysis will be done to investigate the properties of FRC and to find the right convergence settings in DIANA FEA and the PROBAB settings for crack width-based limit states, as will be the case for the final UWC floor model. It also makes use of a nonlinear analysis, which works slightly differently in the PROBAB module.

DISCLAIMER: After we opted not to continue with the PROBAB module, this chapter has also not been continued, nor revised. Please note that some information might be incomplete. Nevertheless, the lessons learned from this exercise were very valuable in some aspects of this thesis. Examples of this are the convergence settings and the experimental validation that was done in this appendix.

G.1. Model

A standard fibre reinforced concrete notched beam will be analysed in accordance with the guidelines given in NEN-EN 14651 (2007). The model and dimensions are shown in figure G.1. A prescribed displacement will be applied in the middle.

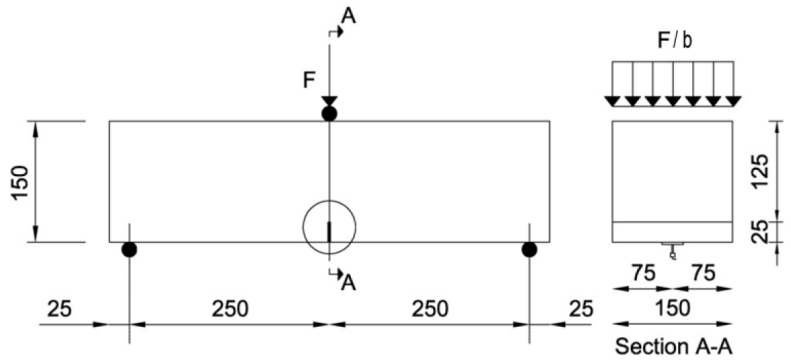

Figure G.1: Model overview, dimensions in mm. From NEN-EN 14651 (2007)

G.2. FEM

The mesh is displayed in Figure G.2. CQ16M and CT12M elements were used with a size of 4mm in

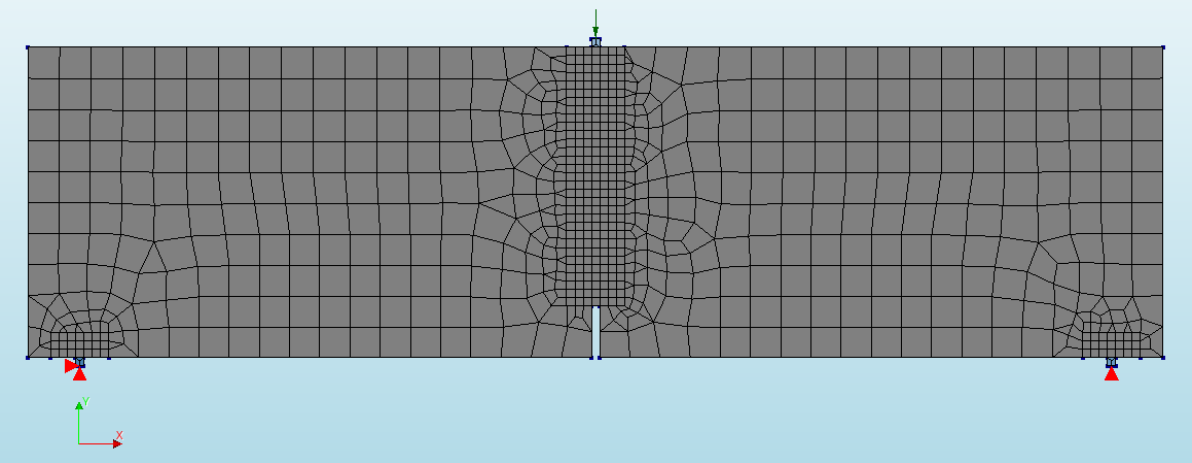

Figure G.2: Mesh of the model

the zones of interest around the supports and along the the crack and 15mm in the rest of the beam. A prescribed displacement of 4 mm was used in the middle of the beam.

Material properties

The material properties are similar to the standard material that is used in the CROW model. This material is based on the properties of C30/37 according to the EC2 and the post cracking behaviour of FRC according to the MC2010 in class 4c with characteristic values $f_{\mathrm{R1k}} = 4.0\,\mathrm{N/mm^2}$ and $f_{\mathrm{R3k}} = 3.6\,\mathrm{N/mm^2}$. The material properties that were deduced from these standards are shown in Figures G.3 and G.4. The corresponding stress - CMOD graph is shown in Figure G.5.

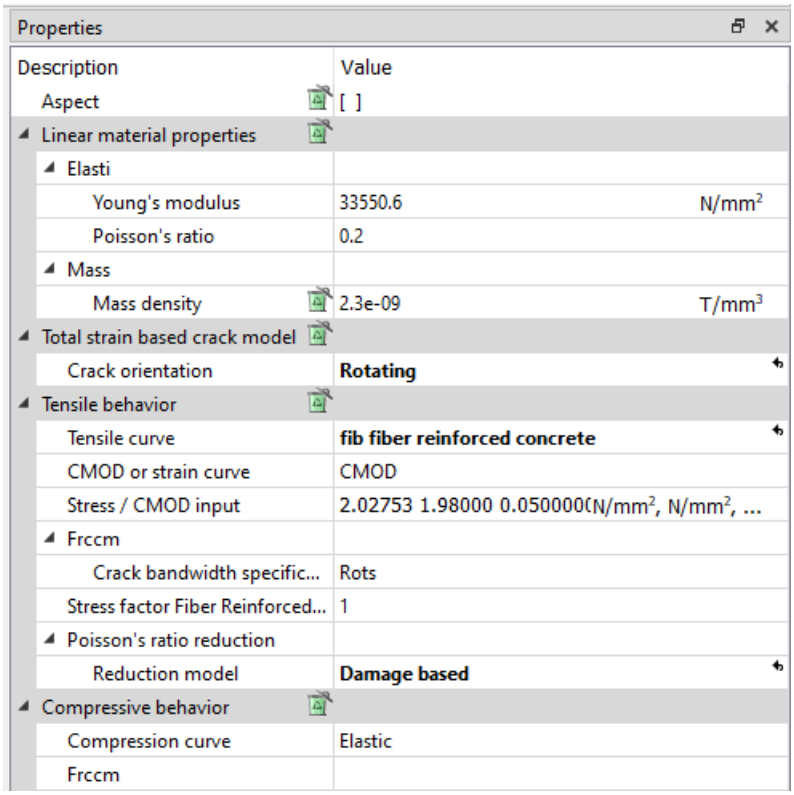

Figure G.3: Material properties

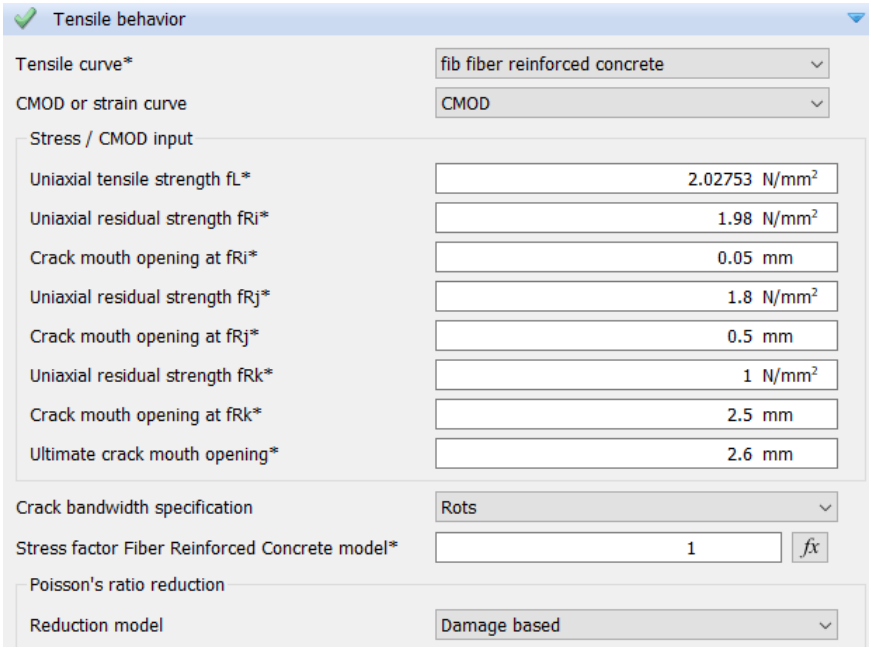

Figure G.4: Tensile behaviour properties

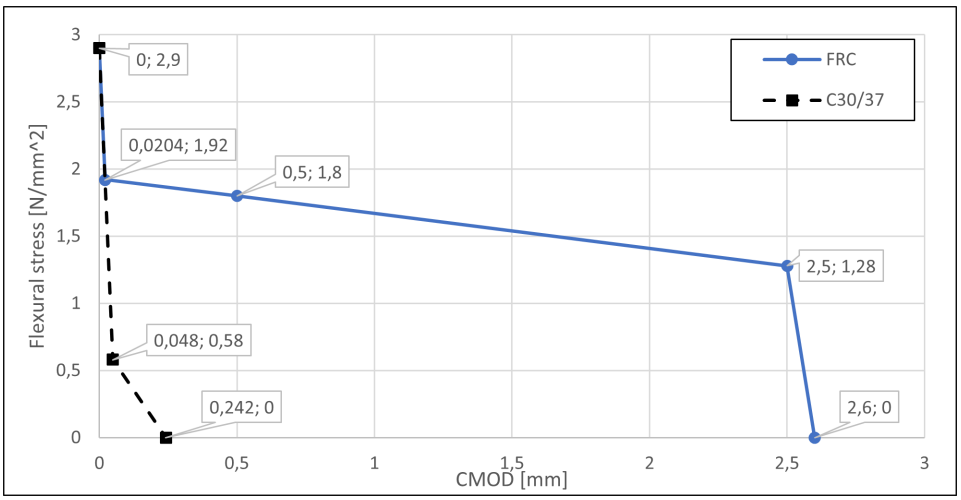

Figure G.5: Stress - CMOD graph of the material input

FEM settings

Figure G.6 shows the force-displacement graph of the model. A couple of different analyses were performed to show the effect of different settings. All analyses have step sizes of 0.01(5) 0.001(150) 0.005(200) 0.01(280). The convergence criteria were varied and are given in table G.1. Model A converges simultaneously on the energy and the force criterion. For models B and C, the force criterion is set to the large value of 0.9, so all the steps will converge on this criterion relatively fast and these models basically only use the energy criterion. This is done so the value of the force criterion is can be plotted in the convergence graphs.

Model	Convergence Criteria
A	Energy (0.001) AND Force (0.01)
B	Energy (0.0001) AND Force (0.9)
C	Energy (0.001) AND Force (0.9)

Table G.1: Convergence Criteria of the different models

Model D is similar to model C, except it uses a slightly different material input. As is shown in Figure G.5, the final point of the graph is situated at a CMOD value of 2.6 mm, which creates an almost straight down branch in the graph. Soetens and Matthys (2014) among other literature suggest a more gentle sloping last branch. In model D the end point is changed to a CMOD value of 5 mm.

Optimization for probabilistic analysis

The quickest of these models had a run time of 25 minutes, which is too long, when it needs to be combined with a probabilistic analysis in DIANA. Therefore a final model E was created which was made as fast as possible, without compromising too much on the results. Model E uses the same convergence criteria as Model A, but uses step sizes of 0.01(30) 0.1(17) and a maximum number of 10 iterations.

G.3. Results

Figure G.5 shows the stress displacement graphs of the models. It can be seen that models A, B and C are all in nice unison with each other. However a kink in the graph can be observed. This kink occurs when the stress in the element that is situated on the low side of the crack (right above the notch) reaches the final point of a CMOD value of 2.6 mm in figure G.5. This element is then essentially broken, which means that the remaining height over the beam is decreased, hence resulting in a kink in the load-displacement graph. This is supported by the fact that model D, which has a higher failure CMOD value of 5 mm, as indicated in the previous section, does not display a kink in the results. Finally The optimized model E for the probabilistic analysis differs a bit from the other results in absolute values, but the behaviour is well described. The model only runs to a displacement of 2 mm, but that is sufficient, since it captures the post peak response and the kink in the graph. Therefore this model will be used in the probabilistic analysis.

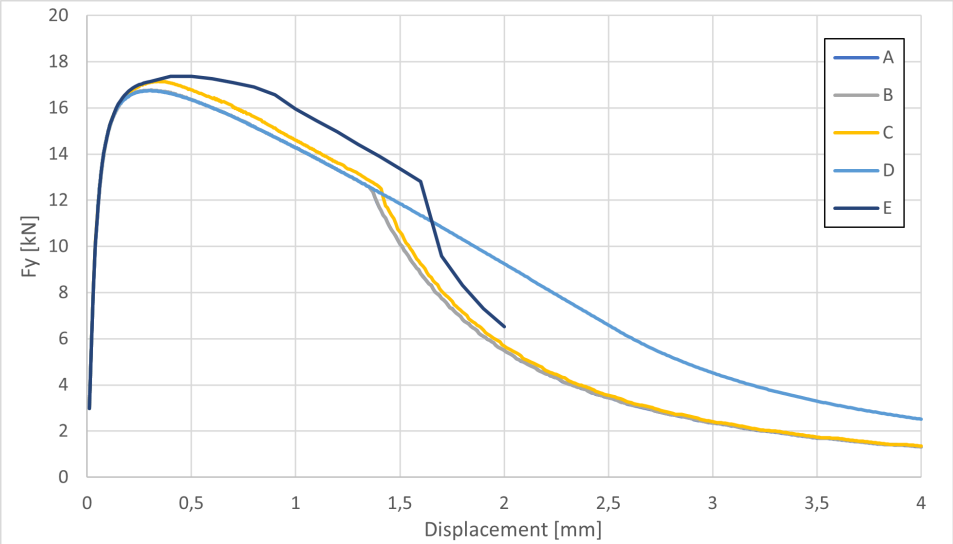

Figure G.6: Force-displacement graph of the FEM

Crack width location

The crack width results can be seen in figure G.7. In the lower element in the crack it can be observed that there is a linear variation of the crack width over the width of the element. This raises the question if this gives a correct value of the crack width when it is needed for the limit state. Therefore, different locations of the crack width were plotted in the crack mouth opening and these were compared with the difference in lateral displacement of the nodes directly on the sides of the crack mouth. These locations included the integration points, the nodes (left, middle and right) and the element center. The results are shown in the figure G.8. From this figure it can be seen that the values for the middle node and the element center exactly correspond with the actual CMOD value. Therefore the element center is chosen as the location to plot the crack widths in the next sections.

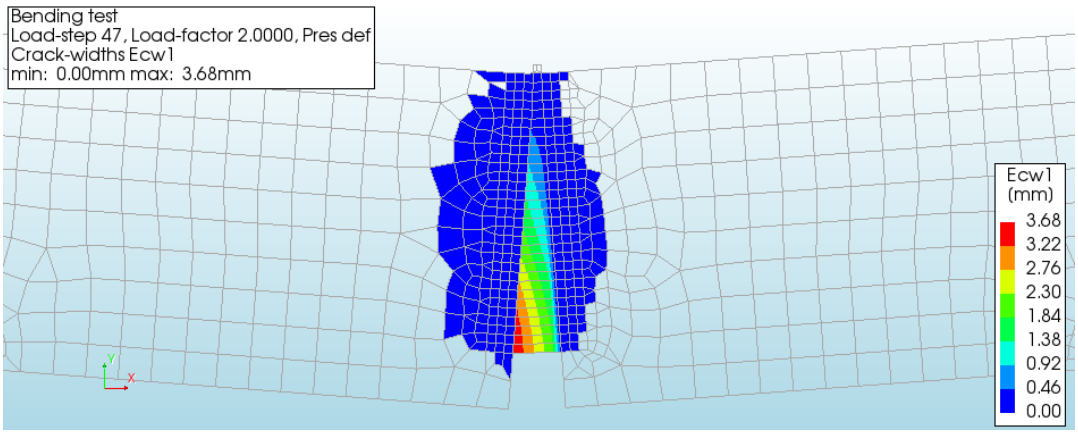

Figure G.7: Crack width results for model E

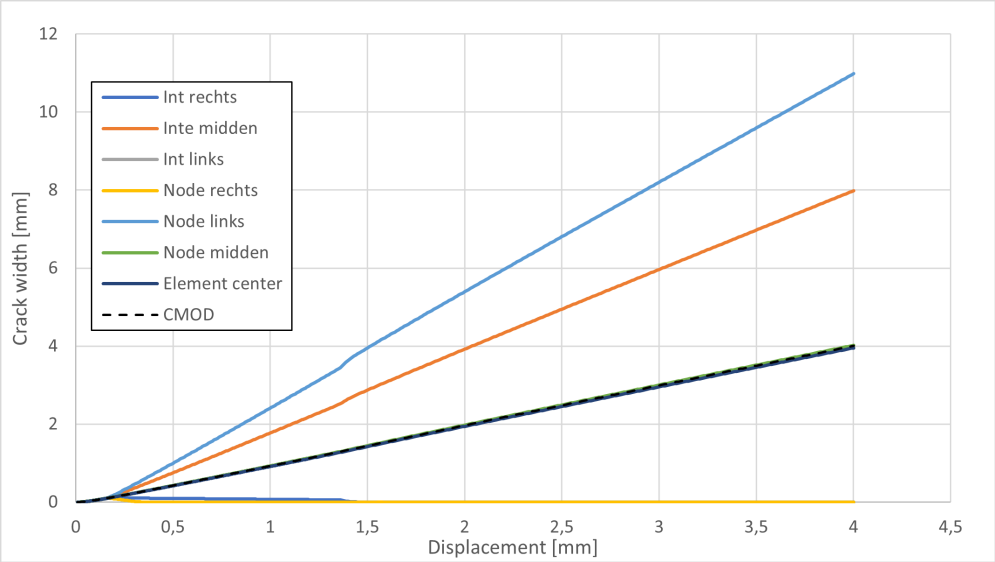

Figure G.8: Crack width values in different locations

Figure G.9 shows that the values of the crack width nicely correspond with each model. Also for the optimized model E, the results are in line with the more elaborate models. It is also observed that the crack width has a more or less 1 to 1 relation with the applied displacement. The cause for this is the geometry of the test specimens.

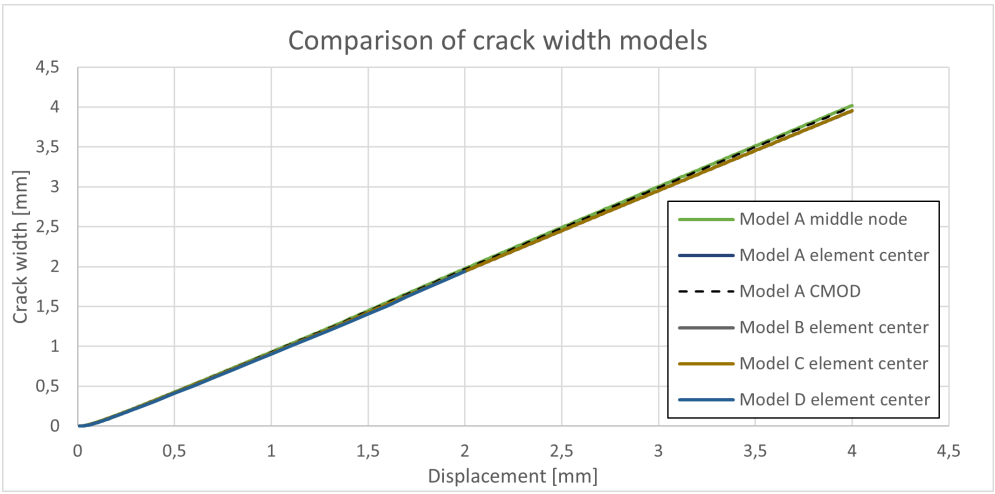

Figure G.9: Crack width values of the different models

The convergence of the model A and E is shown in figures G.10 and G.11. The full model with quite small step sizes has difficulty in convergence. Convergence in the Force criterion seems to not be possible at all. The optimized model shows quite adequate convergence in the energy criterion.

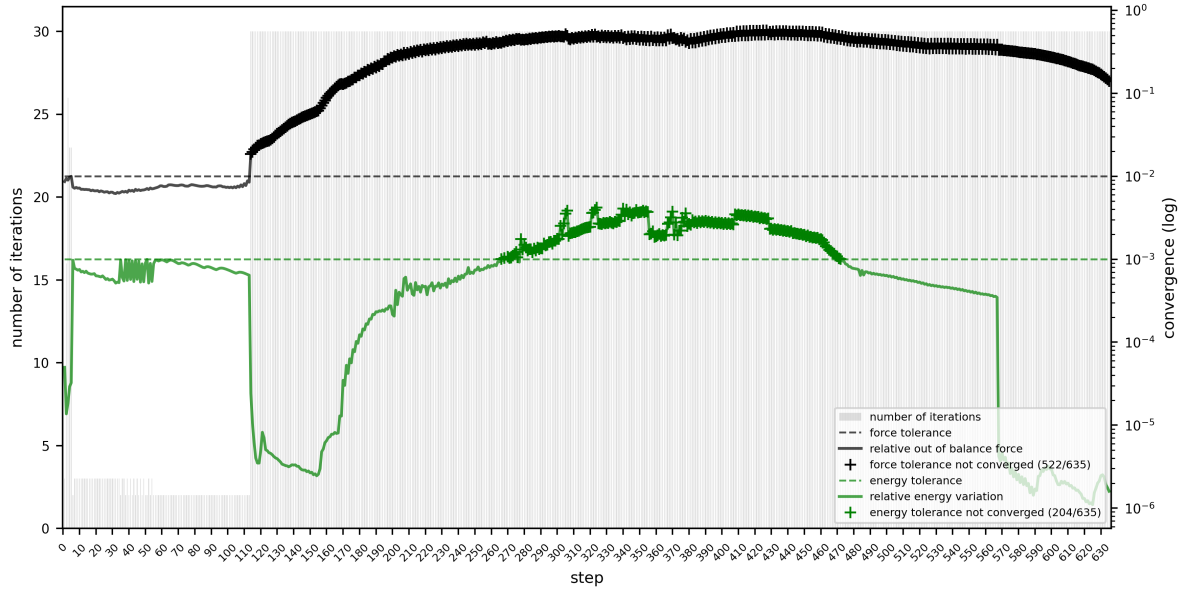

Figure G.10: Convergence of Model A, with step sizes 0.01(5) 0.001(150) 0.005(200) 0.01(280)

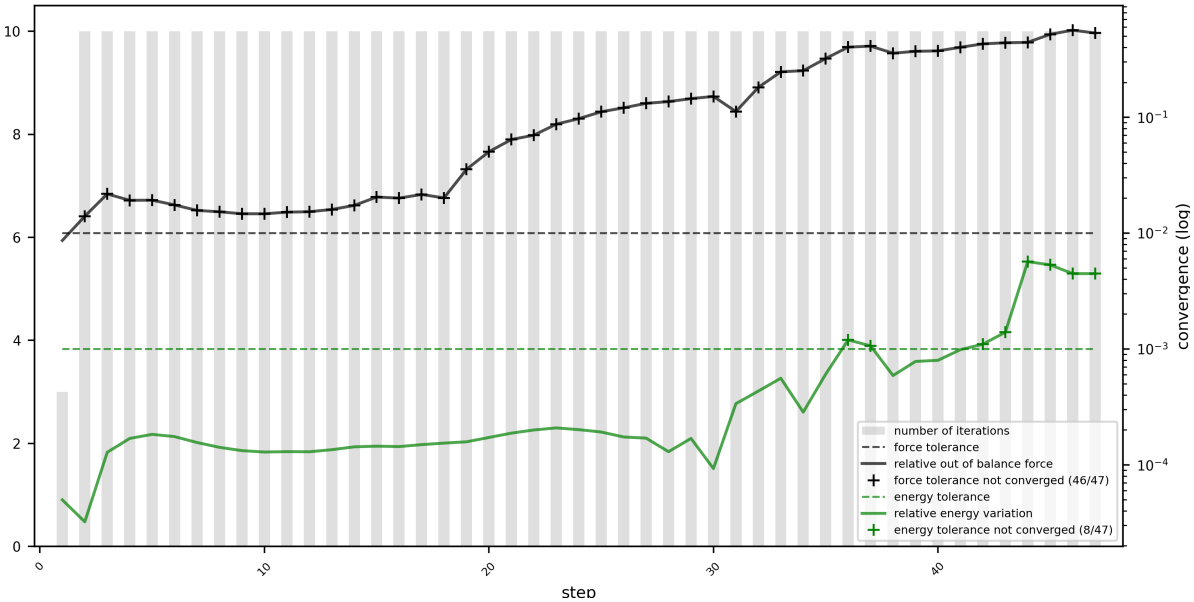

Figure G.11: Convergence of Model E, with step sizes 0.01(30) 0.1(17)

G.4. Probabilistic analysis and results

The model that was optimised for the PROBAB analysis was used to execute three probabilistic analyses. The prescribed deformation was tweaked in such a way that the deterministic FEA returns a crack width of 1.929 mm in the notch. The limit state was based on this value:

$$Z = R - E\{X\} = w_{\text{cr,max}} - w_{\text{cr}}\{X\} = 2\text{ mm} - w_{\text{cr}}\{X\} \tag{LS}$$

For all the models DARS was used.

Where the maximum crack width was set to 2 mm. The first analysis was run with a stochastic limit state. This means that the maximum crack width was set to a Normal distribution with a mean of 2 mm and a standard deviation of 0.1 mm. This model works and returns a failure probability of 0.276. The analytically calculated failure probability that corresponds to this limit state is 0.239.

For the second analysis, the critical limit state parameter was set to a deterministic value of 2mm and the prescribed deformation was made stochastic. A working version of this model was not achieved. In the third model, the FRC Factor was made stochastic with a Normal distribution with a mean of 1 and a standard deviation of 0.1. This model also works but it gives a very small failure probability of 10^{-9} which is not correct.

Since the crack width is directly related to prescribed deformation that is applied, this seems to be a nonsensical model. However, the comparison of the results that are obtained when varying the different parameters might be insightful.

G.5. Experimental reference

In this chapter the model will be run with the material properties from MC 2010, in order to compare it to experimental results.

Material input

As a reference, experimental test data will be used to compare the model. The test results of specimen 3P-SH-40 from the article of Soetens and Matthys (2014) are used to derive the necessary material properties. The mean cube compressive strength $f_{\text{cm,cube}}$ was determined in the experimental program, from which all the other material properties are determined. The characteristic cube compressive strength $f_{\text{ck,cube}}$ is approximated accordingly to Eurocode 2 (EC2) as:

$$f_{\text{ck,cube}} = f_{\text{cm,cube}} - 8\text{ (MPa)} = 68.4 - 8 \approx 60\text{ N/mm}^2 \tag{G.1}$$

Therefore, concrete class C50/60 is assumed, with it's associated properties from EC2. The post-cracking strength of the material can be classified according to the FIB Model code 2010 (MC2010). The following two properties: $5.0 < f_{\text{R1}} < 6.0$ and $f_{\text{R3}}/f_{\text{R1}} = 1.3$, put the material in class 5e. The residual axial strength can be determined from the linear model as described in section 5.6.4 of the MC2010:

$$f_{\text{Fts}} = 0.45 f_{\text{R1}} = 2.43\text{ MPa for } w_{\text{cr}} = 0.5\text{ mm} \tag{G.2}$$

$$f_{\text{Ftu}} = 0.5 f_{\text{R3}} - 0.2 f_{\text{R1}} = 2.44\text{ MPa for } w_{\text{cr}} = 2.5\text{ mm} \tag{G.3}$$

Equation 5.1-9 from MC2010 gives an approximation for the fracture energy since this is not given in the article by Soetens and Matthys (2014). This is necessary to determine the tensile behaviour of regular concrete which intersects with the FRC tensile behaviour to find point C.

$$G_F = 73 \cdot f_{\text{cm}}^{0.18} = 73 \cdot 58^{0.18} \approx 150\text{ N/m} \tag{G.4}$$

Table G.2: Material properties

Material property		Value		Source
Cube mean compressive strength	$f_{\text{cm,cube}}$	68.4	MPa	Soetens and Matthys, 2014
Cube characteristic compr. strength	$f_{\text{ck,cube}}$	60	MPa	NEN-EN 1992
Mean compressive strength	f_{cm}	58	MPa	NEN-EN 1992
Mean tensile strength	f_{ctm}	4.1	MPa	NEN-EN 1992
Residual flexural strength SLS	f_{R1}	5.41	MPa	Soetens and Matthys, 2014
Residual flexural strength ULS	f_{R3}	7.06	MPa	Soetens and Matthys, 2014
Fracture energy	G_F	150	N/m	MC2010

With the fracture energy the properties that are shown in figure G.12 can be calculated:

$$w_1 = G_f / f_{\text{ctm}} = 0.03 \text{ mm} \tag{G.5}$$

$$w_c = 5G_f / f_{\text{ctm}} = 0.18 \text{ mm} \tag{G.6}$$

The graph shown in figure G.13 can be transformed to a stress-CMOD graph in which the following

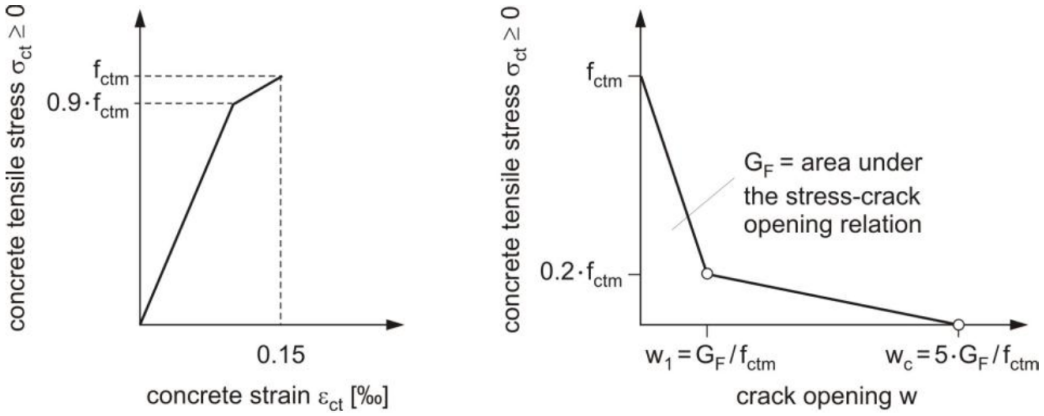

Figure G.12: Schematic representation of the stress-strain and stress-crack opening relation for uniaxial tension in regular concrete. Source: Model Code 2010 (2010)

values can be substituted for the corresponding CMOD values:

$$\begin{aligned} \varepsilon_P &\rightarrow 0 \\ \varepsilon_Q &\rightarrow w_1 \\ \varepsilon_{SLS} &\rightarrow 0.5 \text{ mm} \\ \varepsilon_{ULS} &\rightarrow 2.5 \text{ mm} \\ \varepsilon_C &\rightarrow \text{CMOD}_C \end{aligned}$$

In figure G.13 point C is the crossing between the extension of line segment DE and line BQ. All the values are determined for the different properties and are plotted in figure G.14. The positions C, D and E from figure G.13 correspond with the positions i, j and k from figure G.15 respectively. The exact values are given in figure G.14, which are then used as a input in DIANA.

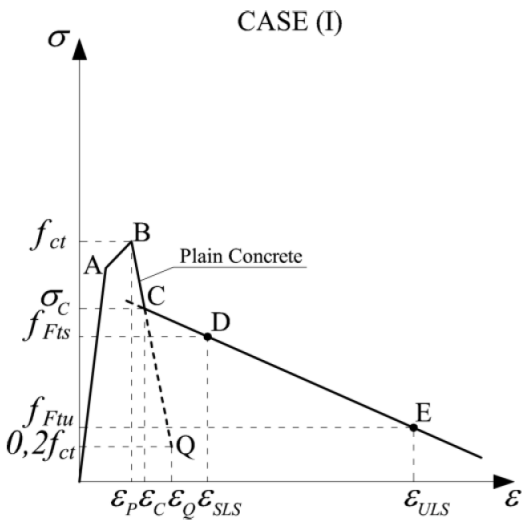

Figure G.13: Stress - strain diagram for the FRC material input.
From Model Code 2010 (2010)

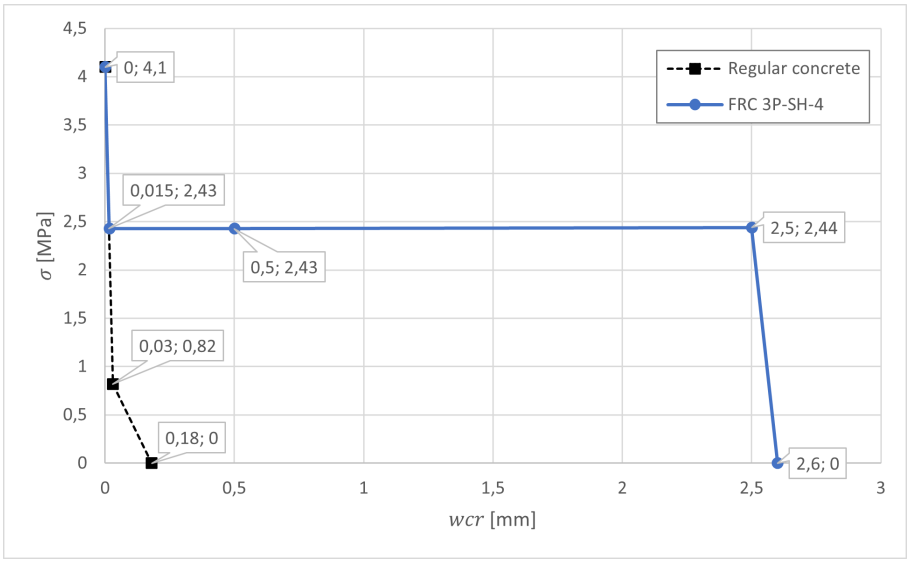

Figure G.14: Stress - CMOD diagram for the FRC material input

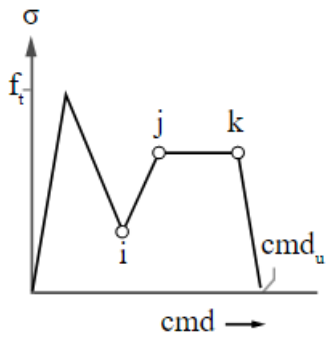

Figure G.15: DIANA FRC crack opening based tensile behaviour model.
From DIANA Documentation (2022)

Results

It is difficult to achieve convergence in this model. The results are shown in figure G.16 and they are compared to the experimental results in figure G.17. However the values of the flexural stress doe seem to compare to the experimental results, until the convergence issues produce the sudden drop. Also the small drop in the flexural stress after reaching the peak in figure G.17 does not occur in the FEM results. This may however have to do with the input material model. Material models exist with a drop after the peak, but this is not the case for the used material model (figure G.14).

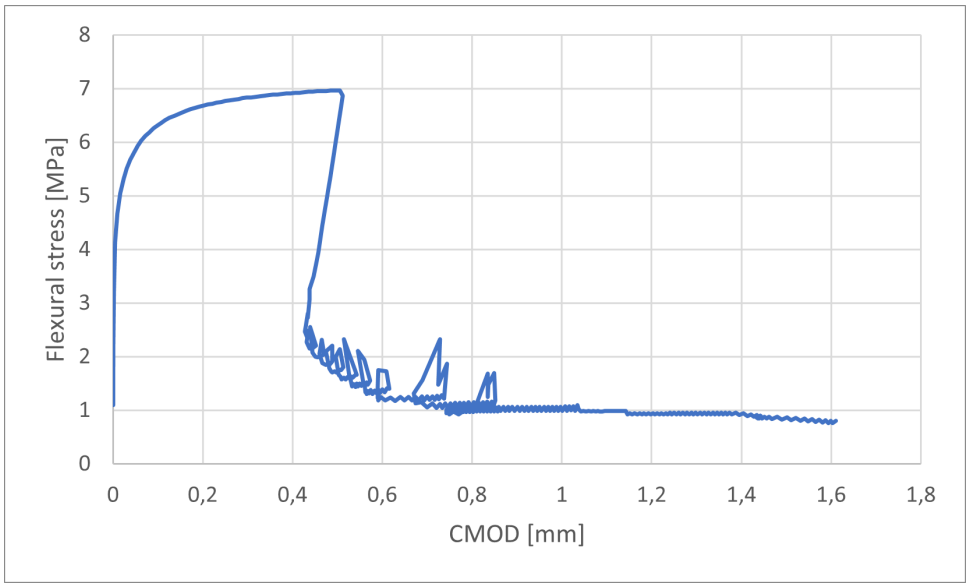

Figure G.16: CMOD-Flexural stress graph of the results

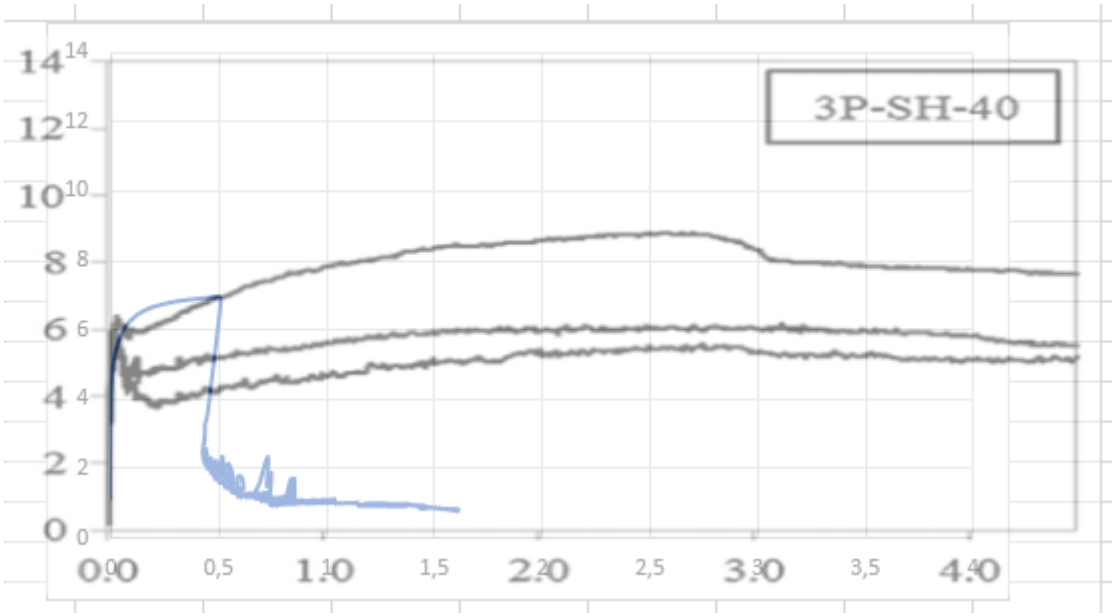

Figure G.17: Comparison of the FE results and the experimental results according to Soetens and Matthys (2014)

In the paper by Soetens and Matthys (2014), the authors also give an approach to reverse engineer the results to find a matching material model. This approach is followed and a new material model is constructed. This is shown in figure G.18. No results are obtained with this model yet due to convergence issues. It can be observed that this material model does include a drop after the peak and the

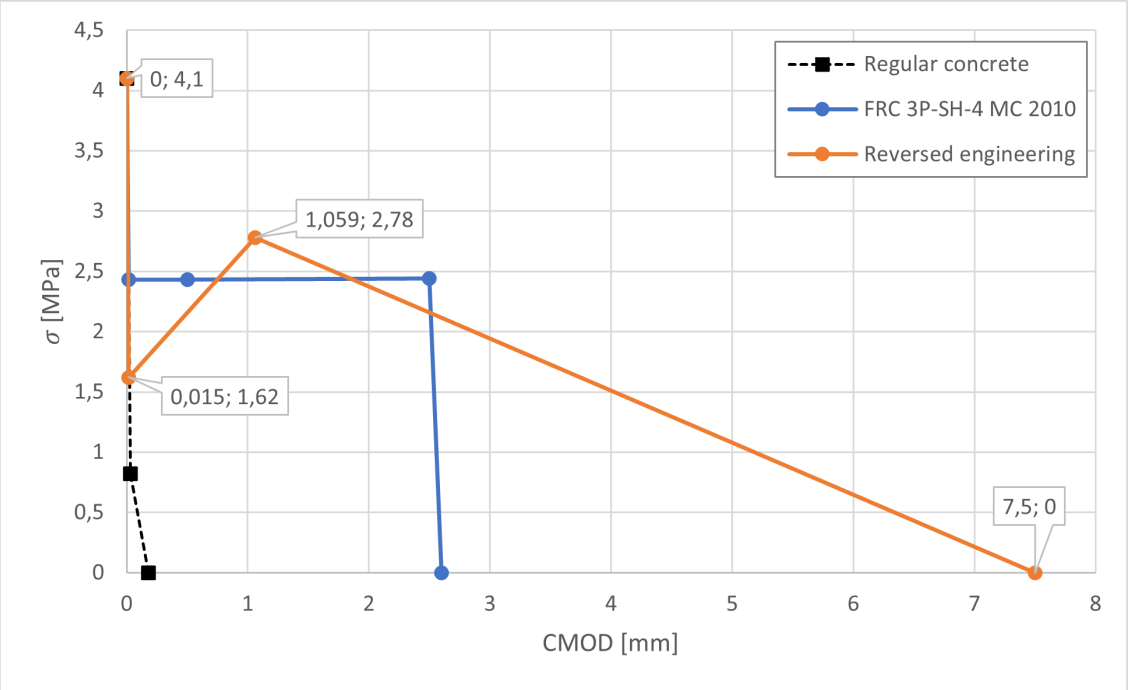

Figure G.18: Input material model according to ”reversed engineering” approach according to Soetens and Matthys (2014)

third point in the graph. It is expected that this will lead to a drop in the graph of the results as was discussed in the previous section.